

# **Improving hydrological process representation in lake and forest dominated watersheds**

by

Ming Han

A thesis

presented to the University of Waterloo

in fulfillment of the

thesis requirement for the degree of

Doctor of Philosophy

in

Civil Engineering (Water)

Waterloo, Ontario, Canada, 2022

© Ming Han 2022

## Examining Committee Membership

The following served on the Examining Committee for this thesis. The decision of the Examining Committee is by majority vote.

External Examiner

Marie-Amélie Boucher  
Professor  
Department of Civil and Building  
Engineering  
Université de Sherbrooke

Supervisor

Bryan Tolson  
Professor  
Department of Civil and Environmental  
Engineering  
University of Waterloo

Internal Member

James Craig  
Associate Professor  
Department of Civil and Environmental  
Engineering  
University of Waterloo Internal Member

Internal Member

Nandita Basu  
Professor  
Department of Civil and Environmental  
Engineering  
University of Waterloo Internal Member

Internal-external Member

Claude Duguay  
Professor  
Department of Geography and  
Environmental  
University of Waterloo

## **Author's Declaration**

This thesis consists of material all of which I authored or co-authored: see Statement of Contributions included in the thesis. This is a true copy of the thesis, including any required final revisions, as accepted by my examiners.

I understand that my thesis may be made electronically available to the public.

## Statement of Contributions

Chapter 2 of this thesis consists of a published paper (Han et al., 2020) co-authored by Dr. Mai, Dr. Tolson, Dr. Craig, Dr. Gaborit, Dr. Liu, and Konhee Lee. I lead the development of the first version of the preliminary ArcGIS version of BasinMaker and the Pan-Canadian Lake-River Routing Product. Dr. Tolson and Dr. Craig and Dr. Tolson provide suggestions on the routing structure and attributes of the routing networks. I did the majority of manuscript drafting with some of this by Dr. Mai. All co-authors contributed to revising the paper.

Chapter 3 of this thesis consists of an unpublished paper for which I am the lead author with co-authors Hongren Shen, Dr. Tolson, Dr. Craig, Dr. Mai, Simon Lin, Dr. Basu, and Dr. Awol. I lead the development of the second version of BasinMaker and the Lake-River Routing Products. Dr. Tolson, Dr. Basu and Dr. Craig provide suggestions on the routing structure and attributes of the routing products. Dr. Mai and Dr. Craig built BasinMaker website. Hongren Shen, Dr. Tolson, and I (as the lead) developed Ontario Lake-River Routing Product. Hongren Shen, Dr. Tolson, Dr. Craig, Dr. Mai and I (as the lead) developed BasinMaker and the North American Lake-River Routing Product documentation. Simon Lin and Dr. Awol extensively tested BasinMaker software.

Chapter 4 of this thesis will be converted into a manuscript. I was primarily responsible for study design, data synthesis and drafting. Dr. Tolson contributed to the study's design and data collection and provided feedback during this study. Dr. Robert Metcalfe and Dr. Jason Leach provided the measurement data for this study.

Chapter 5 of this thesis will be converted into a manuscript. I led the Robin vegetation growth model development and was primarily responsible for study design and drafting. Dr. Tolson, Dr. Craig, Simon Lin, Dr. Leach and Dr. Basu contributed to the study's design and provided feedback on this work during this study. Dr. Leach provided the measurement data for this study. Simon Lin and I preprocessed the data.

## Abstract

Hydrological models are simplified representations of the natural surface water dynamic system. This thesis focuses on improving these representations to make them more realistic and thus more appropriate tools to simulate past and future hydrological behaviors. The two specific hydrological model structural improvements in this thesis focus on the explicit representation of 1) lake representation in complex lake networks and 2) forest growth/disturbance representation in forest headwater catchments.

The first and primary focus of this research is on lake (and reservoir) delineation and subsequent simulation in hydrological models. Lakes and reservoirs have critical impacts on hydrological, biogeochemical, and ecological processes, and they should be an essential component of hydrological and eco-hydrological watershed modelling. Past large-scale hydrological modelling efforts tend to either ignore the impacts of all lakes or explicitly simulate the behavior of only the largest lakes in a watershed. This is practically due to two reasons. First, the difficulties inherent in representing thousands of lakes in various hydrological models. Second, the model without representing lakes can typically provide reasonable streamflow simulation at the watershed outlet. However, the potential impacts of ignoring lakes on the simulated runoff components (i.e., quick runoff, baseflow, infiltration, etc) and streamflow at internal gauges have not been adequately studied.

A suite of Pan-Canadian subwatershed-based lake and river routing GIS products at multiple spatial resolutions has been developed. These are the first routing networks available that explicitly and in a hydrologically consistent way represent lakes for the domain of Canada. The routing networks provide the necessary routing network topology and network attributes to enable vector-based hydrological routing anywhere in Canada. A case study using the Raven hydrological modelling framework to simulate routing from the Hudson Bay watershed shows that eliminating lakes can have a significant detrimental impact on hydrograph quality for some gauge locations and that excluding lakes from large-scale simulations degrades hydrograph quality in lake-dominated watersheds. Results demonstrated the need for a flexible and generic watershed delineation toolbox capable of flexible levels of lake delineation.

An open-source GIS toolbox (BasinMaker) was developed that can automatically and efficiently build vector-based hydrological lake-river routing networks, including flexible discretization choices to represent an arbitrary number of lakes within a watershed. BasinMaker was used to delineate the

North American Lake-River Routing Product v2.1 (available at <http://hydrology.uwaterloo.ca/basinmaker/index.html>) and the Ontario Lake-River Routing Product v1 (available at <https://lake-river-routing-products-uwaterloo.hub.arcgis.com>). Two novel post-processing functions in BasinMaker are ideal customization tools that can simplify the high-resolution large-scale routing networks already delineated by Basin Maker in the above two routing products.

The impacts of ignoring lakes on the simulated runoff components and model performance at internal watershed gauges was investigated by comparing the semi-distributed hydrological model simulation results from two model structures (with and without lakes) for two lake-dominated Northern Ontario watersheds. The larger 4120 km<sup>2</sup> case study watershed model with lakes simulated 316 lakes while the smaller 10 km<sup>2</sup> case study watershed model with lakes simulated 8 lakes. Because of the model compensation behavior, ignoring lakes in the model has significant impacts on the simulated runoff components, which will reduce the quick runoff, increase the infiltration, and increase the baseflow from the soil storage, all relative to the equivalent model that explicitly simulate lakes. Ignoring lakes in a hydrological model will also decrease the model's flexibility/uncertainty in the simulated runoff components in each flow pathway.

The second focus area of the thesis is on forest growth/disturbance modelling. Understanding the impact of disturbance on the eco-hydrological processes in forest headwaters is essential for forest management. Eco-hydrological models are a powerful tool often used to quantify the response of forested catchments to a forest disturbance. However, the forest growth modules in commonly applied eco-hydrological models such as RHESSys and SWAT do not support simulating the forest density, diameter at breast height (DBH), and basal area changes, which is critical for forest describing and assessing management activities, such as forest harvesting and reforestation. Moreover, the vegetation growth modules of eco-hydrological models are typically not modular. Thus, it is difficult for researchers to implement these vegetation growth modules into a different hydrological model, most of which treat vegetation growth in a very rudimentary and indirect fashion.

A vegetation growth library framework (Robin) was developed, which can be easily coupled to any hydrological or land-surface model to add the functionality of crop and vegetation growth functionality. Moreover, a new daily version of the popular 3PG (Physical Processes Predicting Growth) forest growth model, which has been widely used in modelling forest dynamics, was emulated in the Robin vegetation growth library (Robin\_3PG). Robin\_3PG has been successfully compiled with the Raven

Hydrological Modelling Framework (Craig et al. 2020) and then used to build coupled forest growth and hydrological models (Raven\_Robin\_3PG).

The coupled model (Raven\_Robin\_3PG) was applied to a paired-catchment forest harvesting experiment conducted at the extensively-monitored Turkey Lakes Watershed located north of Sault Ste. Marie, Ontario, Canada. The model reasonably simulates the hydrological processes' response to the forest harvest management and the forest's growth and regrowth in the control and forest harvest catchments. Moreover, the coupled model could simulate the response of the two hydrological signatures (annual runoff ratio and Budyko framework) to forest harvest management. In comparison, the model without coupling the Robin\_3PG is unable to simulate these observed responses. The climate inputs and the evapotranspiration process significantly impact the response of the runoff components to the forest disturbance.

## **Acknowledgements**

I would like to thank Dr. Bryan Tolson, my PhD supervisor, for his supervision and support over the last five years.

I would like to thank my thesis committee, Professor Nandita Basu, Professor Claude Duguay, Professor James Craig, and Professor Marie-Amelie Boucher, for their comments and suggestions on this thesis.

I would like to thank Dr. Jason Leach for providing me the forest growth and streamflow measurements.

I would like to thank Dr. Robert Metcalfe for providing me the lake-level observation measurements for the Petawawa watershed.

I would like to thank Dr. Juliane Mai, Hongren Shen and Simon Lin for their help and support in this thesis.

I would like to thank the financial support of this thesis: the Canada First Research Excellence Fund provided to the Lake Futures project of the Global Water Futures Project, the NRCan/Canadian Forest Service G&C Grants #129677 and #129816, and Dr. Tolson's NSERC Discovery Grant.

I would like to thank my wife and my cat for their company over the last five years.

## Table of Contents

Examining Committee Membership.....	ii
Author’s Declaration .....	iii
Statement of Contributions.....	iv
Abstract .....	v
Acknowledgements .....	viii
List of Figures .....	xiv
List of Tables.....	xxiii
Chapter 1 Introduction.....	1
1.1 Overview of surface hydrological modelling .....	1
1.2 Hydrological impacts of lakes .....	3
1.2.1 Function of lakes on routing.....	3
1.2.2 Lake and channel routing models.....	5
1.3 Vegetation growth simulation and monitoring for hydrological modelling .....	7
1.3.1 Function of vegetation growth on hydrological modelling .....	7
1.3.2 Conditioning the hydrological model with remote sensing products .....	8
1.4 Model evaluation metrics in hydrological modelling.....	10
1.5 Research gaps .....	13
1.6 Thesis Contributions.....	13
Chapter 2 Subwatershed-based lake and river routing networks for hydrological and land surface models applied over Canada.....	15
2.1 Summary .....	15
2.2 Introduction .....	16
2.3 Methods .....	18

2.3.1 Pan-Canadian routing networks.....	19
2.3.2 Hydrologic routing with RAVEN.....	25
2.3.3 Routing case study.....	27
2.4 Result and discussion .....	29
2.4.1 The lake-river routing networks .....	30
2.4.2 Impact of lake retention.....	34
2.4.3 Routing network availability and limitation.....	37
2.5 Conclusion.....	38
Chapter 3 Basin Maker 3.0: a GIS toolbox for distributed watershed delineation of complex lake-river routing networks.....	39
3.1 Summary .....	39
3.2 Software and data availability .....	40
3.3 Introduction .....	41
3.4 Overview of the lake-river routing networks produced by BasinMaker .....	45
3.5 Technical implementations.....	47
3.5.1 Overview of BasinMaker Functions.....	47
3.5.2 Methodology in BasinMaker network delineation mode .....	53
3.5.3 Methodology in BasinMaker network post-processing mode .....	57
3.6 BasinMaker Application 1: Development of the North American Lake-River Routing Product v2.1 .....	59
3.6.1 Development of the North American Lake-River Routing Product v2.1 .....	59
3.6.2 Distribution of the North American Lake-River Routing Product v2.1 .....	61
3.7 BasinMaker Application 2: Ontario Lake and River Routing Product v1.....	62
3.7.1 Development of the Ontario Lake and River Routing Product v1 .....	62

3.7.2 Distribution of the Ontario Lake and River Routing Product.....	63
3.8 Limitations.....	64
3.9 Conclusions .....	65
Chapter 4 The impact of ignoring lakes on the simulated runoff components and the value of lake observations in gauged and ungauged watersheds .....	66
4.1 Summary .....	66
4.2 Introduction .....	68
4.3 Material and Methods.....	71
4.3.1 The hydrological model with lakes and without lakes. ....	71
4.3.2 Watersheds and model input data.....	73
4.3.3 The hydrological model.....	76
4.3.4 The model calibration experiment for each research question .....	77
4.4 Results and discussion.....	82
4.4.1 The impact of ignoring lakes on calibrated streamflow and runoff components in each flow pathway. ....	82
4.4.2 How valuable are lake level measurements in the hydrological model calibration in a gauged and ungauged watershed .....	87
4.4.3 Is it a reasonable assumption to estimate lakes' crest width from the lake's drainage area? .....	90
4.5 Discussion .....	93
4.5.1 How other processes may compensate for the ignoring of lakes.....	93
4.5.2 Limitations and future work .....	96
4.6 Conclusions .....	97
Chapter 5 Modelling forest disturbance and growth in hydrological models using the Robin vegetation simulation library .....	99

5.1 Summary .....	99
5.2 Introduction .....	100
5.3 Materials and methods.....	103
5.3.1 The Robin vegetation growth library.....	103
5.3.2 The 3PG forest growth model emulation in Robin.....	105
5.3.3 Site and forest species .....	109
5.3.4 Observations and input data sets .....	111
5.3.5 The Raven and Raven_Robin_3PG hydrological model setups.....	114
5.3.6 Model calibration and evaluation .....	117
5.4 Results and discussion.....	121
5.4.1 Select the best calibration result .....	122
5.4.2 The performance of the selected Raven and Raven_Robin_3PG.....	123
5.4.3 The impact of the forest harvest and forest regrowth on the hydrological processes.....	132
5.4.4 Limitations and future work .....	134
5.5 Conclusions .....	135
Chapter 6 Conclusions and future work .....	136
References .....	141
Appendices .....	167
Appendix A .....	167
A1 The extent of the Hudson Bay watershed.....	167
A2 Attributes in the lake-river routing products .....	167
A3 The hydrological processes used in the Raven model .....	170
A4 The simulated hydrographs and lake levels in Chapter 4 .....	172
A5 Description of the 3PG forest growth model in Robin .....	175

A5.1 Connected Robin with the hydrological model .....	175
A5.2 The input files of the Robin vegetation growth library. ....	177
A5.3 The mathematical equation of the 3PG forest growth model in Robin .....	182
A6 The performance of Raven_Robin_3PG in forest growth modeling.....	191

## List of Figures

- Figure 2-1. An example of watershed delineation results before (A) and after (B) modifying flow directions of lake boundary cells. The two grid cells with black dot are pour points of catchments. The grid cell with red diamond is the pourpoint identified as the lake’s inlet and the grid cell with yellow diamond is the pourpoint identified as the lake’s outlet. The arrows indicate the flow direction of each grid cell. The red arrows indicate the initial flow directions that do not converge to the lake outlet. The blue arrows in (B) indicate corrected flow directions. The different cell colors represent five different delineated catchments. The semi-transparent blue polygon represents a lake and the blue lines mark rivers. .... 20
- Figure 2-2. Drainage basins in Canada (polygon number) with the identifier code from Water Survey of Canada (WSC) and WSC streamflow gauges (black dots) used to estimate bankfull width (BkfWidth;  $w$ ) and depth (BkfDepth;  $d$ ) for the drainage basins Pacific Coastal (01), Yukon (05), Lower Mackenzie (07), Arctic Coast–Islands (08), Keewatin–Southern Baffin Island (16), and Northern Quebec (18) which is colored in yellow. The bankfull width and depth for the other drainage regions in Canada are obtained from Andreadis et al. (2013), which is colored in blue. .... 22
- Figure 2-3. Developed Pan-Canadian routing network L7-Lake1, which is combining the HydroBASINS level 7 product and all lakes with lake area larger than 1 km<sup>2</sup> in HydroLAKES that are connected by the river network. The green polygons indicate the delineated lake catchments in this routing network while the shallow green polygons indicate the delineated non-lake catchments. Blue polygons indicate the lakes and blue lines indicate the rivers. .... 31
- Figure 2-4. Number of lakes included at different lake area bands in the HydroLAKES (blue) and developed products (purple, dark yellow, yellow). “L7-Lake0” means the developed product with HydroBASINS level 7 catchments polygons and lakes with a lake area larger than 0 km<sup>2</sup> in HydroLAKES. “HydroLAKES” means all lakes in HydroLAKES within the product domain. The total number of lakes is 907,599 for HydroLAKES, 86,991 for L12-Lake0, 68,490 for L9-Lake0, and 20,708 for L7-Lake0 (see Table 2-4). .... 32
- Figure 2-5. Percentage of total lake area correspond to cumulated lake area in different drainage regions. “L12-Lake0” means the plotted relationship is developed using lakes in the developed Pan Canadian product, which is a combination of HydroBASINS level 12 catchments polygons and lakes with a lake area larger than 0 km<sup>2</sup> in HydroLAKES. “06GD001”, “03MB002” and

“06LF002” means the plotted relationship is developed using lakes in the drainage region controlled by stream flow gauge “06GD001”, “03MB002” and “06LF002” respectively. More detailed information about streamflow gauge can be found in Table 2-3. .... 33

Figure 2-6. A) Uncalibrated routing model performance (Nash-Sutcliffe Efficiency NSE) at 15 gauging stations (Table 2-3) using various lake scenarios (Table 2-1). Gauges in A are sorting of results by lake area coverage. The lake coverage is the ratio between total lake area in each gauge’s drainage region and the total drainage area of each gauge. The NSE is computed using daily average flows for the simulation period from Jan 1, 2007 to Oct 7, 2010. For all simulations we used the L8-Lake0 as a setup and deactivated lakes below certain areas as indicated in the legend. “Base scenario” means all lakes in the lake-river routing structure were active; “Lake1” means lakes with a lake area smaller than 1 km<sup>2</sup> were inactive compared to the base scenario. “NoLake” means all lakes in the base scenario were inactive and hence the simulation was performed without any lake. B) the impact of the lake coverage on the NSE differences between base scenario (All lake) and no lake scenario. .... 35

Figure 2-7. Hydrograph simulated at gauge 12 (06GD001) by the base scenario (i.e., L08-Lake0; blue line) and the no lake scenario (i.e., L8-NoLake; green line) compared with the observed hydrograph (dashed line). The “Base scenario” means all lakes in the lake river routing network were active; the “NoLake” means all lakes in the base scenario were inactive. The simulation period is Jan 1, 2007 to Oct 7, 2010. .... 37

Figure 3-1. Vector-based routing structure without considering lakes (A) and with lakes (B). The CL represents connected lakes (CL), which are lakes with a lake outlet that is explicitly connected to a downstream non-zero length river channel in the routing structure. The NCL represents non-connected lakes (NCL), which denotes lakes that are defined to drain to the downstream routing network but do not directly flow into an explicit river channel. .... 46

Figure 3-2 Workflow, including inputs and outputs, of the BasinMaker network delineation mode functions for generating a hydrological routing network with lakes and rivers given a DEM and a lake polygon layer. Notes: a) Flow direction raster dataset is optional user input here. b) The channel profile coefficient map to define bankfull channel widths and depths across the extent can alternatively be replaced by coefficients that are constant across the project extent. .... 49

- Figure 3-3. An example BasinMaker intermediate routing network output from ‘Generate\_Hydrologic\_Routing\_Attributes’ (Function #4 in Figure 3-2), in which the subbasins covered by the same lake did not get merged into one lake subbasin yet. This function updates geometry attributes and estimates hydrological parameters for the subbasins, lakes, and rivers in the intermediate hydrological routing network output from Function #3 in Figure 3-2. Note the methodology for delineating control points of headwater subbasins is discussed in Section 3.5.2. .... 50
- Figure 3-4. Example BasinMaker output from ‘Remove\_Small\_Lakes’ function (C and D) and ‘Decrease\_River\_Network\_Resolution’ function (E and F) using intermediate hydrological routing network (A) as input. C) and D) are the intermediate hydrological routing network and the final hydrological routing network, respectively, output from the ‘Remove\_Small\_Lakes’ function (minimum lake area thresholds of 6 km<sup>2</sup> for both CL and NCL). E) and F) are the intermediate hydrological routing network and the final hydrological routing network, respectively, from the ‘Decrease\_River\_Network\_Resolution’ function (minimum subbasin area threshold of 23 km<sup>2</sup>). B) is the final hydrological routing network corresponding to the input intermediate hydrological routing network (A). .... 52
- Figure 3-5. An example of BasinMaker intermediate and final delineation results for the four processing steps detailed in section 3.5.2 (functions #2 through #5 in Figure 3-2). (A) The initial stream network and routing structure without considering lakes from function #2 in Figure 3-2, overlaid with a lake polygon for reference. (B) The intermediate routing network after adding the lake’s inlets and outlet as new subbasin outlets into the initial routing structure, a part of function #3 in Figure 3-2. (C) The intermediate routing network after correcting the flow direction of some lake boundary cells (UBCs), which is the aggregate output from function #3 in Figure 3-2. Note that function #4 in Figure 3-2 will calculate hydrological attributes for subbasins, lakes and rivers in the intermediate routing network of (C). (D) The final routing network delineation results after merging partial lake subbasins from function #5 in Figure 3-2. .... 56
- Figure 3-6. Example vector-based routing networks from (A) BasinMaker v3.0 and (B) BasinMaker v2.0. The hydrological routing networks from BasinMaker v2.0 do not include additional subbasin control points at the beginning of any of the headwater river reaches (defined by the flow accumulation threshold) while v3.0 does include some of these as described previously.

Connected Lakes (CL) and Non-Connected Lakes (NCL) are as defined in previous figures.  
 ..... 60

Figure 3-7. An example of the final routing network in the developed North American Lake-River Routing Product v2.1 and multiple simplifications of the routing networks produced with BasinMaker v3.0 for the 4000 km<sup>2</sup> Petawawa river watershed in Ontario, Canada. (A) full resolution North American lake-river routing network with 557 subbasins and 369 lakes. (B) Final post-processed routing network obtained from using ‘Remove\_Small\_Lakes’ function (thresholds = 5 km<sup>2</sup>). Further post-processed final routing network obtained from using the ‘Decrease\_River\_Network\_Resolution’ function (threshold = 200 km<sup>2</sup>) using routing network in (B) as the input network. Note the network in (C) now has only 58 subbasins and 13 lakes.  
 ..... 61

Figure 3-8. Screenshot of the North American Lake-River Routing Product download website. The popup menu appearing after clicking on a sub-region shows details about the identifier of the product, a download link for the routing network itself as well as a link to download the outline of the region (in shapefile and geoJSON format). ..... 62

Figure 3-9 Screenshot of the Ontario Lake-River Routing Product download website (main page). The Export option in the left is linked to a routing product download site. Google Colab (picture of colab text) in the right is linked to a Google Colab notebook, which enables users to easily simplify the OLRRP via BasinMaker without having to install anything on their local machine. .... 64

Figure 4-1. A schematic overview of the hydrological model without lakes (A) and with lakes (B). The  $RO_l$  is the runoff generated from the land HRUs, and the  $RO_w$  is the runoff generated from the water HRU. The  $Q_{up}$  is the total streamflow from upstream subbasin(s). The  $Q_o$  is the streamflow released from the lake outlet. The  $Q_i$  is the amount of runoff generated from land HRUs within a lake subbasin that reaches the lake after the in-catchment routing process. . 72

Figure 4-2. The delineated watersheds and observation station locations for the hydrological model without lakes (A) and with lakes (B) for the Petawawa watershed. The water level observation gauges and climate stations exist in A and B despite not being shown in both. CL represents connected lakes, and NCL represents non-connected lakes. .... 74

Figure 4-3. The delineated watersheds and streamflow observation station locations for the hydrological model without lakes (A) and with lakes (B) for the Turkey Lake watershed. The observation

stations exist in both A and B despite not being shown in both. CL represents connected lakes, and NCL represents non-connected lakes..... 75

Figure 4-4. The model performance at watershed outlet (calibration) streamflow gauge (02KB001) and internal (validation) channel water level gauges (Crow, LM, and NC) from the hydrological model explicitly simulating lakes (scenario 1-1L) and the model ignoring lakes (scenario 1-1) in the Petawawa watershed. See Table 4-1 for scenario descriptions. For each model scenario, the performance metric (an optimal value of 1.0 in all cases) was calculated from an ensemble of 40 parameter sets, each derived from an independent calibration trial. The calibration budget for each trial was 4000. The metric for channel water level gauges is the Pearson rank correlation coefficient between measured water levels and simulated discharge. The metric for the streamflow gauge 02KB001 is the Kling-Gupta Efficiency (KGE) coefficient between simulated and observed streamflow..... 83

Figure 4-5. The model performance at watershed internal (validation) and outlet (calibration, S5) streamflow gauges from the hydrological model representing lakes (scenario 1-2L) and ignoring lakes (scenario 1-2) in the Turkey Lake watershed. See Table 4-1 for scenario descriptions. For each model scenario, the performance metric was calculated from an ensemble of 40 parameter sets, each derived from an independent calibration trial. The calibration budget for each trial was 4000. The calibration period is from 1985 to 1996, while the validation period is from 1997 to 2012..... 84

Figure 4-6. The aggregated daily runoff components from the hydrological model representing lakes (1-1L and 1-2L) and ignoring lakes (1-1 and 1-2) in the Turkey Lake watershed (1-2L and 1-2) and Petawawa watershed (1-1L and 1-1) at each flow pathway. All scenarios are calibrated to the streamflow measurements at the watershed outlet. See Table 4-1 for scenario descriptions. For each model scenario, the daily fluxes were simulated from an ensemble of 40 parameter sets, each derived from an independent calibration trial. The aggregated daily runoff components are calculated by averaging the simulated daily runoff components of each HRU over the entire watershed and then averaging the results of the previous step over the entire non-ice (from April to the end of November) simulation period. The calibration budget for each trial was 4000..... 86

Figure 4-7. Comparison of different calibration formulations for the Petawawa hydrological model that explicitly simulates 369 lakes. (A) The model performance at the Petawawa watershed outlet

streamflow gauge from scenarios that is only calibrated to streamflow measurement at the watershed outlet (scenario 2-1a) or calibrated to both streamflow and lake level measurements (scenario 2-1b and 2-1c). Scenario 2-1c includes 15 additional lake crest width calibration parameters for each monitored lake compared to 2-1a and 2-1b. See Table 4-2 for scenario descriptions. (B) the aggregated average daily quick runoff across all HRUs from scenarios 2-1a, 2-1b, and 2-1c. For each scenario, the model performance metric and the simulated quick runoff are estimated from an ensemble of 40 parameter sets, each derived from an independent calibration trial. The calibration budget for each trial was 4000. .... 88

Figure 4-8. The simulated streamflow KGE at the outlet in validation mode from the hydrological model calibrated to fifteen lake level gauges (scenario 2-2a) and the hydrological model calibrated to one lake level gauge at lake Cedar (scenario 2-2b). See Table 4-2 for scenario descriptions. For each scenario, an ensemble of 40 parameter sets, each derived from an independent calibration trial, is used to predict streamflow/lake level and calculate evaluation metrics at the watershed outlet gauge ( $KGE_Q$ )..... 90

Figure 4-9. The relationship between calibrated crest width of gauged lakes and their drainage area ( $W \sim DA$ ) from the hydrological model calibrated to both streamflow and lake measurements (scenarios 2-1b and 2-1c) after logarithmic transformations. Each lake's crest widths in scenario 2-1b are estimated using two coefficient parameters in Equation (4-4) (grey lines). While 2-1c directly optimizes the lake crest parameter of each gauged lake (red boxplot). See Table 4-2 for scenario descriptions. Each scenario is calibrated using 40 independent calibration trials. The Redline is the fitted linear relationship using the optimized lake crest width from the best trial of 2-1c. The  $R^2$  and the p-value of this linear relationship are 0.75 and 0.0012, respectively. The black line is the initial  $W \sim DA$  relationship. .... 92

Figure 4-10. The model performance for predicting gauged lake levels when the model is calibrated to streamflow and lake level measurement (scenarios 2-1b and 2-1c). From left to right, the lake's drainage area is increasing. Scenario 2-1c includes 15 additional lake crest width parameters for each lake with lake level gauge compared to 2-1b. See Table 4-2 for scenario descriptions. For each scenario, an ensemble of 40 parameter sets, each derived from an independent calibration trial, is used to predict lake level and calculate evaluation metrics at each lake level gauge ( $KGED$ , Equation (4-7))..... 93

Figure 4-11. The annual cumulative watershed averaged daily lake evaporation ( $E_{lake}$  in mm over the total surface areas of the simulated lakes and the difference ( $R_{in-out}$ ) between the input ( $R_{in}$ ) and output ( $R_{out}$ ) of the routing storage from the best trial of the model representing lakes at Turkey Lake (A, scenario 1-2L) and Petawawa (B, scenario 1-1L) watershed (Table 4-1).  $R_{in}$  is the sum of all runoff components and the precipitation over the lakes. The  $R_{out}$  is the watershed outlet discharge..... 94

Figure 4-12. The cumulative watershed averaged soil evaporation ( $E_{soil}$ ), the difference between fluxes moving in ( $S_{ET_{in}}$ ) and out ( $S_{ET_{out}}$ ) of the ET soil storage ( $S_{ET_{in-out}}$ , top two soil layers), and the difference between fluxes moving in ( $S_{GW_{in}}$ ) and out ( $S_{GW_{out}}$ ) of the groundwater soil storage ( $S_{GW_{in-out}}$ , bottom soil layer) from the best calibration trial of each scenario in Table 4-1. The  $S_{ET_{in}}$  is the infiltration, and  $S_{ET_{out}}$  includes the baseflow from two soil layers and the percolation of the second soil layer. The  $S_{GW_{in}}$  is the percolation from the second soil layer, and the  $S_{GW_{out}}$  is the baseflow of the third soil layer. .... 96

Figure 5-1. The conceptual structure of the Robin vegetation growth library. .... 105

Figure 5-2. The location of the paired-catchment forest harvesting experiment at the Turkey Lakes Watershed. Subbasin C31 and C32 are two headwater catchments. The clear-cut treatment block is the extent of the clear-cut forest treatment, which removed trees with DBH > 10 cm. The forest sampling plots are the location of the forest measurements. Moreover, LAI measurements and the reduced simple ratio (RSR) (Chen et al., 2002) from Landsat images of each sampling plot will be averaged for each LAI group to develop a relationship between measured LAI and the RSR. The derived relationship will be used to generate catchment averaged LAI time series from Landsat images for control and harvest catchment, respectively..... 110

Figure 5-3. The derived relationship between the averaged observed LAI of each sampling group and the averaged reduced simple ratio vegetation index (RSR, Chen et al., 2002) of each sampling group. The scenes from Landsat are used to calculate the RSR of each LAI sampling plot. The LAI sampling plots in Figure 5-2 are grouped into 17 groups. The measured LAI and the RSR of each sampling plot are used to calculate their group averaged values. The fitted relationship between the averaged LAI and the Landsat RSR of each group is:  $LAI = 7.5 - 7 \times \exp(-0.17 \times RSR)$  with  $R^2 = 0.58$ ..... 113

Figure 5-4. The performance of the non-dominated and the selected solutions of Raven and Raven\_Robin\_3PG in the calibration period (A) and validation period (B). The non-dominated solutions of both models are generated from combining the non-dominated solutions of three independent multi-objective model calibration trials and then identifying only those solutions that are non-dominated across all trials. The  $KGE_{Q,s}$  (Equation (5-8)) is the KGE of the averaged streamflow performance from harvest and control catchment during the summer period (July, August, and September). The  $KGE_{Q,ns}$  (Equation (5-9)) is the KGE of the averaged streamflow performance from harvest and control catchment during the non-summer period. The model calibration period is from 1984 to 1996 (before forest harvest), and the model validation period is from 1998 to 2012 (after forest harvest)..... 123

Figure 5-5. The observed and simulated hydrograph from the selected Raven\_Robin\_3PG and Raven calibration solutions at both control and harvest catchment during the first two years of the forest harvest. The forest harvest happened in the year 1997..... 126

Figure 5-6. The observed and simulated hydrograph from the selected Raven\_Robin\_3PG and Raven at both control and harvest catchment during the second two years of the forest harvest. The forest harvest happened in the year 1997..... 126

Figure 5-7. The Landsat-derived LAI observations and the Raven\_Robin\_3PG simulated LAI at harvest(A) and control(B) catchments..... 128

Figure 5-8. The simulated and observed forest development in the control and forest harvest catchment. The dashed arrow represents the forest harvest event in the forest harvest catchment. In the pre-harvest period, the simulated forest growth in control and harvest catchment overlap with each other. The forest development in this period is from the lower right to the upper right. The forest harvest management in the harvest catchment reduces the forest density. Thus, the forest development in the forest harvest catchment at the beginning of the post-harvest period moves to the upper left of the plot (the dashed arrow). ..... 129

Figure 5-9. The annual summer runoff ratio difference calculated from observations and the selected Raven and Raven\_Robin\_3PG models. The difference is between the annual summer (July, August, and September) runoff ratio of the harvest ( $RO_{harvest}$ ) and control ( $RO_{control}$ ) catchment. .... 130

Figure 5-10. Time series of 3-year moving averaged evaporative index (EI) versus aridity index (AI) for the forest harvest catchment (A, B, and C) and the control catchment (D, E, F) in the pre-

and post-harvest period. The EI and AI is calculated from observations (A and D), the selected Raven\_Robin (B and E), and the selected Raven (C and F). The Fu-type Budyko curve is developed using 3-year moving averaged EI and AI in the pre-harvest period..... 131

Figure 5-11. The Raven\_Robin simulated yearly averaged fluxes during the summer (July, August, and September) at the harvest catchment and the control catchment. The CI represents the canopy interception. The Inf represents the infiltration. The AET represents the actual evapotranspiration. The PET represents potential evapotranspiration. The QR represents the quick runoff. The BF[i] represents the baseflow from the i (i = 1, 2, 3) soil layer. The simulated daily fluxes in July, August, and September are used to calculate the yearly average value. The vertical black line represents the year when forest harvest management happened..... 133

## List of Tables

Table 1-1. List of channel routing methods in several hydrological models.....	6
Table 2-1. Estimated relationship between drainage area ( $DA$ ) and bankfull discharge ( $Q$ ) ( $Q=k \times DA^c$ ) in six drainage regions. The bankfull width $w$ and depth $d$ are subsequently derived using the estimated bankfull discharge $Q$ (Equation (2-1))......	23
Table 2-2. Seven lake scenarios used in this study. In the base scenario all lakes are included. The number of included lakes is decreasing with each scenario. ....	28
Table 2-3. The 15 streamflow gauges without reservoir impact used for the case study. The gauge name is the streamflow station name of the Water Survey of Canada. The Gauge ID is the identifier of each gauge used in this work. ....	29
Table 2-4. The Pan-Canadian routing networks and their general attributes. For example, the product “L7-Lake0” specifies the lake-river routing structure developed by using HydroBASINS Level 7 products and all lakes in HydroLAKES with lake area larger than 0 km <sup>2</sup> . The table summarizes the number of catchments and lake catchments as well as their average/median area for the various routing networks derived.....	30
Table 2-5. Routing related attributes included in the developed Pan-Canadian lake-river routing network. The name indicates the attribute name used in the provided routing network files. Besides a description and unit of the attributes, it is specified which method or source is used to derive the attribute. ....	34
Table 3-1. Description of the BasinMaker routing network post-processing mode functions. ....	51
Table 4-1. Comparative model scenarios for the first research question: what is the impact of ignoring the presence of lakes in hydrological models. The lake coefficient parameters calibrated are in Equation (4-4) to estimate lake crest width as a function of the lake drainage area. $KGE_Q$ is the Kling-Gupta evaluation metric (KGE) of the watershed outlet streamflow gauge. ...	79
Table 4-2. Designed model scenarios for the second research question: how valuable are lake level measurements in the hydrological model calibration in a gauged (scenarios 2-1a, b, and c) and ungauged watershed (scenarios 2-2a and b). $KGED_L^{15}$ represent the averaged Kling Gupta Deviation ( $KGED$ , Equation (4-7)) of 15 observed lakes. The $KGED_L^{Ce}$ represent the $KGED$ of lake Cedar. $KGE_Q$ represent the Kling Gupta evaluation metric (KGE) of the watershed outlet streamflow gauge. The calibrated crested width parameters of each observed lake from the scenario 2-1c and the calibrated lake crest width equation (Equation (4-4))	

parameters from the scenario 2-1b will be used to answer the third research question: is the power-law relationship between the lake crest width and the lake's drainage area reasonable? ..... 81

Table 5-1. The performance statistics of the Raven\_Robin\_3PG and Raven in streamflow prediction at the calibration and validation periods. The *PCT\_BIAS* is the percent bias between the simulated and the observed streamflow. The negative *PCT\_BIAS* means the model underestimates the streamflow. The *KGE<sub>Q,s</sub>*, the *KGE<sub>Q,ns</sub>*, and *KGE<sub>Q,f</sub>* are the *KGE* of the streamflow during the summer (July, August, and September), the non-summer, and the full period of each year. .... 125

# Chapter 1

## Introduction

### 1.1 Overview of surface hydrological modelling

The surface water hydrological modelling process can be viewed as an attempt to mathematically describe the dynamics of the surface water system in the region of interest based on the observations and process knowledge we have. However, developing a model that can correctly describe all hydrological processes in the watershed is impossible with current measurement technology and knowledge (Clark et al., 2016). One of the main reasons is that the dynamics of the surface water system are invisible to us. For example, it is impossible to measure either fluxes, state variables or physical properties at every location of the watershed. Generally, we only have some meteorology measurements such as precipitation and air temperature at several points of a watershed, the streamflow at the outlet of a watershed, and a soil type map which can only provide *a priori* estimation of the spatially averaged physical properties. Thus, the hydrological model we build is a simplified representation of the system and different simplification strategies are available, which causes us to hydrological models with different structures and errors (Clark et al., 2008; Gupta et al., 2012).

Generally, four steps are needed to build a hydrological model: developing the conceptual model, specifying the corresponding mathematical model, specifying the computational model, and developing model calibration and validation strategies (Gupta et al., 2012). First, different conceptual strategies are available. For example, we may choose to conceptualize the soil profile into two layers or three layers and may choose to include or neglect the exchange between water bodies and groundwater (Chlumsky et al., 2021; Clark et al., 2008; Craig et al., 2020). Second, different process description equations are available for each hydrological process. For example, the channel routing process can be simulated by diffusive wave model (Cappelaere, 1997) or Muskingum model (Khan, 1993). Thirdly, in the stage of building a computational model, different spatial and temporal aggregation strategies and numerical methods for solving ODE/PDE equations are available (Fenicia et al., 2016; Kavetski et al., 2002; H. Liu et al., 2016). Finally, different strategies are available even in the model calibration and validation stage. For example, we need to make a decision on what kind of data is needed for training our model (Baroni et al., 2019; Wöhling et al., 2015), and how to separate calibration and validation datasets (Razavi & Tolson, 2013; Shen et al., 2022), which metrics should be used for model evaluation (Clark et al., 2021; Fowler et al., 2018; Pechlivanidis et al., 2014), how to select parameters that will be

optimized (Cuntz et al., 2015; Göhler et al., 2013) and which algorithm will be used to optimize the model we built (Kuczera, 1997; Tolson & Shoemaker, 2007).

The well-known quote by statistician George Box is key to remember: “All models are wrong, but some are useful”. To build a useful model, the development of the model should account for the model purpose. For example, if the model's purpose is for flood forecasting, a statistical model (e.g., Shahzad and Plate (2014)) or a simple conceptual model such as GR4J might be appropriate (Gibbs et al., 2018). In contrast, if the model purpose is for watershed agriculture drought evaluation and nutrient management, a semi-distributed or distributed surface hydrological model is preferred because besides streamflow, the spatial distribution of hydrological fluxes and states such as evapotranspiration, soil moisture and flow partitioning also produced by the model is important for these purposes (Ilampooranan et al., 2019; Narasimhan & Srinivasan, 2005; Shafii et al., 2019). Even with an appropriately chosen model, the utility of the hydrological model depends on the resulting model prediction uncertainties/errors, which can come from measurement noise in both input variables, such as precipitation (Kavetski et al., 2006; Lu et al., 2013; Vrugt et al., 2008) and output variables such as streamflow (Ocio et al., 2017), and imperfect model structures induced by spatial and temporal aggregations (Kavetski & Clark, 2010; H. Liu et al., 2016), conceptualizing the real dynamic systems (Foglia et al., 2013; Günther et al., 2019; Gupta et al., 2012), incorrect mathematical equations (Bulygina et al., 2011; Clark et al., 2008) and compensating model parameters (Thyer et al., 2009). Efforts to try to reduce hydrological model prediction uncertainties/errors include using 1) hydrological signatures (M. Hrachowitz et al., 2014; Shafii et al., 2017) and other related measurements in the model training procedure (Lerat et al., 2012; McMillan et al., 2012; Nijzink et al., 2018; Son & Sivapalan, 2007; Zink et al., 2018); 2) the multi-model approach to have an ensemble result instead of using single model prediction (Clark et al., 2011; Moges et al., 2016); 3) data assimilation approaches to reduce the impact of the imperfect model structure (Khaki et al., 2018; Pathiraja et al., 2016).

This hydrological model development process can be more challenging when the nonstationary nature of the hydrological system is considered, which may be caused by the rapid changing of the landuse in the watershed (Muma et al., 2011; Zhou et al., 2013), model structural deficiencies (Hwang et al., 2018; Westra et al., 2014) and other factors (Westerberg et al., 2011). The nonstationary behavior of the hydrological system can be accounted in different ways. For example, a vegetation growth model (additional processes) can be included to account for dynamic vegetation impacts due to changes in temperature and precipitation (Hwang et al., 2018), and a time-varying parameter strategy can also be

used to account for inappropriate representation of hydrological processes (Pathiraja et al., 2016; Westra et al., 2014).

Overall, hydrological modelling is a process of learning. Our understanding of the hydrological dynamic system increases when we attempt to build and apply a hydrological model, analyze and rectify prediction errors and then quantify and potentially reduce model prediction uncertainties.

## **1.2 Hydrological impacts of lakes**

### **1.2.1 Function of lakes on routing**

Lakes and reservoirs play a critical role in routing processes (Huziy & Sushama, 2017). The function of lakes on hydrological response has been evaluated by many researchers from different perspectives. First, the lake routing process has been studied via detailed observations and modelling in several headwater catchments (Leach & Laudon, 2019; Mielko & Woo, 2006; Christopher Spence, 2000; Woo & Mielko, 2007). Observations from headwater catchments in a typical Canadian subarctic region shows that lakes are major storage components in these watersheds (Mielko & Woo, 2006). The level of lakes will be increased with the runoff generated in the spring snowmelt period and the lake outflow will be generated when snowmelt meets the lake's storage deficit, which means that the lake's level is higher than the lake's outlet elevation (Christopher Spence, 2006; Woo & Mielko, 2008). In the continued subarctic dry summer period, lakes may disconnect to the downstream routing network when the lake level drops below the lake's outlet elevation due to the lake's high evaporation and relatively low precipitation rate (Bowling & Lettenmaier, 2010). In a semi-arid environment, Woo and Mielko (2007) report that summer rainfall was sometimes insufficient to overcome the storage deficit to re-establish flow connectivity among all lakes.

In the aforementioned processes, the function of lakes on routing modelling can be summarized into three aspects: 1) the headwater lake storage deficits are very important in the timing and volume of runoff that is transmitted to downstream (Bowling & Lettenmaier, 2010; Mielko & Woo, 2006; Christopher Spence, 2000). Spence (2000) show that in Skeeter Lake Basin, the majority of snowmelt,  $52 \pm 9$  mm or 45 - 64%, went to lake storage. This only left 5 - 9% of the snowmelt ( $7 \pm 2$  mm) available for transport downstream (Spence, 2000). In the Shadow Lake catchment, outflow constitutes 40% of total melt and rainfall in the snowmelt season (Mielko and Woo, 2006). 2) The active contributing area or the flow connectivity of the watershed is controlled by the lakes (C. Spence, 2007; C. Spence et al.,

2010, 2019; Woo & Mielko, 2007, 2008). The active contributing area is the region that not only generated runoff but also hydrologically connected to the downstream of the watershed. For example, Spence et al. (2010) show the active contribution area for the Lower Martin Lake watershed can reach 100% of the watershed area in the beginning of May because of the snow melting, and reach to a minimum 10% of the watershed area at the end of July. 3) The effect of flow attenuation, which will retain water in the lake, smooth the hydrograph at the lake outlet and increase the evaporation lost (Woo and Mielko, 2007).

Several studies include only large lakes (for example  $> 100 \text{ km}^2$ ) into the routing modelling for global and regional studies (Guinaldo et al., 2021; Huziy & Sushama, 2017; Zajac et al., 2017). They found that lakes/reservoirs significantly impact simulated flow duration curves, and including them can improve peak flow simulations (Huziy and Sushama, 2017; Zajac et al., 2017). Research also has shown that 12% of the seasonal variations in terrestrial water storage could be attributed to water management reservoirs (Tang et al., 2010). But the size of lakes represented in these studies were subjectively determined (Huziy and Sushama, 2017; Zajac et al., 2017). Considering the studies on small lakes in headwater catchments, small lakes may also play an important routing role in larger scale modelling applications. Thus, a strategy to objectively select lakes that are important to the routing processes for any given watershed is needed.

The function of lakes on routing is impacted by lake and watershed characteristics. The first characteristic is the relative ratio between lake area and lake drainage area ( $\alpha_{\text{Alake/DAlake}}$ ) (Fitzgibbon & Dunne, 1981; Kusumastuti et al., 2008; Christopher Spence, 2000), which is a factor that describes the lake's storage capacity relative to the total runoff generated in the lake's drainage area. Fitzgibbon and Dunne (1981) found that the lake's impact on hydrograph characteristics such as smoothing and lagging was increasing with the increasing of  $\alpha_{\text{Alake/DAlake}}$ , and the impact of a lake on a hydrograph was significant only when  $\alpha_{\text{Alake/DAlake}}$  was larger than 5%. Similar results are reported by Leach and Laudon (2019). However, results in Woo and Mielko (2007) show that Lois Lake with a low  $\alpha_{\text{Alake/DAlake}}$  of 2% was able to impact the lake outflow, which suggests that the  $\alpha_{\text{Alake/DAlake}}$  ratio alone is not a satisfactory indicator of flow attenuation (Woo and Mielko, 2007). The second factor is the relationship between quick runoff and slow runoff in the lake's drainage area and the lake evaporation rate (Zajac et al., 2017; Mielko and Woo, 2006). In the case of Skeeter Lake, presented by Mielko and Woo (2006), the lake level seldom rises above its outflow threshold. This is because the rate of the lake inflow does not match the rate of lake evaporation, which is attributed to the low ratio between quick runoff and slow

runoff (Mielko and Woo, 2006). Zajac et al. (2017) also found that the watershed with high runoff ratio was more sensitive to lakes in routing modelling. The third factor is the downstream distance between the lake outlet and the point of interest for streamflow estimation and this is measured by the ratio between lake's drainage area relative to the watershed drainage area upstream of the point of interest ( $\alpha_{DA_{lake}/DA_w}$ ) (Leach and Laudon, 2019; Mielko and Woo, 2006). The observation study by Leach and Laudon (2019) show that in a headwater catchment, streamflow contributions from these small lakes can persist (e.g., are a non-negligible part of the observed hydrograph) at least 4.2 km downstream. The result from Leach and Laudon (2019) indicate that the impact of a lake on routing decreases as  $\alpha_{DA_{lake}/DA_w}$  decreases.

### **1.2.2 Lake and channel routing models**

A routing model is a mathematical procedure which determines the hydrograph at a location in a river or immediately downstream of a lake/reservoir using the input hydrograph known at an upstream location of the river or lake/reservoir (Chow, 1959). Depending on the physical system through which the input hydrograph is routed, the routing model can be classified as reservoir/lake routing or river channel routing.

In most practical situations the dynamic characteristics of an incoming flood wave are significantly damped while passing through a reservoir/lake. The outflow of the reservoir/lake is independent of inflow and uniquely determined by reservoir/lake storage or level and influenced by the outlet and topographical characteristics of the reservoir/lake zone. For these reasons the reservoir/lake routing in hydrological models typically uses a lumped form of the continuity equation and the storage/level discharge relationship of the reservoir/lake outlets. The relationship between lake storage/level and discharge could either be measured or modeled (Bowling & Lettenmaier, 2010; Craig et al., 2020; Kouwen, 1988; Neitsch et al., 2011). For example, the broad-crested weir equation can be used to simulate the outflow of natural lakes (Bowling & Lettenmaier, 2010; Craig et al., 2020).

Unlike the reservoir/lake routing, the dynamic nature of a river food wave is difficult to be damped. The routed hydrograph estimated at a location of the river is not only influenced by the characteristics of the river reach but also on the inflow hydrograph such as the rate of rise, magnitude of peak and time to peak as well as the magnitude of lateral flow in the river reach (Chow, 1959). Channel routing methods can be essentially grouped into three categories: storage routing methods, Source-to-Sink routing methods, and Saint Venant equation based methods (Li et al., 2013; Shaad, 2018). The storage

routing method utilize the lumped form of the continuity equation and another storage equation, which expresses the storage as a function of inflow and/or outflow in a channel reach (Chow, 1959). The variable storage routing methods as well as the Muskingum method are two storage-based routing methods which have been widely used in runoff simulations because they are easy to be implemented and computationally efficient (David et al., 2011; Miller et al., 1994; Nguyen et al., 2018; Shaad, 2018). The Saint Venant equation based methods (also known as hydraulic routing) are rooted in the classic Saint Venant equations with simplifications at different levels, such as kinematic wave method and linear diffusive wave method, etc. (Chow, 1959). Both the storage based routing methods and the Saint Venant equation based methods require to discretize the river system into several segments. The storage and outflow of each river segments are modeled. However, to improve the efficiency of the routing model, the Source-to-Sink routing method do not spend resources in flow and storage calculations at these interior river segments, which is not the interest of the modelers (Olivera et al., 2000). The grids in which runoff is produced are called source grids while watershed outlet grids are called sink grids. The runoff from each source is convolved with a lumped source-specific response function to determine the contribution of each source to streamflow at the sink. Total streamflow at the sink at any time is the sum of the contribution from all sources in the watershed (Olivera et al., 2000). The application of routing methods in several hydrological models are provided in Table 1-1.

**Table 1-1.** List of channel routing methods in several hydrological models.

Model Name	Channel routing methods
SWAT (Neitsch et al., 2011)	Storage routing methods
Raven (Craig et al., 2020)	Storage routing methods; Linear diffusive wave
HYPE (Lindström et al., 2010)	Storage routing methods
WatFlood (Kouwen, 1988)	Storage routing methods
CaMa-Flood (Yamazaki et al., 2011)	Diffusive wave equation
Mizu-Route (Mizukami et al., 2016)	Kinematic wave tracking; Storage routing method
RAPID (David et al., 2011)	Storage routing methods
MOSART (H. Li et al., 2013)	Storage routing methods
VIC (Lohmann et al., 1996)	Linear diffusive wave
NLDAS-2 (Xia et al., 2012)	Source-to-Sink Routing

## **1.3 Vegetation growth simulation and monitoring for hydrological modelling**

### **1.3.1 Function of vegetation growth on hydrological modelling**

Vegetation plays a critical role in surface hydrological cycle via altering above ground water and energy fluxes and below ground rooting characteristics (Kelly et al., 2016; Zhang et al., 2018). Recent studies showed that large-scale vegetation changes, caused by both climate change and human interventions, have occurred in many regions and are greatly influencing the terrestrial water cycle (Hampton & Basu, 2022; Murray et al., 2012; Woodward et al., 2004). More specifically, the hydrology cycle is influenced by vegetation in following ways: 1) The Leaf Area Index (LAI) or canopy fraction has significant impact on the hydrological partitioning by influence the canopy interception and evapotranspiration processes (K. E. Bennett et al., 2018; Zhang et al., 2018; Zhao et al., 2010). The vegetation phenology or growing season length, which will influence the temporal dynamics of LAI and then further influence the hydrological processes (Hwang et al., 2018). Vegetation phenology is not a steady-state process, and might be influenced by the temperature (Gunderson et al., 2012) and water stresses (Fisette et al., 2013). For the upper Yadkin basin, Hwang et al. (2018) report that vegetation water use, closely mediated by lengthened growing season and accompanying vegetation growth, has been a key source of hydrological non-stationarity at both decadal and seasonal time scales. Therefore, the changes in vegetation density and growing season length have been the key drivers of the relationships between precipitation and runoff, which determine freshwater availability in this region (Hwang et al., 2018). 3) The root distribution of the vegetation is also an important factor to determine the maximum available water for vegetation and to determine actual evapotranspiration and vegetation water stress (Campos et al., 2016).

Understanding and quantifying the interaction between vegetation and the hydrological cycle could contribute to benefit the hydrological model in terms of improving predictability and decreasing the level of uncertainty (Clark et al., 2017; Kelly et al., 2016). Naseem et al. (2015) show in a modelling study, performed across 27 catchments in the Murray–Darling Basin in Australia, that the merged ecohydrological models (combining vegetation growth and traditional hydrological modelling) were capable of improving streamflow prediction compared to hydrological models alone, while also providing as good estimates of LAI as dynamic vegetation models alone. Campos et al. (2016) developed a procedure to estimate the maximum total available water in the root zone and demonstrate that the simulated evapotranspiration and the water stress from a water balance model were improved

with this estimated value (Campos et al., 2016). Hwang et al. (2018) shows that their model performance was improved by including a dynamic vegetation scheme to account for the consistent increases in LAI and annual ET with longer growing seasons. Jaskierniak et al. (2016) show that their model under predicts streamflow during drought periods as it lacks representation of dynamic ecohydrological (vegetation) processes that reduced growth rates or rainfall interception during drought.

Despite the importance of vegetation dynamics, many hydrological models like HYPE (Lindström et al., 2010) and Raven (Craig et al., 2020) do not have a vegetation growth procedure and assume steady-state vegetation conditions. This is not reasonable, as warmer temperatures have led to earlier green-up, delayed senescence, and longer growing seasons (Gunderson et al., 2012). In addition, coupling vegetation growth and hydrological models are needed to understand the spatial distribution of state variables and fluxes for developing watershed management strategies (Rajagopalan et al., 2018). A flexible vegetation growth library, that contains multiple vegetation growth procedures and can be easily coupled with any hydrological model, would benefit a large suite of hydrological models.

### **1.3.2 Conditioning the hydrological model with remote sensing products**

Given the magnitude of errors and uncertainties in most hydrological modelling applications, a model producing a reasonable streamflow simulation result does not mean that we have an accurate simulation of the whole dynamic surface water system, especially for spatial and temporal representation of state variables and fluxes such as actual evapotranspiration (Mendiguren et al., 2017; Rajib, Merwade, et al., 2018; Stisen et al., 2011). Thus, efforts are required to reduce the uncertainties and improve the spatial and temporal representation of hydrological models (Clark et al., 2017). Hydrological model parameter estimation is being increasingly based on remote sensing products with the increasing availability of these products (e.g., Nijzink et al. (2018); Hrachowitz and Clark, (2017)).

The remotely sensed products that have been used for conditioning the hydrological model parameters include: soil moisture (Y. Li et al., 2018; Xie et al., 2018), Snow Cover (Finger et al., 2015) evaporation products (Herman et al., 2018), land surface temperature (Zink et al., 2018), the total water storage from Gravity Recovery and Climate Experiment (Lo et al., 2010) and leaf area index (Naseem et al., 2015; Parr et al., 2015). Generally, these remote sensing products were used in hydrological modelling in three different ways: 1) The products have been used to update and improve the simulated hydrological model state variables with data assimilation techniques (e.g., Alvarez-

Garreton et al., 2016; Ines et al., 2013; Y. Liu et al., 2012; Moradkhani et al., 2005; Zou et al., 2017). Data assimilation is a procedure that applies Bayes' theorem to condition the states of a dynamical systems model on observations (G. Nearing et al., 2018); 2) Alternatively, data from remote sensing product can be directly used as a calibration target to constrain the parameters in the hydrological model (e.g., Zink et al., 2018; Nijzink et al., 2018; Tang et al., 2019); 3) Data from remote sensing product could be directly inserted into the hydrological model (e.g., Mendiguren et al., 2017; Roy et al., 2010).

Before applying any approaches to incorporate remote sensing data into a hydrological model, several assumptions need to be made, due to spatial and temporal mismatches between hydrological model's state/variables/outputs and remotely sensed data. First, all three approaches need to aggregate outputs from hydrological models and observations from remote sensing to the same spatial and temporal resolution (G. Nearing et al., 2018; Nijzink et al., 2018; Xu et al., 2014). For example, data from remote sensing are usually averaged to each grid cell or each subbasins of hydrological model (Naseem et al., 2015; Zink et al., 2018). During these spatial aggregation processes, information about the spatial variations within each grid or sub basin contained in both remote sensed product and model simulation result are neglected. Second, all three approaches need to make assumptions about hydrological processes in a specific watershed and build a hydrological model to describe these processes (Naseem et al., 2015). By examining the improvement of five conceptual hydrological models in 27 watersheds due to utilization of the multiple remote sensed products, Naseem et al. (2015) show that the improvement of hydrological model predictions with certain remote sensed products varied with different model structures at different watersheds, which means that the efficiency of utilizing the information in remote sensing products is different among different model structures. Thirdly, a metric that evaluates the similarity between a remote sensed product and a model simulation result needs to be selected. The root mean squared error can be used if there is high confidence in the remote sensed product, Alternatively, two spatial patterns can be compared in a relative way if we do not trust the absolute value of the remote sensed products (Pauwels et al., 2001; Zink et al., 2018).

Because of these approximations and assumptions, the information contained in any remote sensing product might not be fully utilized in a hydrological model (Nearing & Gupta, 2018). And the quality or efficiency of incorporating remote sensing products into a hydrological model are influenced by aforementioned three assumptions. Previous studies have assessed the added value of different remote sensing products, either for data assimilation or model calibration (Ines et al., 2013; Zou et al., 2017; Liu et al., 2012; Alvarez-Garreton et al., 2016; Moradkhani et al., 2005). However, little attention has

been paid to evaluating the impact of these assumptions on efficiency of incorporating remote sensing products. The studies presented by Naseem et al. (2015) applied the remotely sensed products as well as models all in a lumped, catchment- averaged manner. The potential hydrological model improvement from remote sensing products by improving the spatial aggregation resolution is still not clear. This is especially true given that recently developed remote sensed yearly high resolution landuse maps (Boryan et al., 2011) provide the potential to aggregate remote sensing product and model simulation results into even finer resolution. Furthermore, the improvement of hydrological model performance has been observed after adding vegetation growth model to account for the vegetation dynamic of the system (Campos et al., 2016; Hwang et al., n.d.; Kelly et al., 2016; Naseem et al., 2015). Several remote sensing products are closely related to the vegetation growth processes such as actual evapotranspiration, LAI and soil moisture. Thus, the inclusion of integrating vegetation growth modelling potentially could show an even greater benefit (hydrological model improvement) of remote sensing products.

The pending NASA SWOT satellite mission (see <https://swot.jpl.nasa.gov/>) promises to measure lake levels at resolutions (temporal, spatial, and vertical) that have the potential to be used to calibrate the hydrological model in gauged/ungauged watersheds. However, how valuable these lake-level observations are in gauged/ungauged watersheds is not well quantified.

#### **1.4 Model evaluation metrics in hydrological modelling**

Model evaluation metrics are important in hydrological modelling as they can be used to quantify our beliefs in the model, to characterize relevant aspects of model performance and to evaluate the different hypothesis in the model (Clark et al., 2016; Gupta et al., 2012). When evaluating alternative models, model performance metrics form the basis for our assessment of relative model performance. Generally, the model evaluation metrics can be divided into four categories described in the following paragraphs.

First, model performance can be evaluated in the measurement space and can be measured in terms of the degree of fit, which are functions of the residuals between the modeled and observed quantities, such as Nash–Sutcliffe model efficiency coefficient (NSE), Root Mean Square Error (RMSE), Mean absolute area (MAE), coefficient of determination (R<sup>2</sup>) and Kling–Gupta efficiency (KGE; (Gupta et al., 2009; Pechlivanidis et al., 2014)). Metrics in this group can be easily calculated and applied when we have multidimensional observations (Rajib, Evenson, et al., 2018). For example, the NSE of each observation type can be either treated as different objectives in a full multiple-criteria optimization

problem, or grouped together to a related single-criterion optimization problem (Gupta et al., 2009). The KGE metric proposed by Gupta et al. (2009), overcame problems in using NSE in model optimization such as overestimation of model skill for highly seasonal variables and underestimation of the runoff peak flows.

Besides the aforementioned metrics, model performance can also be evaluated by model selection criteria such as AIC, BIC, and KIC (Akaike Information Criterion, Bayesian Information Criterion, and Kashyap Information Criterion, respectively), which have been widely used to determine the model weight in the Bayesian model averaging framework (Höge et al., 2018; Lu et al., 2013; Ye et al., 2008). These model selection criteria not only evaluate the goodness of fit in measurement space, but also include penalty terms that account for model parameter dimensionality, which is referred as the Occam factor (MacKay, 1992). The Occam factor reflects the principle of parsimony or Occam's razor: If any number of competing models shows the same quality of fit, the least complex one should be used to explain the observed effects (MacKay, 1992; Wöhling et al., 2015). Both KIC and BIC are an approximation of the likelihood of observed data given a prior distribution of parameters, while AIC is the approximation of the loss of information when using an alternative model instead of the 'true' model (Poeter & Anderson, 2005; Schöniger et al., 2014; Ye et al., 2008). Thus, AIC require the (true) model that generated the observational data is included in the set of candidate models. The rank as well as the weight of candidate models determined from the AIC, BIC, and KIC, could contradict each other (Schöniger et al., 2014; Wöhling et al., 2015) and these are can be impacted by the model error covariance structure (Lu et al., 2013; Höge et al., 2018), observation data set size, and numerical methods to estimate likelihood of observed data (Schöniger et al., 2014).

Second, model performance can be evaluated by using mutual information from information theory, which quantifies how much of the uncertainty about a random variable Y can be reduced by knowing variable X and a specific model structure M (Amarocho & Espildora, 1973; Gong et al., 2013; G. S. Nearing & Gupta, 2015; Ruddell et al., 2019). The uncertainty of a variable is commonly measured by entropy, proposed by (Shannon, 1997). Calculating the mutual information require large computational resources to analyze the distribution and joint/conditional distribution of variables, even in a one dimensional problem. In addition, the mathematical framework for multidimensional hydrological problems has yet to be introduced to the hydrology community. Assuming mutual information is computationally tractable, the benefit of applying mutual information is that we can quantify the information contained in data and model structure in term of prediction of Y (Gong et al., 2013; Nearing

and Gupta, 2015) and quantify the efficiency of data assimilation technologies (Nearing and Gupta, 2015).

Third, model performance can be evaluated with hydrological signatures, which has been widely used in hydrological modelling such as improving the model consistency (Martinez & Gupta, 2011; Nijzink et al., 2018; Shafii et al., 2017; Shafii & Tolson, 2015) and model structure comparison and hypothesis testing (Coxon et al., 2013; Fenicia et al., 2016; S. Gharari et al., 2014). A signature-based calibration approach does not aim to calibrate the model directly to observed streamflow. Instead, it seeks to identify hydrologically meaningful patterns of system behavior in the data, and to calibrate the model to these signatures (Pechlivanidis et al., 2014; Zhang et al., 2018b). The literature shows a variety of signatures, which measures different aspects of watershed function or system behaviors, have proven to be useful for hydrological modelling including: the rising and declining limb density (Shamir et al., 2005), flow duration curves (Westerberg et al., 2011b), baseflow and runoff coefficient (Shafii and Tolson, 2015) and others (Nijzink et al., 2018; Yilmaz et al., 2008; Y. Zhang et al., 2018). Recently, Shafii et al. (2017) showed that inclusion of flow partitioning coefficients estimated from L'vovich (1979) was able to increase model consistency and parameter identifiability compared with using traditional hydrological signatures.

Fourth, model performance can be evaluated at each hydrological process level by using the transfer entropy from information theory (A. Bennett et al., 2019; Goodwell & Kumar, 2017; Ruddell et al., 2019). The hydrological system will be first conceptualized into an information flow process networks, which includes state variables of a hydrological system and corresponding linkage between state variables (Goodwell & Kumar, 2017; Ruddell et al., 2019). Then the amount of directed transfer of information between state variables is measured by the transfer entropy or mutual information, which is a measure of the strength of functional interactions between state variables (Goodwell & Kumar, 2017; Ruddell et al., 2019). Information flow process networks have been used to investigate information processing in neural systems in terms of information transfer, storage and modification (Wollstadt et al., 2014) and to explain the complex nature of forcing and feedback within an ecohydrological system (Goodwell and Kumar, 2017). To reasonably estimate the transfer entropy between state variables in an information flow process network, detailed measurements of the state variables are required, which is not typically available for rainfall-runoff watershed modelling. The application of this approach is limited to specific site where detailed observations are available (Ruddell et al., 2019; Goodwell and Kumar, 2017).

## 1.5 Research gaps

Past large-scale hydrological modelling efforts tend to either ignore the impacts of all lakes or explicitly simulate the behavior of only the largest lakes in a watershed. This is practically due to difficulties inherent in representing thousands of lakes in various hydrological models. However, an open-source GIS toolbox that can automatically and efficiently build vector-based hydrological routing networks with an arbitrary number of lakes does not exist in the literature. Moreover, the existing vector-based routing networks in the literature do not explicitly and properly represent lakes.

Another reason why past hydrological modelling efforts tend to ignore the impacts of lakes is that the model without lakes can provide reasonable streamflow simulation at the watershed outlet. However, the potential impacts of ignoring lakes on the simulated runoff components (i.e., quick runoff, baseflow, infiltration, etc.) and streamflow at internal gauges have not been quantitatively studied.

Lastly, understanding the impact of disturbance on the eco-hydrological processes in the forest headwaters is essential for forest management. Eco-hydrological models are a powerful tool to quantify the response of the forest headwater catchment to forest disturbance. However, the forest growth module in various eco-hydrological models (i.e., RHESSys (Tague & Band, 2004), SWAT (Arnold et al., 2012) and MESH (Pietroniro et al., 2007)) do not support simulating the forest density, Diameter at breast height (DHB), and basal area changes, which are critical for simulating forest management, such as forest harvesting and reforestation. Moreover, the vegetation growth module of eco-hydrological models is often not modular. Thus, it is tough for researchers to implement these vegetation modules into a different hydrological model.

## 1.6 Thesis Contributions

This thesis has five core contributions as follows.

1. A proof of concept study showing that it was a) feasible to develop a large-scale (Pan-Canadian) vector-based lake-river routing product that incorporates hundreds of thousands of lakes in routing networks and b) feasible to simulate hydrologic routing across a massive region (Hudson Bay drainage basin totaling  $\sim 3,860,000 \text{ km}^2$ ) and c) beneficial in terms of improving uncalibrated simulated hydrographs to explicitly represent numerous, including modest-sized, lakes.

2. An open-source GIS toolbox (BasinMaker) was developed that can automatically and efficiently build vector-based hydrological lake-river routing networks, including flexible discretization choices to represent any number of lakes. BasinMaker was used to delineate the North American Lake-River Routing Product v2 (available at <http://hydrology.uwaterloo.ca/basinmaker/index.html>) and the Ontario Lake-River Routing Product v1 (available at <https://lake-river-routing-products-uwaterloo.hub.arcgis.com>). Two novel post-processing functions in BasinMaker are ideal customization tools that can simplify the high-resolution large-scale routing networks already delineated by Basin Maker in the above two routing products.
3. The compensation behavior of the hydrological model when the lakes are ignored in the model was identified. The impact of the ignoring lakes on the simulated runoff at each flow pathway and the streamflow at the internal gauges was demonstrated.
4. The relationship between calibrated lake crest width parameter in the broad-crested weir equation of fifteen gauged lakes and the lake's drainage area was assessed, showing that the calibrated lake crest width parameter has a linear relationship with the lake's drainage area in log-log space. This result validates the assumption used in the literature to parametrize the outflow structure of lakes.
5. Calibrating only to internal lake level measurements substantially improves the streamflow simulation quality at both internal locations as well as the watershed outlet
6. A vegetation growth library framework (Robin) was developed, which can be easily coupled to any hydrological or land-surface model to add the functionality of crop and vegetation growth functionality. Moreover, a new daily version of the popular 3PG (Physical Processes Predicting Growth) forest growth model, which has been widely used in modelling forest dynamics, was emulated in the Robin vegetation growth library (Robin\_3PG). This thesis reports primarily on the development and application of the forest growth module of Robin. The testing of the crop growth component of Robin is incomplete and not reported in this thesis.

## Chapter 2

# Subwatershed-based lake and river routing networks for hydrological and land surface models applied over Canada

This chapter is a mirror of the following published article with minor changes to increase its consistency with the body of the thesis. Changes were only made in the Summary (abstract). References are unified at the end of the thesis.

Han, M., J. Mai, B. A. Tolson, J. R. Craig, E. Gaborit, H. Liu, K. Lee (2020), Subwatershed-based lake and river routing products for hydrologic and land surface models applied over Canada, *Canadian Water Resources Journal*, 45(3), doi.org/10.1080/07011784.2020.1772116.

### 2.1 Summary

Lakes and reservoirs have critical impacts on hydrological, biogeochemical, and ecological processes, and they should be an essential component of regional-scale hydrological and eco-hydrological models. This is particularly important in Canada with its tens of thousands of lakes. Past large-scale hydrological modelling efforts tend to either ignore the impacts of all lakes or explicitly simulate the behaviour of only the largest lakes in a watershed.

This research derives a suite of Pan-Canadian subwatershed-based lake and river routing GIS products at multiple spatial resolutions. These publicly available data products supply all the necessary hydrological routing model inputs, including network topology, subwatershed geometry, channel characteristics (slope, length, roughness, and geometry), and lake characteristics (area, volume, and outlet description), and were derived primarily from the HydroLAKES, HydroBASINS and HydroSHEDS databases. All Water Survey of Canada streamflow gauging stations are used to define subwatershed outlets in the products.

The routing network is used to inform a hydrological routing model in the Raven hydrological modelling framework. This is the first demonstration of Raven in routing-only mode. As a case study, the Hudson Bay drainage basin (~40% of Canada) is simulated using GEM-Surf land surface model gridded runoff and recharge as inputs and includes more than 20,000 river reaches and more than 10,000 lakes explicitly represented at an hourly timestep. Uncalibrated streamflows compare reasonably well to measured streamflows at select locations. The sensitivity of the routing model prediction quality to

the discretization level for represented lakes is evaluated and shows, for example, that ignoring multiple smaller lakes can have a significant impact on predictions.

## 2.2 Introduction

Lakes and reservoirs are a key component in hydrological modelling. In routing processes, for example, lakes and reservoirs can retain parts of snow melt and precipitation in spring and summer, and supply water to rivers in winter and autumn (Bowling & Lettenmaier, 2010; Huziy & Sushama, 2017). Because of this effect, up to 80% of snow meltwater can go into storage each year and may not contribute to streamflow (Bowling and Lettenmaier 2010; Huziy and Sushama 2017). Moreover, lakes and reservoirs significantly impact simulated flow duration curves. Accounting for them explicitly in hydrological models can improve peak flow simulations (Hughes et al. 2014; Huziy and Sushama 2017; Spence 2006; Zajac et al. 2017). Lake-groundwater interactions are likewise important in hydrological and geochemical modelling (Karan et al. 2014; Shaw, White, and Gammons 2013). As inferred from the HydroLAKES database (Messenger et al. 2016), Canadian lakes represent 39% of the total global lake area and approximately 10% of Canada is covered by lakes. Lakes are therefore a critical component of various hydrological and eco-hydrological studies in Canada.

The lake-river routing structure, which here refers to both the topology of the stream network and the contributing areas to individual lakes and stream reaches, is a fundamental input to hydrological models. The lake-river routing structure in hydrological model will transport vertical fluxes generated by land surface model or hydrological models horizontally through drainage networks (Li et al. 2013; Lehner and Grill 2013). The inclusion of lakes in a hydrological routing network usually requires manual processing. For small and local-scale studies, the domain of interest might only contain one or two lakes which can easily be added into the lake-river routing structures (Lin et al., 2015; Christopher Spence, 2006). For regional or global studies, however, only large lakes are usually incorporated into the lake-river routing structure. For example, only lakes with an area larger than 100 km<sup>2</sup> were included in a global study by Zajac et al. (2017). This is due to the large number of smaller lakes and the significant processing time typically required to manually insert all lakes in the lake-river routing structure (Lehner and Grill 2013). The HydroLAKES database (Messenger et al. 2016), however, indicates that lakes with an area smaller than 100 km<sup>2</sup> take more than ~37% of total global lake area. The function of these neglected small lakes can become important for hydrological modelling (Spence

2006). Thus, a geospatial product that explicitly represents the lake-river routing structures is required to enhance the quality of regional and global hydrological studies.

Besides the HydroBASINS product with inserted lakes (Lehner and Grill 2013), here referred to as HydroBASINS -L, no further lake-river routing network is available over the domain of Canada. However, HydroBASINS-L was produced by clipping sub-basin polygons with lake polygons and bisecting the remaining subbasin catchment using the mainstream reach polyline. When a lake contained the outlet of a sub-basin, the sub-basin was split into a left and a right part along its main stream reach (Lehner and Grill 2013). The water released from the right part of a split sub-basin has to flow first into its corresponding left part before it flows into the lake (Lehner and Grill 2013). This leads to three problems when this product is used for hydrological modelling: 1) it is not possible to calculate a representative river length for the left and right sub-basin since the sub-basin was split along the main river; 2) the lake-river routing structure is not hydrologically or topologically correct; and 3) the local contributing area to the lake and the portions of the adjacent sub-basins which are upstream or downstream of the lake are all indeterminate. Thus, the HydroBASINS-L product has limitations when used for hydrological modelling applications.

In this work we will develop a pan-Canadian lake-river routing network that 1) includes all lakes connected by the river network, 2) represents lake-river routing structures in a hydrologically consistent way, and 3) includes all derived routing attributes/parameters required to hydrologically route distributed fluxes of streamflow through a lake-river routing network. The proposed product combines catchment polygons from the HydroBASINS product (Lehner and Grill 2013), hydrologically conditioned raster datasets with 15s arc-second resolution from HydroSHEDS product (Lehner, Verdin, and Jarvis 2008) and lakes from the HydroLAKES product (Messenger et al. 2016). In total twelve routing networks are developed within this work using watershed delineations at six different spatial resolutions and two lake-retention strategies (with either all lakes represented or only lakes with an area larger than 1 km<sup>2</sup> represented). Once a lake-selection strategy is chosen, one can still define if a lake is explicitly represented within the hydrological model or not (without changing the routing structure). We refer to this method as the active-lake definition strategy.

The developed lake-river routing network is here coupled with the routing capabilities of the open source Raven hydrological modelling framework (Craig et al. 2020). Raven is a robust and flexible hydrological modelling framework that can be setup such that it serves only as a vector-based

hydrological routing model, which can route runoff generated by a land surface scheme (LSS) in conventional gridded format. This study is the first time Raven is applied in routing-only mode and demonstrated for continental-scale routing simulation.

Existing standalone routing models include mizuRoute (Mizukami et al. 2016), RAPID (David et al. 2011), CaMa-Flood (Yamazaki et al. 2011) and HydroROUT (Lehner and Grill 2013). mizuRoute is a stand-alone open-source routing tool for grid- or vector-based routing of runoff generated by a land surface scheme or other regional-scale hydrological model. It has been deployed at the scale of the continental United States but does not currently support lake, reservoir, or wetland routing.

Compared with existing stand-alone routing models such as RAPID (David et al. 2011), mizuRoute (Mizukami et al. 2016) or the WatRoute algorithm (Kouwen, 1988), the Raven model has the following advantages: 1) Raven supports several different routing algorithms for in-catchment routing, in-channel routing, and lake/ reservoir routing processes, whereas most other routing models support only one option for these processes. Of the above model-independent routing tools, only WatRoute supports lake simulation, but only on a gridded network; 2) Raven can simulate both grid-based and subbasin/reach representation of the stream network; 3) Raven supports spatially variable reach and lake characteristics; 4) Raven has robust support for reservoir management and irrigation demand representation. 5) Lastly, since we develop a pan-Canadian routing network and hence enable pan-Canadian studies, we have to handle large datasets. RAVEN supports multiple input formats, such as ASCII and NetCDF. The latter format is known to be efficient for large gridded datasets.

In this study, we will apply and evaluate the developed routing network over the domain of the Hudson Bay (3.98 million km<sup>2</sup>), demonstrating the utility and efficiency of Raven as a routing model for systems with many lakes and showing that the explicit representation of lakes in the routing network leads to improved hydrographs relative to observations, even without model calibration.

### **2.3 Methods**

In this section, we will first briefly introduce how we derived this lake-river routing network. The hydrological modelling framework Raven for hydrological routing will be introduced in the second section. The Raven routing modelling framework will then use the lake-river routing network in a routing case study application of the Hudson Bay watershed, which is described in the third section.

### 2.3.1 Pan-Canadian routing networks

The lake-river routing network has three components: 1) the routing topology, 2) the geometry of contributing areas, and 3) the routing related attributes for lakes and stream reaches. In this section we first introduce the methods that were used to develop the lake-river routing topology and then the methods employed to generate routing attributes for each catchment in the newly developed product will be described.

#### 2.3.1.1 Lake-river routing topology and catchment areas

The lake-river routing topology is developed based on a combination of the HydroBASINSS (Lehner and Grill 2013), HydroSHEDS (Lehner, Verdin, and Jarvis 2008) and HydroLAKES (Messenger et al. 2016) geospatial databases. HydroBASINS is a series of polygon layers that depict watershed boundaries and sub-basin delineations various scales (Lehner and Grill 2013). HydroSHEDS is a hydrologically consistent geospatial dataset including gridded flow accumulation, gridded flow directions, and a hydrologically conditioned digital elevation model (Lehner, Verdin, and Jarvis 2008). All gridded datasets are at 15 arc-second resolution. Twelve sub-basin layers from Level 1 to Level 12 were published in the HydroBASINS database, where Level 1 is a very coarse resolution delineation (i.e., the Mackenzie river basin is a single basin) and Level 12 is the finest resolution. HydroLAKES is a database that includes shoreline polygons of all global lakes with a surface area of at least 10 ha (Messenger et al. 2016). In total, 21 lake attributes are included in the HydroLAKES database such as lake area, lake averaged depth, and lake volume.

Twelve lake-river routing topologies are developed by combining six HydroBASINS products (level 7 to 12) and two lake-selection strategies (lakes with an area larger than 0 or 1 km<sup>2</sup> in the HydroLAKES database), additionally seeded with the locations of 6372 Water Survey of Canada (WSC) stream gauge. All developed lake-river routing topologies are generated with the same procedure. The development of lake-river routing topology for combination of HydroBASINS Level 8 and HydroLAKES with lake area larger than 0 km<sup>2</sup> (labeled L8-Lake0) is used as an example and described in following section.

Two steps are required to generate a lake-river routing topology: (1) generate the local river network and pour points for each catchment polygon in the HydroBASINS Level 8 product, and (2) insert lakes and local lake catchment areas into the HydroBASINS Level 8 product. Pour points refer to the drainage outlet location for individual sub-basins.

In step (1), the river network of each catchment is generated by tracking the flow paths from upstream catchment inlet to the downstream catchment outlet (pour point) based on the HydroSHEDS gridded flow direction map. The highest flow accumulation point within the catchment is identified as the pour point of the catchment.

In step (2), first, pour points of each catchment from step (1) need to be modified and updated to insert lakes into the routing topology, where the lake extents are represented by polygons. The modified pour points include: (a) the original pour points in step (1) except for those within a lake polygon, (b) lake outlet, which is the point having the highest flow accumulation value within each lake's extent, and (c) lake inflow pour points, which are identified as the intersection between a lake boundary and its surrounding rivers. Only one lake outlet was identified for each lake in the routing networks. The number of the lake inflow pour points can be 0 or any number larger than 0. An example of lake insertion and the identified pour points is shown in Figure 2-1A.

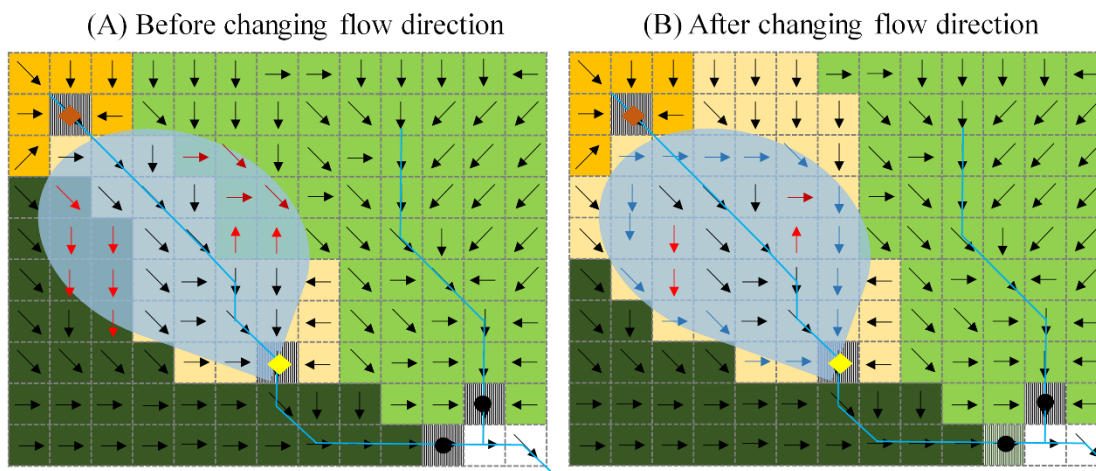


**Figure 2-1.** An example of watershed delineation results before (A) and after (B) modifying flow directions of lake boundary cells. The two grid cells with black dot are pour points of catchments. The grid cell with red diamond is the pourpoint identified as the lake's inlet and the grid cell with yellow diamond is the pourpoint identified as the lake's outlet. The arrows indicate the flow direction of each grid cell. The red arrows indicate the initial flow directions that do not converge to the lake outlet. The blue arrows in (B) indicate corrected flow directions. The different cell colors represent five different delineated catchments. The semi-transparent blue polygon represents a lake and the blue lines mark rivers.

Second, the “Watershed” function of the Hydrology toolbox in ArcMap (ESRI 2001) is used to generate an updated routing topology using the set of updated pour points and the original flow direction map from HydroSHEDS. A lake catchment (a catchment which drains directly to the lake) will be generated for all lakes (light yellow in Figure 2-1A). After obtaining the lake-river routing topology, each lake catchment will be re-evaluated with respect to lake polygons. If a lake catchment polygon (yellow grid cells in Figure 2-1A) completely contains the lake polygon (light blue polygon), the lake catchment will be accepted.

However, if a lake polygon is not fully contained by the generated lake catchment polygon (Figure 2-1A; lake is not covered completely by light yellow grid cells), then the grid cells at the boundary of the lake polygon will be identified and the flow direction of these grid cells will be corrected to ensure that all water received by these grid cells flows to the lake outlet (Figure 2-1B; flow direction (blue arrows) adjusted). This is justified in part because flow direction within flat regions such as lakes is typically indeterminate and therefore local gridded flow direction within lakes is often only a by-product of DEM processing which enforces hydrological consistency. Afterwards, the modified flow direction map as well as the updated pour points is used to re-generate the final lake-river routing topology (see Figure 2-1B, where light-yellow domain got extended to cover the lake completely). In this way it is ensured that: a) each lake polygon is fully covered by a lake catchment; b) each lake outlet is the outlet of the lake catchment; c) every lake inlet is represented by a pour point of an upstream catchment and hence enables explicit lake inflow representation and simulation.

### 2.3.1.2 Estimation of routing attributes

The routing attributes that are derived from information beyond the DEM will be described in this section.

Bankfull width, depth, and discharge for lake-river routing structure. A global bankfull width  $w$ , depth  $d$ , and discharge  $Q$  for each channel reach of the HydroBASINS default (finest scale) river system was developed by Andreadis et al. (2013). This information is here used to estimate the bankfull width  $w$ , depth  $d$ , and discharge  $Q$  for each catchment in the lake-river routing network. The original product by Andreadis et al. (2013), however, is only available for drainage regions below the latitude of 60°N (notably, the same is true for the publicly available HydroBASINS product). We hence use the methodology applied in Andreadis et al. (2013) to derive the bankfull width, depth and discharge for

channel reaches of the HydroBASINS default river system in the drainage regions above latitudes of 60°N.

The drainage regions above the 60 °N in the domain of Canada including the Pacific Coastal, Yukon, Lower Mackenzie, Arctic Coast–Islands, Keewatin–Southern Baffin Island, and Northern Quebec (Figure 2-2). The bankfull discharge ( $Q$  in [ $\text{m}^3/\text{s}$ ]) and the drainage area ( $DA$  in [ $\text{km}^2$ ]) relationship ( $Q=k \times DA^c$ ) for each drainage region (Figure 2-2) is derived using data from streamflow gauges with more than ten years of annual mean flow observations (Table 2-1). The stream gauges observations are obtained from the National Water Data Archive HYDAT (HYDAT 2018). The  $Q$  of each river reach in HydroBASINS river system were estimated based on the developed relationship between  $Q$  and  $DA$ . Finally, the bankfull width  $w$  (in [m]) and depth  $d$  (in [m]) for HydroBASINS river system are derived by the following relationship introduced by Andreadis et al. (2013):

$$w=7.2Q^{0.5}; d=0.27Q^{0.39} \quad (2-1)$$

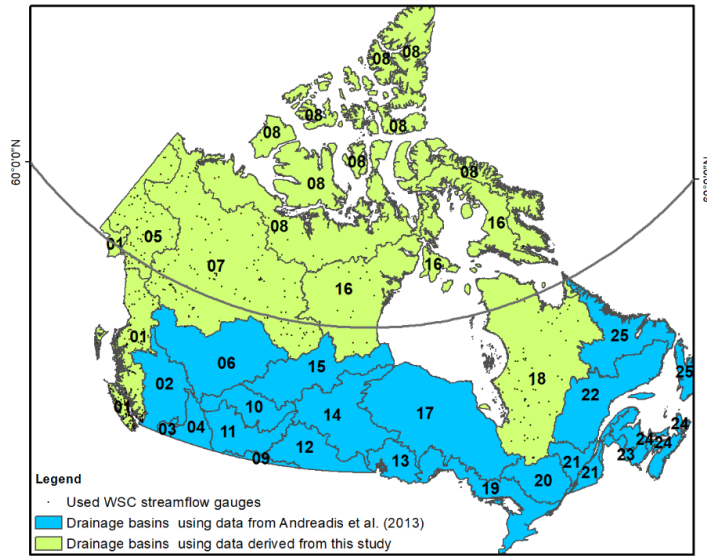


**Figure 2-2.** Drainage basins in Canada (polygon number) with the identifier code from Water Survey of Canada (WSC) and WSC streamflow gauges (black dots) used to estimate bankfull width (BkfWidth;  $w$ ) and depth (BkfDepth;  $d$ ) for the drainage basins Pacific Coastal (01), Yukon (05), Lower Mackenzie (07), Arctic Coast–Islands (08), Keewatin–Southern Baffin Island (16), and Northern Quebec (18) which is colored in yellow. The bankfull width and depth for the other drainage regions in Canada are obtained from Andreadis et al. (2013), which is colored in blue.

**Table 2-1.** Estimated relationship between drainage area ( $DA$ ) and bankfull discharge ( $Q$ ) ( $Q=k \times DA^c$ ) in six drainage regions. The bankfull width  $w$  and depth  $d$  are subsequently derived using the estimated bankfull discharge  $Q$  (Equation (2-1)).

Drainage Basin Code	Drainage Basin Name	$k$	$c$
01	Pacific Coastal	0.165	0.790
05	Yukon	0.018	0.935
07	Lower Mackenzie	0.048	0.837
08	Arctic Coast–Islands	0.004	1.013
16	Keewatin–Southern Baffin Island	0.040	0.814
18	Northern Quebec	0.016	1.011

Estimated bankfull width, depth, and discharge for each channel reach in the HydroBASINS default (finest scale) river system are first derived across the whole domain of Canada. Two steps are then needed to estimate the representative bankfull width, depth, and discharge for each catchment in the developed lake-river routing topology. First, river channel reaches in the HydroBASINS default river system belonging to the primary flow path of each catchment in the developed lake-river routing topology are identified. A GIS spatial overlay operation between the HydroBASINS default river system and the river system for each of the 12 lake-river routing topologies is applied for this purpose. Then, the bankfull width  $w$ , depth  $d$ , and discharge  $Q$  for each delineated catchment are calculated by taking the reach-length weighted-average of these properties along the single main reach.

Main channel Manning’s coefficient. The main channel Manning’s roughness coefficient  $n$  (in [-]) for each catchment of the developed routing topology is estimated by rearranging the Manning’s equation and solving for  $n$  as shown in Equation (2-1):

$$n = A_{ch} R^{2/3} S_{chn}^{1/2} Q^{-1} \quad (2-2)$$

where  $A_{ch}$  is the channel bankfull cross-section area (in [m<sup>2</sup>]),  $R$  is the hydraulic radius (in [m]),  $S_{chn}$  is the main channel slope (in [m<sup>2</sup>/m<sup>2</sup>]), and  $Q$  is the bankfull discharge (in [m<sup>3</sup>/s]) as above.

The channel cross-section  $A_{ch}$  and the hydraulic radius  $R$  are generated using bankfull width  $w$  and depth  $d$  of each catchment following the approach applied in the Soil and Water Assessment Tool (SWAT), which can be found in section “7.1.1 Channel Characters” of SWAT user manual (Neitsch et al. 2011). The slope of the main channel  $S_{chn}$  of each catchment of the developed routing network is calculated by:

$$S_{chn} = (MaxDEM - MinDEM)/rivlength \quad (2-3)$$

where *MaxDEM* and *MinDEM* are the maximum and minimum DEM elevations along the river channel (in [m]), and *rivlength* is the river channel length in the catchment (in [m]). The first two are derived from the DEM, the *rivlength* is calculated by the “Calculate Geometry” function in ArcGIS 10.6 (ESRI 2001).

Flood plain manning’s coefficient. The flood plain manning’s coefficient *FloodP\_n* of each catchment in the lake-river routing topology is estimated from the land cover grids along the river channel of each catchment. The 500m resolved MODIS Land Cover Type product MCD12Q1 (Myneni, R., Knyazikhin, Y., Park 2015) is used to estimate the flood plain manning’s coefficient. First, a flood plain Manning’s coefficient based on the value provided in Asante et al. (2007) is assigned to each land cover type. Then, land cover grid cells that are intersected by river network of each catchment are identified. Finally, each catchment is assigned with the average value of the flood plain Manning’s coefficient over all identified grid cells.

Estimation of lake routing attribute. The relationships between lake area, lake depth, lake storage, and lake outflow are essential for simulation of lake routing. The simplest assumption is that lakes are prismatic, which means that the lake area does not change with lake depth. Lake outflow can be simulated with the broad-crested weir equation (e.g., Bowling and Lettenmaier 2010) or empirical functions of lake storage (e.g., Kouwen 2018). Under this simplest assumption, the required lake routing characteristics are the lake area, lake volume, lake averaged depth, lake outflow, weir width and (optionally) weir elevation.

The lake area (*LakeArea*), lake averaged depth (*LakeDepth*), lake volume (*LakeVol*) and lake type (*Laketype*) are included in the lake-river routing topology by using the values from the HydroLAKES database (Messenger et al. 2016). The lake outlet weir width is assumed the same as the estimated bankfull width *BkfWidth* of the lake catchment. Thus, the lake routing characteristics that can support lake routing with these simplest assumptions are all included in the developed lake-river routing topology. An additional attribute, *IsLake*, is included to indicate whether each catchment in the routing network is a lake catchment.

Additional product attributes. Around 6372 streamflow observation gauges from the HYDAT database (HYDAT 2018) are included into the routing topology. Streamflow observation gauges are first automatically snapped to the closest river reach of HydroBASINS river system and then treated as catchment outlets. A flag called *IsObs* is used to indicate whether streamflow observations are available

for the catchment. Further, the Water Survey of Canada station number of each gauge *Station\_Nu* is also included in the developed lake-river routing network.

### **2.3.2 Hydrologic routing with RAVEN**

The Raven hydrological modelling framework (Craig et al. 2020), as consistent with its flexible design philosophy, can be configured for in-catchment, in-channel, and in-lake routing using a variety of different algorithms, and run at multiple spatial and temporal resolutions. It is designed to run both as a stand-alone hydrological model and as a routing model, which can be coupled to land surface schemes or other hydrological models. As a routing model, Raven requires as forcing input at the very least spatially distributed runoff data, which is typically provided as a gridded data product of water fluxes released from the land surface (as may be generated by a land surface scheme). Runoff contributions to individual catchments are estimated from the area-weighted average of runoff from any grid cells overlapping the basin. For simulation of reservoir/lake mass balance, it also requires spatially distributed temperature, precipitation, and/or evaporation rates. Lastly, it can support spatially distributed (gridded) recharge data, which can be used to estimate groundwater baseflow, which can likewise be stored and released to the routing network. This option is used in this study and groundwater baseflow is simulated using a linear groundwater reservoir approach.

Neglecting the simulation of routing in wetlands, which is not addressed here, there are three primary components of the Raven runoff algorithm. First, runoff shed from the landscape or released as groundwater baseflow is routed to the local basin outlet using in-catchment routing, treated using a transfer function/unit hydrograph approach. Multiple transfer functions are available (e.g., triangular, gamma distribution, Nash unit hydrographs, or an instantaneous release); here, the instantaneous release approach is used and thus all of the water released from the catchment to surface water over a time step appears in the channel at the catchment outlet at the end of the time step. Second, routing within channels of the stream network may be simulated using an in-channel hydrological routing algorithm (e.g., Muskingum-Cunge, lag and route, storage coefficient, level pool routing, diffusive wave, or kinematic wave routing). In all cases, the routing characteristics are impacted by the channel geometry, slope and roughness; stage-flow relationships are informed by Manning's equation, as is the local calculation of representative reach diffusivity and celerity. The diffusive wave approach is used here where an analytical solution to the diffusive wave equation is used to relate inflow and outflow in each reach. The stream network is assumed to be a unidirectional branching network such that flows

move solely from upstream to downstream. Backwater effects and cyclical networks are not supported. Lastly, a single Newton-Raphson algorithm with additional support for operational reservoir constraints is used to simulate routing of water through lakes and reservoirs. The lake routing algorithm supports simulation of groundwater seepage and open water evaporation, using one of more than a dozen PET estimation algorithms.

Raven supports a range of methods for determining the outflow from a reservoir or lake using either stage discharge relationships or operational constraints such as flow and stage targets or a user-specified time series of outflows. Each reservoir may have two stage-discharge curves to represent, for example, combined tunnel underflow and spillway overflow. In addition, known inflows or outflows from the reservoir (e.g., irrigation diversions) can be simulated. In this study, all water bodies are treated as natural lakes.

In this study, natural lake outflows are assumed to be governed by the broad-crested weir equation:

$$Q(h) = \frac{2}{3}CL(h - h_{crest})^{2/3}\sqrt{2g} \quad (2-4)$$

where  $g$  is the gravitational constant (in  $[m/s^2]$ ),  $C$  is the weir coefficient [-] with constant value 0.6,  $L$  is the weir crest width (in  $[m]$ ), and  $h$  is the lake surface level (in  $[m]$ ), and  $h_{crest}$  is the weir crest elevation. By default, the absolute elevations are not used in simulations; the crest height of each lake is assigned an elevation of zero and this zero reference level is only used for lake level simulation purposes. Here, we further assume that lakes are prismatic which means that the lake area does not change with lake depth (although Raven can utilize a stage-area-volume curve). Under this assumption, the lake surface level relative to the bottom of lake,  $h$ , can be estimated as the ratio between volume of water in the lake storage and the lake area. For each lake simulated in Raven, the lake routing attributes in the developed lake river routing networks (section 2.1.2) are used to assign lake routing inputs and parameters as follows. The crest height and crest width are set equal to the lake averaged depth (*LakeDepth*) and the lake catchment bankfull width (*BkfWidth*), respectively. The lake area input is set equal to the *LakeArea* routing network attribute. In addition, the initial  $h$  for each lake is set equal to the crest height, which assumes that each lake has no outflow at the beginning of the simulation.

A unique feature of Raven is that it can directly read gridded forcing inputs (forcing inputs of any shape) and then it internally converts the inputs to catchment specific fluxes. The following equation shows this conversion for each catchment in the routing network:

$$F_j = \frac{\sum_{i=1}^N F_i \cdot A_{ij}}{\sum_{i=1}^N A_{ij}} \quad (2-5)$$

where  $F_j$  is the forcing (surface runoff or groundwater recharge) value in catchment  $j$  at each time step,  $F_i$  is the forcing value for cell grid  $i$  obtained from the SVS land surface scheme,  $A_{ij}$  is the overlap area between the catchment (polygon) and the grid cell  $i$ , and  $N$  is the total number of grid cells.

### 2.3.3 Routing case study

The Hudson Bay watershed, with an area of 3.5 million km<sup>2</sup> (~40% of Canada), is selected to evaluate the developed pan-Canadian lake-river routing network and the Raven hydrological routing model for large scale routing modelling. This section first describes the SVS land-surface scheme used to produce surface runoff, lateral flow, and drainage estimates over the study domain, the Raven routing model set up for the Hudson Bay watershed is described in second part of this section, and the case study routing experiments is described in the third part of this section.

#### 2.3.3.1 The SVS (Soil, Vegetation, Snow) land-surface scheme

The SVS (Soil, Vegetation, Snow) land-surface scheme (Alavi et al., 2016; Husain et al., 2016) was developed by Environment and Climate Change Canada (ECCC). The purpose of SVS is to overcome the limitations of the old land surface scheme (ISBA) used by the Meteorological Service of Canada.

SVS is generally used at ECCC as part of the GEM-Surf model (Bernier et al., 2011). GEM-Surf is the surface prediction system used at ECCC to run the surface component of the GEM atmospheric model. GEM-Surf represents five types of surfaces, including land (represented by ISBA or SVS), water, glaciers, ice over water, and urban areas.

In this study, GEM-Surf outputs (surface runoff, lateral flow, and drainage) were used as input for the RAVEN routing model over the entire Hudson Bay watershed. GEM-Surf resolution was 0.09° (~10 km), but its outputs were aggregated to a 0.5° resolution (~50 km), with a mean grid cell size of 1594 km<sup>2</sup>, because the resolution of ECCC's internal gridded routing scheme over this watershed was 0.5°. GEM-Surf was run with a 5-minute time step and produced hourly outputs. The model was run from Jan 1, 2007 to October 7, 2010.

### 2.3.3.2 The Raven routing model set up for the Hudson Bay watershed

The developed HydroBASINS level 8 with all lakes routing network (L8-Lake0) is used to setup the Raven routing model and tested over the domain of the Hudson Bay watershed. There are 26,419 catchments in the L8-Lake0 product over the watershed (compared to the 90,455 pan-Canadian catchments in total for this product). The average catchment area is 133 km<sup>2</sup>. The total number of lake catchments in the L8-Lake0 product over the watershed is 14,975 (compared to the 40,674 pan-Canadian catchments in total for this product) with a median lake area of 1.0 km<sup>2</sup>. The Raven model routing simulation uses an hourly time step simulating the time period January 1, 2007 to October 7, 2010. Lake evaporation is accounted in the land surface model thus is not simulated by the routing model. Raven is run in routing-only mode, thus disabling all runoff generation procedures; only linear baseflow and routing are simulated.

### 2.3.3.3 Case study routing experiments with various lake resolutions

Several lake representation scenarios are developed by deactivating lakes in the routing model based upon different area thresholds. If a lake is deactivated, the lake is replaced by the channel of the longest river channel within the lake catchment and the water from the upper catchment will be transferred via in-channel routing instead of lake routing. A total of seven lake representation scenarios are tested (Table 2-2). Six of them are defined by using different lake area thresholds defining the minimum size for lakes to be explicitly simulated (lake area >0, >1, >4.24, >10, >50, and >100 km<sup>2</sup>). The seventh scenario (NoLake) deactivates the lakes of all lake catchments and is hence entirely ignoring the presence of lakes.

**Table 2-2.** Seven lake scenarios used in this study. In the base scenario all lakes are included. The number of included lakes is decreasing with each scenario.

Scenarios	Description
Lake0 (Base scenario)	Including all connected lakes
Lake1	Disable lakes with area smaller than 1 km <sup>2</sup> in base scenario
Lake4.24	Disable lakes with area smaller than 4.24 km <sup>2</sup> in base scenario
Lake10	Disable lakes with area smaller than 10 km <sup>2</sup> in base scenario
Lake50	Disable lakes with area smaller than 50 km <sup>2</sup> in base scenario
Lake100	Disable lakes with area smaller than 100 km <sup>2</sup> in base scenario
NoLake	Disable all lakes in base scenario

The impact of lakes on the routing results is evaluated by the Nash–Sutcliffe efficiency (NSE) at multiple streamflow observation gauges. In total, fifteen streamflow gauges that are not influenced by upstream reservoirs in the Hudson Bay watershed are selected for the analysis (Table 2-3 and Figure A1-1). Neither SVS nor Raven is calibrated. The *NSE* for daily flows for each gauge and all lake scenarios is computed by:

$$NSE = 1 - \frac{\sum_{i=1}^n (sim_i - obs_i)^2}{\sum_{i=1}^n (sim_i - \overline{obs})^2} \quad (2-6)$$

where  $obs_i$  is the flow observation at day  $i$ ,  $\overline{obs}$  is the observed daily mean flow,  $sim_i$  is the simulated averaged daily discharge at day  $i$ . The  $obs_i$  is calculated by average the simulated hourly value into daily.

**Table 2-3.** The 15 streamflow gauges without reservoir impact used for the case study. The gauge name is the streamflow station name of the Water Survey of Canada. The Gauge ID is the identifier of each gauge used in this work. Appendix A maps the location of all these gauges.

Gauge ID	Gauge Name	Drainage Area (km <sup>2</sup> )
1	05UG001	3273
2	05UH001	1584
3	05OJ005	263223
4	06FD002	1942
5	04HA001	118496
6	03KC004	40597
7	03LF002	88519
8	04LG004	61565
9	04ME003	26809
10	04AB001	103162
11	04DC001	47903
12	06GD001	48176
13	03MB002	29822
14	06SB001	7535
15	06OA007	5138

## 2.4 Result and discussion

In this section, we will first introduce our developed pan-Canadian lake-river routing networks. The evaluation of the developed routing networks and effect of lake retention in Hudson Bay watershed will

be introduced in second part of this section. Finally, routing network availability and limitation is provided in the third part of this section.

#### 2.4.1 The lake-river routing networks

In total, twelve lake-river routing networks were created (Table 2-4). An example of the lake-river routing network is shown in Figure 2-3. There are 20,5376 catchments and 86,991 lake catchments in the L12-Lake0 product. From L12-Lake0 to L7-Lake0, both the number of catchments and lakes decrease (Table 2-4).

**Table 2-4.** The Pan-Canadian routing networks and their general attributes. For example, the product “L7-Lake0” specifies the lake-river routing structure developed by using HydroBASINS Level 7 products and all lakes in HydroLAKES with lake area larger than 0 km<sup>2</sup>. The table summarizes the number of catchments and lake catchments as well as their average/median area for the various routing networks derived.

Product Name	Number of catchments	Average catchment area (km <sup>2</sup> )	Number of lake catchments	Median lake area (km <sup>2</sup> )
L7-Lake0	53,219	230	20,708	0.79
L8-Lake0	90,455	135	40,674	0.74
L9-Lake0	149,419	82	68,490	0.69
L10-Lake0	198,481	62	85,362	0.67
L11-Lake0	205,309	60	86,982	0.66
L12-Lake0	205,376	60	86,991	0.66
L7-Lake1	40,387	303	11,416	3.00
L8-Lake1	62,626	195	19,956	3.10
L9-Lake1	100,684	121	31,277	2.90
L10-Lake1	137,415	89	37,493	2.80
L11-Lake1	142,608	86	37,856	2.80
L12-Lake1	143,372	85	38,088	2.80

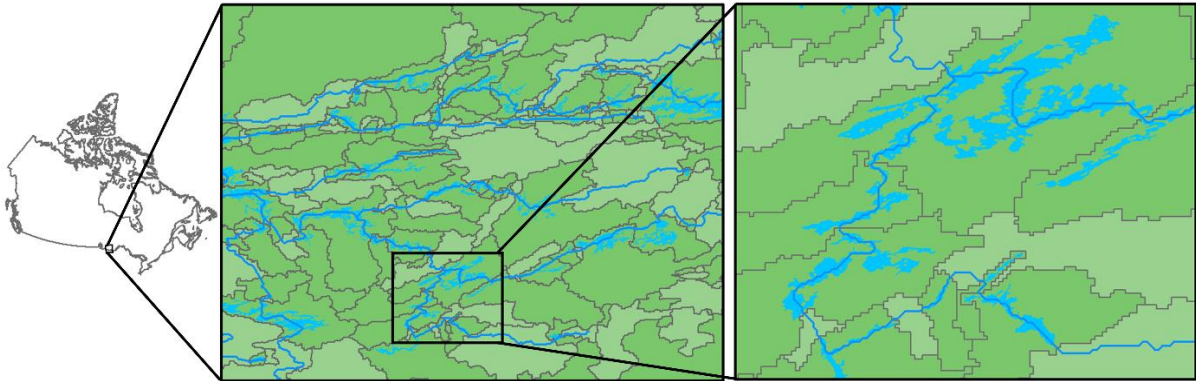


**Figure 2-3.** Developed Pan-Canadian routing network L7-Lake1, which is combining the HydroBASINS level 7 product and all lakes with lake area larger than 1 km<sup>2</sup> in HydroLAKES that are connected by the river network. The green polygons indicate the delineated lake catchments in this routing network while the shallow green polygons indicate the delineated non-lake catchments. Blue polygons indicate the lakes and blue lines indicate the rivers.

The lake area distribution for lakes included in each developed product and original HydroLAKES database is shown in Figure 2-4 (blue bars). The number of lakes is reduced from the HydroLAKES database to L7-Lake0 (Figure 2-4: compare blue and yellow bars). When we simplify the routing structure from L12-Lake0 to L7-Lake0, mainly small lakes are lost (lake area smaller than 10 km<sup>2</sup>).

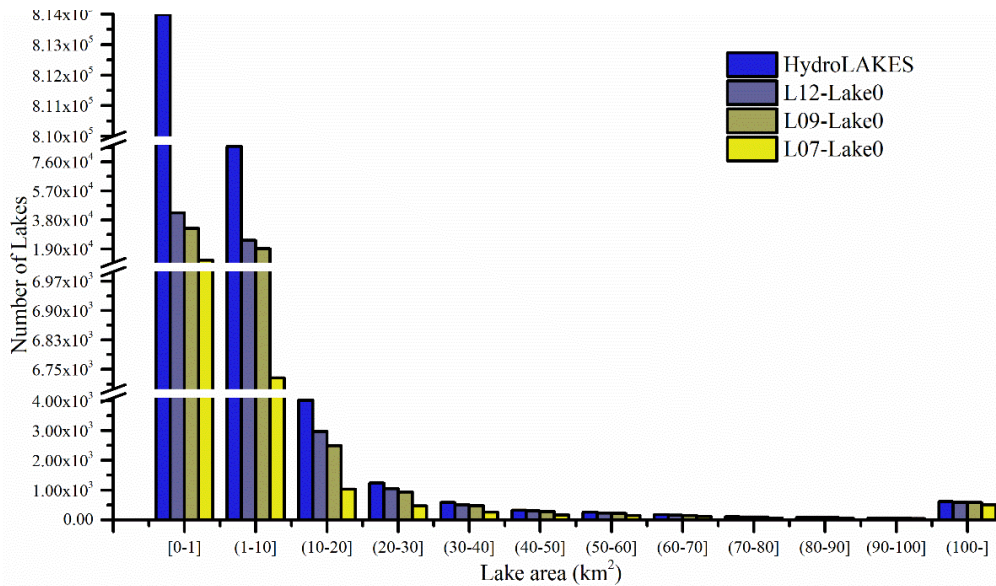


**Figure 2-4.** Number of lakes included at different lake area bands in the HydroLAKES (blue) and developed products (purple, dark yellow, yellow). “L7-Lake0” means the developed product with HydroBASINS level 7 catchments polygons and lakes with a lake area larger than 0 km<sup>2</sup> in HydroLAKES. “HydroLAKES” means all lakes in HydroLAKES within the product domain. The total number of lakes is 907,599 for HydroLAKES, 86,991 for L12-Lake0, 68,490 for L9-Lake0, and 20,708 for L7-Lake0 (see Table 2-4).

The ratio between cumulated lake area and total lake area in the L12-Lake0 product is shown in Figure 2-5. The lakes with an area smaller than 100 km<sup>2</sup> are 50% of the total lake area (Figure 2-5). And this ratio can larger than 0.7 in watershed controlled by streamflow gauge 06GD001 and 03MB002 (Figure 2-5). However, most studies focus on the impact of large lakes on routing. For example, only lakes with lake area larger than 100 km<sup>2</sup> were evaluated in a global routing model (Zajac et al. 2017). The impact of the remaining lakes on the routing modelling is neglected and the impact of this simplification is unknown. The developed product enables the support of such studies.

All routing related attributes included in the lake river routing network are shown in the Table 2-5.

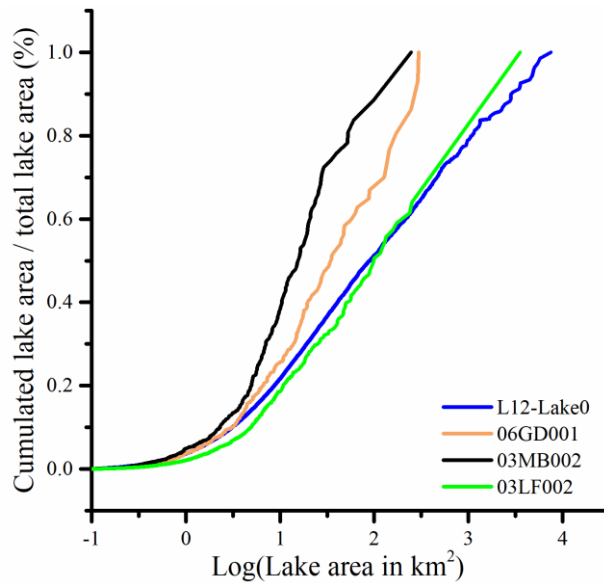


**Figure 2-5.** Percentage of total lake area correspond to cumulated lake area in different drainage regions. “L12-Lake0” means the plotted relationship is developed using lakes in the developed Pan Canadian product, which is a combination of HydroBASINS level 12 catchments polygons and lakes with a lake area larger than 0 km<sup>2</sup> in HydroLAKES. “06GD001”, “03MB002” and “06LF002” means the plotted relationship is developed using lakes in the drainage region controlled by stream flow gauge “06GD001”, “03MB002” and “06LF002” respectively. More detailed information about streamflow gauge can be found in Table 2-3.

**Table 2-5.** Routing related attributes included in the developed Pan-Canadian lake-river routing network. The name indicates the attribute name used in the provided routing network files. Besides a description and unit of the attributes, it is specified which method or source is used to derive the attribute.

Name	Description	Method	Unit
SubId	Subbasin ID	ArcGIS	-
DowSubId	Downstream subbasin ID	ArcGIS	-
Area	Area of the catchment	ArcGIS	m <sup>2</sup>
Rivlen	The length of the river channel within catchment	See 2.3.1.2	m
RivSlope	The slope of the river channel segment	See 2.3.1.2	-
BasinSlope	The averaged slope of the catchment	ArcGIS	m/m
Ch_n	The manning's coefficient of the river channel segment	See 2.3.1.2	-
FloodP_n	The flood plain manning's coefficient	See 2.3.1.2	-
BkfWidth	The bankfull width $w$ of the river channel segment	See 2.3.1.2	m
BkfDepth	The bankfull depth $d$ of the river channel segment	See 2.3.1.2	m
Q_Mean	The annual mean discharge (also bankfull discharge) of the river channel segment	See 2.3.1.2	m <sup>3</sup> /s
IsLake	0 catchment is not a lake catchment otherwise, 1	HydroLAKES	-
HyLakeId	The HydroLAKES ID of the lake	HydroLAKES	-
LakeVol	The lake volume	HydroLAKES	km <sup>3</sup>
LakeDepth	The lake depth	HydroLAKES	m
LakeArea	The lake area	HydroLAKES	km <sup>2</sup>
Laketype	The lake type (1 for natural lakes, 2 for reservoir and 3 for natural with regulation structure)	HydroLAKES	-
IsObs	-9999 means no streamflow observations at subbasin outlet, otherwise, 1	HYDAT	-
Station_Nu	The Water Survey of Canada station number	HYDAT	-
MeanElev	The mean elevation of the catchment	ArcGIS	m
INSIDE_X	The longitude of the centroid of the catchment	ArcGIS	degree
INSIDE_Y	The latitude of the centroid of the catchment	ArcGIS	degree

#### 2.4.2 Impact of lake retention

The simulated NSEs at each gauge for each lake routing network for the period from Jan 1, 2007 to October 7, 2010 are shown in Figure 2-6. Overall the mean NSE for the base scenario at all gauge is 0.52 while 53% of them are larger than 0.5. Since the routing model is not calibrated, this result is deemed acceptable. At the same time, the base scenario provides the best simulation result for 10 of the 15 gauges, where the performance at 2 gauges is only nominally impacted by the discretization level.

The impact of lakes on predicted streamflow is different across the 15 stream gauges (Figure 2-6A). For some stream gauges, the NSE is not significantly impacted when the number of lakes that are active in the routing model is reduced (e.g., gauge 06SB001 and 06OA007 in Figure 2-5A). In contrast, the NSE significantly degrades in some sub-basins when we deactivate lakes in the routing model (e.g., gauge 05OJ005 and 04AB001 in Figure 2-6A). The lake size thresholds that influence the routing result differ across the 15 gauges. For gauge 05OJ005, the most drastic change in NSE performance is observed when lakes with a lake area smaller than 10 km<sup>2</sup> are deactivated, while the steepest change in NSE for sub-basins 04AB001 and 06GD001 is observed when lakes with a lake area smaller than 100 km<sup>2</sup> are deactivated. The relative impact of including lakes upon model performance is illustrated in Figure 2-6B, where performance improvement between the all lakes and no-lakes cases is plotted against percent lake coverage. There is clearly a trend in performance improvement, whereby basins with higher lake coverage receiving greater benefit from the presence of lakes in the model. It is concluded from the results shown in Figure 2-6 that (1) despite the lack of model calibration, the Raven-GEM-Surf product adequately represents most of the observed basin hydrographs and (2) there is a general degradation of model performance with removal of lakes, and this degradation is more salient in basins where lakes cover more of the basin.

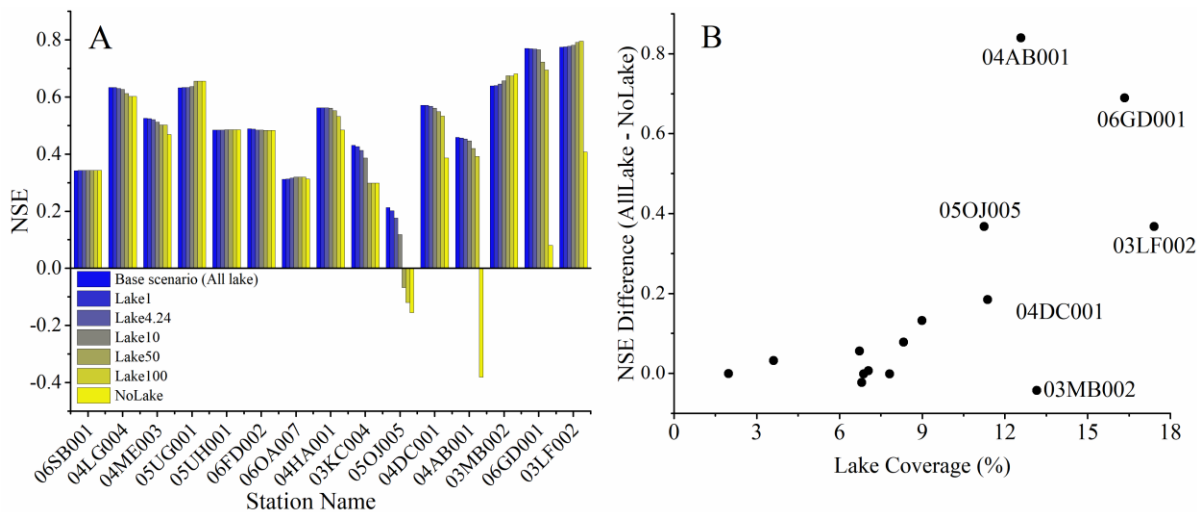


**Figure 2-6.** A) Uncalibrated routing model performance (Nash-Sutcliffe Efficiency NSE) at 15 gauging stations (Table 2-3) using various lake scenarios (Table 2-1). Gauges in A are sorting of results by lake area coverage. The lake coverage is the ratio between total lake area in each gauge’s drainage region and the total drainage area of each gauge. The NSE is computed using daily average flows for the

simulation period from Jan 1, 2007 to Oct 7, 2010. For all simulations we used the L8-Lake0 as a setup and deactivated lakes below certain areas as indicated in the legend. “Base scenario” means all lakes in the lake-river routing structure were active; “Lake1” means lakes with a lake area smaller than 1 km<sup>2</sup> were inactive compared to the base scenario. “NoLake” means all lakes in the base scenario were inactive and hence the simulation was performed without any lake. B) the impact of the lake coverage on the NSE differences between base scenario (All lake) and no lake scenario.

The function of lakes on routing is impacted by lake and watershed characteristics. The first characteristic is the relative ratio between lake area and lake drainage area ( $\alpha_{\text{Alake/DAlake}}$ ) (Fitzgibbon and Dunne, 1981; Kusumastuti et al., 2008; Spence, 2000), which is a factor that describes the lake’s storage capacity relative to the total runoff generated in the lake’s drainage area. Fitzgibbon and Dunne (1981) found that the lake’s impact on hydrograph characteristics such as smoothing and lagging was increasing with the increasing of  $\alpha_{\text{Alake/DAlake}}$ , and the impact of a lake on a hydrograph was significant only when  $\alpha_{\text{Alake/DAlake}}$  was larger than 5%. Similar results are reported by Leach and Laudon (2019). However, results in Woo and Mielko (2007) show that Lois Lake with a low  $\alpha_{\text{Alake/DAlake}}$  of 2% was able to impact the lake outflow, which suggests that the  $\alpha_{\text{Alake/DAlake}}$  ratio alone is not a satisfactory indicator of flow attenuation (Woo and Mielko, 2007). The second factor is the relationship between quick runoff and slow runoff in the lake’s drainage area and the lake evaporation rate (Zajac et al., 2017; Mielko and Woo, 2006). In the case of Skeeter Lake, presented by Mielko and Woo (2006), the lake level seldom rises above its outflow threshold. Because the rate of the lake inflow does not match the rate of lake evaporation, which is attribute to the low ratio between quick runoff and slow runoff (Mielko and Woo 2006). Zajac et al. (2017) also found that the watershed with high runoff ratio was more sensitive to lakes in routing modelling. The third factor is the downstream distance between the lake outlet and the point of interest for streamflow estimation and this is measured by the ratio between lake’s drainage area relative to the watershed drainage area upstream of the point of interest ( $\alpha_{\text{DAlake/DAw}}$ ) (Leach and Laudon, 2019; Mielko and Woo, 2006). The observation study by Leach and Laudon (2019) show that in a headwater catchment, streamflow contributions from these small lakes can persist (e.g., are a non-negligible part of the observed hydrograph) at least 4.2 km downstream. The result from Leach and Laudon (2019) indicate that the impact of a lake on routing decreases as  $\alpha_{\text{DAlake/DAw}}$  decreases.

The hydrographs of gauge 12 simulated by the base scenario and the NoLake scenario are shown in Figure 2-7. The base scenario gives better performance than the NoLake scenario, since the peak flow is significantly reduced and delayed by including lakes. Thus, the developed routing network can

provide reasonable stream flow simulation and the impact of lakes was reasonably simulated by the routing network.

The serial runtime of Raven in routing mode, using the model setup in previous sections, for a 10-day simulation run at an hourly computational time step for the Hudson Bay watershed (3.53 million km<sup>2</sup>, 26419 catchments including 14975 lake catchments) is 3.2 minutes. The runtime is an average of multiple runs performed on a compute cluster (Graham Compute Canada cluster).

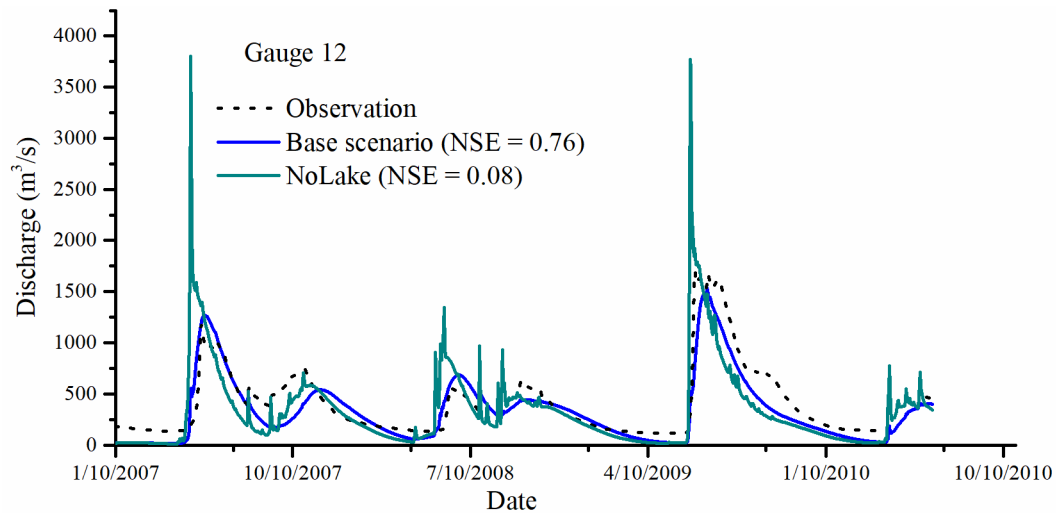


**Figure 2-7.** Hydrograph simulated at gauge 12 (06GD001) by the base scenario (i.e., L08-Lake0; blue line) and the no lake scenario (i.e., L8-NoLake; green line) compared with the observed hydrograph (dashed line). The “Base scenario” means all lakes in the lake river routing network were active; the “NoLake” means all lakes in the base scenario were inactive. The simulation period is Jan 1, 2007 to Oct 7, 2010.

### 2.4.3 Routing network availability and limitation

The publicly available developed routing networks can support hydrological modelling at different scales and are accessible online (Han et al. 2020) in the form of ESRI shapefiles and corresponding database tables. For example, the routing network topologies can form the basis for watershed discretization in distributed hydrological modelling studies and such an approach would eliminate or minimize DEM processing. Once users select the routing network of interest and extract the region of interest using appropriate GIS tools, they can directly use the watershed delineations in a number of catchment-delineated hydrological models.

Limitations of the proposed lake-river routing network are following: First, we assume that each lake in the routing network can only have one outlet. This assumption is not appropriate when lake have two or more outlets. Second, not all lakes in HydroLAKE database are included in the lake-river routing network. Only lakes that are connected by the HydroBASINS river system are selected and included in the lake-river routing network. Third, only two lake selection strategies are provided in this lake river routing network. The routing network cannot support user to customize their own lake selection strategies.

## **2.5 Conclusion**

This research presents the development of twelve publicly available pan-Canadian lake-river routing networks. These are the first routing networks available that explicitly and in a hydrologically consistent way represent lakes for the domain of Canada. The routing networks provide the necessary routing network topology and network attributes to enable vector-based hydrological routing anywhere in Canada. A case study using the Raven hydrological modelling framework to simulate routing from the Hudson Bay watershed, the first application of this tool in routing-only mode, shows that the effect of lakes on routing can be adequately simulated by using the default routing attributes from this product. In addition, the case study simulation results demonstrate that the elimination of lakes can have a significant detrimental impact on hydrograph quality for some gauge locations, and that exclusion of lakes from large-scale simulations degrades hydrograph quality in lake-dominated watersheds.

The derived routing networks provide a useful starting point for subwatershed-based spatially distributed modelling applications in Canada as any of the example networks could be directly adopted as the subwatershed discretization in the case study area of interest. Beyond this benefit, as demonstrated, the derived routing networks can be used to build a routing-only model for routing any hydrological or land surface model fluxes with these fluxes being supplied to Raven in routing-only mode as gridded, subwatershed, or any other shaped model outputs.

## Chapter 3

### **Basin Maker 3.0: a GIS toolbox for distributed watershed delineation of complex lake-river routing networks**

This chapter is a mirror of a complete draft manuscript to be submitted to the journal *Environmental Modelling and Software*. Contributing authors on this work at this time are M. Han, H. Shen, B. A. Tolson, J. R. Craig, J. Mai, S. Lin, F. Awol, and N. Basu. Contents in this chapter have been drafted primarily by M. Han and secondly by H. Shen and B. A. Tolson.

#### **3.1 Summary**

Lakes and reservoirs have critical impacts on hydrological, biogeochemical, and ecological processes, and they should be an essential component of hydrological and eco-hydrological watershed models. Past large-scale hydrological modelling efforts tend to either ignore the impacts of all lakes or explicitly simulate the behavior of only the largest lakes in a watershed. This is due to practical difficulties inherent in representing thousands of lakes in various hydrological models. We introduce an open-source GIS toolbox (BasinMaker) that can automatically and efficiently build vector-based hydrological routing networks, including subbasin extents for systems with an arbitrary number of lakes. The toolbox is hydrological model-independent in that, by default, it outputs a complete lake-river routing network in shapefile format. BasinMaker also generates estimates of all the necessary hydrological routing model inputs, including network topology, subbasin/catchment geometry, channel characteristics (slope, length, roughness, and geometry), and lake characteristics (area, volume, and outlet description). A lake-river routing network from BasinMaker therefore includes both the network topology/connectedness plus the aforementioned routing model inputs as shapefile attributes. The two main BasinMaker software operation modes are: 1) Network delineation mode using any DEM and any lake polygon dataset as inputs to delineate a lake-river routing network and 2) Network post-processing mode, providing a set of useful functions to post-process any existing lake-river routing network already generated by BasinMaker. BasinMaker is applied here to build two high resolution vector-based lake-river routing products each defining a collection of routing networks across large regions: the North American Lake-River Routing Product v2.1 using the Multi-Error-Removed Improved-Terrain DEM (90×90 m) and the Ontario Lake-River Routing Product v1 using Ontario Integrated Hydrology (OIH) Datasets (30×30 m). Both routing products include all lakes over 10 ha identified in the

HydroLAKES dataset. BasinMaker is unique compared with other routing network delineation tools in terms of lake representation and is especially helpful for modelers who need to represent numerous lakes in their watershed simulation models explicitly.

### 3.2 Software and data availability

BasinMaker 3.0 software is freely available. BasinMaker is a GIS toolbox written in the Python programming language. The installation of BasinMaker and examples of using BasinMaker can be found at <http://hydrology.uwaterloo.ca/basinmaker/index.html>. Users can install the BasinMaker Light version of the software (network post-processing mode only) or a full version of the software (network delineation mode as well as network post-processing mode). Note that installation procedures for the full version of the software is more complex. Detailed developer documentation for all BasinMaker functions can be found at [https://basinmaker.readthedocs.io/en/latest/basinmaker\\_tools.html](https://basinmaker.readthedocs.io/en/latest/basinmaker_tools.html). BasinMaker in network post-processing mode (light version of the software) can also be used online on Google Colab. A Google Colab example notebook, [located here](#), enables users to easily simplify the existing lake-river routing networks via BasinMaker without installing anything on their local machine. The source code of BasinMaker is available via Github (<https://github.com/dustming/basinmaker>) under the GNU General Public License v3.0. BasinMaker's installation and documentation is available via Readthedocs (<https://basinmaker.readthedocs.io/en/latest/overview.html>) where BasinMaker Light includes only the network processing mode capabilities of the software and BasinMaker Full includes both the delineation mode and the post-processing mode. The BasinMaker main webpage ([http://hydrology.uwaterloo.ca/basinmaker/examples\\_overview.html](http://hydrology.uwaterloo.ca/basinmaker/examples_overview.html)) provides three application examples. Links to the large scale, high resolution routing products also developed and described in this paper are:

- The North American Lake-River Routing Product v2.1 developed using BasinMaker is available at <http://hydrology.uwaterloo.ca/basinmaker/index.html>
- BasinMaker generated Ontario Lake-River Routing Product v1 is available at <https://lake-river-routing-products-uwaterloo.hub.arcgis.com>.

### 3.3 Introduction

Lakes and reservoirs play a critical role in the regional scale water balance. First, they can retain runoff from the upstream catchment and release water later to the downstream rivers, which influences the timing and volume of runoff that is transmitted to the downstream (Bowling & Lettenmaier, 2010; Huziy & Sushama, 2017; Christopher Spence, 2000; Woo & Mielko, 2007; Zajac et al., 2017). Further, the active contributing area or the flow connectivity of the watershed is often controlled by lakes (Costa et al., 2020; Woo & Mielko, 2007). Moreover, the interactions between lakes/reservoirs and groundwater are key components in both hydrological and geo-chemical processes that can affect both water quantity and quality (Hughes et al., 2014; Spence, 2006). Therefore, considering lakes and reservoirs as a component in hydrological models can increase the models capacity to simulate critical processes and potentially improve model performance (Golden et al., 2016; Karan et al., 2014; Shaw et al., 2013).

Lakes, reservoirs and wetlands also play a crucial role in biogeochemical processes. Cheng and Basu (2017) analyzed data across 600 sites to show the importance of small water bodies (lakes, reservoirs, and wetlands) for retaining nitrogen (N) and phosphorus (P), thus regulating their movement to downstream waters. Harrison et al. (2009) reports that small lakes account for 65% of the N removal in all lakes. Downing (2010) reports that organic carbon burial rates in small lakes and reservoirs exceed those of larger lakes by more than an order of magnitude.

To build an environmental simulation model of any watershed that explicitly represents both small and large water bodies such as lakes, reservoirs, and wetlands, modellers need to define the lake characteristics and build the lake-river routing structure (Evenson et al., 2016, 2015; Han et al., 2020). Necessary lake characteristics typically include the location and extent of the lake, the crest height of the lake outlet, and a relationship that defines the lake surface area and volume as a function of lake depth. A detailed lake characterization may require lake bathymetry, which is unavailable for most lakes in a lake-dominated watershed. Several global lake databases, such as HydroLAKES (Messenger et al., 2016) and GLOBathy (Khazaei et al., 2022), provide the estimated location and extent of the lake, lake area, lake volume, and lake averaged depth for lakes with lake area larger than 10 ha. With information from these databases, the lake characteristics may be estimated with some assumptions. For example, Han et al. (2020) assume that lakes are prismatic, which means that the lake area does not

change with lake depth, and the lake crest elevation relative to the lake bottom, is the same as the lake averaged depth.

In hydrological models, lakes and/or reservoirs are represented as a part of the routing structure (Lehner & Grill, 2013). The routing structure is generally used to formally represent water flow pathways from land to streams, lakes/reservoirs, and eventually converging to the watershed outlet. It is a topologically consistent system of stream networks and local contributing areas of lakes and stream reaches (e.g., subbasins), and the connections between them, typically in the form of a hierarchical network. Here, a watershed *routing structure* only defines how the subbasins, stream reaches and lakes/reservoirs in the watershed are connected. Hydrological routing simulation using such a routing structure also requires routing-relevant parameters and attributes (e.g., lake area and river channel slope). Throughout this paper, we consider a hydrological *routing network* to be the combination of routing structure/topology plus the corresponding routing attributes of the lakes, channels and subbasins necessary for hydrological routing. We also define a collection of routing networks covering a large geographic region and delineated from the same source DEM and lake polygons as a *routing product*.

A routing structure, and hence a hydrological routing network, can be represented in a gridded approach (see, e.g., Gaborit et al., 2017; Miller et al., 1994) or vector-based approach (Lin et al., 2018; Yamazaki et al., 2013). Compared with the gridded approach, the vector-based routing structure can more accurately represent the drainage area boundaries and location of hydrological features and can represent the watershed with fewer computational objects and thus is computationally more efficient (Lin et al., 2018; Yamazaki et al., 2013). Gharari et al. (2020) also call for land surface modellers to adopt flexible vector-based spatial configurations to better model at the scale of interest. Hydrological compartments in a vector-based routing structure can be well represented by GIS-based feature classes such as polygons and polylines, and the topology relationships between these GIS features. GIS features for a vector-based routing structure without lakes can be readily generated from a digital elevation model (DEM) using various GIS tools, such as ArcSWAT (Winchell et al., 2007), ArcHydro (Maidment, 2002), TATOO (Mitterer, 2022), TauDEM (Tarboton, 2015) or other hydrology toolsets within GIS platforms (ESRI, 2012; Neteler et al., 2012). In the resultant stream-only routing structures, water is transmitted from one subbasin to another and the flow pathways are simulated as converging from land to streams, and then flowing to the outlet.

However, it is more complicated to produce a vector-based routing structure including lakes (a lake-river routing structure). Generally, the approaches to generate a lake-river vector-based routing structure can be classified into two categories. First, a lake-river vector-based routing structure can be generated by collectively overlaying the lake shoreline polygon onto the subbasin polygons of a vector-based routing structure without lakes, and then updating the properties of the newly-derived polygons and the new network topology (Molina-Navarro et al., 2018). This approach has been used to produce the HydroSHEDS routing network with inserted lakes (Lehner & Grill, 2013). And, a recently developed GIS toolkit called SWAT2lake (Molina-Navarro et al., 2018) can automatically insert a single lake into a vector-based routing structure without lakes with this procedure. As noted by the author, the limitation of this approach includes: 1) many small polygons around the lakes would be generated after the overlay operation and these small polygons are data redundancies rather than true subbasins (Molina-Navarro et al., 2018); 2) the drainage area of the lake is not accurately represented (Lehner & Grill, 2013). In addition to generating excessive numbers of small subbasins, SWAT2lake is not built to handle watersheds with numerous lakes and does not provide a GIS-based default lake outlet characterization (a required hydrological routing input).

Second, a lake-river vector-based routing structure can be alternatively generated by directly modifying the flow direction dataset. The flow direction dataset is a raster dataset derived from a digital elevation model (DEM), indicating the flow direction of each DEM grid cell. In this approach, the flow direction dataset is manipulated to ensure that water in grid cells that are covered by the lake will drain to the lake outlet. The lake outlet and inlets are also identified and treated as additional subbasin pour points. This approach can be implemented with ArcHydro tools (Maidment, 2002). However, the ArcHydro tools (Maidment, 2002) manipulate the flow direction dataset such that the grid cells covered by lake will flow to the closest derived river reaches under the lake rather than to the lake outlet. The result of this manipulation can divide a lake into multiple separate subbasins on the basis of unreliable DEM elevations under the lake, potentially leading to more than one lake outflow river reach. Han et al. (2020) avoided the problem in the ArcHydro tools by modifying flow direction grids such that water flows to the designated HydroLakes lake outlet point. However, the approach in Han et al. (2020) cannot be applied to the high-resolution DEM due to the excessive computational burden, in addition, the implementation of Han et al. (2020) relied on proprietary GIS software.

This paper proposes a new open-source GIS toolbox (BasinMaker version 3.0), which can efficiently and correctly delineate (and conveniently simplify via post-processing) a vector-based hydrological

routing network (topology plus the corresponding routing attributes) in lake-dominated watersheds from any hydrologically consistent DEM. BasinMaker version 1.0 was an unreleased tool developed based on ArcGIS functionalities and was used to derive a suite of Pan-Canadian subwatershed-based lake and river routing GIS products at multiple spatial resolutions (Han et al. 2020). BasinMaker version 2.0 was a distributed but unpublished toolbox with enhanced features and was developed using the open-source QGIS and GRASS GIS platforms. BasinMaker version 3.0 has even more enhanced features and attributes and also relies on using the open-source QGIS and GRASS GIS platforms. Unless otherwise noted, BasinMaker throughout the rest of this paper will refer to version 3.0 of the tool.

The main improvements of BasinMaker version 2.0 & 3.0 over version 1.0 are the following: 1) it is based on open source GIS platforms; 2) a new much more efficient flow direction manipulation method is applied for merging lakes into the drainage network; 3) additional discretization within each subbasin into Hydrologic Response Units (HRUs) based on up to three user input GIS layers is now possible; 4) routing networks can alternatively be delineated directly from a user-provided flow direction grid, one for example that has been manually corrected, instead of a DEM; 5) a more robust approach to including user-defined points of interest (e.g., streamflow gauge locations) as subbasin outlets; 6) the vector-based routing structure generated from DEM analysis can now be efficiently simplified and customized by BasinMaker post-processing tools (without further terrain analysis). Key BasinMaker post-processing operations on an existing hydrological routing network include: a) Extract a subregion of interest b) Simplify the lake-river routing network (by decreasing the resolution of the stream network and thus increasing the size of subbasins or by removing the lakes from it) c) Define HRUs to subdivide each subbasin and generate model setup files for the Raven hydrological modelling framework based on user-provided landuse and soil layer polygons. These post-processing tools are useful for users keen to utilize a routing network of interest already delineated by BasinMaker, such as those networks included in the North American Lake-River Routing Product v2.1 (available at <http://hydrology.uwaterloo.ca/basinsmaker/index.html>) and the Ontario Lake-River Routing Product v1 (available at <https://lake-river-routing-products-uwaterloo.hub.arcgis.com>). Both of these routing products are also introduced for the first time in this paper. With a baseline hydrological routing network, these tools save BasinMaker from DEM terrain processing and make it feasible and efficient to produce a well-delineated routing structure tailored to purpose. To our knowledge, such a collection

of efficient post-processing tools for generating and simplifying lake-river routing networks have not been reported elsewhere.

The remainder of this paper is structured as follows: Section 3.4 overviews the lake-river routing network produced by BasinMaker. Section 3.5 details the delineation functions available in BasinMaker and describes the technical implementation of some of the core functions. Section 3.6 describes the use of BasinMaker to create the North American Lake-River Routing Product which is a set of highly resolved hydrological routing networks covering Canada and the USA, including all lakes over 10 ha in area. Section 3.7 describes the use of BasinMaker to create the Ontario Lake-River Routing Product, which is a set of even higher resolution hydrological routing networks covering the ~1 million km<sup>2</sup> Province of Ontario, Canada. Section 3.8 describes limitations of BasinMaker and developed routing products. Section 3.9 contains the study conclusions.

### **3.4 Overview of the lake-river routing networks produced by BasinMaker**

Before introducing the methodology and application of BasinMaker, the differences between a routing network without considering lakes and a routing network with lakes defined by BasinMaker is introduced in this section. Differences in routing networks are reflected in the routing structure defining how subbasins, river channels and lakes are connected.

An example vector-based routing structure without considering lakes is shown in Figure 3-1A. Subbasins in such a routing structure are only determined by river reaches. An example of a routing structure with lakes is shown in Figure 3-1B for the same watershed as Figure 3-1A. A lake subbasin is defined as in Han et al. (2020) by the following rules: 1) The extent of a lake subbasin will fully cover the lake; 2) a lake outlet defines the outlet of the lake subbasin; 3) each of a lake's significant inlets (i.e., those associated with streams above a specified flow accumulation threshold) is defined by an upstream subbasin outlet. In this way, both inflow and outflow of each lake can be explicitly simulated by hydrological routing models.

Lakes are divided into two categories by BasinMaker: (1) Connected lakes (CL), which are lakes with a lake outlet that is explicitly connected to a downstream non-zero length river channel in the routing structure; and (2) Non-connected lakes (NCL), which denotes lakes that are defined to drain to the downstream routing network but do not flow through any explicit river channel (see small yellow subbasin in Figure 3-1B). By default, both CL and NCL within a watershed are considered to be contributing areas of the watershed, though this assumption can be reversed for NCLs when

appropriate. The only difference between CL and NCL is that a CL always drains into an explicitly represented river channel that is connected to the lake outlet while a NCL does not. NCLs can exist because the user-defined minimum drainage area (flow accumulation threshold) for defining/starting a new river reach can sometimes be larger than the drainage area of smaller lakes, particularly for headwater lakes. In this way, BasinMaker separately identifies NCL and enables users to treat them separately from the CL lakes. The control points shown in Figure 3-1 define the location of a subbasin outlet, and for any non-lake subbasin, the BasinMaker delineation strategy described later determines the control point locations in a way that favours the creation of fewer subbasins.

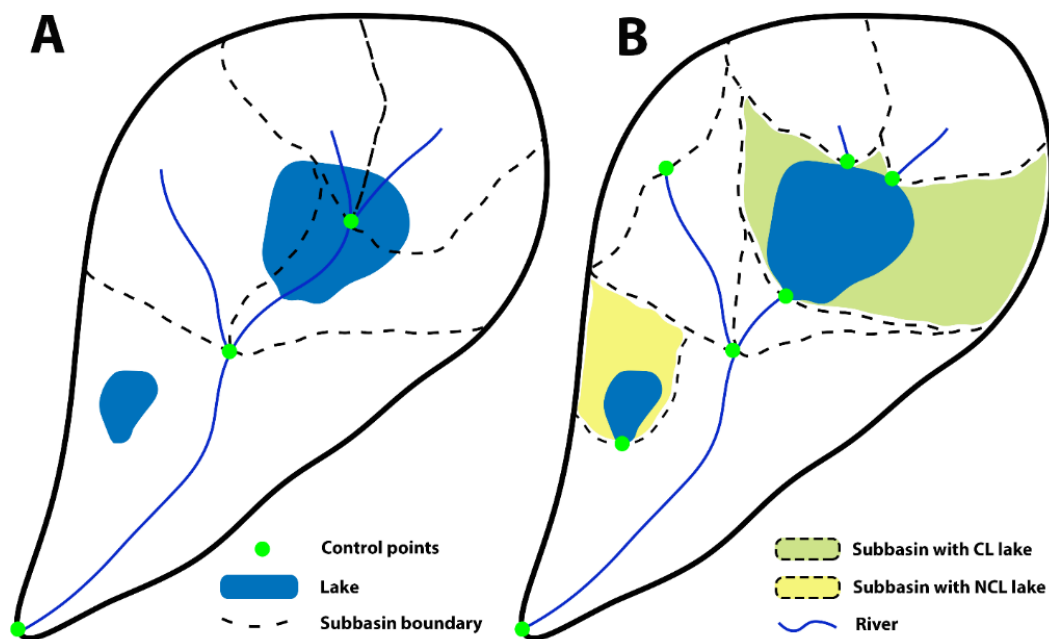


**Figure 3-1.** Vector-based routing structure without considering lakes (A) and with lakes (B). The CL represents connected lakes (CL), which are lakes with a lake outlet that is explicitly connected to a downstream non-zero length river channel in the routing structure. The NCL represents non-connected lakes (NCL), which denotes lakes that are defined to drain to the downstream routing network but do not directly flow into an explicit river channel.

The proposed routing structure generated with BasinMaker describes the network topology (connectedness and flow directions) of the component subbasins, river channels and lakes. In order to simulate hydrological routing through such a structure, additional component attributes (physical

characteristics and parameters) are also required, and these are estimated and then output by BasinMaker. The additional component attributes produced by BasinMaker can be categorized into four groups: the attributes of the lake, attributes of the river channel, the attributes of subbasins and the attributes of points of interest (POI). Lakes (including reservoirs) in BasinMaker are assumed by default to be prismatic with a broad-crested weir as the outlet structure, and as such BasinMaker reports the lake area, lake depth, and crest width for the lake outlet. BasinMaker also includes an attribute indicating whether the subbasin has one CL lake, one NCL lake, or no lake. With a maximum of one river channel per subbasin, BasinMaker derives the river channel length, cross-section profile, slope and both the main channel and floodplain Manning's coefficients. For the subbasin's attributes, BasinMaker includes the subbasin area and the average subbasin slope. The methodology to calculate each of these attributes is described in section 3.5.2.

### **3.5 Technical implementations**

This section introduces techniques implemented in BasinMaker. Section 3.5.1 summarizes the main functions of BasinMaker in its two working modes: 1) delineating a hydrological routing network from a DEM (delineation mode); 2) post-processing an existing routing network previously produced by BasinMaker to generate a new simplified/customized hydrological routing network (post-processing mode). Section 3.5.2 and 3.5.3 introduce the methodology applied in network delineation mode and network post-processing mode, respectively.

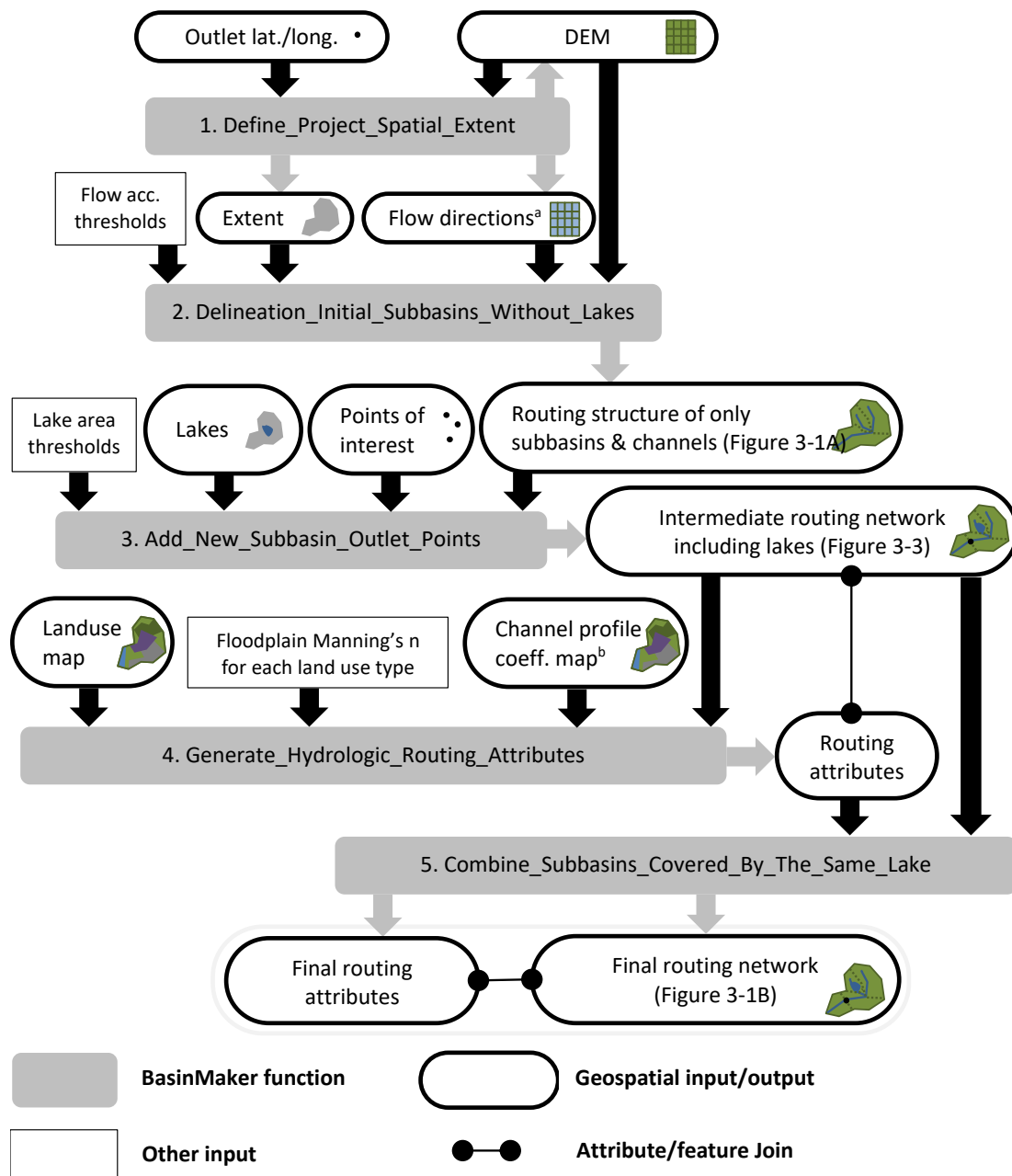
#### **3.5.1 Overview of BasinMaker Functions**

BasinMaker is a GIS toolbox written in the Python programming language. BasinMaker functions all rely on geoprocessing functions from the GIS environment it is configured to use. Users can apply BasinMaker post-processing mode functions in either QGIS, ArcGIS Pro, or Google Colab (which uses Geopandas GIS environment created by Jordahl et al., 2020) environments. BasinMaker delineation mode functions rely on the both QGIS and GRASS GIS environment. Although not precisely the same in each GIS environment, BasinMaker Light (post-processing mode) uses equivalent geoprocessing functions from Geopanda (Jordahl et al., 2020), QGIS or ArcGIS pro.

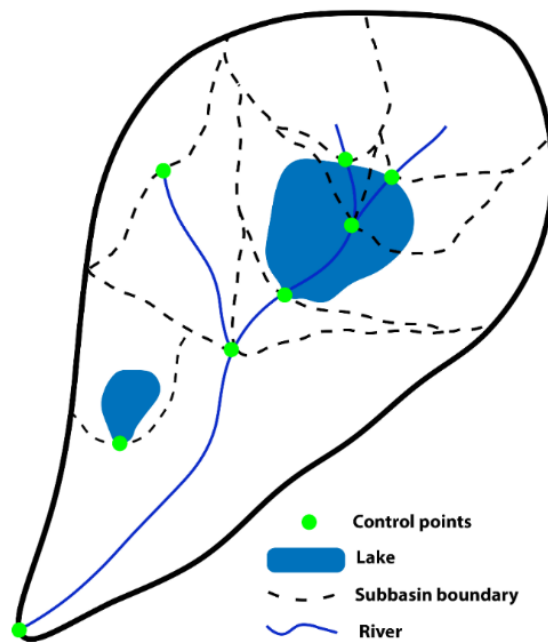
##### **3.5.1.1 Overview of BasinMaker Functions in network delineation mode**

Figure 3-2 describes the workflow associated with the five key network delineation functions in BasinMaker, applied sequentially to generate a routing network from a hydrologically conditioned

DEM and optional inputs includes lake polygons, flow direction raster dataset, landuse raster dataset, bankfull width and depth of channel polyline dataset, and a points of interest dataset. The 'Define\_Project\_Spatial\_Extent' function generates the spatial processing extent of the current project. BasinMaker will clip all input data with this spatial extent and delineate lake-river routing network(s) within this spatial extent. The 'Define\_Project\_Spatial\_Extent' function includes several options, which allow the user to directly specify the spatial extent of the input DEM as the spatial extent of the project or alternatively determine the spatial extent of the project from a watershed outlet latitude and longitude. The 'Delineation\_Initial\_Subbasins\_Without\_Lakes' function generates an initial routing structure without considering lakes (Figure 3-1A). The 'Add\_New\_Subbasin\_Outlet\_Points' function can add lake inlets, lake outlets or other points of interest as new subbasin outlets into the initial routing structure (see Figure 3-3 for an example result). The 'Generate\_Hydrologic\_Routing\_Attributes' function updates geometry attributes and estimates hydrological parameters for the subbasins, lakes, and rivers generated previously from the 'Add\_New\_Subbasin\_Outlet\_Points' function. Appendix A2 lists all attributes added by the 'Generate\_Hydrologic\_Routing\_Attributes' function. The output of the 'Generate\_Hydrologic\_Routing\_Attributes' function is an intermediate hydrological routing network because it represents some lakes with multiple subbasins (Figure 3-3). The function 'Combine\_Subbasins\_Covered\_by\_the\_Same\_Lake' generates the finalized hydrological routing network (Figure 3-1B). Note that depending on the user-specified option for the first 'Define\_Project\_Spatial\_Extent' function, the resulting routing network may not be a single watershed and instead may include a number of subbasins that drain external to the DEM extents. The post-processing mode function #3 in Table 3-1 below can be applied to focus the delineated network on a single watershed and/or strip away small watersheds along the boundary of the original spatial extent.



**Figure 3-2** Workflow, including inputs and outputs, of the BasinMaker network delineation mode functions for generating a hydrological routing network with lakes and rivers given a DEM and a lake polygon layer. Notes: a) Flow direction raster dataset is optional user input here. b) The channel profile coefficient map to define bankfull channel widths and depths across the extent can alternatively be replaced by coefficients that are constant across the project extent.



**Figure 3-3.** An example BasinMaker intermediate routing network output from ‘Generate\_Hydrologic\_Routing\_Attributes’ (Function #4 in Figure 3-2), in which the subbasins covered by the same lake did not get merged into one lake subbasin yet. This function updates geometry attributes and estimates hydrological parameters for the subbasins, lakes, and rivers in the intermediate hydrological routing network output from Function #3 in Figure 3-2. Note the methodology for delineating control points of headwater subbasins is discussed in Section 3.5.2.

The finalized hydrological routing network output of BasinMaker network delineation mode includes the following GIS shapefiles: a) Lake polygons (Figure 3-1B), b) points of interest, c) subbasin polygons and river polylines for intermediate hydrological routing network (output of the function ‘Generate\_Hydrologic\_Routing\_Attributes’ showed in Figure 3-2), and d) subbasin polygons and river polylines for the finalized hydrological routing network (Figure 3-1B). We will refer to GIS files from a) to d) as BasinMaker delineation mode outputs in the following section. The intermediate hydrological routing network outputs of the function ‘Generate\_Hydrologic\_Routing\_Attributes’ are included in BasinMaker delineation mode outputs because they are the required inputs of BasinMaker post-processing functions that simplify a BasinMaker delineated hydrological routing network (section 3.5.1.2). Any BasinMaker produced hydrological routing network (in either network delineation mode or network post-processing mode) is defined by the above four GIS shapefiles. Note that the attributes

of all four attribute groups are all assigned to subbasin polygon shapefile of the hydrological routing network.

### 3.5.1.2 Overview of BasinMaker Functions in network post-processing mode

Given a pre-existing hydrological routing network delineated by BasinMaker, users can apply network post-processing functions #1, #2, and #3 in Table 3-1 independently to customize and simplify (i.e., remove detail from an existing hydrological routing network. Although the core BasinMaker routing network data are model agnostic, users can apply functions #4 and #5 in Table 3-1 sequentially to export routing relevant input files for the Raven hydrological modelling framework (Craig et al. 2020). Functions #1 and #2 are described here in detail while the BasinMaker website (<http://hydrology.uwaterloo.ca/basinmaker/index.html>) describes functions #3, #4 and #5.

**Table 3-1.** Description of the BasinMaker routing network post-processing mode functions.

Function #	Function description	Function name in BasinMaker	User-defined parameters	Resultant outputs
1	Simplify a drainage network by removing lakes	Remove_Small_Lakes	Lake area thresholds below which lakes are to be removed, and an optional list of lakes to be retained	Simplified hydrological routing network
2	Simplify a drainage network by increasing subbasin areas	Decrease_River_Network_Resolution	A subbasin drainage area threshold below which subbasins are to be merged into adjacent ones	Simplified hydrological routing network
3	Extract a given subregion by subbasin topology	Select_Subregion_Of_Routing_Structure	A subbasin outlet ID	Local hydrological routing network
4	Create HRUs and update their attributes	Generate_HRUs	A minimum HRU area threshold and up to 3 other GIS layers	HRU map and associated attributes for end-use
5	Export routing model input files in Raven format (ASCII)	Generate_Raven_Model_Inputs	Model name for emulation in Raven, and subbasin group information	Raven input files for end-use

The input for functions #1 and #2 in Table 3-1 is the intermediate hydrological routing network (Figure 3-4A) in BasinMaker delineation mode outputs. Note the intermediate routing network GIS files, not the finalized network GIS files, are the required inputs here; they include the information required to properly simplify and thus recalculate attributes for a lower resolution routing network. The

output of simplifying function #1 (Figures 3-4C and D) and function #2 (Figures 3-4E and F) for the simplified (post-processed) network are equivalent to BasinMaker delineation mode outputs defined in section 3.5.1.1.

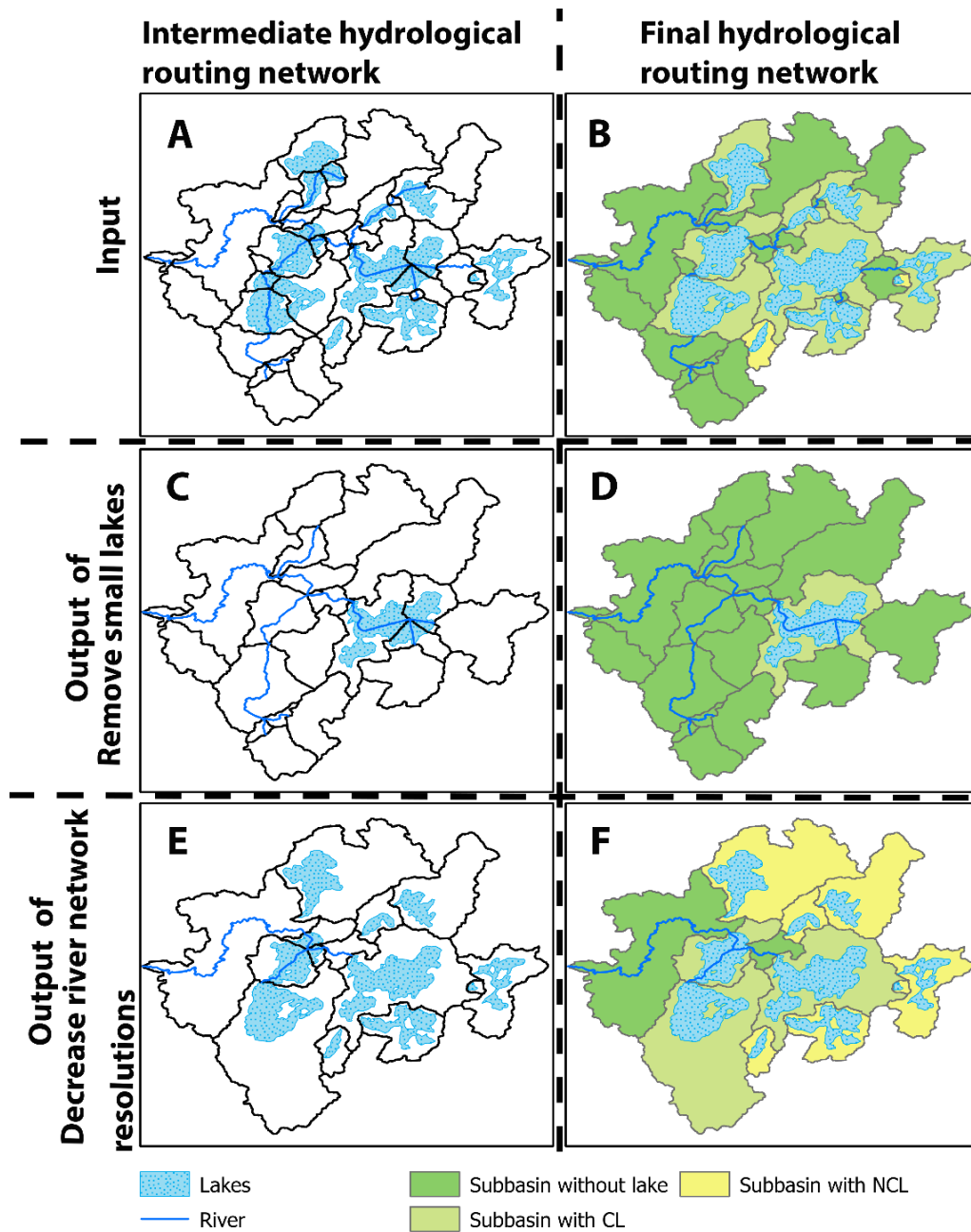


**Figure 3-4.** Example BasinMaker output from ‘Remove\_Small\_Lakes’ function (C and D) and ‘Decrease\_River\_Network\_Resolution’ function (E and F) using intermediate hydrological routing

network (A) as input. C) and D) are the intermediate hydrological routing network and the final hydrological routing network, respectively, output from the ‘Remove\_Small\_Lakes’ function (minimum lake area thresholds of 6 km<sup>2</sup> for both CL and NCL). E) and F) are the intermediate hydrological routing network and the final hydrological routing network, respectively, from the ‘Decrease\_River\_Network\_Resolution’ function (minimum subbasin area threshold of 23 km<sup>2</sup>). B) is the final hydrological routing network corresponding to the input intermediate hydrological routing network (A).

The “Remove\_Small\_Lakes” function removes lakes from the input network based on lake area thresholds for connected lakes and non-connected lakes. Figures 3-4C and D demonstrate the outputs from the function ‘Remove\_Small\_Lakes’ using the routing network shown in Figure 3-4A as input. The “Decrease\_River\_Network\_Resolution” function increases the size of subbasins size and reduces the river network’s resolution from the input when subjected to a larger drainage area threshold. Subbasins with their drainage area smaller than this threshold are merged with their downstream subbasins. Figures 3-4E and F demonstrate the outputs from the function ‘Decrease\_River\_Network\_Resolution’ using the routing network shown in Figure 3-4A as input.

### **3.5.2 Methodology in BasinMaker network delineation mode**

Once the project spatial extent is defined, BasinMaker network delineation mode requires four steps to produce a hydrological routing network from a hydrologically consistent digital elevation model (DEM). These steps are functions #2 through #5 in Figure 3-2.

Given a user defined DEM, function #2 in Figure 3-2 will create an initial stream network and routing structure without considering lakes using GRASS.GIS terrain analysis functions (r.stream.basins and r.watershed). The ‘r.watershed’ function will determine each DEM cell’s flow direction (Figure 3-5A) and flow accumulation. Optionally, instead of processing the DEM, users can input the flow direction grid directly. Then function ‘r.stream.basins’ will identify streams and subbasins (Figure 3-5A) from the flow accumulation map based upon a user-provided flow accumulation threshold. Note that function #2 leaves headwater drainage areas (a subbasin with a headwater river segment) to be delineated into subbasins only after lakes are considered in the next step. Generally, function #2 will generate a coarser stream network and fewer subbasins when using a larger flow accumulation threshold value. The outlet of each subbasin in Figure 3-5A is identified as control points to be used in later steps.

Given a set of lake polygons and an optional set of points of interest, function #3 in Figure 3-2 will further process the outputs from function #2 (Figure 3-5A shows such an example output as well as a lake relative to that output layer) to add lake inlets, outlets, the initiation points of select headwater river segments, and points of interest as new control points (new subbasin outlets) into the intermediate routing network. A point of interest is a location where the user wants to define a subbasin outlet. This function will ensure the delineated routing structure of the network meets the following criteria: a) the water within a lake will move to the lake outlet; b) any lake outlets are subbasin outlets; 3) any lake inlets are subbasin outlets. BasinMaker only adds a new control point to the initiation point of a headwater river segment if the headwater river segment is not at all covered by a lake (see Figure 3-5A which shows two such headwater river segments partially covered by a lake and one that is not). The lake-covered headwater river segment initiation points in Figure 3-5B are not new control points since each of these would create an extra tiny subbasin between the headwater river segment initiation point and the lake (Figure 3-5B). Such tiny subbasins are unnecessary for hydrological modeling and would increase the computational burden.

Function #3 will first add lake inlets and outlets into the initial routing structure. It distinguishes user-provided lake polygons as connected lakes or non-connected lakes and only retains lakes with a lake area larger than the user-provided lake area threshold. BasinMaker uses the retained lake polygons to identify lake outlets and inlets and regards them as additional pour points. A lake outlet is determined as the cell having the highest flow accumulation value within each lake polygon. Lake inlets are determined from the intersection points among the lake boundary cells and river network cells. BasinMaker identifies one lake outlet only for each lake, while the number of lake inlets may vary. BasinMaker will directly use the points of interest input (e.g., a map of point locations of streamflow gauges) as pour points. Note that only points of interest within a user-specified snapping distance threshold of the delineated stream network are automatically included as a pour point using the 'r.stream.snap' function in GRASS GIS. Afterward, an updated routing structure, including subbasin polygons, is generated based on the updated pour points and the flow direction map from step 1, as shown in Figure 3-5B.

Second, function #3 will identify lakes for which part of the lake area did not belong to the intermediate lake outlet contributing area (Figure 3-5B). In Figure 3-5B, the left part of the lake belongs to a subbasin that does not drain to the lake outlet. The right part of the lake is covered by three subbasins (green filled subbasins in Figure 3-5B) flowing to the lake outlet. We define these three

subbasins that partially cover the lake and flow to the lake outlet as the partial lake subbasins of this lake.

Third, function #3 will correct the flow direction of cells within the identified lakes. As shown in Figure 3-5B, the correction needed is to ensure the water in the left part of the lake flows to the lake outlet. The correction is achieved with a minimum of processing time by modifying the flow direction of only the lake boundary cells. For example, any of these cells (red boundary cells in Figure 3-5C) with their flow directions not pointing toward the three right partial lake subbasins, referred to as the un-converged boundary cells (UBCs), are corrected. The flow directions of UBCs are corrected in two steps: a) the flow directions of the two UBC cells that are at the three lake subbasin boundaries (cells shown in Figure 3-5C with the yellow color) are manipulated to make the water at each UBC flow to one of the adjacent three partial lake subbasins (three right lake subbasins in Figure 3-5B). b) change the flow direction of the remaining UBCs (grid cells with the green color in Figure 3-5C) to make water in these cells move to the closest yellow cells in Figure 3-5C. With this modified flow direction dataset, all lake cells now drain to the lake outlet and an updated routing structure will be generated (Figure 3-5C).

Next, function #4 in Figure 3-2 estimates physical attributes for each subbasin, river reach, lake, and point of interest shown in Figure 3-5C. Appendix A2 lists all attributes added by this function. Most of these attributes are estimated using the methods described in Han et al. (2020) for developing the Pan-Canadian routing network. Except for bankfull width ( $w$  in [m]), bankfull depth ( $d$  in [m]), and bankfull discharge ( $Q$  in [m<sup>3</sup>/s]), the rest of the attributes are estimated as described in Han et al. (2020) are calculated here using the same methods. Andreadis et al. (2013) use the following two equations to calculate the  $w$  and  $d$  of each subbasin:  $w=7.2Q^{0.5}$  and  $d=0.27Q^{0.39}$ , respectively. They estimated  $Q$  using a power law relationship between  $Q$  and the drainage area ( $DA$  in [km<sup>2</sup>]),  $Q=k \times DA^c$ . Thus, to calculate the  $w$  and  $d$  of each subbasin, we need to assign  $k$  and  $c$  for each subbasin, which will be referred to as the channel profile coefficients. Two options are available: the user can provide constant channel profile coefficients for all subbasins or the user can provide a channel profile coefficients polygon GIS layer. Each channel profile coefficients zone in the channel profile coefficients layer has a unique pair of  $k$  and  $c$  values. This function will use the  $k$  and  $c$  values from the channel profile coefficients zone with the largest intersection area with each subbasin.

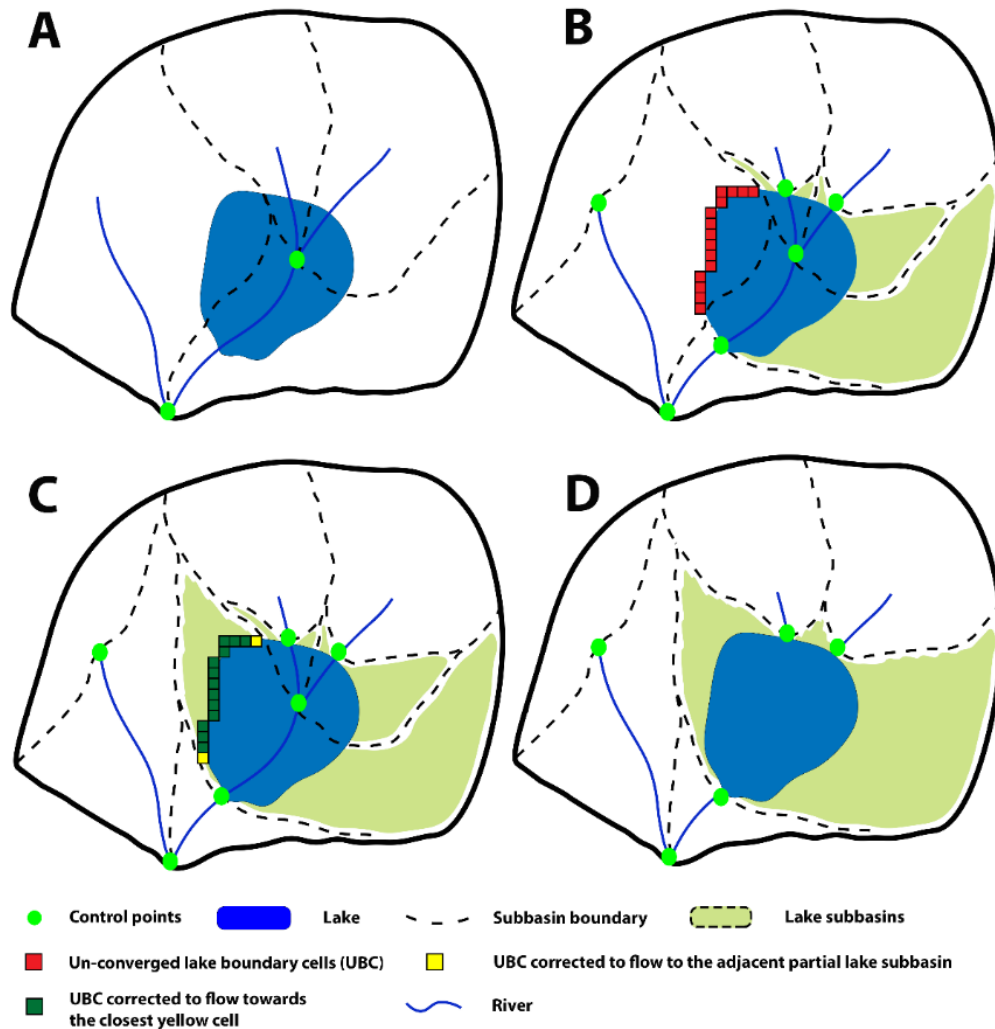


**Figure 3-5.** An example of BasinMaker intermediate and final delineation results for the four processing steps detailed in section 3.5.2 (functions #2 through #5 in Figure 3-2). (A) The initial stream network and routing structure without considering lakes from function #2 in Figure 3-2, overlaid with a lake polygon for reference. (B) The intermediate routing network after adding the lake's inlets and outlet as new subbasin outlets into the initial routing structure, a part of function #3 in Figure 3-2. (C) The intermediate routing network after correcting the flow direction of some lake boundary cells (UBCs), which is the aggregate output from function #3 in Figure 3-2. Note that function #4 in Figure 3-2 will calculate hydrological attributes for subbasins, lakes and rivers in the intermediate routing network of (C). (D) The final routing network delineation results after merging partial lake subbasins from function #5 in Figure 3-2.

Then function #5 in Figure 3-2 merges the three partial lake subbasins in Figure 3-5C and generates one lake subbasin completely containing the lake (Figure 3-5D). When merging partial lake subbasins into one lake subbasin, note that the resultant lake subbasin has no river channels. Subbasin attributes of the partial lake subbasins are carefully merged into a single attribute value for the lake subbasin. For example, lake subbasin properties like average slope and aspect are computed with an area-weighted average of the corresponding partial lake subbasins while lake subbasin area is computed as the sum of the corresponding partial lake subbasins' area.

These four steps ensure that: (1) Each lake polygon is fully contained by a lake subbasin representing its local contributing area; (2) Each lake outlet is the outlet of the lake subbasin; (3) Each lake inlet is represented by a pour point of an upstream subbasin, thus enabling lake inflow processes to be explicitly represented.

### **3.5.3 Methodology in BasinMaker network post-processing mode**

Although BasinMaker provides five post-processing GIS tools (Table 3-1), this section introduces the methodologies behind the two functions used for network simplification: 1) 'Remove\_Small\_Lakes' and 2) 'Decrease\_River\_Network\_Resolution'. We focus on these functions because these are unique of the software. Both post-processing functions are used to modify the intermediate hydrological routing networks generated by BasinMaker in delineation mode (Figure 3-4A).

Comparing the intermediate network inputs (Figure 3-4A) and outputs (Figure 3-4C) of function 'Remove\_Small\_Lakes', it is clear that the river network is generally same, but the outputs retain only one lake. This function uses the following steps to merge/simplify subbasins:

- 1) Identify lakes in the input routing network with lake area smaller than the user-provided lake area thresholds;
- 2) Change the lake related attributes (Appendix A2) to zero for lakes being removed;
- 3) From upstream to downstream, merge subbasins in the intermediate hydrological routing networks (Figure 3-4A) when the subbasins meet all of the following conditions: a) subbasins are directly connected, b) they have the same lake attributes (they are either lake subbasins overlapping the same lake or non-lake subbasins); alternately, the most downstream subbasin in the group contains a non-connected lake, and c) subbasins all drain to the same river reach;

4) Update the attribute values of merged subbasins. Similar to the step 4 in previous section, attributes of merged subbasins are carefully merged into a single attribute value for the various attribute groups. For example, select river channel properties are merged using channel length-weighted averaging and select subbasins attributes are merged using subbasin area-weighted averaging.

Lastly, the 'Remove\_Small\_Lakes' function will internally call the function 'Combine\_Subbasins\_Covered\_by\_The\_Same\_Lake' to generate the final hydrological routing networks (Figure 3-4D).

Comparing the input (Figure 3-4A) and output (Figure 3-4E) routing networks from function 'Decrease\_River\_Network\_Resolution', it is seen that the same lakes are retained but the outputs include only three river reaches. This function uses the following steps to merge/simplify subbasins:

1) Identify input subbasins (Figure 3-4A) with a drainage area smaller than the user-provided minimum drainage area threshold;

2) Remove river reaches of the identified subbasins;

3) Change all lakes upstream of the removed subbasin outlet to non-connected;

4) From upstream to downstream, merge subbasin polygons in the intermediate routing networks (Figure 3-4A) when the subbasins meet all of the following conditions: a) subbasins are directly connected, b) they have the same lake attributes (they are either lake subbasins overlapping the same lake or non-lake subbasins); alternately, the most downstream subbasin in the group contains a non-connected lake, c) subbasins drain to the same river reach and d) upstream subbasins do not include a point of interest;

5) Update the attribute table of merged subbasins. Attributes are updated using channel length-weighted averaging and subbasin area-weighted averaging as described above.

Lastly, the 'Decrease\_River\_Network\_Resolution' function will remove river reaches from the input intermediate hydrological routing networks by these steps (Figure 3-4E) and then internally call the function 'Combine\_Subbasins\_Covered\_by\_The\_Same\_Lake' to generate the final hydrological routing network (Figure 3-4F).

## **3.6 BasinMaker Application 1: Development of the North American Lake-River Routing Product v2.1**

### **3.6.1 Development of the North American Lake-River Routing Product v2.1**

We use BasinMaker v2.0 to develop version 2.1 of the North American Lake-River Routing Product (referred to as the NA Routing Product). The input data includes MERIT DEM (Yamazaki et al. 2017), HydroLAKES (Messenger et al. 2016) databases for lake polygons, points of interest comprising of 7791 streamflow gauges from Water Survey of Canada (WSC) and 28164 streamflow gauge from United States Geological Survey (USGS), and the global bankfull width, depth and discharge estimate for each channel reach of the finest scale HydroSHEDS river system (Andreadis et al. 2013).

The MERIT DEM is a high accuracy global DEM at 3-arcsecond resolution (~90 m at the equator) developed by eliminating major error components from existing spaceborne DEMs (Yamazaki et al. 2017). HydroLAKES is a database that includes shoreline polygons of all global lakes with a surface area of at least 10 ha (Messenger et al., 2016). Compared with datasets used to develop the Pan-Canadian lake-river routing network (Han et al. 2020), DEM resolution is substantially finer, now 3 arcseconds instead of 15 arcseconds.

The NA routing product was generated using: 1) a constant flow accumulation threshold (2000 90 m × 90 m cells, corresponding to 16 km<sup>2</sup>) to define the initial stream network and subbasins; 2) a zero lake area threshold to include all lakes from the HydroLAKES database. With this setup, the average subbasin size in the NA Routing Product is roughly 10 km<sup>2</sup>. In comparison, the average subbasin size in the Pan-Canadian lake-river routing network is 60 km<sup>2</sup> (Han et al. 2020). The channel profile coefficients map for the drainage region above the N60° from Han et al. (2020) is used here. For the drainage region below the N60°, we inversely calculated the spatial distribution of channel profile coefficients using the global bankfull width, depth, discharge product from Andreadis et al. (2013). The MODIS Land Cover Type product MCD12Q1 (Friedl and Sulla-Menashe, 2015) landuse map is utilized for floodplain roughness estimation along with flood plain Manning's coefficients from Chow (1959) corresponding to each landuse type.

The resulting NA Routing Product includes 650,971 lakes in total, with areas ranging from 0.1 km<sup>2</sup> to 117,326 km<sup>2</sup>. The NA Routing Product v2.1 does not include coastal watersheds with a drainage area smaller than 8500 km<sup>2</sup>. Attribute values were checked to ensure physical plausibility and the allowable

ranges for various attributes are provided in Table A2-1. Attribute values that could be measured in the field (such as river reach length and slope) were not evaluated against field data and hence should be taken as an initial starting point in any analysis or modelling of the delineated network. In total, the NA Routing Product successfully includes 19391 points of interest, which is 53% of the specified points of interest. The 47% that could not be included in the NA Routing Product include 4648 streamflow gauges from WSC and 11916 streamflow gauges from USGS. The input streamflow gauges are not included in the NA Routing Product because of two reasons: 1) the gauge is in a smaller coastal watershed and thus not covered by the NA Routing Product or 2) the distance between the gauge and the closest river segment delineated in the NA Routing Product is larger than 2 km.

The NA Routing Product generated by BasinMaker v2.0 does not include additional subbasin control points at the beginning of the headwater river reaches (defined by the flow accumulation threshold) if it is not overlaid by a lake. This key difference between v2.0 and v3.0 of BasinMaker is depicted in Figure 3-6. Also, the NA Routing Product generated by BasinMaker v2.0 does not include the following attributes that are produced by v3.0: 1) the longest flow path of the subbasin's entire upstream drainage area 2) the average slope of the subbasin's entire upstream drainage area 3) the slope of river channel along the longest flow path and 4) the subbasin outlet longitude and latitude.

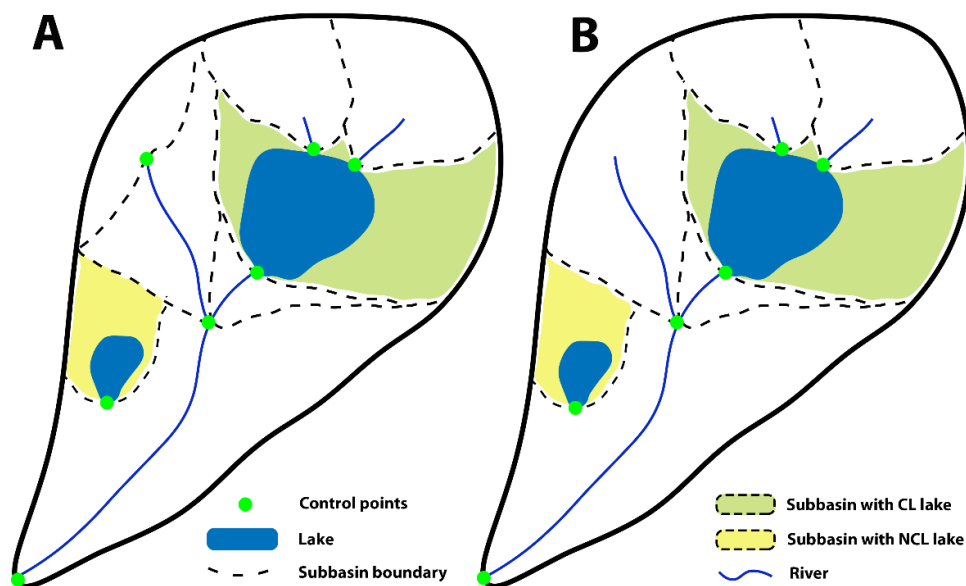


**Figure 3-6.** Example vector-based routing networks from (A) BasinMaker v3.0 and (B) BasinMaker v2.0. The hydrological routing networks from BasinMaker v2.0 do not include additional subbasin

control points at the beginning of any of the headwater river reaches (defined by the flow accumulation threshold) while v3.0 does include some of these as described previously. Connected Lakes (CL) and Non-Connected Lakes (NCL) are as defined in previous figures.

Figure 3-7 demonstrates an example routing network from the NA Routing Product v2.1 and multiple post-processed simplified routing networks produced with BasinMaker v3.0 for the 4000 km<sup>2</sup> Petawawa river watershed in Ontario, Canada.

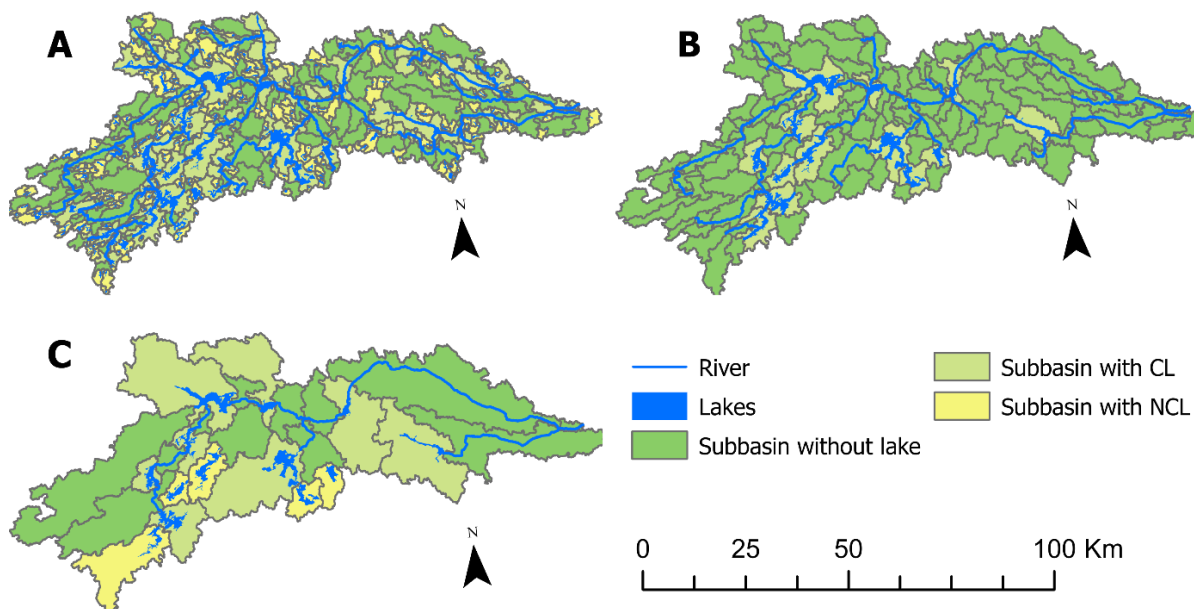


**Figure 3-7.** An example of the final routing network in the developed North American Lake-River Routing Product v2.1 and multiple simplifications of the routing networks produced with BasinMaker v3.0 for the 4000 km<sup>2</sup> Petawawa river watershed in Ontario, Canada. (A) full resolution North American lake-river routing network with 557 subbasins and 369 lakes. (B) Final post-processed routing network obtained from using ‘Remove\_Small\_Lakes’ function (thresholds = 5 km<sup>2</sup>). Further post-processed final routing network obtained from using the ‘Decrease\_River\_Network\_Resolution’ function (threshold = 200 km<sup>2</sup>) using routing network in (B) as the input network. Note the network in (C) now has only 58 subbasins and 13 lakes.

### 3.6.2 Distribution of the North American Lake-River Routing Product v2.1

The Basin Maker generated NA Routing Product v2.1 is freely available for download using a map-based online tool at [http://hydrology.uwaterloo.ca/basinmaker/download\\_continental.html](http://hydrology.uwaterloo.ca/basinmaker/download_continental.html). Custom

download options include continental, regional or local scale downloads. To locate a specific streamflow gauge station within the NA Routing Product, i.e. to identify which package to download, the “Gauge lookup” website can be used ([http://hydrology.uwaterloo.ca/basinmaker/download\\_gauges.html](http://hydrology.uwaterloo.ca/basinmaker/download_gauges.html)). Figure 3-8 is a screenshot of the routing product download website.

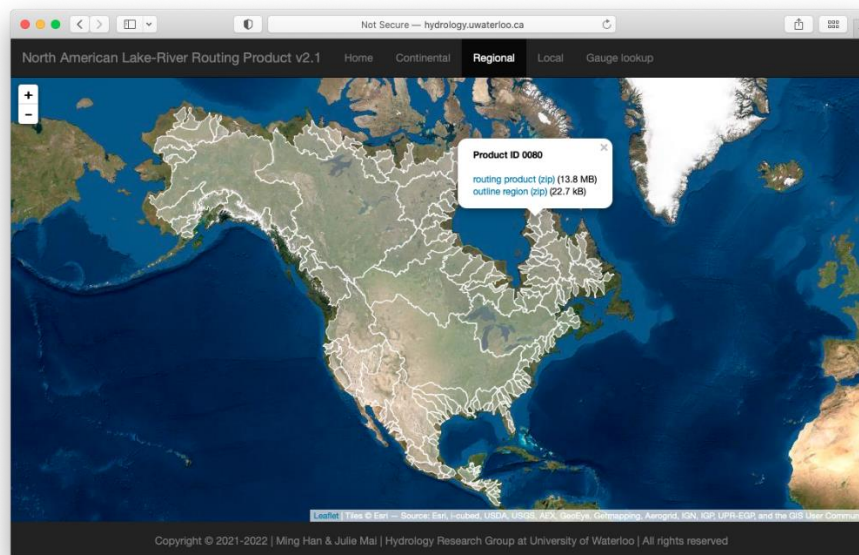


**Figure 3-8.** Screenshot of the North American Lake-River Routing Product download website. The popup menu appearing after clicking on a sub-region shows details about the identifier of the product, a download link for the routing network itself as well as a link to download the outline of the region (in shapefile and geoJSON format).

### 3.7 BasinMaker Application 2: Ontario Lake and River Routing Product v1

#### 3.7.1 Development of the Ontario Lake and River Routing Product v1

We use BasinMaker 3.0 to develop version 1.0 of the Ontario Lake and River Routing Product (OLRRP). This Province of Ontario Canada product covers an area of ~ 1 million km<sup>2</sup>, at a finer spatial resolution than in the NA Routing Product. The inputs of this application include the Enhanced DEM and the Enhanced flow direction (FDR) raster layers (30 m × 30 m) from the Ontario Integrated Hydrology (OIH) Datasets, HydroLAKES (Messenger et al. 2016) databases, points of interest including

1100 Ontario observation gauges from the National Water Data Archive HYDAT database, 439 active water quality monitoring gauges from the Ontario Provincial Water Quality Monitoring Network (PWQMN), and 1981 subbasin outlets extracted from the Quaternary Ontario Watershed Boundaries.

Parameters provided to BasinMaker include the following: 1) a constant flow accumulation threshold (5000 30 m × 30 m cells, corresponding to 4.5 km<sup>2</sup>) to define the initial stream network and subbasins; 2) zero as the lake area threshold to include all lakes from the HydroLAKES database. Bankfull width and depth attribute estimation procedures for the OLRRP are the same as those used in the NA Routing Product (see section 3.7.1).

The resulting routing product has an average subbasin size 4.5 km<sup>2</sup>. The product includes 82,001 lakes in total, with areas ranging from 0.1 km<sup>2</sup> to 4506.0 km<sup>2</sup>. The OLRRP does not include coastal watersheds with a drainage area smaller than 250 km<sup>2</sup>. Attribute values were checked to ensure physical plausibility and the allowable ranges for various attributes are provided in Table A2-1. Attribute values were not evaluated against field data and hence should be taken as an initial starting point in any analysis or modelling of the delineated network. In total, The OLLRP successfully includes 3326 point of interest, which is 94% of the input points of interest. The snap distance threshold in this application was 2 km. The 6% that could not be included in the OLRRP were mostly HYDAT gauges (109) and OIH Quaternary watershed outlets (103). Many of the points not included were sites on large lakes that could not be reliably moved to an inlet or outlet location of the lake.

### **3.7.2 Distribution of the Ontario Lake and River Routing Product**

A convenient distribution website (<https://lake-river-routing-products-uwaterloo.hub.arcgis.com/>) for the OLRRP enables users to dynamically view and download Ontario Lake-River Routing Product. Besides that, the website also provides a link to an example Google Colab website which enables users to easily simplify the routing networks via BasinMaker v3.0 software without installing anything on their local machine. Figure 3-9 is a screenshot of the Ontario Lake-River Routing Product download website.

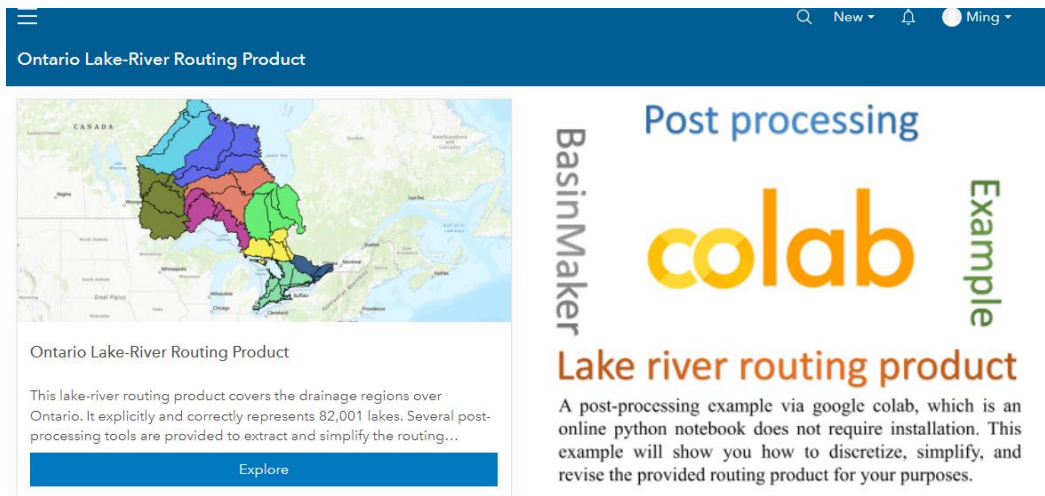


**Figure 3-9** Screenshot of the Ontario Lake-River Routing Product download website (main page). The Export option in the left is linked to a routing product download site. Google Colab (picture of colab text) in the right is linked to a Google Colab notebook, which enables users to easily simplify the OLRRP via BasinMaker without having to install anything on their local machine.

### 3.8 Limitations

Currently, BasinMaker cannot correctly handle the non-contributing areas present in the source DEM unless the source DEM is specially preprocessed. Such non-contributing areas are prevalent for example in the prairie pothole region of North America. In reality, the runoff generated in a non-contributing area does not drain to the downstream river network. However, the default delineated routing network from BasinMaker will connect subbasins in the non-contributing area to the downstream river network. Because of this limitation, non-contributing areas are not represented in either the Ontario Lake-River Routing Product or the NA Routing Product. A special version of the NA Routing product is available for the Nelson River drainage basin (covering a large part of the prairie pothole region) that correctly delineates non-contributing areas (e.g., the sink subbasin for each non-contributing area is simply assigned a downstream subbasin ID of -1). This particular version is available upon request.

The attributes of lakes/reservoirs in the delineated lake-river routing product include the volume, area, averaged depth, and lake type from the HydroLake database. The lake/reservoir bathymetry, the lake outflow structure, and the reservoir management data are not included in the lake-river routing

product. Thus, modelers must make several assumptions when building hydrological models using these lake-river routing products. For natural lakes, two key assumptions are the following: First, a modeler must assume the lakes are prismatic, which means that the lake area does not change with lake depth. Under this assumption, the lake surface level (relative to the bottom of a lake) can be estimated as the ratio between the volume of water in the lake storage and the lake area. Second, a modeler must make some assumptions about the lake outflow structures. For example, using the broad crest weir equation to simulate the outflow of the lakes. The simulation errors from any of these assumptions that turn out to be erroneous are impacted by the lake shoreline length, the slope of the lake shoreline, and the magnitude of the annual water level changes. Modelers likely need to obtain reservoir operating rules and reservoir stage-area-volume relationships to model the reservoirs in the lake-river routing network correctly.

### **3.9 Conclusions**

An open-source GIS toolbox called BasinMaker that can automatically and efficiently build vector-based hydrological routing networks including an arbitrary number of lakes is introduced here. Multiple versions are reported on (v2.0 and v3.0). BasinMaker has two main functions: 1) delineate the lake-river routing network from a DEM and 2) post-processing the existing lake-river routing network generated by BasinMaker in order to simplify network resolution, extract a watershed or generate HRUs. The routing network from BasinMaker includes all the necessary hydrological routing model inputs and can be used to build semi-distributed hydrological models. Discretizing Raven (Craig et al., 2020) semi-distributed hydrological models (or routing only models) is particularly efficient now given BasinMaker also has a post-processing function to write Raven model specific input files describing the watershed discretization.

Two novel post-processing functions in BasinMaker are a) Simplify the lake-river routing network by decreasing the resolution of the stream network and thus increasing the size of subbasins and b) Simplify the lake-river routing network by removing the lakes from it.

These post-processing tools are handy for users keen to utilize large-scale routing networks already delineated by BasinMaker, such as the North American Lake and River Routing network v2.1 (available at <http://hydrology.uwaterloo.ca/basinmaker/index.html>) and the Ontario Lake and River Routing network v1 (available at <https://lake-river-routing-products-uwaterloo.hub.arcgis.com>).

## Chapter 4

# The impact of ignoring lakes on the simulated runoff components and the value of lake observations in gauged and ungauged watersheds

### 4.1 Summary

Past hydrological modelling efforts tend to ignore the impacts of lakes because the model without representing lakes can provide reasonable estimates of streamflow simulation at the watershed outlet. However, the potential impacts of ignoring lakes on the simulated runoff components (i.e., quick runoff, baseflow, infiltration, etc.) and streamflow at internal gauges have not been quantitatively studied. This study investigates these impacts by comparing the simulated results from two model structures (with and without lakes) at two Canadian watersheds (Turkey Lake and Petawawa). Both models are calibrated to the streamflow measurement at the watershed outlets with forty independent calibration trials. Moreover, we evaluated the value of the lake level measurements in the ungauged and gauged watersheds using measurements from fifteen lake level gauges in the Petawawa watershed. Furthermore, we evaluated the assumptions that have been used to parameterize the outflow structure of lakes in the hydrological model.

Compared to a model which ignores lakes, a model representing lakes increases the model performance at internal streamflow/channel water-level gauges and slightly decreases the performance at the watershed outlet streamflow gauge. Because of the model compensation behavior, ignoring lakes in the model has significant impacts on the simulated runoff components, which will reduce the quick runoff, increase the infiltration, and increase the baseflow from the soil storage. The ignoring of lakes will also decrease the model's flexibility/uncertainty in the simulated runoff components at each flow pathway.

In a gauged watershed, calibrating to the additional lake level measurements in the Petawawa watershed can improve the streamflow simulation. In an ungauged watershed, the hydrological model calibrating to fifteen lake level gauges can provide a reasonable streamflow simulation at the Petawawa watershed outlet. However, when calibrating to only one lake level gauge, the hydrological model failed to provide reasonable streamflow simulations.

The calibrated lake crest width parameter of fifteen gauged lakes has a significant linear relationship with the lake's drainage area in log-log space, suggesting the assumption used in literature to parameterize the outflow structure of lakes is reasonable.

Results provide novel insights into the model's compensation behavior for ignoring lakes, utilizing lake-level measurements, and parameterizing the lake outflow structures.

## 4.2 Introduction

Lakes, wetlands, and reservoirs play a critical role in hydrological processes. It can attenuate the streamflow (Bowling & Lettenmaier, 2010; Huziy & Sushama, 2017; Christopher Spence, 2000; Zajac et al., 2017), control the watershed's flow connectivity (C. Spence et al., 2019; Woo & Mielko, 2008), and interact with groundwater storage (Hughes et al., 2014; C. Spence, 2007). Therefore, considering lakes and reservoirs as a part of modules in hydrological modelling can enhance the model's validity/appropriateness (Golden et al., 2016b; Karan et al., 2014; Shaw et al., 2013).

To build an environmental simulation model that explicitly represents lakes/wetlands, modelers need to define the lake characteristics, delineate the lake's upstream drainage area, build the topology between lakes and river reaches, and parameterize the lake's outflow structures (Evenson et al., 2015, 2016; Han et al., 2020). It requires considerable work in a lake/wetland-dominated watershed. Moreover, explicitly representing lakes will significantly increase the computational burden for a lake-dominated watershed. For example, the model explicitly representing lakes/wetlands in Evenson et al. (2016) increases the number of computational units or the hydrological response units (HRUs) by more than fifty times. Thus, past hydrological modelling practices tend to either ignore lakes/wetlands or include them with some conceptual simplifications. Only a few studies tried to explicitly represent lakes/wetlands in surface water models of the lake-dominated watersheds (Evenson et al., 2015, 2016; Han et al., 2020).

Representing lakes with conceptual simplifications requires making assumptions about lakes' characteristics, the topology between lakes and rivers, and lake outflow structures. For the lake's characteristics and topology, the simplest way to represent lakes/wetlands is to aggregate them within one subbasin/grid into one lumped lake (Craig et al., 2020; Guinaldo et al., 2021; Huziy & Sushama, 2017; Lindström et al., 2010). The lumped lake does not receive input from the upstream subbasin/grid and only receives a fraction of runoff from the non-lake part of this grid/subbasin (Arnold et al., 2012; Craig et al., 2020; Lindström et al., 2010). The lake characteristics, such as the relationship between lake level, area, and volume of the lumped lake, are defined using the total open water area of this grid/subbasin and an empirical function between the lake area and depth (Arnold et al., 2012; Craig et al., 2020; Lindström et al., 2010). This lake representation approach has been widely deployed in grid-based and vector-based hydrological models such as Raven (Craig et al., 2020), SWAT (Arnold et al., 2012), HYPE (Lindström et al., 2010), and ISBA-CTRIP (Guinaldo et al., 2021). Building on this lake

representation approach, several more complex lake representation approaches exist in the literature. For example, most hydrological models allow the user to define a reservoir-type lake at the outlet of subbasin/grids (Arnold et al., 2012; Craig et al., 2020). The reservoir-type lake can receive the inflow from upstream subbasin/grids and the characteristics of which can be defined from measurements. This way, modelers can define some big instream lake/wetland as a reservoir-type lake. Moreover, modelers can also estimate the area and volume of the lumped lake in each subbasin/grid using a high-resolution digital elevation model instead of parameterizing them with a predefined function (Rajib et al., 2020).

Different assumptions have been developed for the lake outflow structures in hydrological model. For example, some studies have used the broad crest weir equation to model the outflow from each lake (Bowling & Lettenmaier, 2010; Grimson et al., 2013; Han et al., 2020; Huziy & Sushama, 2017). While some studies assumed that all water above the lake crest height would move to downstream immediately (Evenson et al., 2016; Rajib et al., 2020). The sensitivity experiment in four different watersheds from Guinaldo et al. (2021) found that the crest width in the broad crest weir equation parameter significantly impacts the simulated streamflow.

The uncalibrated models show the importance of lake representation in some watershed via lake sensitivity analyses (Evenson et al., 2016; Han et al., 2020; Guinaldo et al., 2021). While modelling applications with these simplifications or ignoring lakes can successfully provide reasonable streamflow simulation results in some cases (Zajac et al., 2017; Rajib et al., 2020). For example, Zajac et al. (2017) found that the routing model with lakes did not significantly improve the streamflow simulation compared to the model without lakes by comparing two routing model in 171 catchments worldwide. After calibrating the routing model with lakes and without lakes, they found that the introduction of lakes improved the NSE for 67% of the catchments with a median improvement of 0.09, while the NSE worsened for 22% of the catchments with a median deterioration of 0.04. Rajib et al. (2020) suggests that using wetland area and volume from a high-resolution DEM to parameterize the characteristic of the lumped wetland in each subbasin did not improve the streamflow simulation at the watershed outlet.

However, we cannot conclude that explicitly representing lakes/wetlands in our hydrological model is unnecessary because we may get the right answer for the wrong reason. For example, other model parameters may compensate for ignoring lakes, or for simplified conceptual lumping of multiple lakes, during the model calibration process. The model parameter compensation behavior may change the

simulated runoff components from the calibrated model. These potential impacts from lake simplification have not been studied in the literature.

At the same time, when we use the broad crest weir equation to model the outflow from each lake, calibrating the crest width of each lake could be very challenging because there may be hundreds of crest width parameters (each lake requires one crest width parameter) in the model. Researchers have linked the crest width parameter with different measurable lake characteristics to reduce the number of parameters that need to be calibrated. For example, Bowling et al. (2010) assume that the crest width parameter is a function of lake circumference. Bowling et al. (2010) could adjust the crest width parameter of all lakes by changing the coefficient parameters in this function. Guinaldo et al. (2021) assume that the crest width parameter is a function of the mean annual discharge. Han et al. (2020) assume that the crest width is a function of the lake's drainage area. Nevertheless, no research has evaluated these relationships, especially the potential errors from such assumptions, due to a lack of lake-related observations.

Moreover, the pending NASA SWOT satellite mission (see <https://swot.jpl.nasa.gov/>) promises to measure lake levels at resolutions (temporal, spatial, and vertical) that have the potential to be used to calibrate the hydrological model in gauged/ungauged watersheds. However, how valuable these lake-level observations are in gauged/ungauged watersheds is not well quantified.

This study will investigate these research gaps by using several recent developments in defining the lake's characteristics and topology. For example, several global lake databases have been developed, such as HydroLAKES (Messenger et al., 2016) and GLOBathy (Khazaei et al., 2022). These lake databases provide lake shoreline polygons and characteristics (i.e., lake's area, volume, and depth) for all global lakes with a surface area of at least 10 ha. Moreover, building on the HydroLake database, Han et al. (2020) developed an initial vector-based lake-river routing product covering major watersheds in North American, which describes the topology between lakes and rivers. This lake-river routing product, and the subsequent products described in Chapter 3, represents the lake's inlets and the outlet as subbasin outlets. The hydrological model developed with a routing network from these routing products can explicitly simulate each lake's inflow and outflow.

More specifically, we will compare the simulated results from two model structures (with and without lakes) at two Canadian watersheds (Turkey Lake and Petawawa) to quantitatively investigate the impacts of ignoring lakes on the simulated runoff components (i.e., quick runoff, baseflow, and

infiltration, etc). In addition, we evaluate the value of the lake level measurements in the ungauged and gauged watersheds using measurements from fifteen lake level gauges in the Petawawa watershed. Furthermore, we will use the calibrated lake's crest width of gauged lakes to check the assumptions made by Han, et al. (2020), in parameterizing the outflow structure of lakes.

### 4.3 Material and Methods

Section 4.3.1 introduces the differences between the hydrological model that explicitly represents lakes and the equivalent model that ignores lakes. Section 4.3.2 introduces the watersheds and data used in this study. Section 4.3.3 introduces the Raven hydrological modelling framework and the hydrological models used for this study. Section 4.3.4 introduces the scenarios developed for each research question.

#### 4.3.1 The hydrological model with lakes and without lakes.

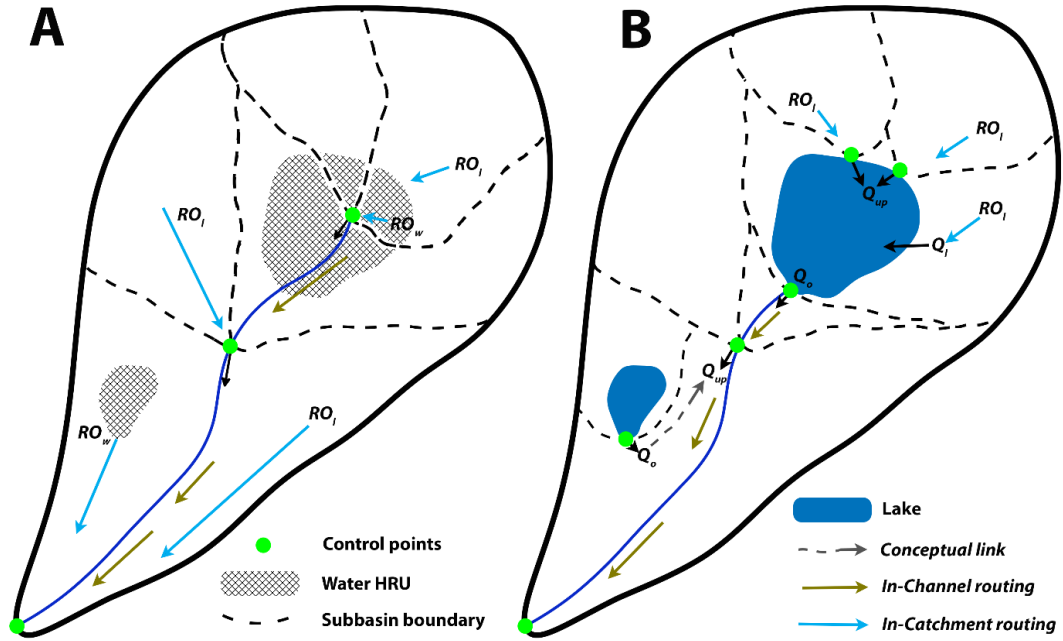
This study evaluates the potential impacts of ignoring lakes on the simulated runoff components and streamflow at internal gauges by comparing results from the hydrological model with and without lakes. This section will describe the differences between the hydrological model with lakes and without lakes. The models are built in the Raven hydrological modelling framework.

Figure 4-1 shows a schematic overview of the hydrological model without (Figure 4-1A) and with lakes (Figure 4-1B). The watershed discretization in Figure 4-1A ignores all lakes and defines the subbasin based on the river network only. Using this watershed discretization (Figure 4-1A), the hydrological model does not explicitly simulate the lake processes. It will aggregate all water surface area within one subbasin into a non-lake water HRU. The runoff generated from the water HRU ( $RO_w$ ) and land HRU ( $RO_l$ ) will move to the subbasin outlet via in-catchment routing processes and then the outflow will be hydrologically routed through the downstream channel network to the watershed outlet.

The non-lake water HRU in each subbasin only receives precipitation, and runoff generated from this HRU is calculated by:

$$RO_w = \max(P - E_w, 0) \quad (4-1)$$

where the  $RO_w$  is the runoff generated from the water HRU of each subbasin in [L/T],  $P$  is the precipitation over the water HRU in [L/T] and the  $E_w$  is the open water evapotranspiration rate in [L/T].  $RO_w$  in units of depth across the water HRU is then routed to its corresponding subbasin outlet and converted to units of [L<sup>3</sup>/T] using the water HRU area.



**Figure 4-1.** A schematic overview of the hydrological model without lakes (A) and with lakes (B). The  $RO_l$  is the runoff generated from the land HRUs, and the  $RO_w$  is the runoff generated from the water HRU. The  $Q_{up}$  is the total streamflow from upstream subbasin(s). The  $Q_o$  is the streamflow released from the lake outlet. The  $Q_l$  is the amount of runoff generated from land HRUs within a lake subbasin that reaches the lake after the in-catchment routing process.

The watershed discretization in Figure 4-1B represents each lake as a lake HRU within a lake subbasin, defined by the following rules: 1) The extent of the lake subbasin will fully cover the lake; 2) the outlet of the lake subbasin is the same as the outlet of the lake, and 3) each lake's inlets are treated as a subbasin outlet. Using this watershed discretization (Figure 4-1B), the hydrological model can explicitly simulate the lake processes. The inflow of the lake includes three parts. The streamflow from the upstream subbasin ( $Q_i^{up}$ ), the precipitation over the lake  $P$ , and the runoff from the land part of the subbasin ( $RO_l$ ). The  $P$  is directly added to the lake storage. The  $RO_l$  will reach to the lake after the in-catchment routing process, which is represented by  $Q_l$  in Figure 4-1.

The mass balance of each explicitly simulated lake is the following:

$$\frac{dV}{dt} = P(A) + Q_{up} + Q_l - ET(A) - Q_o(h) \quad (4-2)$$

where the  $\frac{dV}{dt}$  is the lake storage dynamic in a given day [L<sup>3</sup>/T],  $Q_{up}$  is the sum of lake inflows from all upstream subbasins in [L<sup>3</sup>/T],  $Q_l$  is the in-catchment routed amount of the  $RO_l$  that moves into the lake in [L<sup>3</sup>/T],  $A$  is the lake area in [L<sup>2</sup>],  $ET$  is the open water evaporation rate over the lake in [L/T],  $P$  is the precipitation received on the lake surface in [L/T],  $Q_o(h)$  is the lake outflow in [L<sup>3</sup>/T] at a given lake level elevation  $h$  in [L]. This study does not model the interaction between the lake and groundwater storage and always assumes lakes are prismatic (constant area).

The outflow of each lake is simulated using the broad crest weir equation:

$$Q_o(h) = \frac{2}{3} \times c \times w \times \sqrt{2 \times g} \times (h - h_{crest})^{\frac{2}{3}} \quad (4-3)$$

where the  $c$  is the weir coefficient [-], with a constant value of 0.6.  $g$  is the gravitational constant.  $s$  is the lake level relative to the crest height.  $w$  is the crest width [L]. The parameterization of the  $w$  and  $A(h)$  of each lake in the model are introduced in section 4.3.3.

The lake's outflow is directly moved to the downstream channels and routed through the channel system via in-channel routing processes (Figure 4-1B). The small lake that is not directly connected by the delineated river network is defined as a non-connected lake. The outflow of the non-connected lake will be directly moved to the head of the river channel of the downstream subbasin (Figure 4-1B).

In summary, the difference between the two model structures is that the model representing lakes has additional lake storage to attenuate and evaporate the simulated runoff from the lake's drainage area. A more detailed description of the full hydrological model is in section 4.3.3.

### 4.3.2 Watersheds and model input data

This section will introduce two study watersheds, the Petawawa and the Turkey lake watershed.

The Petawawa watershed is located in northeastern Ontario, Canada (Figure 4-2). It drains towards a Water Survey Canada (WSC) streamflow gauge 02KB001. The drainage area of the watershed is 4,120 km<sup>2</sup>. The primary land cover type includes lakes and forests. Furthermore, the primary soil type based on Soil Landscapes of Canada is bedrock. The lakes from the HydroLAKE database (Messenger et al. 2016) and the 30 m Digital Elevation Model (DEM) from Ontario Integrated Hydrology dataset are used as input of BasinMaker to delineate the routing network with lakes (Figure 4-2B) and without lakes (Figure 4-2A). BasinMaker is a GIS-tool box developed in Chapter 3 to delineate the lake-river

routing structures. There are 369 lakes in this watershed, and the total lake area is 316 km<sup>2</sup>. All lakes are simulated for the model representing lakes.

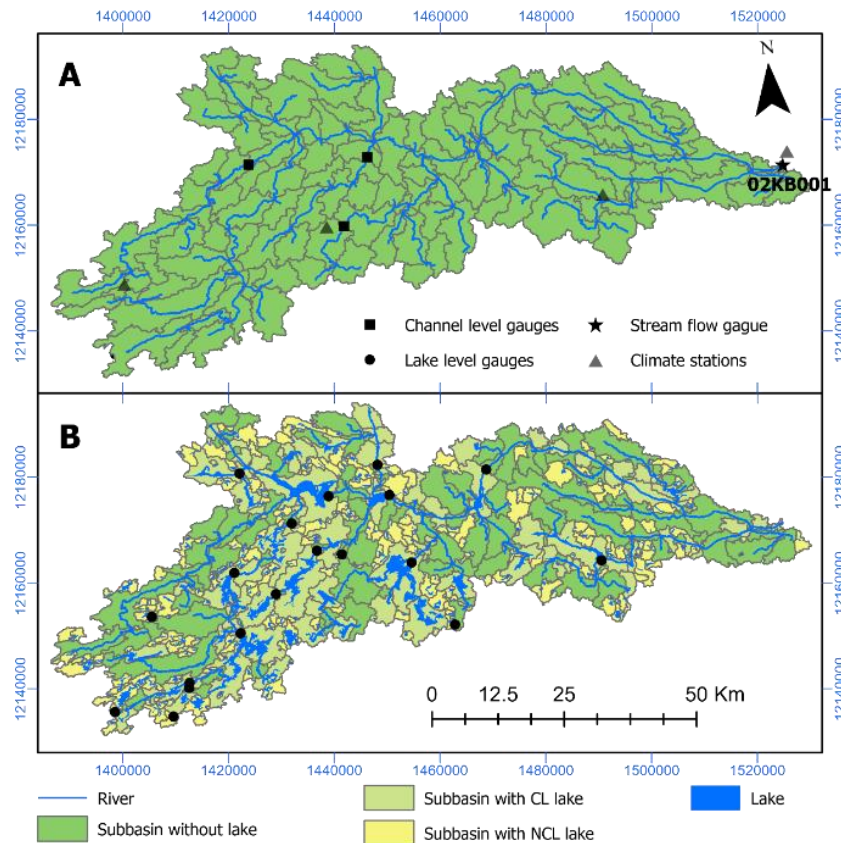


**Figure 4-2.** The delineated watersheds and observation station locations for the hydrological model without lakes (A) and with lakes (B) for the Petawawa watershed. The water level observation gauges and climate stations exist in A and B despite not being shown in both. CL represents connected lakes, and NCL represents non-connected lakes.

We have 15 lake level measurement gauges in this watershed and four-channel water level measurement gauges (Figure 4-2). The water levels in the lake and channel are measured with 30 mins intervals. The lake level measurements start on 6/26/2015 and end on 10/6/2020. The channel water level measurements start on 8/24/2017 and end on 9/30/2020. The daily averaged channel water level and the lake water level are recalculated to match the daily time step of the model. We will compare the measured channel water level with streamflow simulation result. The simulated streamflow from Raven is daily averaged values. Thus, we calculated the daily averaged channel water level by averaging the measurement within each day. We will compare the simulated lake level with the

measured lake level and Raven export the simulated water level of lakes at the end of each day. Thus, we calculated the daily averaged lake water level by averaging the measurement at 23:30, 23:45, 24:00, 00:15, 00:30. This watershed has four meteorological stations. Three of them belong to the Ontario Ministry of Northern Development and Mines. One of them belongs to Environment and Climate Change Canada. Daily minimum and maximum temperature and precipitation from 8/01/2015 to 20/10/2020 were used as input for the hydrological model.

The Turkey lake watershed is located approximately 60 km north of Sault Ste. Marie, Ontario, Canada. The drainage area of the watershed is around 10 km<sup>2</sup>. The primary land cover type includes lakes and forests. Furthermore, the primary soil type is predominantly podzols. The lakes from HydroLAKE database (Messenger et al. 2016) and the 5 m Digital Elevation Model (DEM) are used as input of BasinMaker to delineate the routing network with lakes (Figure 4-3B) and without lakes (Figure 4-3A).

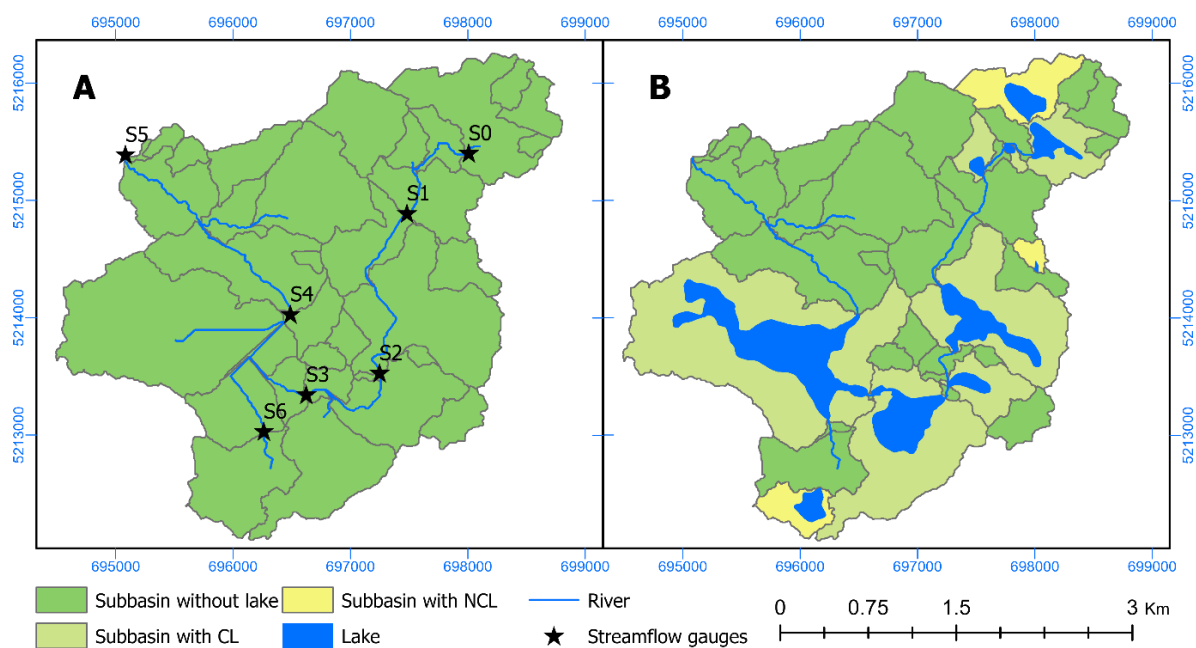


**Figure 4-3.** The delineated watersheds and streamflow observation station locations for the hydrological model without lakes (A) and with lakes (B) for the Turkey Lake watershed. The observation stations exist in both A and B despite not being shown in both. CL represents connected lakes, and NCL represents non-connected lakes.

There are seven streamflow gauges in the Turkey Lake watershed (Figure 4-3) operated by Environment and Climate Change Canada. The daily streamflow measurement is available from

1981/01/01 to 2012/12/31. One meteorology gauge belongs to the Canadian Air, and Precipitation Monitoring Network is located just outside the watershed. The daily meteorology measurements, including air temperature, wind speed and direction, relative humidity and vapor pressure, barometric pressure, and solar radiation, have been available since 1980.

### **4.3.3 The hydrological model**

The hydrological models with and without lakes are built with the Raven hydrological modelling framework (version 3.0.4) developed by James R. Craig at the University of Waterloo (Craig et al. 2020). The Raven is an object-oriented modelling framework that gives users full flexibility regarding hydrological process description. It supports customization of the hydrological processes (i.e., with/without snow/percolation/baseflow processes, number of soil layers et al.) and hydrological flux algorithms for each process (i.e., linear/power-law function).

The hydrological processes in the Raven model can be categorized into two groups. The first group is the processes applied at each HRU to determine how much runoff will be generated at each flow pathway. The second group includes processes applied at each subbasin, channel, and lake to deliver generated runoff through the routing network to the watershed outlet.

The hydrological model without representing lakes for Petawawa and Turkey lake watersheds are built with routing networks shown in Figure 4-2A and Figure 4-3A, respectively. The model without representing lakes includes two types of HRUs, the land HRU, and the water HRU. While the hydrological model includes lakes for Petawawa and Turkey lake watersheds are built with routing networks shown in Figure 4-2B and Figure 4-3B, respectively. All lakes shown in Figure 4-2B and Figure 4-3B will be explicitly modeled. The model representing lakes includes two types of HRUs, the land HRU, and the Lake HRU. The hydrological processes applied in the land HRU is described in Appendix A3 and is the same for both model structure. The hydrological processes of water HRU and Lake HRU are described in section 4.3.1.

To simulate the lake mass balance with Equation (4-2) and Equation (4-3) in section 4.3.1, we must define the relationship between the lake's stage, area, and volume of each lake. This study assumed that lakes are prismatic, which means that the lake area does not change with lake depth. Under this assumption, the lake surface level (relative to the bottom of a lake) can be estimated as the ratio between the volume of water in the lake storage and the lake area. For each lake simulated in Raven, the lake crest height (relative to the bottom of the lake) and area set equal to the lake averaged depth and the

area from the HydroLAKE database. We assume lake crest width can be approximately estimated from the lake's drainage area using a power-law relationship:

$$w_i = \alpha \times (DA_i)^n \quad (4-4)$$

where the  $w_i$  is the crest width of lake  $i$ ,  $DA_i$  is the drainage area of lake  $i$  in [km<sup>2</sup>].  $\alpha$  and  $n$  are two coefficient parameters. The initial  $\alpha$  and  $n$  of both watersheds are obtained by assuming the lake crest width is the same as the channel width at the lake outlet. Moreover, the channel width at the lake outlet can also be estimated from a global river channel bankfull width dataset following the methodology described in Han, et al (2020).

The in-catchment and channel routing processes are also the same for both model structures and are described in Appendix A3.

The simulation period of the hydrological models in the Petawawa watershed is from 2013-08-01 to 2020-10-20. From 2013-08-01 to 2016-01-01 is the model warmup period. Because of the length of the data, no temporal validation period is considered for models in the Petawawa watershed. All measurements since 2016-01-01 were used to train the model.

The simulation period of the hydrological models in the Turkey Lake watershed is from 1981-01-01 to 2012-12-01. The model warmup period is from 1981-01-01 to 1984-01-01. The model calibration period is from 1984-01-01 to 1996-12-01. And from 1997-01-01 to 2012-12-01 is the model validation period.

Specific calibration formulations to match each research question will be described in section 4.3.4

#### **4.3.4 The model calibration experiment for each research question**

This section introduces the model calibration experiments designed to answer three research questions. Each model calibration experiment will be calibrated using the dynamically dimensioned search (DDS) algorithm (Tolson & Shoemaker, 2007). The DDS is a neighborhood search algorithm that can find quality calibration solutions based on a user-specified model evaluation budget (Tolson & Shoemaker, 2007). For each model calibration experiment, the model evaluation budget (number of Raven model simulations) is 4000, and we repeat 40 independent optimization trials using randomly generated initial parameter sets.

#### 4.3.4.1 The model calibration experiment for the first research question

Table 4-1 lists the model calibration experiments for the research question: what is the impact of ignoring lakes in the hydrological model on the simulated runoff at each flow pathway and the simulated streamflow at internal streamflow gauges? We calibrated the hydrological models with (1-1L and 1-2L) and without lakes (1-1 and 1-2) to the outlet streamflow gauge of Petawawa (1-1L and 1-1) and Turkey Lake (1-2L and 1-2) watershed (Table 4-1). The Kling-Gupta efficiency (KGE) metric (Gupta et al., 2009) is used to compare the simulated and the observed streamflow at the daily time step as:

$$KGE = 1 - \sqrt{(1 - r)^2 + \left(\frac{\sigma_{sim}}{\sigma_{obs}} - 1\right)^2 + \left(\frac{\mu_{sim}}{\mu_{obs}} - 1\right)^2} \quad (4-5)$$

where  $r$  is the linear correlation between observed and simulated flows,  $\sigma_{sim}$  and  $\sigma_{obs}$  are the standard deviation of observations and simulations, respectively. And  $\mu_{sim}$  and  $\mu_{obs}$  are the observation mean and simulation mean, respectively.

The performance metrics at each internal gauge and the simulated runoff at each flow pathway from the two model structures were compared at each watershed. The performance of two model structures at internal streamflow gauges in the Turkey Lake watershed is also evaluated with KGE. The performance of two model structures at the internal channel water level gauges in the Petawawa is evaluated by comparing the simulated streamflow and the channel water level measurements using Spearman's rank correlation coefficient (*SPRC*):

$$SPRC = \frac{\text{cov}(R(L_{ch}), R(Q_{sim}))}{\sigma_{R(L_{ch})} \times \sigma_{R(Q_{sim})}} \quad (4-6)$$

where  $R(L_{ch})$  and  $R(Q_{sim})$  are the rank of the observed channel water level measurement and the simulated streamflow, respectively,  $\text{cov}(R(L_{ch}), R(Q_{sim}))$  is the covariance of the rank variables, and  $\sigma_{R(L_{ch})}$  and  $\sigma_{R(Q_{sim})}$  are the standard deviations of the rank variables.

**Table 4-1.** Comparative model scenarios for the first research question: what is the impact of ignoring the presence of lakes in hydrological models. The lake coefficient parameters calibrated are in Equation (4-4) to estimate lake crest width as a function of the lake drainage area.  $KGE_Q$  is the Kling-Gupta evaluation metric (KGE) of the watershed outlet streamflow gauge.

Model scenarios	Watershed	Routing structure	Objective function	Number of calibrated hydrological model parameters + lake coefficient parameters
1-1L	Petawawa	With lake (Figure 4-2B)	$KGE_Q$	29 + 2
1-1	Petawawa	No lake (Figure 4-2A)	$KGE_Q$	29 + 0
1-2L	Turkey Lake	With lake (Figure 4-3B)	$KGE_Q$	29 + 2
1-2	Turkey Lake	No lake (Figure 4-3A)	$KGE_Q$	29 + 0

#### 4.3.4.2 The model calibration experiment for the second research question

This section will discuss the model calibration experiment to the second research question: How valuable are lake level observations in hydrological modelling? We will evaluate the value of lake observation from two perspectives. First, we will investigate if we can improve the hydrological model by calibrating additional lake-level observations in a gauged watershed. Second, we will evaluate if we can use the lake level measurements to calibrate the hydrological model in an ungauged watershed. We will introduce how we compare the observed and simulated lake levels in the model calibration experiments before describing the scenarios designed for the first and second purposes.

To calibrate the hydrological model to the lake level measurement, we must define and calculate the performance metric between the simulated and observed lake levels at each gauge. However, we cannot calculate the performance metric between the observed and simulated lake level directly because they are reported with respect to different vertical datums. The measured lake level is the distance between the lake surface and the sensor. In contrast, the simulated lake level is the distance between the lake's surface and the lake's bottom. Moreover, the difference between the two references system is unknown. Thus, we compare the normalized observed lake level ( $N(obs_l)$ ) and the normalized simulated lake level ( $N(sim_l)$ ) to remove the impact from references. The  $N(obs_l)$  is the difference between the observed lake level and the observed mean value. The  $N(sim_l)$  is the difference between the simulated

lake level and the simulated mean values. Then we use the KGE to compare the normalized observed lake levels and the normalized simulated lake levels. Because  $\mu_{N(sim_L)} = \mu_{N(obs_L)} = 0$ , the KGE is equation is changed to the following for lake level measurements:

$$KGED = 1 - \sqrt{\left(1 - r(N(sim_L), N(obs_L))\right)^2 + \left(\frac{\sigma_{N(sim_L)}}{\sigma_{N(obs_L)}} - 1\right)^2} \quad (4-7)$$

where  $r$  is the linear correlation between normalized observed ( $N(obs_L)$ ) and simulated ( $N(sim_L)$ ) lake water level,  $\sigma_{N(sim_L)}$  and  $\sigma_{N(obs_L)}$  are the standard deviation of normalized lake level observations and simulations, respectively.

Finally, the performance metric of lakes is the unweighted averaged  $KGED$  of the fifteen lake level gauges ( $\overline{KGED}_L^{15}$ ).

For the first purpose, the model calibration experiments are labelled scenarios 2-1a, 2-1b, and 2-1c in Table 4-2. In scenario 2-1a, we calibrated the hydrological model to streamflow measurement at the Petawawa watershed outlet (scenario 2-1a). And scenarios 2-1b and 2-1c will calibrate the hydrological model to both streamflow and lake level measurement. Scenario 2-1c includes 15 additional lake crest width parameters for each lake with lake level measurement compared to scenarios 2-1a and 2-1b.

We will compare the model performance at the Petawawa watershed outlet streamflow gauge from scenarios 2-1a, 2-1b, and 2-1c to evaluate whether including lake level measurement can improve the streamflow prediction. And we will also compare the uncertainties of the simulated fluxes at each flow pathway from scenarios 2-1a, 2-1b, and 2-1c to investigate if including lake level measurement can reduce the model simulation uncertainties. The uncertainties of the simulated fluxes at each flow pathway are approximated using the simulated fluxes from 40 independently calibrated models.

Scenarios 2-2a and 2-2b in Table 4-2 are the calibration experiment for the second purpose, which is to evaluate the value of the lake measurement for the ungauged watershed. We calibrate the hydrological model with 15 lake level gauges ( $\overline{KGED}_L^{15}$ , 2-2a) and with one lake level gauge at lake Cedar ( $KGED_L^{ce}$ , 2-2b), respectively. Then we will analyze the model performance at the Petawawa watershed outlet streamflow gauge. Lake Cedar is the largest lake in the Petawawa watershed. The area of lake Cedar is 25.93 km<sup>2</sup>. The drainage area of lake Cedar is 1540.47 km<sup>2</sup>, which is 37% of the drainage area of the Petawawa watershed.

**Table 4-2.** Designed model scenarios for the second research question: how valuable are lake level measurements in the hydrological model calibration in a gauged (scenarios 2-1a, b, and c) and ungauged watershed (scenarios 2-2a and b).  $\overline{KGED}_L^{15}$  represent the averaged Kling Gupta Deviation ( $KGED$ , Equation (4-7)) of 15 observed lakes. The  $\overline{KGED}_L^{Ce}$  represent the  $KGED$  of lake Cedar.  $KGE_Q$  represent the Kling Gupta evaluation metric ( $KGE$ ) of the watershed outlet streamflow gauge. The calibrated crested width parameters of each observed lake from the scenario 2-1c and the calibrated lake crest width equation (Equation (4-4)) parameters from the scenario 2-1b will be used to answer the third research question: is the power-law relationship between the lake crest width and the lake’s drainage area reasonable?

Model scenarios	Watershed	Routing network	Objective function	Number of calibrated hydrological model parameters + lake coefficient parameters + lake crest width parameters
2-1a	Petawawa	with lakes (Figure 4-2B)	$KGE_Q$	$29 + 2^a + 0$
2-1b	Petawawa	with lakes (Figure 4-2B)	$0.5 \times KGE_Q + 0.5 \times \overline{KGED}_L^{15}$	$29 + 2^a + 0$
2-1c	Petawawa	with lakes (Figure 4-2B)	$0.5 \times KGE_Q + 0.5 \times \overline{KGED}_L^{15}$	$29 + 2^b + 15$
2-2a	Petawawa	with lakes (Figure 4-2B)	$\overline{KGED}_L^{15}$	$29 + 2^b + 15$
2-2b	Petawawa	with lakes (Figure 4-2B)	$\overline{KGED}_L^{Ce}$	$29 + 2^c + 1$

- a) Equation (4-4) under calibrated parameters generates crest widths for all 369 simulated lakes.
- b) Equation (4-4) under calibrated parameters generates crest widths for 354 simulated lakes.
- c) Equation (4-4) under calibrated parameters generates crest widths for 368 simulated lakes.

#### 4.3.4.3 The model calibration experiment for the third research question

This section will discuss the model calibration experiment to the third research question: is the power-law relationship (Equation (4-4)) between the lake crest width and the lake’s drainage area reasonable? To answer this research question, we will evaluate the calibrated lake crest width parameter of fifteen gauged lakes from two model calibration experiments (2-1b and 2-1c in Table 4-2). The hydrological model in both calibration experiments will be calibrated to lake level measurement at 15 lake level gauges and streamflow measurement at the Petawawa watershed outlet. Scenario 2-1b estimates the

lake crest widths of each gauged lake by calibrating the relationship between lake crest width and the lake's drainage area ( $W \sim DA$ , Equation (4-4)). While scenario 2-1c directly optimizes the lake crest parameter of each gauged lake.

## **4.4 Results and discussion**

### **4.4.1 The impact of ignoring lakes on calibrated streamflow and runoff components in each flow pathway.**

This section presents results obtained by calibrating the hydrological models with lakes (1-1L and 1-2L) and without lakes (1-1 and 1-2) to the Petawawa (1-1L and 1-1) and Turkey Lake (1-2L and 1-2) watershed outlet streamflow gauges (Table 4-1). The internal streamflow or water level gauges in each watershed are used as a validation dataset to assess the impact of ignoring lakes on the model performance. Section 4.4.1.1 presents the impact of ignoring lakes on the performance of the watershed internal and outlet gauges. Section 4.4.1.2 demonstrates the impact of ignoring lakes on the simulated runoff components at each flow pathway.

#### **4.4.1.1 The impact of ignoring lakes on calibrated streamflow**

For each watershed and model structure combination, an ensemble of 40 parameter sets, each derived from an independent calibration trial, is used to predict streamflow and calculate evaluation metrics at the watershed outlet gauge and the internal validation locations. Figure 4-4 shows the performance metrics at each location for the Petawawa watershed, which had no temporal validation. Figure 4-5 shows the performance metrics at each location for the Turkey Lakes watershed during both the calibration and validation periods. The minimum calibrated KGE at the watershed outlets (the 02KB001 in Figure 4-4 and S5 in Figure 4-5) for both model structures is above 0.85, which suggests that both models are well-calibrated to their respective watershed outlets in every trial. Thus, all calibrated parameter sets are deemed valid calibration results and can be used to investigate the impact of ignoring lakes on the simulated streamflow at internal gauges and runoff components at each flow pathway.

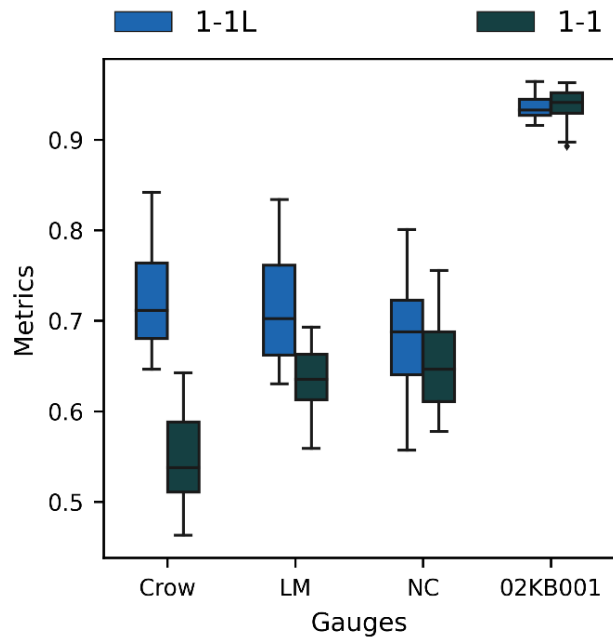


**Figure 4-4.** The model performance at watershed outlet (calibration) streamflow gauge (02KB001) and internal (validation) channel water level gauges (Crow, LM, and NC) from the hydrological model explicitly simulating lakes (scenario 1-1L) and the model ignoring lakes (scenario 1-1) in the Petawawa watershed. See Table 4-1 for scenario descriptions. For each model scenario, the performance metric (an optimal value of 1.0 in all cases) was calculated from an ensemble of 40 parameter sets, each derived from an independent calibration trial. The calibration budget for each trial was 4000. The metric for channel water level gauges is the Pearson rank correlation coefficient between measured water levels and simulated discharge. The metric for the streamflow gauge 02KB001 is the Kling-Gupta Efficiency (KGE) coefficient between simulated and observed streamflow.

Focusing on only the best KGE at the watershed outlet from the 40 calibrated parameter sets suggests that the model structure ignoring lakes provides similar or even marginally better streamflow simulations than the model structure representing lakes at the watershed outlet (see the 02KB001 in Figure 4-4 and S5 in Figure 4-5). However, ignoring lakes in hydrological models decreased, often substantially, the best metrics for the internal streamflow gauge locations. For example, for the Turkey Lake watershed (Figure 4-5), the best KGEs for all six internal gauges are degraded (by up to 0.2 KGE units). Similar degradations are seen for the Petawawa (Figure 4-1), with the best Spearman's Rank Correlation Coefficient (SRCC) for the three internal channel water level gauges decreasing by roughly

0.05 to 0.2 SRCC units when lakes were ignored. The uncertainties of KGE at S6 in the model represent the uncertainties in the calibrated crest width of the small upstream lake (Figure 4-3). In the current setup, we estimated each lake’s crest width as a function of the lake’s drainage area (Equation (4-4)) and calibrated the two coefficients in this function. We can improve the KGE of S6 by adding the crest width of this small lake as an independent parameter in the model calibration process. The daily simulated and observed streamflow from the model with lakes (1-1L) and the ignoring lakes (1-1) at gauges 02KB001 in the Petawawa watershed are shown in Figure A4-1. The daily simulated and observed streamflow from the model with lakes (1-2L) and the ignoring lakes (1-2) at gauges S5 and S1 in the Turkey Lake watershed are shown in Figure A4-2.

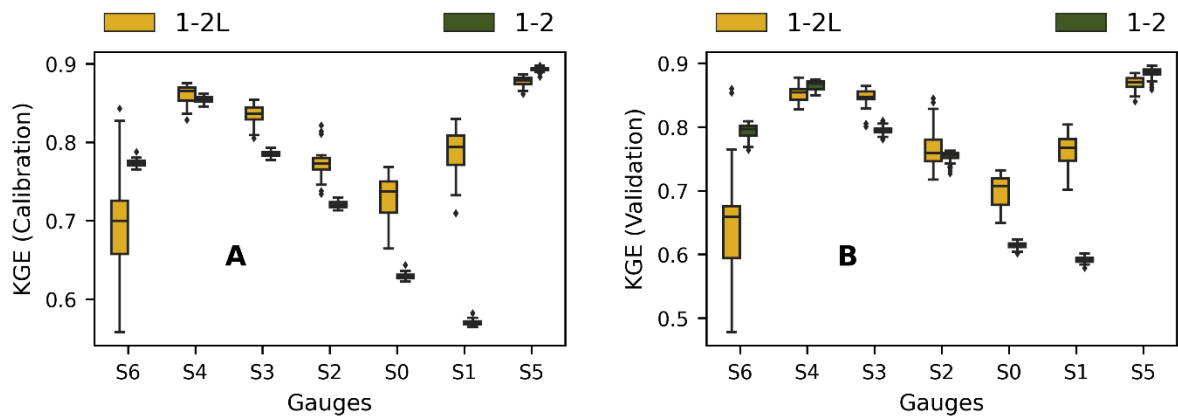


**Figure 4-5.** The model performance at watershed internal (validation) and outlet (calibration, S5) streamflow gauges from the hydrological model representing lakes (scenario 1-2L) and ignoring lakes (scenario 1-2) in the Turkey Lake watershed. See Table 4-1 for scenario descriptions. For each model scenario, the performance metric was calculated from an ensemble of 40 parameter sets, each derived from an independent calibration trial. The calibration budget for each trial was 4000. The calibration period is from 1985 to 1996, while the validation period is from 1997 to 2012.

The improvement observed at the internal gauges comes from the lake attenuation effect. The lake attenuation effect may impact the calibrated streamflow differently for gauges at the different parts of the watershed. The Petawawa watershed's three internal water level gauges are downstream of a lake-dominated region (Figure 4-2). The simulated streamflow from the model ignoring lakes includes more unexpected fluctuations in the low flow period at these gauges. While Turkey lake’s internal streamflow gauges S1 and S0 are upstream of a lake-dominated region (Figure 4-3). Without modelling the lake

attenuation effect from downstream lakes, the model ignoring lakes have to use soil storage upstream of the gauges S1 and S0 to attenuate the runoff to avoid streamflow overprediction at the watershed outlet. Thus, the simulated streamflow from the model ignoring lakes underpredict the high flow at gauges S1 and S0 (Figure A4-2).

#### 4.4.1.2 The simulated runoff components in each flow pathway

Ignoring lakes not only impacts the simulated streamflow at watershed internal and outlet gauges (see section 4.4.1.1) but also impacts the simulated runoff components at each flow pathway. This section presents results obtained by calibrating the hydrological models with (1-1L and 1-2L) and without lakes (1-1and 1-2) to the Turkey Lake (1-2L and 1-2) and Petawawa (1-1L and 1-1) watershed outlet streamflow gauges (scenarios in Table 4-1). For each watershed and model structure combination, the simulated runoff components at each flow pathway are estimated from an ensemble of 40 parameter sets, each derived from an independent calibration trial.

Figure 4-6 demonstrates the aggregated daily quick runoff, infiltration, ET zone baseflow, and non-ET zone baseflow from each calibrated parameter set of each model scenario. The aggregated daily runoff components are calculated by averaging the simulated daily runoff components of each HRU over the entire watershed and then averaging the result from the previous step over the entire non-ice (from April to the end of November) simulation period. Ignoring lakes in the hydrological model significantly impacts the median and range of the aggregated daily runoff components at each flow pathway in both watersheds (Figure 4-6). First, comparing the median of the aggregated daily runoff components in Figure 4-6, the model without lakes infiltrates more precipitation to the ET soil layer (the top two soil layers, Figure 4-6A and B) and release more water from the non-ET soil layer storage (the third soil layer, Figure 4-6D). The aggregated daily quick runoff from the model without lakes is close to zero at both watersheds (Figure 4-6A). Second, the range of the aggregated daily runoff component is different between the model with and without lakes at both watersheds. The runoff component range in Figure 4-6 represents a model's flexibility in simulating this runoff component to obtain a good streamflow simulation result at the watershed outlet because each point in Figure 4-6 is calculated from a valid/acceptable calibration result (Figure 4-4 and Figure 4-5). The model without lakes has less flexibility than the model representing lakes in simulating the infiltration (Figure 4-6B) and quick runoff (Figure 4-6A), ET zone baseflow (Figure 4-6C), and the bottom soil layer baseflow (Figure 4-6D) at both watersheds. In summary, the result from Figure 4-6 suggests that ignoring lakes

in the model will reduce the quick runoff, increase the baseflow from the non-ET soil layer, and decrease the model's flexibility in simulating runoff components at each flow pathway.

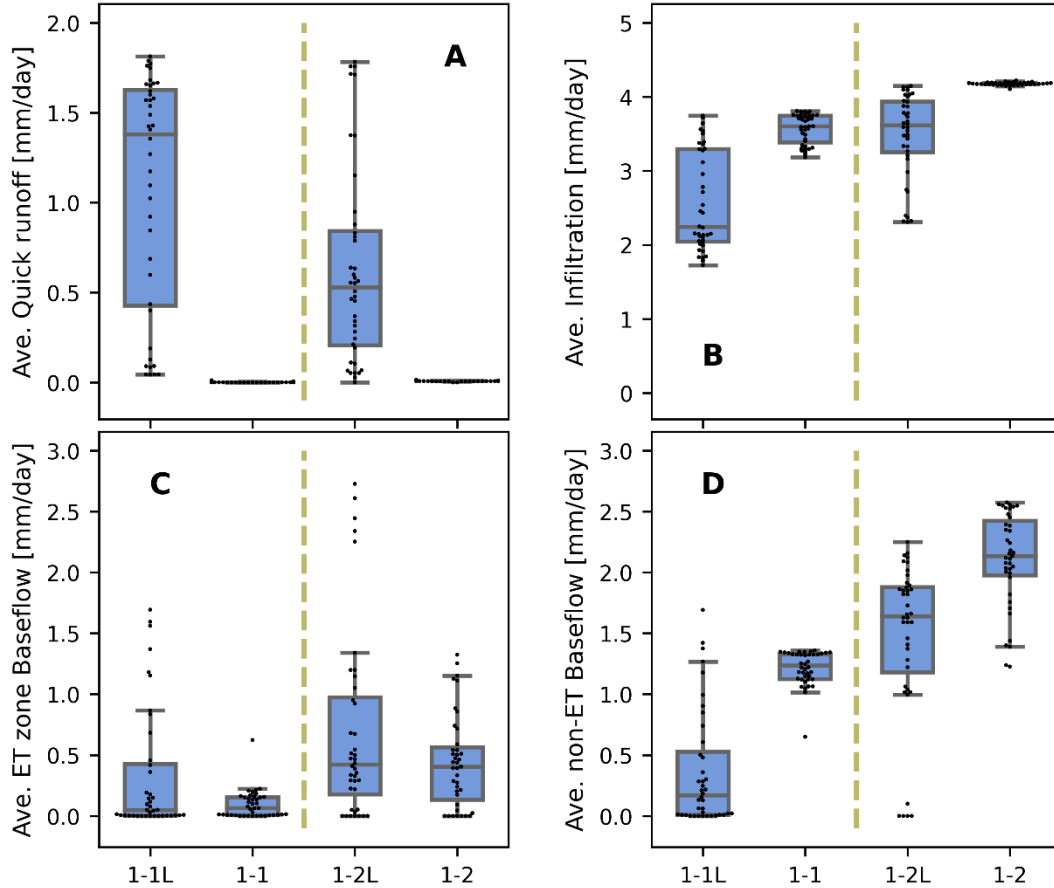


**Figure 4-6.** The aggregated daily runoff components from the hydrological model representing lakes (1-1L and 1-2L) and ignoring lakes (1-1 and 1-2) in the Turkey Lake watershed (1-2L and 1-2) and Petawawa watershed (1-1L and 1-1) at each flow pathway. All scenarios are calibrated to the streamflow measurements at the watershed outlet. See Table 4-1 for scenario descriptions. For each model scenario, the daily fluxes were simulated from an ensemble of 40 parameter sets, each derived from an independent calibration trial. The aggregated daily runoff components are calculated by averaging the simulated daily runoff components of each HRU over the entire watershed and then averaging the results of the previous step over the entire non-ice (from April to the end of November) simulation period. The calibration budget for each trial was 4000.

#### 4.4.2 How valuable are lake level measurements in the hydrological model calibration in a gauged and ungauged watershed

This section will discuss the value of lake observation in hydrological modelling from two perspectives. Section 4.4.2.1 demonstrates whether we can improve the hydrological model by calibrating additional lake-level observations in a gauged watershed. Section 4.4.1.2 evaluates if we can use the lake level measurements to calibrate the hydrological model in an ungauged watershed.

##### 4.4.2.1 The value of lake level measurements in a gauged watershed

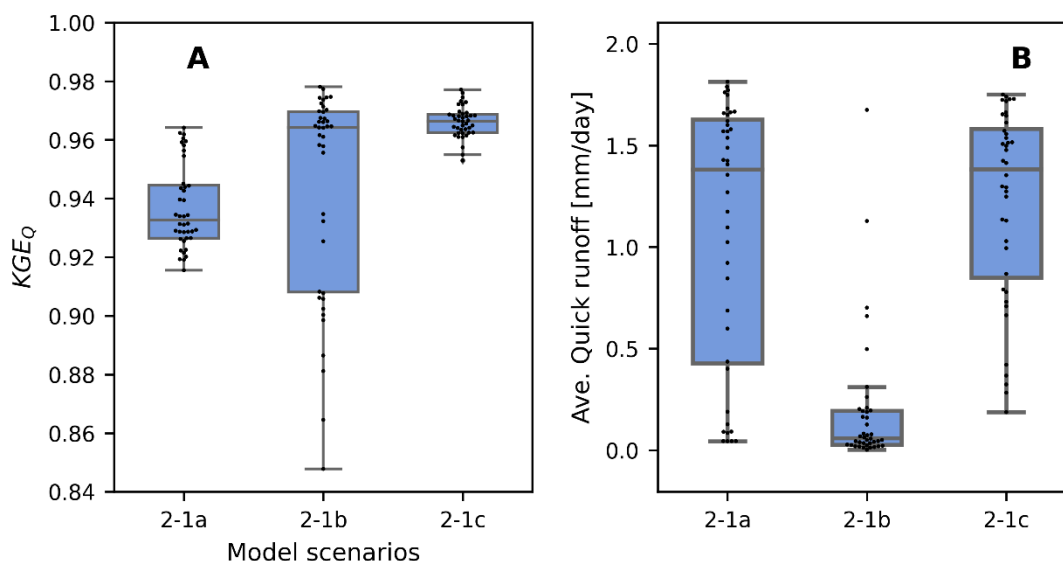
This section compares the model performance at the Petawawa watershed's outlet streamflow gauge and the uncertainties of the simulated runoff components from the hydrological model only calibrated to streamflow measurement ( $KGE_Q$ , scenario 2-1a) and the hydrological model calibrated to both streamflow and lake level measurement ( $0.5 \times KGE_Q + 0.5 \times \overline{KGED}_L^{15}$ , scenario 2-1b and 2-1c). Scenario 2-1c includes 15 additional lake crest width parameters for each lake with lake level measurement compared to scenarios 2-1a and 2-1b. See Table 4-2 for scenario descriptions. For each scenario, the model performance metric and the simulated runoff components are estimated from an ensemble of 40 parameter sets, each derived from an independent calibration trial.

Figure 4-7A shows the calibrated KGE of streamflow at the watershed outlet in the Petawawa watershed from each calibrated parameter set of each scenario. Compared to the scenario that is only calibrated to the streamflow (scenario 2-1a), the scenario calibrated to both streamflow and lake observations (scenarios 2-1a and 2-1c) improves the streamflow prediction in terms of median streamflow KGE and the best streamflow KGE (Figure 4-7A). However, scenario S2-1b, which did not include additional lake crest parameters, increases the uncertainty of the calibrated streamflow KGE and decreases the minimum calibrated KGE compared to scenario S2-1c.

Figure 4-7B demonstrates the aggregated daily quick runoff from 2-1a, 2-1b, and 2-1c, which is calculated by averaging the simulated quick runoff of each HRU over the entire watershed and then averaging the previous result over the entire non-ice simulation period (from April to the end of November). We only include the quick runoff in Figure 4-7B because the impact of calibrating to additional lake level measurement on simulated runoff components is similar. The scenario that calibrates to lake level measurement without adding the lake crest width parameter (S2-1b) narrows the distribution/uncertainty of the aggregated quick runoff compared to scenario S2-1a, which is only calibrated to streamflow at the watershed outlet. However, scenario S2-1c, with additional lake crest

parameters, provides a similar quick runoff distribution/uncertainty with scenario 2-1a. This suggests that the value of lake measurement with respect to constraining the simulated quick runoff components is degraded by including additional parameters in calibration. This is despite the reduction in outlet KGE variability when calibrating with these 15 additional lake parameters.

Combining the result from Figure 4-7A and B, we can see that calibrating to additional lake levels in a gauged watershed can improve the streamflow simulation. Nevertheless, it can constrain the range of simulated runoff components only when no additional parameters are calibrated.



**Figure 4-7.** Comparison of different calibration formulations for the Petawawa hydrological model that explicitly simulates 369 lakes. (A) The model performance at the Petawawa watershed outlet streamflow gauge from scenarios that is only calibrated to streamflow measurement at the watershed outlet (scenario 2-1a) or calibrated to both streamflow and lake level measurements (scenario 2-1b and 2-1c). Scenario 2-1c includes 15 additional lake crest width calibration parameters for each monitored lake compared to 2-1a and 2-1b. See Table 4-2 for scenario descriptions. (B) the aggregated average daily quick runoff across all HRUs from scenarios 2-1a, 2-1b, and 2-1c. For each scenario, the model performance metric and the simulated quick runoff are estimated from an ensemble of 40 parameter sets, each derived from an independent calibration trial. The calibration budget for each trial was 4000.

#### 4.4.2.2 The value of the lake measurement for ungauged watershed

In this section, the model performances at the Petawawa watershed outlet streamflow gauge from the hydrological model calibrated with 15 lake level gauges ( $\overline{KGED}_L^{15}$ , 2-2a) and the hydrological model calibrated with one lake level gauge at lake Cedar ( $KGED_L^{ce}$ , 2-2b) are used to investigate the value of the lake measurements in an ungauged watershed. Lake Cedar was selected here as it is one of the largest lakes (area of lake Cedar is 25.93 km<sup>2</sup>, drainage area of lake Cedar is 1540.47 km<sup>2</sup>, which is 37% of the drainage area of the Petawawa watershed) while also not being too close to the streamflow gauge. See scenario descriptions in Table 4-2. For each scenario, an ensemble of 40 parameter sets, each derived from an independent calibration trial, is used to predict streamflow/lake level and calculate evaluation metrics at the watershed outlet gauge and the lake level gauges.

The minimum calibrated  $\overline{KGED}_L^{15}$  from the scenario 2-2a calibrated to 15 lake level gauges and the minimum calibrated  $KGED_L^{ce}$  from the scenario 2-2b calibrated to lake level gauge of lake Cedar (scenario 2-2b) are both above 0.75, suggesting that all trials from each model scenario are well-calibrated. Thus, all calibrated parameter sets are deemed valid calibration results and can be used to investigate the model performance at the streamflow simulation at watershed outlets.

Figure 4-8 shows the KGE of discharge at the Petawawa watershed outlet from the hydrological model calibrated to fifteen lake level gauges (scenario 2-2a) and the hydrological model calibrated to one lake level gauge (scenario 2-2b). Note that outlet streamflow quality here reflects validation performance assessment since this gauge was not used in calibration for these two scenarios. The median and the minimum KGE of the streamflow from the hydrological model calibrating to fifteen lake level gauges (scenario 2-2a) are around 0.75 and 0.60, respectively. This indicates that the calibrated hydrological model with fifteen lake level gauges (scenario 2-2a) can provide a reasonable quality outlet streamflow simulation. However, the median and the minimum KGE of the streamflow from the hydrological model calibrating to one lake level gauges (scenario 2-2b) are roughly 0.50 and 0.20, respectively. This suggests that the calibrated hydrological model with one lake level gauge does not lead to a reasonable streamflow simulation. The result from Figure 4-8 indicates that when we calibrate the hydrological model using lake level measurements in an ungauged watershed, we need to utilize more than one lake level gauge.

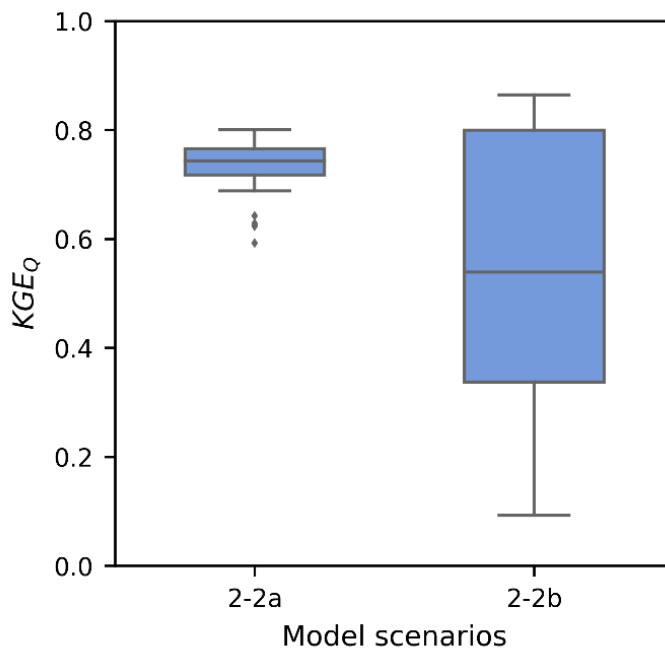


**Figure 4-8.** The simulated streamflow KGE at the outlet in validation mode from the hydrological model only calibrated to fifteen lake level gauges (scenario 2-2a) and the hydrological model calibrated to one lake level gauge at lake Cedar (scenario 2-2b). See Table 4-2 for scenario descriptions. For each scenario, an ensemble of 40 parameter sets, each derived from an independent calibration trial, is used to predict streamflow/lake level and calculate evaluation metrics at the watershed outlet gauge ( $KGE_Q$ ).

#### 4.4.3 Is it a reasonable assumption to estimate lakes' crest width from the lake's drainage area?

In the literature, the lake crest width in hydrological models is often estimated from the lake's drainage area using an equation similar to Equation (4-4) (Bowling & Lettenmaier, 2010; Guinaldo et al., 2021; Han et al., 2020). This section will evaluate the quality of this assumption using the calibrated lake crest width parameter of fifteen gauged lakes from the hydrological model calibrated to lake level and streamflow measurements (2-1b and 2-1c in Table 4-2). Scenario 2-1b estimates the lake crest widths of each gauged lake by calibrating the relationship between lake crest width and the lake's drainage area ( $W \sim DA$ , Equation (4-4)). While scenario 2-1c directly optimizes the lake crest parameter of each gauged lake. For each scenario, the model was calibrated with 40 independent calibration trials. The calibration budget for each trial was 4000.

Figure 4-9 demonstrates the calibrated relationship between the calibrated lake crest width parameter and the lake drainage area ( $W \sim DA$ ) from scenario 2-1b and the calibrated lake crest width parameter of fifteen gauged lakes from scenario 2-1c after logarithmic transformations. There is a log-linear relationship between calibrated lake crest width from scenario 2-1c and the lake's drainage area on a log-log scale, especially for lakes with a drainage area larger than 10 km<sup>2</sup> (Red boxplot in Figure 4-9). The coefficient of determination ( $R^2$ ) for the fitted linear relationship using the optimized lake crest width from the best trial of scenario 2-1c is 0.75 with  $P\text{-value} = 0.0012 < 0.01$  (Redline in Figure 4-9).

Furthermore, the crest width of gauged lakes from the calibrated  $W \sim DA$  relationship (grey lines in Figure 4-9, scenario 2-1b) is not entirely inconsistent with the directly calibrated lake crest width from scenario 2-1c (Red boxplot in Figure 4-9). The calibrated  $W \sim DA$  relationship from scenario 2-1b would underestimate the lake crest width for lakes with a small drainage area and overestimate lake crest width for the lake close to the watershed outlet compared to the calibrated lake crest from scenario 2-1c. The black line in Figure 4-9 represents the initial  $W \sim DA$  used in this study. The differences between the initial  $W \sim DA$  and the calibrated  $W \sim DA$  suggest that the initial  $W \sim DA$  in the lake river routing network is reasonable and likely to overestimate the lake crest width. In other words, for all monitored lakes in the Petawawa watershed, the default approach to estimating lake crest widths (e.g., what is used in the Chapter 3 routing products) provides an upper bound for each lake such that the individually calibrated crest widths are mostly smaller (or roughly equal in two case) than these default crest widths. This is a useful observation when bounding lake crest width parameters in future calibration studies involving Canadian Shield lakes like those in the Petawawa watershed.

Figure 4-11 shows the lake level performance at each lake level gauge from scenarios 2-1b and 2-1c. Scenario 2-1c, which is calibrated with additional lake crest parameters of gauged lakes, outperforms scenario 2-1b, which is only calibrated with the  $W \sim DA$  relationship. Moreover, scenario 2-1c has better streamflow simulation performance at the watershed outlet than scenario 2-1b (Figure 4-7A). This indicates that the scenario without adding additional lake crest parameters (2-1b) decreases the model performance in streamflow and lake level simulation. The daily simulated and observed lake levels from the hydrological model calibrated to lake observations and the streamflow with 15 additional lake crest with parameters (2-1c, Table 4-2) is shown in Figure A4-3.

In summary, it is reasonable to assume the lake crest width has a power-law relationship with the lake's drainage area and use this relationship to parameterize the model when there is no lake level

measurement. Moreover, we should add additional lake crest parameters for each gauged lake when lake observation is available.

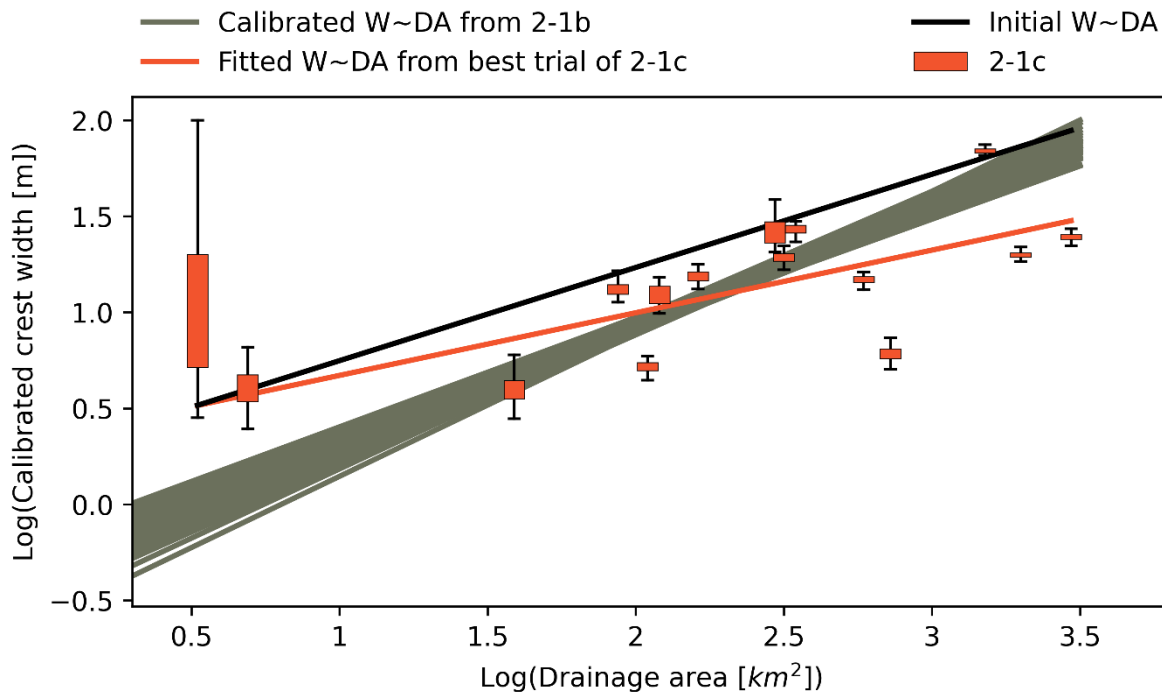


**Figure 4-9.** The relationship between calibrated crest width of gauged lakes and their drainage area ( $W \sim DA$ ) from the hydrological model calibrated to both streamflow and lake measurements (scenarios 2-1b and 2-1c) after logarithmic transformations. Each lake's crest widths in scenario 2-1b are estimated using two coefficient parameters in Equation (4-4) (grey lines). While 2-1c directly optimizes the lake crest parameter of each gauged lake (red boxplot). See Table 4-2 for scenario descriptions. Each scenario is calibrated using 40 independent calibration trials. The Redline is the fitted linear relationship using the optimized lake crest width from the best trial of 2-1c. The  $R^2$  and the p-value of this linear relationship are 0.75 and 0.0012, respectively. The black line is the initial  $W \sim DA$  relationship.

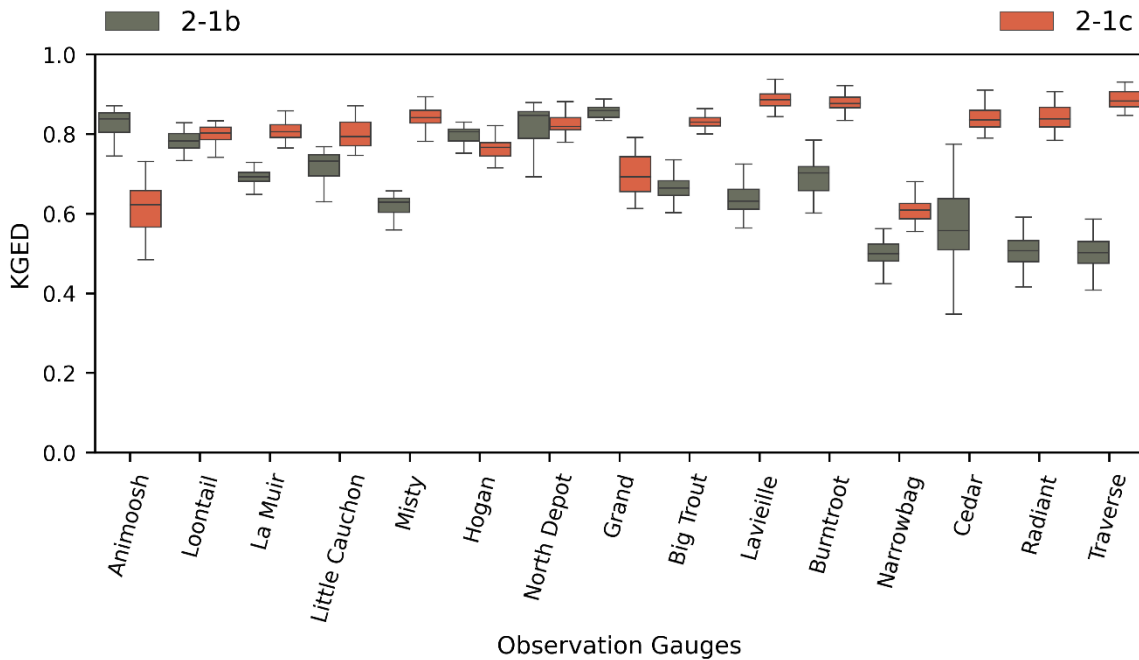


**Figure 4-10.** The model performance for predicting gauged lake levels when the model is calibrated to streamflow and lake level measurement (scenarios 2-1b and 2-1c). From left to right, the lake’s drainage area is increasing. Scenario 2-1c includes 15 additional lake crest width parameters for each lake with lake level gauge compared to 2-1b. See Table 4-2 for scenario descriptions. For each scenario, an ensemble of 40 parameter sets, each derived from an independent calibration trial, is used to predict lake level and calculate evaluation metrics at each lake level gauge (*KGED*, Equation (4-7)).

## 4.5 Discussion

### 4.5.1 How other processes may compensate for the ignoring of lakes

The results in section 4.4.1 show that ignoring lakes in the hydrological model significantly impacts the simulated runoff components in each pathway and the streamflow at internal gauges. We hypothesize that this is due to the hydrological model’s compensation behavior for ignoring the lake’s functions. This section will demonstrate the simulated lakes’ functions from the hydrological model with lakes. And then, we will investigate how other hydrological processes may compensate for lakes’ functions when we ignore them. The results were obtained by calibrating the hydrological models with

(1-1L and 1-2L) and without lakes (1-1 and 1-2) to the Petawawa (1-1L and 1-1) and Turkey Lake (1-2L and 1-2) watershed outlet streamflow gauges (Table 4-1).

Lakes in the hydrological model have two primary functions: evaporation and attenuation. Figure 4-11 shows the cumulative watershed averaged daily lake evaporation ( $E_{lake}$ ) and the difference ( $R_{in-out}$ ) between the input ( $R_{in}$ ) and output of the routing storage via watershed outlet ( $R_{out}$ ). The  $R_{in}$  is the sum of all runoff components (quick runoff and baseflow from three soil layers) and the precipitation over the lakes. The  $R_{out}$  is the watershed outlet discharge. The time series' are from the best trial of the hydrological model representing lakes at Turkey Lake (Figure 4-12A, scenario 1-2L) and Petawawa (Figure 4-12B, scenario 1-1L) watershed (Table 4-1). Because of the lake evaporation, the  $R_{in-out}$  is positive and has a maximum value of around 80 mm each year at both watersheds (blue line in Figure 4-11). This indicates that not all runoff generated from the land HRUs will be released to the watershed outlets.

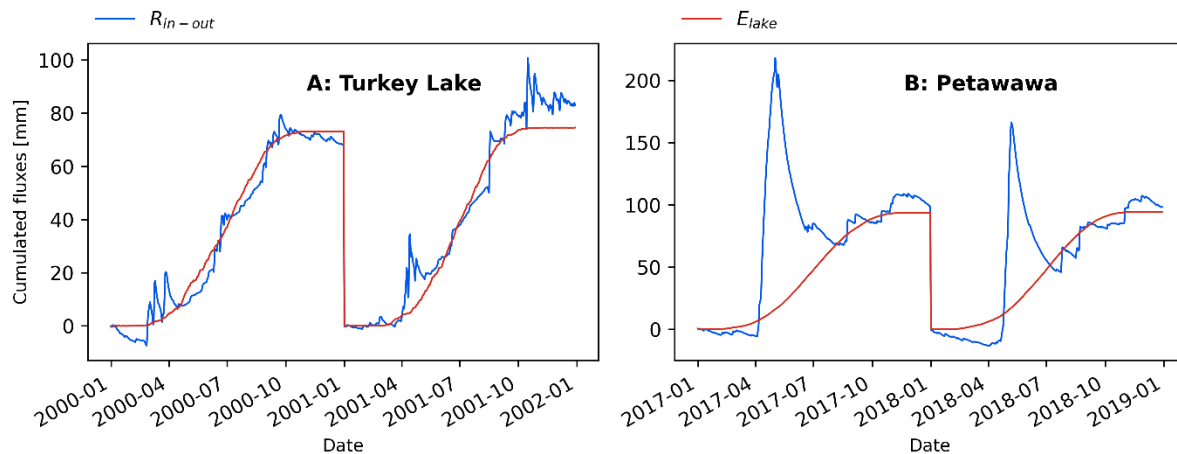


**Figure 4-11.** The annual cumulative watershed averaged daily lake evaporation ( $E_{lake}$  in mm over the total surface areas of the simulated lakes and the difference ( $R_{in-out}$ ) between the input ( $R_{in}$ ) and output ( $R_{out}$ ) of the routing storage from the best trial of the model representing lakes at Turkey Lake (A, scenario 1-2L) and Petawawa (B, scenario 1-1L) watershed (Table 4-1).  $R_{in}$  is the sum of all runoff components and the precipitation over the lakes. The  $R_{out}$  is the watershed outlet discharge.

If we assume the routing storage has no streamflow attenuation effect, the  $R_{in-out}$  should monotonically increase due to the lake evaporation process. However, the  $R_{in-out}$  (blue line) in Figure 4-11) fluctuates in some parts of the simulation period, indicating that the routing storage can hold the

input runoff and release it later in the following time steps. The routing storage attenuation effect shown in Figure 4-11 mainly comes from the lakes because the maximum watershed averaged channel storage during the entire modelling period is less than 10 mm, which is neglectable compared to the fluctuates of  $R_{in-out}$  in Figure 4-11.

The hydrological model will compensate for the absence of lakes by adjusting the processes in other storage components. Figure 4-12 shows the cumulative watershed averaged soil evaporation ( $E_{soil}$ ), the difference between fluxes moving in ( $S_{ET_{in}}$ ) and out ( $S_{ET_{out}}$ ) of the soil storage layers where ET can remove water ( $S_{ET_{in-out}}$ , top two soil layers), and the difference between fluxes moving in ( $S_{GW_{in}}$ ) and out ( $S_{GW_{out}}$ ) of the groundwater soil storage ( $S_{GW_{in-out}}$ , bottom soil layer) from each scenario in Table 4-1. The  $S_{ET_{in}}$  is the infiltration into the top layer, and  $S_{ET_{out}}$  includes the baseflow from two soil layers plus the percolation out of the second soil layer. The  $S_{GW_{in}}$  is the percolation from the second soil layer to the third soil layer (a conceptual groundwater store in the model of the Petawawa), and  $S_{GW_{out}}$  is the baseflow out of the third soil layer.

Compared to the model representing lakes (Figure 4-12A and B), the model ignoring lakes has larger cumulated soil evaporation (Figure 4-12C and D), which is a compensation for ignoring the lake's evaporation. Moreover, the groundwater storage in the model ignoring lakes (Figure 4-12C and D) has a larger water attenuation effect than in the model representing lakes at both watersheds, which is a compensation for the ignoring lake's attenuation. At the same time, we can observe that the  $S_{ET_{in-out}}$  is highly impacted by the soil evaporation processes, which may explain why models do not use it as storage to attenuate the water.

Such compensation behaviors explain why ignoring lakes in the model will reduce the quick runoff, increase the baseflow from the third soil layer, and decrease the model's flexibility in the simulated runoff components at each flow pathway (section 4.4.1).

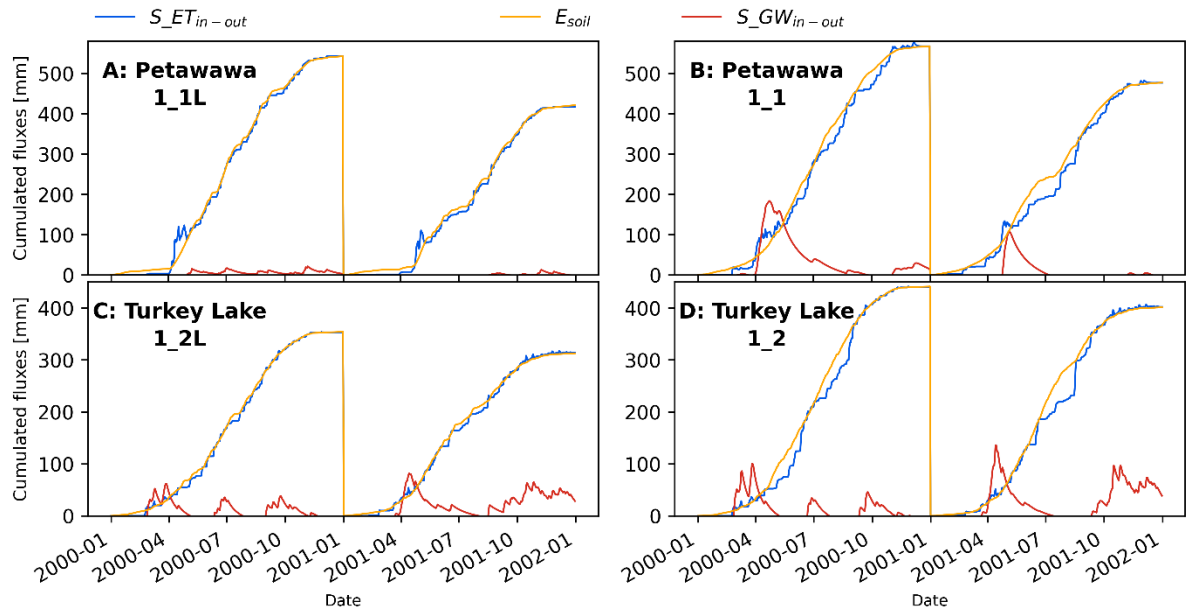


**Figure 4-12.** The cumulative watershed averaged soil evaporation ( $E_{soil}$ ), the difference between fluxes moving in ( $S_{ET_{in}}$ ) and out ( $S_{ET_{out}}$ ) of the ET soil storage ( $S_{ET_{in-out}}$ , top two soil layers), and the difference between fluxes moving in ( $S_{GW_{in}}$ ) and out ( $S_{GW_{out}}$ ) of the groundwater soil storage ( $S_{GW_{in-out}}$ , bottom soil layer) from the best calibration trial of each scenario in Table 4-1. The  $S_{ET_{in}}$  is the infiltration, and  $S_{ET_{out}}$  includes the baseflow from two soil layers and the percolation of the second soil layer. The  $S_{GW_{in}}$  is the percolation from the second soil layer, and the  $S_{GW_{out}}$  is the baseflow of the third soil layer.

#### 4.5.2 Limitations and future work

This study demonstrates the hydrological model’s compensation behavior when lakes are not explicitly simulated and the resulting runoff component changes in various flow pathways using model structures under two extreme hypotheses. The model with lakes explicitly simulates the lake evaporation, the lake inflow from the delineated upstream drainage area, and the lake outflow. In contrast, the model ignoring lakes assumes that the lake in a subbasin is a water HRU, which only receives input from precipitation and will instantly move all “effective precipitation” over the lake to the channel network.

In the literature, the hydrological model could include lakes with different simplifications, which lie between the two hypotheses made in this study. The example simplifications are 1) only simulating the lake’s evaporation process and ignore other lake processes by allowing the lake to evaporate water from

the runoff generated in the land parts of the subbasin or 2). we can aggregate all lakes within one subbasin into one lumped lake that can receive precipitation, evaporate water from its storage and release outflow based on the outflow structures. The inflow of the lumped lake is a fraction of the runoff generated in the land part of the subbasin. In this case, the inflow to the lake and the lake's topology are not correctly simulated, which may lead to inadequate stimulation of the lake's evaporation and attenuation effect.

This study did not evaluate the hydrological model's compensation behavior using these lake simplification approaches. Moreover, we agree that the hydrological model's compensation behavior is impacted by watershed conditions such as local climate and the percentage of the area occupied by lakes. It is an open question for further research to investigate how the lake simplification method and watershed conditions may impact the hydrological model's compensation behaviors. Moreover, the hydrological model's compensation behaviors for other model assumptions are also worth further investigation, such as the assumptions between the lumped and distributed models and the assumptions in HRU and subbasin discretization.

We only evaluated the value of the lake level observations for the hydrological model calibration in one watershed with 15 lake levels measured. However, a more comprehensive evaluation of this research question may require evaluating the lake observation's values at multiple watersheds. We will continue to obtain more lake level observations and investigate this research question.

This study demonstrates a case where over-simplifying the hydrological processes would reduce the uncertainty/flexibility in simulated runoff components to compensate for the errors resulting from such simplification. This may suggest that the uncertainty/flexibility in the simulated runoff components at each flow pathway could be an additional metric to compare different model structures, especially when they have similar performance at the watershed outlet. To properly formulate this metric and examine the metric's application scopes is another potential open question for further research.

## **4.6 Conclusions**

This study compares the hydrological model structure with and without lakes at two watersheds of different sizes. Both model structures are calibrated to the streamflow measurements at the watershed outlet with forty independent calibration trials. The performance of streamflow prediction at the watershed outlet and internal gauges and the simulated runoff components at each pathway are compared.

The conclusions from this comparison are the following: representing lakes in the model can substantially increase the performance of streamflow prediction at internal gauges at both watersheds with negligible changes in the predictions at the watershed outlet gauge. Because of the model compensation behavior, ignoring lakes in the model significantly impacts the simulated runoff components at each flow pathway. It will reduce the quick runoff, increase infiltration, and increase the baseflow from the soil storage. Moreover, ignoring the lakes in the model will also decrease the model's flexibility/uncertainty of the simulated runoff components at each flow pathway.

Our finding of this model structure comparison suggests that lakes need to be represented, or the assumptions of the lakes need to be examined for hydrological modelling applications, such as watershed-scale nutrient modelling. Moreover, our result demonstrates a case where over-simplifying the hydrological processes would reduce the uncertainty/flexibility in the simulated runoff components to compensate for the errors resulting from such simplification. This may suggest that the uncertainty/flexibility in the simulated runoff components at each flow pathway could be an additional metric to compare different model structures, especially when they have similar performance at the watershed outlet.

Besides comparing the model structure with and without lakes, we also use lake-level measurements at fifteen lakes to investigate the value of these measurements for calibrating the hydrological model in gauged and ungauged watersheds. Calibrating the additional lake level measurements can improve the streamflow simulation at the watershed outlet in a gauged watershed. In an ungauged watershed, the hydrological model calibrating to fifteen lake-level gauges can provide reasonable streamflow simulation at the watershed outlet. However, calibrating to one lake level gauge, for a large lake draining almost 37% of the watershed, the hydrological model failed to provide reasonable streamflow simulations. This finding indicates that lake-level measurements of multiple lakes are needed to calibrate the hydrological model in an ungauged watershed.

Finally, we compared the relationship between calibrated lake crest width parameter in the broad crest weir equation of each gauged lake and the lake's drainage area. This comparison shows that the calibrated lake crest width parameter has a significant linear relationship with the lake's drainage area in log-log space. This result validates the assumption used in literature to parametrize the outflow structure of lakes. Results also show the routing products from Chapter 3 provide an upper bound estimate to the lake crest widths for the Petawawa watershed.

## Chapter 5

### Modelling forest disturbance and growth in hydrological models using the Robin vegetation simulation library

#### 5.1 Summary

Robust forest and watershed management relies on an understanding of the impact of disturbance (e.g., forest harvest, reforestation, and fire) on the eco-hydrological processes in the forest headwaters because it impacts the water quality and aquatic ecosystem health at downstream locations. However, existing hydrological models typically either do not explicitly account for interactions and feedback between vegetation changes and the hydrological cycle or they do not model the forest allometric (e.g., the forest density, stem biomass, and DBH) dynamics. This chapter presents a novel computational library, Robin, of dynamic vegetation growth algorithms for forested and agricultural landscapes that can be easily coupled with any hydrological model. For forest applications, the library is intended to help hydrological models effectively simulate the impacts of forest harvesting, reforestation, and wildfire on water resources. A new daily version of the popular 3PG (Physical Processes Predicting Growth) forest growth model, which has been widely used in modelling forest dynamics, was emulated in the Robin vegetation growth library (Robin\_3PG). Robin\_3PG has been successfully compiled with the Raven (Craig et al. 2020) hydrological modelling framework (Raven\_Robin\_3PG). The coupled model (Raven\_Robin\_3PG) is applied to a paired-catchment forest harvesting experiment conducted at the extensively-monitored Turkey Lakes Watershed located north of Sault Ste. Marie, Ontario, Canada.

The coupled model was calibrated and validated using streamflow observations, forest allometric measurements (e.g., stem biomass and density), and Landsat-derived leaf area index in pre-and post-harvest periods. Moreover, the performance of the coupled model in modelling the response of the hydrological system to the forest harvest management was evaluated using two hydrological signatures.

The result suggests that the Raven\_Robin\_3PG model could reasonably simulate the hydrological response to forest harvest management and the forest growth and regrowth in both the control and forest harvest catchments. The simulated response of the hydrological process to forest harvest management also highlights that the climate variability as well as the evapotranspiration process in each soil layer significantly impacts the response of the runoff components to the forest disturbance. This study

demonstrates the usefulness of Raven\_Robin\_3PG to simulate/quantify the response of the hydrological processes to the forest disturbances, such as forest harvest management or fire.

## 5.2 Introduction

The importance of the forest headwaters has never been in question because they provide critical commercial and ecological benefits, and they are one of the primary drinking water sources (Brown et al., 2008; N.C Coops et al., 1998). The disturbances from forest management practices (e.g., forest harvest and reforestation) or forest fire change water, sediment, and nutrient transport processes (Caldwell et al., 2020; Hampton et al., 2022; Nunes et al., 2020), which impact the water quality and aquatic ecosystem health at downstream locations (Basso et al., 2019). Thus, understanding the impact of disturbance on the eco-hydrological processes in the forest headwaters is essential for forest management.

One of the research questions appearing in the literature is how to statistically quantify the response and the recovery time of the streamflow in forest headwater catchments to forest disturbance, which requires detecting the changes in the streamflow between pre-and post-disturbance periods. Studies have used the time series of hydrological signatures (e.g., runoff ratio, the slope of the flow duration curve, low flow, and high flow) in the pre-and post-disturbance periods (Hou et al., 2022; Iroumé et al., 2021; Niemeyer et al., 2020; Wagenbrenner et al., 2021) to detect the change of the streamflow. The limitation of such analysis is that it cannot separate the streamflow changes caused by forest disturbance from the climate variations. Several studies have demonstrated that the changes from climatic drivers may overwhelm anticipated changes in hydrological signature from disturbance (Khaledi et al., 2022; Kurzweil et al., 2021). The paired-catchment approach is the most accurate method to quantify streamflow response to forest fire under changing climate (Caldwell et al., 2020; Crampe et al., 2021; Oda et al., 2021; Shimizu et al., 2021; Webster et al., 2021). The impact of changes in climate drivers can be removed by comparing the relationship of hydrological signatures between control and disturbed catchment in both pre-and post-disturbance periods. However, the paired-catchment approach requires the long-term streamflow measurement from two similar catchments, which is not always available for most studies. Thus, several studies have included the climate factor (e.g., precipitation and evapotranspiration) in their statistical model (Giles-Hansen & Wei, 2021; Hampton & Basu, 2022; Khaledi et al., 2022) to separate the impact of the forest disturbance on the streamflow in the forest headwater catchment under a changing climate. For example, Hampton & Basu, (2022) demonstrate

that the Budyko framework can be used to separate the contribution of forest fire-driven versus climate-driven changes in streamflow of forest headwater catchments.

The limitation of statistically quantifying observed changes in the streamflow is that it cannot assess the changes in hydrological processes inside the headwater catchments, which is essential because these changes could lead to changes in sediment and nutrient concentrations at the headwater catchment (Caldwell et al., 2020; Nunes et al., 2020). The hydrological processes in several headwater catchments have been measured and modeled to quantify the impact of forest disturbance on these processes. For example, the forest disturbance changes the snow accumulation and ablation rates and overall snow storage amounts (Broxton et al., 2021; Dickerson - Lange et al., 2021; Moeser et al., 2020). Forest cutting can reduce canopy interception, which is shown by (Oda et al., 2021) to account for most of the runoff response following forest cutting and the subsequent runoff recovery based on the observations from a paired headwater catchment in Japan. Forest harvest and reforestation management can change evapotranspiration (Collar et al., 2021; Roche et al., 2018), runoff partitioning (Buttle et al., 2019; Meerveld et al., 2019), and runoff mean travel time (Leach et al., 2020).

However, these experimental and statistical results cannot be directly applied to a different forest headwater catchment because the response of hydrological processes to the forest disturbance has spatial variations. These responses are impacted by the humidity (Collar et al., 2021; Giles-Hansen & Wei, 2021; Khaledi et al., 2022), the disturbance area (Guo et al., 2021) and disturbance intensity (Smith Tripp et al., 2021), the catchment size (Vore et al., 2020) and the land use within the catchment (Christopher Spence et al., 2020). Moreover, the data availability (e.g., canopy interception, snow storage, and soil moisture) to support empirical analyses of the impact of the forest disturbance on the hydrological processes is limited (Boisramé et al., 2019). More importantly, the impact of forest disturbance changes with the forest recovery/reforestation processes. Thus, the results based on the current measurements cannot be extended to the future without a reasonable prediction of the forest recovery processes (Boisramé et al., 2019)

Therefore, researchers have applied different models to quantify the response of the forest headwater catchment to the forest disturbance (Bart et al., 2021; Boisramé et al., 2019). The impact of the vegetation on hydrological processes can be represented in the hydrological and hydrological land surface model with different approaches. First, the hydrological model, such as Raven (Craig et al., 2020), HYPE (Lindström et al., 2010) or SUMMA(Clark et al., 2015), can use input vegetation

variables (i.e., LAI, root depth, height, et al.) to simulate the impact of vegetation on the hydrological processes such as canopy interception and potential evapotranspiration. This approach does not stimulate vegetation growth (and hence the vegetation variables). The limitation of this approach in modeling the impact of forest disturbance is that it does not simulate the evolution of the vegetation state variables in the post-disturbance period, as the input vegetation variables of these models come from observations from the past. Second, several hydrological or hydrological land surface models, such as RHESSys model (Tague & Band, 2004), SWAT (Arnold et al., 2012), MESH-CTEM (Pietroniro et al., 2007), explicitly couple the vegetation growth processes and hydrological processes. With this ability, these models can integrate the knowledge from current field observations and test the different hypotheses about the behavior of the forest headwater catchment to the changing climates and forest disturbances (Bouaziz et al., 2022; Hwang et al., 2018). For example, Boisramé et al. (2019) developed a fire extent and severity map from Landsat images and then estimated forest fire impacts of removing the litter and biomass within the mapped fire extents via simulation of the RHESSys (Tague & Band, 2004) model. The biomass removal within the RHESSys model impacts the evapotranspiration, canopy interception, and snow melting processes (Bart et al., 2021; Boisramé et al., 2019). After properly calibrating the model to the streamflow observations, Boisramé et al. (2019) developed several forest fire scenarios (i.e., burned and unburned scenarios) to investigate the model simulated differences in the snow pack, streamflow, evaporation, and transpiration caused by the forest fire.

However, the forest growth module in the RHESSys model (Tague & Band, 2004) as well as other eco-hydrological models like SWAT (Arnold et al., 2012) and MESH-CTEM (Pietroniro et al., 2007), do not support simulating the forest density, DHB, and basal area changes, which is critical for forest management, such as forest harvesting and reforestation. Moreover, the vegetation growth module in these models is typically not modular. Thus, it is tough for researchers to export these vegetation modules for implementation into a different hydrological or hydrological land surface model.

This study adapts the 3-PG (Physiological Principles Predicting Growth) stand-level process-based forest growth model, developed by Landsberg & Waring (1997), into the Robin vegetation growth library. The Robin vegetation growth library is designed to be easily coupled to basically any hydrological or land-surface model to add the functionality of crop and vegetation growth. Then, the 3PG forest growth model in the Robin vegetation growth library (Rabin\_3PG) was coupled with the Raven hydrological modelling framework (Raven). The coupled model is used to simulate the hydrological response of a small forest headwater catchment to forest harvest experiments conducted

at the extensively-monitored Turkey Lakes Watershed in Northern Ontario, Canada. The coupled model is calibrated with the observed streamflow and forest allometric measurements from control and harvest catchments at pre-and-post-harvest periods. Moreover, the coupled model's performance in modelling the streamflow response to forest harvest is evaluated using two hydrological signatures. Then, the calibrated coupled model is used to quantify the response of the hydrological processes to the forest harvest and continued forest regrowth.

## **5.3 Materials and methods**

The Robin vegetation growth library is first introduced in section 5.3.1. Section 5.3.2 describes the 3PG forest growth model emulation in the Robin vegetation growth library (Robin\_3PG). Then, the paired-watershed forest harvest experiment in the Turkey lake watershed, followed by the measurements to calibrate the model are introduced in sections 5.3.3 and 5.3.4, respectively. Section 5.3.5 describes the model setups for the Raven hydrological model framework (Raven) and the coupled model, which combine Raven and the Robin\_3PG (Raven\_Robin\_3PG). Finally, the model calibration strategies are introduced in section 5.3.6.

### **5.3.1 The Robin vegetation growth library**

The Robin vegetation growth library can be easily coupled to a variety of hydrological or land-surface models to add the functionality of crop and vegetation growth. It is a flexible vegetation growth library that includes multiple vegetation growth models. The hydrological model can use different vegetation models in Robin to simulate different vegetation growth processes for each hydrological response unit (HRU). The Robin vegetation growth library has stand-alone input and output files. Thus, coupling any hydrological model with Robin does not need to modify the existing input files and adjust the source code to read/write new input/output files. The Robin vegetation growth library provides several interface functions. Modelers only need to call these interface functions in the source code of the hydrological model to include Robin simulation modules. It supports modelling the vegetation changes due to the land use change or disturbance from land management or forest fire. The following content describes how Robin simulates the vegetation growth of each HRU in the hydrological model. Appendix A5 provides more detailed information about the Robin vegetation growth library, such as how to use the Robin interface functions to couple it with the hydrological model and the input of the Robin.

The grid/subbasin in a distributed or semi-distributed hydrological model can be further divided into different hydrological computational units (HRU). An HRU is a subregion within a grid or subbasin, which can be non-contiguous, that is simulated as one computational element (inputs, characteristics and simulated outputs are each treated as constant across an HRU). Depending on the model/application, different spatial layers can be used to discretize grids/subbasins into HRUs. Figure 5-1 shows that the land use information over different HRUs can be different, and it may change over time. For example, the HRU1 in Figure 5-1 represents agricultural land use. The crop growing in this HRU1 may change every year to keep the soil healthy. HRU2 represents the forest land use type. The forest may suffer from disturbances, such as forest fires and forest harvest management. After the disturbance, the new forest type different from forest type in the pre-disturbance period (regrowth forest) would grow in this HRU.

The land use information of each HRU in each growing season is summarized and represented as vegetation type arrays in the Robin (Figure 5-1). In the simple example shown in Figure 5-1, there are only two vegetation type arrays. In an actual application, the number of the vegetation type arrays is smaller than the number of HRUs because HRUs may be defined by combining information from multiple sources, such as subbasin, soil, land use, and elevation band. It is expected that many HRUs share the same land use (vegetation) information.

Each vegetation type in the vegetation type arrays is linked with a user-defined vegetation growth model. In the simple example shown in Figure 5-1, both undisturbed and regrowth forests are modeled with the 3PG forest growth model, and the maize and soybean are modeled with the EPIC vegetation growth model used in SWAT. Currently, Robin only includes two vegetation growth models and will include more vegetation growth models in the future. The vegetation model of each vegetation type is parameterized separately. In this way, even though both regrowth and undisturbed forests use the 3PG forest model, the parameters of the 3PG model for regrowth and undisturbed forests can be different.

Robin creates a vegetation instance for each HRU of the hydrological model. It includes the HRU ID, the simulated vegetation state variables (e.g., LAI, root distribution at each soil layer, and biomass in each storage component), and the vegetation type array of this HRU. Thus, the HRU of the hydrological model is not linked to a specific vegetation growth model and is linked to the vegetation type array instead. With this structure, Robin can simulate all kinds of land use changes in each HRU with different vegetation models.

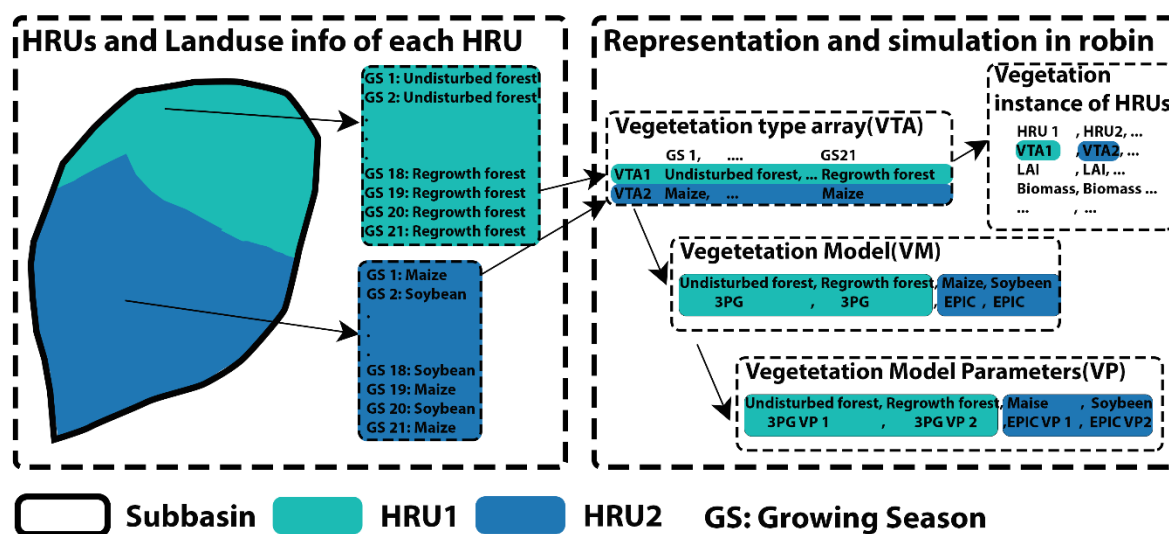


**Figure 5-1.** The conceptual structure of the Robin vegetation growth library.

The vegetation growth module in SWAT and the 3PG forest growth model have been emulated in Robin. This study applies Robin\_3PG and couples it with the Raven hydrological model. Section 5.3.2 describes 3PG forest growth emulation in Robin, and section 5.3.5 describes how Robin is coupled with the Raven.

### 5.3.2 The 3PG forest growth model emulation in Robin

This section provides an overview of the 3PG forest growth model in section 5.3.2.1. Then, the forest phenology module and the forest reproduction module added to the 3PG forest growth model are introduced in sections 5.3.2.2 and 5.3.2.3, respectively.

#### 5.3.2.1 Overview of the 3PG

The 3-PG (Physiological Principles Predicting Growth) model, developed by Landsberg & Waring (1997), is a stand-level process-based forest growth model designed for even-aged monospecific forests. Even-aged and monospecific meaning the modeled forest by 3PG is the same specie with the same age. It is a compromise between empirical and detailed tree-level models, replacing complex leaf- or tree-level physiological relationships with simpler stand-level relationships (Forrester & Tang, 2016; Landsberg & Waring, 1997).

The 3-PG forest growth model simulates the net primary production and allocates carbon to roots, foliage, and stems at a monthly time step. The biomass accumulation and the allocation are affected by

age and environmental variables, such as temperature, vapor pressure deficit, available soil water, and site fertility (N.C Coops et al., 1998; Landsberg & Waring, 1997). The stem population is simulated via two mortality processes: age-induced forest mortality and density-induced forest mortality. The 3PG model does not simulate forest reproduction processes, which means that the 3PG forest growth model can only decrease the number of trees. The 3PG model uses two user-specified parameters (month of leaf on and leaf fall) for the deciduous forest to simulate the forest phenology. The forest phenology represents the seasonal forest leaf dynamics. A more detailed description of the 3PG forest growth model can be found in Landsberg & Waring (1997) and Coops et al. (1998).

The 3PG forest growth model has been tested and applied to simulate the growths of different types of species under different climate and site conditions (Almeida et al., 2004; Fontes et al., 2006; Miehle et al., 2009; Paul et al., 2007; Pérez-Cruzado et al., 2011; Rodríguez et al., 2009; Sands & Landsberg, 2002). More importantly, the 3PG forest growth model has been validated to different kinds of measurements, such as: woody biomass (Miehle et al., 2009; Sands & Landsberg, 2002), stem biomass (Almeida et al., 2004; Paul et al., 2007), root biomass (Almeida et al., 2004; Paul et al., 2007), leaf area index (Sands & Landsberg, 2002), leaf biomass (Paul et al., 2007; Pérez-Cruzado et al., 2011), volume (Almeida et al., 2004; Fontes et al., 2006; Miehle et al., 2009; Pérez-Cruzado et al., 2011), DBH (Paul et al., 2007; Pérez-Cruzado et al., 2011), and basal area (Fontes et al., 2006; Pérez-Cruzado et al., 2011).

Three fundamental assumptions of the 3PG forest growth model were recently modified, allowing for it to be coupled with hydrological models and calibrated to remote sensing observations (Almeida et al., 2016; Almeida & Sands, 2016; N.C Coops et al., 1998; Nicholas C Coops et al., 2012; Du et al., 2016; Feikema et al., 2010; Smettem et al., 2013; Waring et al., 2010). First, the timestep of the 3PG model has been changed from monthly to daily (Almeida et al., 2016). Second, the monospecific forest assumption was relaxed to simulate forest growth in elevation zones of a watershed (Du et al., 2016; Smettem et al., 2013) and 8 km x 8 km grids (N.C Coops et al., 1998), where multiple vegetation species with different ages exist. These applications implicitly assume that the state variable such as LAI, DBH, and AET simulated by the 3PG forest growth model is an area-averaged value of multiple species of different ages. The third assumption changed in literature is that the spatial scale of the 3PG forest growth model extends from stand-level to grids/elevation zones (N.C Coops et al., 1998; Du et al., 2016; Smettem et al., 2013).

To adapt the 3PG forest growth model to Robin, these three fundamental assumptions in 3PG also need to be changed as follows. It is assumed that the 3PG emulation in Robin is an HRU-level process-based forest growth model with a daily time step. It is designed to simulate the area-averaged forest state variables without considering the mixing effects of mixed-species or uneven-aged forests within the HRU. Building on this assumption, a phenology module was added to improve the LAI simulation for the deciduous forest (section 5.3.2.2) and a forest reproduction module to simulate the short-term forest recovery processes after the wildfire or harvest management (section 5.3.2.3).

### 5.3.2.2 Add forest phenology development

The original 3PG forest growth model does not include forest phenology development because it is a monthly timestep model and focuses on the forest LAI dynamic on a decade time scale (N.C Coops et al., 1998; Landsberg & Waring, 1997). However, a forest phenology development component is needed for a daily 3PG forest growth model to improve the LAI simulation within one growing season due to the following two reasons. First, using two user-specified parameters (month of leaf on and) is reasonable to start the deciduous forest's growth and dormant seasons for a monthly timestep 3PG model. However, applying the same approach to a daily timestep is unreasonable as the date of leaf on and leaf fall of the deciduous forests are impacted by the day length and temperature, and it changes every year. Second, the monthly 3PG model did not simulate the leaf fall processes as it is a monthly model and the leaf fall process typically happens within one month. Nevertheless, it is unreasonable to ignore the leaf fall processes in a daily timestep model and remove the deciduous forest leaf within one day. To improve the daily LAI simulation, the forest phenology development procedure in the Canadian Terrestrial Ecosystem Model (CTEM, Arora & Boer, 2005) was adapted into the Robin\_3PG. This section describes the concept of forest phenology development applied in Robin\_3PG. The detailed equations can be found in section Appendix A5.

The actual growth of a deciduous forest is divided into four-leaf phenology periods: the maximum growth stage, the normal growth stage, the leaf fall stage, and the dormancy stage (Arora & Boer, 2005). In the CTEM model, the deciduous forest would end the dormant stage and move to the maximum growth stage when the net primary production calculated using a “virtual leaf” concept is positive over seven consecutive days. The “virtual leaf” is the leaf biomass assumed to be existed to allow the deciduous forest to initialize the growth processes at the beginning of the growing season. However, the net primary production from the 3PG model is always positive as it assumes the net primary

production is 60 percent of the gross primary production (N.C Coops et al., 1998; Landsberg & Waring, 1997). Thus in Robin\_3PG, the condition for the deciduous forest to move from the dormant stage to the maximum growth stage is changed to several consecutive days with a daily averaged temperature larger than a threshold temperature. In the maximum growth stage, all NPP is allocated to the leaf, and environmental stress-induced leaf biomass loss was neglected in this stage.

The deciduous forest would end the maximum growth stage and move to the normal growth stage when leaf biomass reaches a certain percentage of the maximum leaf biomass, given that stem and root biomass can support it (Arora & Boer, 2005). The 3PG forest growth model determines the biomass allocation between leaf and stem using the DBH of the forest and does not simulate the maximum leaf biomass. Thus, in Robin\_3PG emulation, the yearly maximum leaf biomass [kg/ha] is determined based on the forest's averaged DBH and the forest's density [number of trees/ha] at the beginning of each growing season. The forest's DBH calculates the maximum leaf biomass of a single tree [kg/tree]. The NPP is allocated to the leaf, root, and stem in the normal growth stage. Moreover, the NPP allocation to the leaf is zero when the leaf biomass reaches its current yearly maximum leaf biomass [kg/ha]. In the normal growth stage, the water availability and daily average temperature can reduce the leaf biomass.

The deciduous forest would transit to the leaf fall stage based on the day length below certain hours and average air temperature smaller than a threshold temperature for several consecutive days. The NPP only allocates to the stem and root in the leaf fall stage. And the leaf biomass is lost due to two drivers: 1) the water and air temperature stresses and 2) the constant leaf fall rate.

The deciduous forest moves from the leaf fall stage to the dormant stage when several consecutive days with a daily averaged temperature smaller than the threshold temperature occurs.

### 5.3.2.3 Add forest reproduction module

The 3PG forest growth model does not simulate the forest reproduction processes to increase the forest density [number of tree/ha], but it includes the forest density-induced mortality to decrease the modeled forest density [number of trees/ha] using the self-thinning line (N.C Coops et al., 1998; Landsberg & Waring, 1997). The self-thinning line is an observed relationship between averaged stem biomass [kg/tree] or DBH [cm/tree] and forest density [number of tree/ha] in the mature forest (Landsberg & Waring, 1997; Pickard, 1983; Zeide, 2010). It shows that the forest density of a mature forest would decrease with the increase of the forest averaged stem biomass [kg/tree] or DBH [cm/tree]. The forest

models like 3PG (N.C Coops et al., 1998; Landsberg & Waring, 1997) and the LANDIS PRO (Wang et al., 2013) use the forest density on this line as a threshold value. The forest density-induced mortality occurs when the modeled forest density [number of trees/ha] is larger than the forest density [number of trees/ha] on the self-thinning line. In this way, the modeled relationship between averaged stem biomass/DBH and forest density will eventually be along with the observed self-thinning line.

After the forest harvest management or fire, the forest density would increase and approach the self-thinning line before the density-induced mortality occurs. However, without the reproduction module, the 3PG forest growth model cannot simulate the increase of forest density in the forest recovery processes (N.C Coops et al., 1998; Landsberg & Waring, 1997). The concept from the LANDIS PRO, a large-scale forest growth model, was used in Robin\_3PG to simulate the forest reproduction processes.

Building on the self-thinning line, Wang et al. (2013) introduce two similar concepts: the full-occupancy line and the maximum stand density line, which parallel the self-thinning line. The forest density on the self-thinning line is larger than the forest density on the full-occupancy line and smaller than the forest density on the maximum stand density line. The full-occupancy line represents the forest density when the forest occupies all the open spaces. When the modeled forest density is smaller than the forest density on this line, the forest reproduction is free of competition for resources. When the modeled forest density is larger than the forest density on the full-occupancy line, the forest reproduction rate starts to slow down due to resource competition. The forest reproduction rate is zero when the forest density is equal to the forest density on the maximum stand density line, representing the maximum number of trees or forest density acceptable to the environment. The detailed equations of Robin\_3PG can be found in section Appendix A5.

### **5.3.3 Site and forest species**

The paired-catchment forest harvest experiment is conducted in the two headwater catchments in the Turkey lake watershed (Subbasin C31 and C32 in Figure 5-2), located at approximately 60 km north Sault Ste.Marie, Ontario, Canada. The drainage area of the subbasin C31 and C32 are 0.052 and 0.067 km<sup>2</sup>, respectively.

The forest in the Turkey lake watershed is undisturbed, with the majority of the forest species being sugar maple (Jeffries et al., 1988). The forest harvest experiment happened in the fall of 1997. The extent of the harvest management is shown in Figure 5-2. The harvest management means all trees with a diameter of greater than 20 cm were harvested, and all trees with a diameter between 10 and 20 cm

were felled and left on site (Buttle et al., 2019). After forest harvest management, the primary tree species regenerating at this site is the pin cherry. In general, two types of forest exist in the headwater catchments: the undisturbed forest and the regrowth forest.

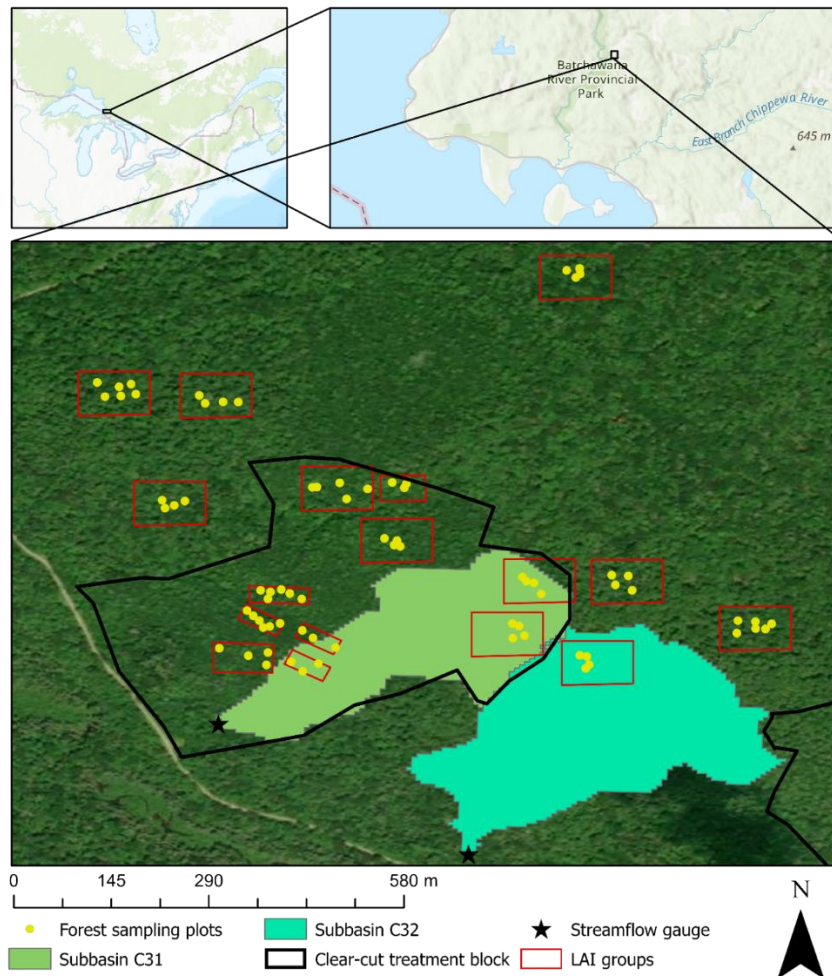


**Figure 5-2.** The location of the paired-catchment forest harvesting experiment at the Turkey Lakes Watershed. Subbasin C31 and C32 are two headwater catchments. The clear-cut treatment block is the extent of the clear-cut forest treatment, which removed trees with DBH > 10 cm. The forest sampling plots are the location of the forest measurements. Moreover, LAI measurements and the reduced simple ratio (RSR) (Chen et al., 2002) from Landsat images of each sampling plot were averaged for each LAI group to develop a relationship between measured LAI and the RSR. The derived relationship was used to generate catchment averaged LAI time series from Landsat images for control and harvest catchment, respectively.

### 5.3.4 Observations and input data sets

This section introduces the input and calibration datasets for the Raven and Raven\_Robin\_3PG model. Section 5.3.4.1 introduces the measured tree growth data, streamflow, and meteorological data. Section 5.3.4.2 describes ground-based forest measurements. Section 5.3.4.3 describes how daily catchment averaged LAI time series was derived using Landsat images. Section 5.3.4.4 describes how stem biomass observations and Robin\_3PG parameters were derived.

#### 5.3.4.1 Geospatial inputs, model forcing, and streamflow response data

The 5 m Digital Elevation Model (DEM) is used to delineate the watershed boundary for the control catchment(C32) and the harvest catchment (C31) (Figure 5-2). One 10m meteorology measurement tower belonging to the Canadian Air, and Precipitation Monitoring Network is located just 1.5 km southeast of the catchment boundary. The 10 min intervals meteorology measurements, including air temperature, wind speed and direction, relative humidity and vapor pressure, barometric pressure, and solar radiation, have been available since 1981. The 10 min intervals of meteorology measurements are aggregated into daily values to force the Raven and Raven\_Robin\_3PG models.

Daily mean streamflow at the outlet of the harvest and control catchments was estimated from stage-discharge relationships developed using v-notch weirs, stilling wells, and water level loggers (Buttle et al., 2019; Leach et al., 2020). Weirs were installed around 20 cm in depth to capture all flow from the catchments. However, there was the potential for some subsurface flow to bypass the weirs (Buttle et al., 2019; Leach et al., 2020).

#### 5.3.4.2 Ground-based forest system response data

The forest allometric variables for the undisturbed forest at control sites (outside of the clearcut treatment block in Figure 5-2) and the regrowth forest in the clearcut treatment block (Figure 5-2) are measured during the growing seasons (between July and September) before and after the forest harvest management. The forest stocking [number of trees/ha] and basal area [ $\text{m}^2/\text{ha}$ ] were measured in each sampling plot (Figure 5-2) in 1996 (pre-harvest), 1997 (post-harvest), 2003, 2008, and 2013. The forest leaf area index (LAI, [ $\text{m}^2/\text{m}^2$ ]) was measured in each sampling plot (Figure 5-2) in 1996, 1997, 1998, 1999, 2002, 2006, 2007, and 2012. The forest stocking [number of trees/ha] and basal area [ $\text{m}^2/\text{ha}$ ] were measured following the methodology described in Morrison (1990). The measurement of forest LAI is described in Fleming (2022, unpublished data). The measured forest stocking [number of trees/ha] and

basal area [m<sup>2</sup>/ha] at sampling plots within and outside of the clearcut treatment block were averaged each year (Figure 5-2). The yearly averaged measurements from control and clearcut treatment sites are used to calibrate the Robin\_3PG forest growth parameters for two types of forest in the study area: the undisturbed forest and the regrowth forest. The procedure for processing the measured LAI in each sampling plot is described in section 5.3.4.3.

Moreover, following the method described in Morrison (1990), the relationships between DHB and leaf biomass ( $w_{leaf}$  [kg/tree]) and the relationship between DBH and aboveground biomass ( $w_{above}$  [kg/tree]) are developed for the undisturbed and regrowth forest.

For the undisturbed forests,

$$w_{leaf} = 0.1372 \times DBH^{1.2603} \quad (5-1)$$

$$w_{above} = 0.5005 \times DBH^{2.0451} \quad (5-2)$$

For the regrowth forest,

$$w_{leaf} = 0.0554 \times DBH^{1.5203} \quad (5-3)$$

$$w_{above} = 0.3051 \times DBH^{2.1417} \quad (5-4)$$

#### 5.3.4.3 Remotely sensed system response data

In order to properly calibrate the Robin\_3PG forest growth model for the regrowth and undisturbed forest, the daily LAI time series are derived for the regrowth and undisturbed forest in harvest and control catchment, respectively.

To estimate the LAI of the forest from the Landsat images requires three steps. First, identify the pixel of sampling plots (Figure 5-2) from the Landsat scenes that were taken within two days of the date when the ground LAI measurement took place. Second, extract the remote sensing data for each LAI sampling plot (Figure 5-2) and calculated the reduced simple ratio (RSR) using the following equation (Chen et al., 2002):

$$RSR = \frac{\rho_{nir}}{\rho_{red}} \left( 1 - \frac{\rho_{swir} - \rho_{swir\_min}}{\rho_{swir} - \rho_{swir\_max}} \right) \quad (5-5)$$

where  $\rho_{nir}$ ,  $\rho_{red}$  and  $\rho_{swir}$  are the reflectance in NIR, RED, and SWIR bands, respectively.  $\rho_{swir\_min}$  and  $\rho_{swir\_max}$  are the minimum and maximum SWIR reflectance found in each image and defined as the 10% minimum and maximum cut-off points in the histograms of SWIR reflectance in a watershed-

wide scene. Third, to reduce the errors in comparing the ground LAI measurement and the RSR from the extracted Landsat  $30\text{ m} \times 30\text{ m}$  pixel of each sampling plot, group the LAI sampling plot into 17 groups (Figure 5-2). And then, build a relationship between group averaged LAI and RSR ( $\text{LAI} = 7.5 - 7.1\exp(-0.17 \times \text{RSR})$  with  $R^2 = 0.58$ ), as shown in Figure 5-3.

Finally, the forest growing season cloud-free images from Landsat 5 and 7 were selected for the control and harvest catchment. The Landsat 5 and 7 cloud-free images are available on 157 dates from 1986 to 2012 for the two catchments. For each catchment, the RSR is calculated from each selected Landsat image and used the relationship in Figure 5-3 to derive the LAI map. The LAIs in the LAI map of each catchment were averaged at each date. In the end, 157 catchment-averaged Landsat LAI measurements were obtained from 1986 to 2012 for control and harvest catchments, respectively.

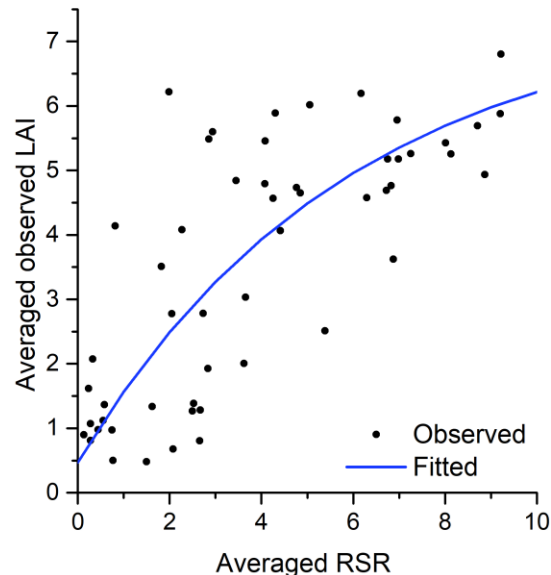


**Figure 5-3.** The derived relationship between the averaged observed LAI of each sampling group and the averaged reduced simple ratio vegetation index (RSR, Chen et al., 2002) of each sampling group. The scenes from Landsat are used to calculate the RSR of each LAI sampling plot. The LAI sampling plots in Figure 5-2 are grouped into 17 groups. The measured LAI and the RSR of each sampling plot are used to calculate their group averaged values. The fitted relationship between the averaged LAI and the Landsat RSR of each group is:  $\text{LAI} = 7.5 - 7 \times \exp(-0.17 \times \text{RSR})$  with  $R^2 = 0.58$ .

#### 5.3.4.4 Derived the stem biomass and Robin\_3PG parameters

The modeled DBH [cm] and the stocking [number of trees/ha] determine the basal area [ $\text{m}^2/\text{ha}$ ] in the Robin\_3PG model (Equation (A5-34)). Thus, the DBH [cm] for both regrowth and undisturbed forests can be estimated using the directly observed basal area [ $\text{m}^2/\text{ha}$ ] and the stocking [number of trees/ha]. Using Equation (5-2 and 5-4) and the estimated DBH [cm], the leaf [kg/tree] and aboveground biomass [kg/tree] can be estimated for regrowth and undisturbed forests. And with the measured stocking [number of the trees/ha], the leaf [kg/ha] and aboveground biomass [kg/ha] of the regrowth and the undisturbed forests can be obtained. The stem biomass [kg/ha] is calculated as the difference between the estimated aboveground biomass [kg/ha] and the leaf biomass [kg/ha].

The model was calibrated to the stem biomass [kg/ha], the stocking [number of the trees/ha], and the LAI because other measurements are automatically fitted by Robin\_3PG. The reason is that first, the simulated DHB in Robin\_3PG is a function of the simulated stem biomass (kg/ha) and the stocking (Equation (A5-33)). Thus, the two coefficient parameters in Equation (A5-33) can be determined by the derived stem biomass [kg/ha], stocking [number of trees/ha] and DBH measurement. With these two coefficient parameters fixed, reasonable DBH simulation results were obtained when Robin\_3PG was calibrated to the derived stem biomass [kg/ha] and direct stocking measurement [number of tree/ha]. Second, Robin\_3PG also uses Equations (5-1 and 5-3) to estimate the yearly maximum leaf biomass. Thus, A reasonable leaf biomass simulation were obtained when the Robin\_3PG provides good DBH simulation. Third, the DBH was derived from the measured basal area and stocking using Equation (A5-34) in Robin\_3PG. Thus a reasonable basal area simulation were obtained when Robin\_3PG provides good DBH and stocking simulation.

#### 5.3.5 The Raven and Raven\_Robin\_3PG hydrological model setups

In this study, both Raven and Raven\_Robin\_3PG were built for both harvest and control catchments. Section 5.3.1 describes the Raven hydrological model for both catchments. And then, section 5.3.5.2 describes the Raven\_Robin\_3PG model setup for both catchments.

##### 5.3.5.1 The Raven-only model

The Raven hydrological modelling framework is developed by James R. Craig at the University of Waterloo (Craig et al. 2020). The Raven is an object-oriented modelling framework that gives users full flexibility regarding hydrological process descriptions. It supports customization of the

hydrological processes (i.e., with/without snow/percolation/baseflow processes, number of soil layers et al.) and hydrological flux algorithms for each process (i.e., linear/power-law function). What is more, Raven also provides a blend option, where users can provide weights for multiple hydrological flux algorithms, and Raven internally uses a weighted sum of the calculated fluxes in each model simulation time step (Chlumsky et al., 2021).

In this study, the purpose of the Raven model is to serve as a benchmark for the coupled Raven\_Robin\_3PG. So the performance of the hydrological model without Robin\_3PG can be demonstrated. For this purpose, the same LAI inputs were used in Raven model for the control and harvest catchment in the pre-and post-harvest period.

To build a semi-distributed hydrological model with Raven, the control and harvest catchments were further discretized into HRUs based on the three slopes ( $0^\circ \sim 5^\circ$ ,  $5^\circ \sim 20^\circ$ , and  $20^\circ \sim 90^\circ$ ) and two aspects (north and south face) categories. The number of HRUs in the harvest and control catchments is four and three, respectively. The simulation period is from 1981-00-01 to 2013-12-31. From 1981-01-01 to 1983-12-31 is the model warmup period. The streamflow measurement data from 1984-01-01 to 1996-12-31 at both catchments are used to calibrate the model. The streamflow data at both catchments from 1998-01-01 to 2012-12-31 was used to validate the model.

A detailed description of the hydrological processes applied in this case study is described in Appendix A3. This section focus on the Raven model processes that are different from the Raven\_Robin\_3PG model. The Priestley-Taylor method in the Raven was used to calculate the potential evapotranspiration (PET) for each HRU. Furthermore, the PET was adjusted ( $PET_{adj}$ ) by a PET correction coefficient parameter before Raven uses it to remove water from the soil profile of each HRU. The same PET correction coefficient parameter was applied to all HRUs in both catchments and unchanged during the whole simulation period.

The actual evapotranspiration from the Raven is simulated by the “SOILEVAP\_SEQUEN” method (Craig et al. 2020), which removes the water from the top two soil layers in sequence. The amount of water evaporated in each soil layer is linearly proportional to the soil saturation; the top layer storage is exhausted first. The remaining ET can be withdrawn from the lower layer.

The precipitation intercepted by the canopy is simulated by the “PRECIP\_ICEPT\_LAI” method (Craig et al. 2020). The interception percentages of precipitation are given as a linear function of the LAI. Raven allows users to provide twelve constant monthly LAI values. The monthly mean LAI was

calculated from the Landsat-derived LAI time series (1986-2012) of the control catchment (section 5.3.4.2). Then the same monthly mean LAI is applied to both harvest and control catchments in pre- and post-harvest periods. It is reasonable because most hydrological models do not support input LAI changes between years.

#### 5.3.5.2 The Raven\_Robin\_3PG model

In the Raven\_Robin\_3PG application, two forest types representing the undisturbed forest and the regrowth forest were included. Both forest types are modeled by the Robin\_3PG forest growth model with different parameters. Two vegetation type arrays were defined. The first forest type array represents the forest growth status for the control catchment, where the undisturbed forest is grown from 1981 to 2013. The first forest type array was connected to HRUs within the control catchment. The second forest type array represents the forest growth status in the harvest catchment, where the undisturbed forest grew from 1981 to 1997, and then the regrowth forest started to grow from 1998 to 2013. The second forest type array was connected to the HRUs within the harvest catchment. Robin\_3PG initialize the forest state variables of each HRU within the harvest catchment in the year 1998 with input initial conditions for the regrowth forest. The direct and derived measurements (section 5.3.4) in 1997 (post-harvest) were used to set the initial condition for the regrowth forest. Moreover, the initial condition of the undisturbed forest is calibrated since no measurements were available in the year 1981.

The Raven\_Robin\_3PG model is built by connecting Robin\_3PG to the Raven hydrological model described in section 5.3.1. This connection between models is described in the following paragraphs.

In this application, the actual and potential evapotranspiration rate ratio (AET/PET) was used to indicate the water stress suffered by the forest and reduce the forest growth rate (section Appendix A5). The AET/PET of each HRU is calculated by the Raven, and provided to Robin\_3PG.

The simulated forest state variables of each HRU modifies several hydrological processes of this HRU. First, the LAI of each HRU in Raven is updated at each time step using the Robin\_3PG simulated forest LAI of this HRU, which impacts the canopy interception processes. Second, instead of using a constant PET correction coefficient parameter to adjust PET calculated from the Priestley-Taylor method (section 5.3.5.1), the PET of each HRU is adjusted using the Robin\_3PG calculated crop coefficient ( $k_c$ ) of this HRU. The  $k_c$  is calculated as:

$$kc_i = kc_{min,j} + (kc_{max,j} + kc_{min,j}) \times \frac{LAI_i - LAI_{min,j}}{LAI_{max,j} - LAI_{min,j}} \quad (5-6)$$

where the  $kc_i$  is the crop coefficient of one HRU in the day  $i$ . The  $kc_{max,j}$  and  $kc_{min,j}$  are the minimum and the maximum of the  $kc$  of vegetation type  $j$ . And the  $LAI_{max,j}$  and the  $LAI_{min,j}$  are the minimum and maximum of the LAI of the vegetation type  $j$ . Then the  $PET_{adj}$  of each HRU on each day is calculated by  $kc_i \times PET$ .

Third, the soil evaporation process is also modified. In the Raven\_Robin\_3PG, the  $PET_{adj}$  is allowed to remove water from all three soil layers. For each HRU, the fraction of the  $PET_{adj}$  distributed to each soil layer is determined by the soil layer depth and root depth described in the SWAT model (Arnold et al., 2012). Then the soil evaporation from each layer is calculated by:

$$AET_{m,i} = PET_{adj,i} \times root\_frac_{m,i} \times (stor_{m,i} - wilt_m) / (strs\_factor_j \times (fc_m - wilt_m)) \quad (5-7)$$

where the  $AET_{m,i}$  is the actual evapotranspiration rate of one HRU from soil layer  $m$  at the time  $i$ . The  $PET_{adj,i}$  is the adjusted the PET by  $kc_i$ . The  $root\_frac_{m,i}$  is the fraction of the root in soil layer  $m$  at day  $i$ . The  $stor_{m,i}$  is the soil water storage at soil layer  $m$  at day  $i$ . The  $strs\_factor_j$  is a vegetation stress coefficient range from 0 – 1 for vegetation type  $j$ . The  $wilt_m$  and the  $fc_m$  are the wilting point and field capacity soil water storage of soil layer  $m$ . This study applies a constant root depth of 2 meters to both undisturbed and regrowth forests.

### 5.3.6 Model calibration and evaluation

This section first introduces the model calibration procedures for Raven and Raven\_Robin\_3PG in the control and harvest catchment (section 5.3.6.1). Then section 5.3.6.2 introduces the two hydrological signatures and one streamflow performance metric used to evaluate the calibrated performance of the Raven and Raven\_Robin\_3PG models.

#### 5.3.6.1 Model calibration procedures

The streamflow measurement at both harvest and control catchments in the pre-harvest period (1985-1996) were used to calibrate the Raven model and use the streamflow measurements in the post-harvest period (1998-2012) at both catchments to validate the model. Raven is calibrated to two streamflow objectives at the same time. The first objective is the averaged KGE of streamflow in the summer (July, August, and September) at the control ( $KGE_{Q,S}^{control}$ ) and forest harvest catchment ( $KGE_{Q,S}^{harvest}$ ):

$$KGE_{Q,s} = 0.5 \times KGE_{Q,s}^{harvest} + 0.5 \times KGE_{Q,s}^{control} \quad (5-8)$$

The second objective is the averaged KGE of streamflow in the non-summer period at the control ( $KGE_{Q,ns}^{control}$ ) and harvest catchment ( $KGE_{Q,ns}^{harvest}$ ):

$$KGE_{Q,ns} = 0.5 \times KGE_{Q,ns}^{harvest} + 0.5 \times KGE_{Q,ns}^{control} \quad (5-9)$$

The KGE of each period is calculated by:

$$KGE = 1 - \sqrt{(1-r)^2 + \left(\frac{\sigma_{sim}}{\sigma_{obs}} - 1\right)^2 + \left(\frac{\mu_{sim}}{\mu_{obs}} - 1\right)^2} \quad (5-10)$$

where  $r$  is the linear correlation between observed and simulated flows,  $\sigma_{sim}$  and  $\sigma_{obs}$  are the standard deviation of observations and simulations, respectively. And  $\mu_{sim}$  and  $\mu_{obs}$  are the observation mean and simulation mean, respectively.

The multi-objective calibration of Raven is done using the Pareto archived dynamically dimensioned search (PA-DDS) algorithm (Asadzadeh & Tolson, 2009) with three independent trials and a budget of 20000 model evaluations for each trial.

For the Raven\_Robin model, two rounds of model calibration are involved. The first round of calibration aims to optimize the Robin\_3PG forest growth parameters for undisturbed and regrowth forests. First, the undisturbed forest parameter were calibrated to the  $KGE$  of the LAI ( $KGE_{LAI}^{control}$ ), the relative mean absolute error of stocking ( $RMAE_{stocking}^{control}$ ) and the stem biomass ( $RMAE_{stem}^{control}$ ) in the control catchment. The objective function is defined as:

$$Obj_V^{UF} = KGE_{LAI}^{control} - 0.5 \times RMAE_{stocking}^{control} - 0.5 \times RMAE_{stem}^{control} \quad (5-11)$$

The relative mean absolute error (RMAE) is calculated as:

$$RMAE = \frac{\sum_{i=1}^n |obs_i - sim_i| / obs_i}{n} \quad (5-12)$$

where  $n$  is the number of the observation,  $obs_i$  and the  $sim_i$  are the  $i$ th simulated and observed values, respectively. Note that the RMAE is used here because the unit of the stocking [number of trees per hac] and the stem biomass [kg/ha] are different. For the  $Obj_V^{UF}$ , all measurements in both pre-and-post harvests are used.

After obtaining the best calibrated Robin\_3PG forest growth parameters for the undisturbed forest. The Robin\_3PG forest growth parameters for the regrowth forest were calibrated to the  $KGE$  of the LAI ( $KGE_{LAI}^{harvest}$ ), the relative mean absolute error of stocking ( $RMAE_{stocking}^{harvest}$ ) and the stem biomass ( $RMAE_{stem}^{harvest}$ ) in the harvest catchment. The objective function is:

$$Obj_V^{RF} = KGE_{LAI}^{harvest} - 0.5 \times RMAE_{stocking}^{harvest} - 0.5 \times RMAE_{stem}^{harvest} \quad (5-13)$$

The Raven\_Robin calibrations in the first round are calibrated using the dynamically dimensioned search (DDS) algorithm with one trial and a 5000 model evaluations budget (Tolson & Shoemaker, 2007). The DDS is a neighborhood search algorithm that can find good quality calibration solutions based on a user-specified model evaluation budget (Tolson & Shoemaker, 2007).

After the first round of the model calibration, the calibrated Robin\_3PG parameter of undisturbed and regrowth forests were obtained. Most of them were fixed in the following model calibration step. In the second round of calibration, the hydrological parameters of the Raven\_Robin\_3PG were calibrated using a multi-objective calibration of both streamflow and forest growth observations. The three objectives of this round of calibration are: 1) the average of  $Obj_V^{RF}$  and  $Obj_V^{UF}$ , 2)  $KGE_{Q,s}$ , and 3)  $KGE_{Q,ms}$ , respectively. In this round, both hydrological parameters and some of the Robin\_3PG forest growth parameters of both forests were calibrated. The calibrated Robin\_3PG parameter includes  $strs\_factor$ ,  $kc_{max}$ ,  $kc_{min}$ , and  $LAI_{min}$ . These four Robin\_3PG parameters were assumed to be the same for undisturbed and regrowth forests.

The multi-objective calibration of the Raven\_Robin is calibrated using the Pareto archived dynamically dimensioned search (PA-DDS) algorithm with three independent trials and a budget of 20000 model evaluations for each trial.

Note that for all calibration experiments solved with PADDs, the resulting non-dominated solutions from each trial were combined and then those solutions that are non-dominated across all trials were identified. The best solution was selected based on the tradeoff of identified non-dominated solution between calibration objectives.

### 5.3.6.2 Hydrological signatures and evaluation metric

After the model calibration, the model performance in the streamflow simulation was also evaluated by the percent bias between the simulated and the observed streamflow ( $PCT\_BIAS$ ):

$$PCT\_BIAS = 100 \times \frac{\sum_1^n obs_i - sim_i}{\sum_1^n obs_i} \quad (5-14)$$

where  $n$  is the number of the observation,  $obs_i$  and the  $sim_i$  are the  $i$ th simulated and observed values, respectively. A negative  $PCT\_BIAS$  means the model underestimates the streamflow.

Besides directly comparing the observed and simulated streamflow, the calibrated Raven and Raven\_Robin\_3PG model was also evaluated by two hydrological signatures: the annual summer runoff ratio difference and with the Budyko framework (Hampton & Basu, 2022).

The annual summer runoff ratio difference is the difference between the annual summer runoff ratio of the harvest ( $RO_{harvest}$ ) and control ( $RO_{control}$ ) catchment. By comparing the difference between the harvest and control catchment in the pre- and post-harvest periods, this signature excludes the impacts of climate variations. It can demonstrate the impact of forest harvest management on streamflow. The annual summer runoff ratio is calculated by:

$$RO = \frac{Q_{summer}}{P_{summer}} \quad (5-15)$$

where the  $Q_{summer}$  and  $P_{summer}$  are the total streamflow in [mm] during the summer period (July, August, and September) and precipitation [mm] of harvest or control catchment.

Hampton & Basu, (2022) demonstrate that the Budyko-based approach can be used to quantify post-forest-fire streamflow responses. Thus, the method in Hampton & Basu, (2022) was followed to compare the observations and the model simulations in Budyko-space. The Budyko-space is defined as the relationship between the evaporative index (EI) and aridity index (AI). The EI of each year is the ratio between the yearly actual evapotranspiration (AET) and the total precipitation (P). The AI of each year is the ratio between yearly potential evapotranspiration (PET) and total precipitation. Based on the result of Hampton & Basu, (2022), given the same AI, the observed EI in the harvest catchment during the post-harvest period should be smaller than the EI in the pre-harvest period. Moreover, this difference would decrease with the recovery of the forest. While in the control catchment, the observed AI and EI in the pre-and post-harvest period should share a similar pattern.

The AI and EI from observations, the calibrated Raven model, and the calibrated Raven\_Robin\_3PG model at each catchment were compared. To reduce the impact of the watershed storage, the three-year moving average EI and AI were used to construct Budyko-space. For example, the EI of 2000 is calculated using averaged yearly AET and P in 2000, 2001, and 2002. The same annual P and PET

values were used to calculate the AI of observations, the calibrated Raven, and the calibrated Raven\_Robin\_3PG at each catchment. Thus, The AI from observations, the calibrated Raven, and the calibrated Raven\_Robin\_3PG at each catchment are the same. The annual values of the P come from the observations, and the PET comes from the simulated PET of the control catchment using calibrated Raven\_Robin\_3PG. For each catchment, the annual AET of the observation is the difference between observed yearly precipitation (P) and discharge (Q) at the catchment outlet. And the annual AET of the Raven and Raven\_Robin\_3PG is obtained from their simulated results at each catchment.

Following Hampton & Basu, (2022), the yearly AI and EI in the pre-harvest period were used to develop a Fu-type Budyko curve. The distance between EI in the post-harvest period and the developed Fu-type Budyko curve was analyzed. The Fu-type Budyko curve is defined as:

$$EI_i = 1 + AI_i - (1 + (AI_i)^w)^{1/w} \quad (5-16)$$

where the  $w$  is a parameter calibrated to pre-harvest three-year moving average data for *ith* year (time series of  $EI_i$  and  $AI_i$ ) from observations, calibrated Raven, or calibrated Raven\_Robin\_3PG) for each watershed

By comparing the calculated two hydrological signatures between the observations, the calibrated Raven model and Raven\_Robin\_3PG model in the pre- and post-harvest periods, the performance of Raven and Raven\_Robin\_3PG in simulating the impact of forest harvest management on streamflow can be evaluated.

## 5.4 Results and discussion

This section first introduces the selected best-calibrated model of the Raven and Raven\_Robin model from the PA-DDS calibration (section 5.4.1). Section 5.4.2 demonstrates the performance of the best-calibrated model in streamflow prediction, forest growth prediction, and simulating the streamflow response to forest harvest with two hydrological signatures. Finally, section 5.4.3 uses the best calibrated Raven\_Robin to quantify the impact of the forest harvest management and the continued forest regrowth/recovery on the hydrological processes.

#### 5.4.1 Select the best calibration result

This section presents results obtained by: 1) the multi-objective calibration of Raven and 2) two rounds of model calibration of Raven\_Robin. More details about the model calibration setup for both Raven and Raven\_Robin are in section 5.3.6.

After the first round of the Raven\_Robin calibration, the optimized Robin\_3PG forest growth parameters of both undisturbed and regrowth forests were obtained. With this optimized parameter set, the KGE of LAI for control and harvest catchment are 0.8 and 0.69, respectively. The relative mean absolute error (*RMAE*) of stem biomass [kg/ha] for regrowth forest in the harvest catchment and undisturbed forest in the control catchment are 0.05 and 0.03. The *RMAE* of the stocking [number of trees/ha] for regrowth forest in the harvest catchment and undisturbed forest in the control catchment are 0.18 and 0.02, respectively. The calibrated objective function for undisturbed forest  $Obj_V^{UF}$  (Equation (5-11)) and regrowth forest  $Obj_V^{RF}$  (Equation (5-13)) was larger than 0.6.

The second round of the Raven\_Robin model calibration used the optimized Robin\_3PG forest growth parameters of undisturbed and regrowth forests from the first-round model calibration. This round of Raven\_Robin\_3PG model calibration aims to calibrate the hydrological parameters with a multi-objective calibration. The three objectives in this round of the Raven\_Robin model calibration are the averaged KGE of the streamflow at the control and harvest catchment in the summer period (July, August, and September,  $KGE_{Q,s}$ , Equation (5-8)) and the non-summer period ( $KGE_{Q,ns}$ , Equation (5-9)) and the average of  $Obj_V^{UF}$  (Equation (5-11)) and  $Obj_V^{RF}$  (Equation (5-13)). Three independent PA-DDS trials with a 20000 budget in each trial were applied to calibrate the Raven\_Robin model. The average of the  $Obj_V^{UF}$  and the  $Obj_V^{RF}$  from all non-dominated solutions of three PA-DDS trials were larger than 0.6. Thus,  $KGE_{Q,s}$  and  $KGE_{Q,ns}$  were used to select the best solution from all non-dominated solutions of three PA-DDS trials.

The non-dominated solutions, generated from all non-dominated solutions of three PA-DDS trials of the Raven\_Robin and Raven model in the calibration period, are shown in Figure 5-4A. Both Raven and the Raven\_Robin\_3PG models perform similarly in streamflow predictions during the summer and non-summer periods. The select best solutions of the Raven and Raven\_Robin\_3PG model are located in the upper right corner of their Pareto front to balance the trade-off between  $KGE_{Q,s}$ ,  $KGE_{Q,ns}$ .

The performance of the non-dominated solutions and the selected solutions of both models in the model validation period (post forest harvest, 1997 - 2012) is shown in Figure 5-4B. The selected

solution of both models did not provide the best performance in the validation period compared with their other non-dominated solutions. In the validation period, both models did not provide a good simulation of streamflow in the summer period, as the  $KGE_{Q,s}$  from both models are smaller than 0.2. The selected and non-dominated solutions from both models perform similarly in the validation period. In the following section, the selected solution of both models were evaluated with more metrics and explain why the low performance in the summer period from both models were accepted.

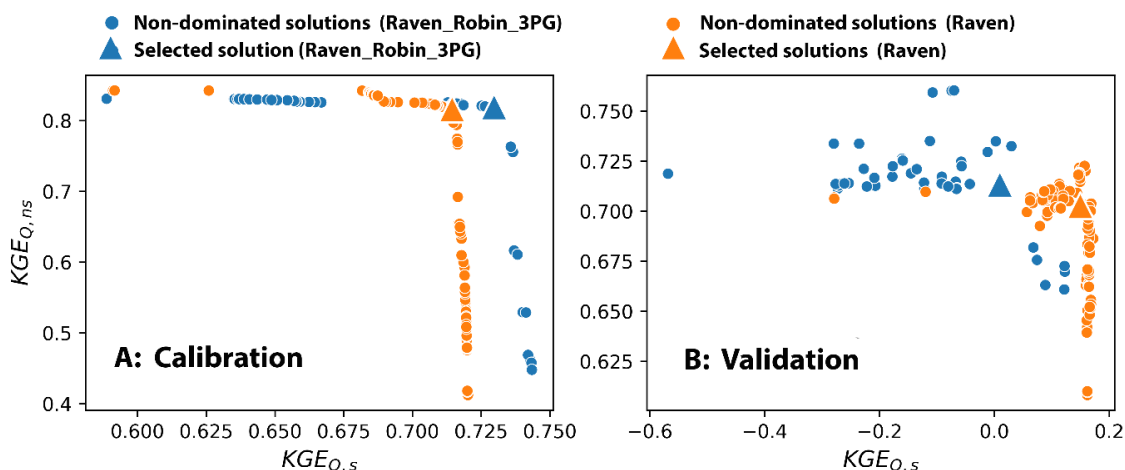


**Figure 5-4.** The performance of the non-dominated and the selected solutions of Raven and Raven\_Robin\_3PG in the calibration period (A) and validation period (B). The non-dominated solutions of both models are generated from combining the non-dominated solutions of three independent multi-objective model calibration trials and then identifying only those solutions that are non-dominated across all trials. The  $KGE_{Q,s}$  (Equation (5-8)) is the KGE of the averaged streamflow performance from harvest and control catchment during the summer period (July, August, and September). The  $KGE_{Q,ns}$  (Equation (5-9)) is the KGE of the averaged streamflow performance from harvest and control catchment during the non-summer period. The model calibration period is from 1984 to 1996 (before forest harvest), and the model validation period is from 1998 to 2012 (after forest harvest).

#### 5.4.2 The performance of the selected Raven and Raven\_Robin\_3PG

In this section, the performance of the selected Raven and Raven\_Robin in streamflow prediction (section 5.4.2.1), forest growth simulation (section 5.4.2.2), and hydrological signatures simulation (section 5.4.2.3) were evaluated.

#### 5.4.2.1 The performance of selected Raven and Raven\_Robin\_3PG in streamflow

Table 1 demonstrates the performance statistics of the selected Raven\_Robin\_3PG and Raven model for streamflow prediction at harvest and control catchment during the calibration and two validation periods. The performance statistics include the percentage of model simulation bias ( $PCT\_BAS$ ) and the KGE of streamflow in the summer period (July, August, and September,  $KGE_{Q,s}$ ), the non-summer period ( $KGE_{Q,ns}$ ), and the full period ( $KGE_{Q,f}$ ). The selected Raven\_Robin\_3PG and Raven provide a reasonable streamflow simulation at both catchments in the calibration period. The  $KGE_{Q,s}$ ,  $KGE_{Q,ns}$ , and  $KGE_{Q,f}$  from both models at both catchments are larger than 0.7. Moreover, the  $PCT\_BAS$  of streamflow at both catchments from both models is within 5% in the model calibration period.

The model performance of both models at both catchments decreases in the entire validation period (1998 - 2012). In the control catchment, the  $KGE_{Q,s}$  of both models are smaller than zero in the entire validation period. While in the harvest catchment, the Raven model provides a better  $KGE_{Q,s}$  and a larger  $PCT\_BAS$  error than the Raven\_Robin\_3PG. The  $KGE_{Q,f}$  from both models at both catchments is larger than 0.6, and the  $PCT\_BAS$  is smaller than 20% in this period. The performance of both models is acceptable considering the potential streamflow measurement errors at such catchments ( $\sim 0.05 \text{ km}^2$ ) and with such small streamflow (the mean daily observed streamflow is around  $\sim 0.0008 \text{ m}^3/\text{s}$ ).

When comparing the model performance in streamflow simulation from 1998 to 2002 (five years post forest harvest), Raven\_Robin\_3PG provides a better streamflow simulation than Raven in all the evaluation metrics (Table 5-1) at the forest harvest catchment. The  $KGE_{Q,s}$  of both models in the control catchment are smaller than zero. The simulated and the hydrograph from both models at both catchments during the first two years (1998-1999) and the second two years (2000-2002) after forest harvest are shown in Figures 5-5 and 5-6, respectively. Both models provide a similar hydrograph (Figures 5-5 and 5-6) in the control catchment. However, at the forest harvest catchment, the simulated summer (July, August, and September) streamflow from the Raven\_Robin\_3PG is closer to the measurements (Figures 5-5 and 5-6).

The drier and warmer climate (Buttle et al., 2019; Leach et al., 2020) transition from the pre-harvest to post-harvest period may explain the decrease of the  $KGE_{Q,s}$  from both models in the control catchment (Table 5-1). Both models do not capture the response of the hydrological system to such climate variations between the calibration and validation period. Moreover, the forest harvest management trend towards increasing the runoff in the forest harvest catchment, while the drier and

warmer climate trend decreases the runoff in the forest harvest catchment. Thus, the previous empirical study suggests that the drier and warmer climate may diminish the impact of the forest harvest on the hydrological system (Buttle et al., 2019; Leach et al., 2020). This may explain why the  $KGE_{Q,s}$  from the Raven, which do not represent the response of the hydrological system to both drivers, in the harvest catchment is still larger than 0.6 in the validation period (1998-2012).

**Table 5-1.** The performance statistics of the Raven\_Robin\_3PG and Raven in streamflow prediction at the calibration and validation periods. The  $PCT\_BIAS$  is the percent bias between the simulated and the observed streamflow. The negative  $PCT\_BIAS$  means the model underestimates the streamflow. The  $KGE_{Q,s}$ , the  $KGE_{Q,ns}$ , and  $KGE_{Q,f}$ , are the  $KGE$  of the streamflow during the summer (July, August, and September), the non-summer, and the full period of each year.

Type	From	To	Catchment	PCT_BIAS		KGE <sub>Q,f</sub>		KGE <sub>Q,s</sub>		KGE <sub>Q,ns</sub>	
				Raven_Robin_3PG	Raven	Raven_Robin_3PG	Raven	Raven_Robin_3PG	Raven	Raven_Robin_3PG	Raven
Calibration	1984	1997	Harvest (C31)	-1.7%	-5.8%	0.82	0.82	0.70	0.72	0.81	0.81
			Control (C32)	5%	2.5%	0.83	0.83	0.75	0.70	0.82	0.81
Validation	1998	2012	Harvest (C31)	<b>-1.13%</b>	<b>-20%</b>	0.69	0.61	<b>0.11</b>	<b>0.63</b>	0.66	0.60
			Control (C32)	12%	12%	0.75	0.78	<b>-0.09</b>	<b>-0.33</b>	0.76	0.80
Validation	1998	2002	Harvest (C31)	<b>0.021%</b>	<b>-35%</b>	0.76	0.54	<b>0.41</b>	<b>0.29</b>	0.74	0.56
			Control (C32)	-4.3%	-2.3%	0.70	0.79	<b>-0.13</b>	<b>-0.81</b>	0.68	0.78

The forest harvest management in the first five years of the post-harvest period (1998-2002) has a dominant impact on the hydrological system of the forest harvest catchment. Because of this, the Raven\_Robin\_3PG, which represents the forest harvest management and forest regrowth, provides better performance than the Raven in streamflow simulation in the forest harvest catchment during this period. However, the forest harvest's impact decreases with the forest's recovery in the forest harvest catchment. And then, the impact of the forest harvest and climate variations on the hydrological system of the forest harvest catchment may cancel out after more than five years of the forest harvest. This

might explain why the Raven model provides a better KGE of streamflow in the full validation period (1998-2012) than the Raven\_Robin\_3PG model.

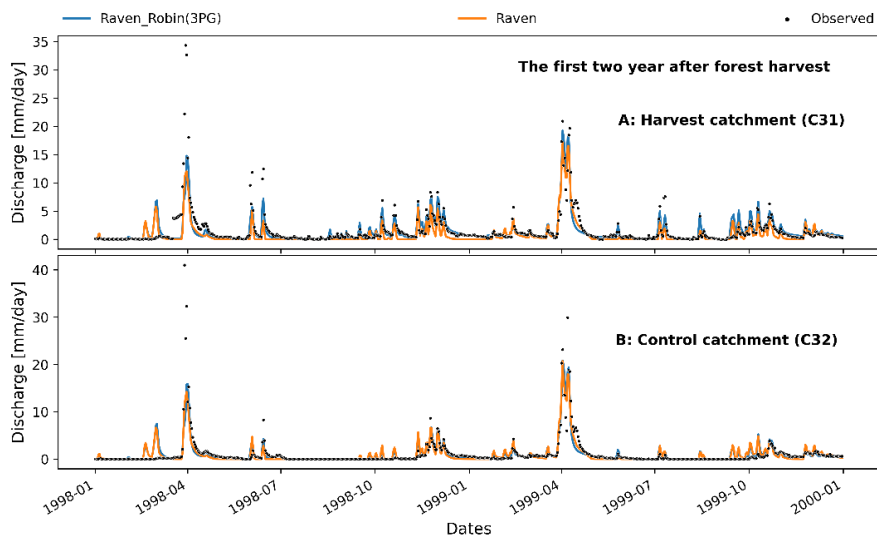


**Figure 5-5.** The observed and simulated hydrograph from the selected Raven\_Robin\_3PG and Raven calibration solutions at both control and harvest catchment during the first two years of the forest harvest. The forest harvest happened in the year 1997.

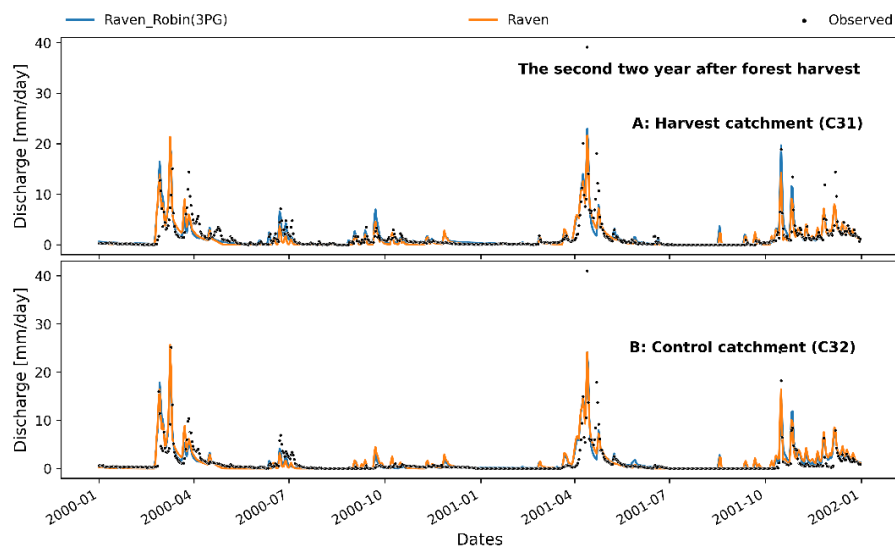


**Figure 5-6.** The observed and simulated hydrograph from the selected Raven\_Robin\_3PG and Raven at both control and harvest catchment during the second two years of the forest harvest. The forest harvest happened in the year 1997.

In summary, the selected Raven and Raven\_Robin\_3PG can provide reasonable streamflow simulation in both calibration and validation periods. The significant decrease of the  $KGE_{Q,s}$  from both models at the control catchment in the validation period might suggest that the impact of a drier and warmer climate on the hydrological system is not well accounted for in both models. The Raven\_Robin\_3PG provides better streamflow simulation in the first five years of the post forest harvest period.

#### 5.4.2.2 The calibrated Raven\_Robin\_3PG performance for forest growth

Before evaluating the two models with hydrological signatures, the selected Raven\_Robin\_3PG model performance in the forest growth simulation is evaluated in this section.

The  $KGE$  of the LAI from the selected Raven\_Robin\_3PG for the forests in the forest harvest and control catchments during the entire simulation period (1985-2012) are 0.80 and 0.69, respectively. The Landsat-derived LAI observations and the Raven\_Robin\_3PG simulated LAI at both catchments are shown in Figure 5-7. The Raven\_Robin\_3PG provides a reasonable LAI simulation at the control and forest harvest catchment (Figure 5-7), and the increments of the LAI in the forest harvest catchment during the post forest harvest period are reasonably simulated by the Raven\_Robin\_3PG. One of the limitations of simulated LAI from the selected Raven\_Robin\_3PG is that the LAI interannual dynamic is not well captured. The interannual dynamic of Landsat-derived LAI may come from the response of the forest to environmental stresses such as precipitation and temperature. However, the observed annual mean temperature and total precipitation failed to explain the Landsat LAI interannual dynamic. Moreover, modelling the response of the LAI to environmental stresses is not the focus of this study. Thus, the Raven\_Robin\_3PG simulated LAI at both catchments is acceptable for this study.

The relative mean absolute error (RMAE, Equation (5-12)) of the stocking (number of trees/ha) is 0.18 and 0.02 for the regrowth forest in the harvest catchment and undisturbed forest in the control catchment, respectively. The RMAE of the stem biomass was 0.06 and 0.04 for the regrowth and undisturbed forest, respectively. The RMAE of the basal area was 0.08 and 0.03 for the regrowth and undisturbed forest, respectively. The simulated and the observed stocking, stem biomass, and basal area of the regrowth and undisturbed forest are shown in Figures A5-1, A5-2, and A5-3, respectively. The selected Raven\_Robin\_3PG could provide a reasonable simulation of the forest stocking, stem biomass, and the basal area in control and the forest harvest catchment.

The observed and simulated forest development in the control and forest harvest catchment are shown in Figure 5-8. In the pre-forest harvest period (before 1997), the simulated forest development in both catchments is on the right trajectory shown in Figure 5-8. In this period, the simulated forest stocking at both catchments decreases due to age-induced forest mortality. And the simulated forest stem biomass per tree increases due to the decrease in the stocking [number of trees/ha] (Figure A5-1) and increase in stem biomass [kg/ha] (Figure A5-2). In the post-harvest period, the forest development of the control catchment continues with the right trajectory shown in Figure 5-8. However, the forest development in the forest harvest catchment is different. First, after the forest harvest management, which removes the trees with DBH larger than 10 cm, the initial condition of the forest in the forest harvest catchment is the move to the left of Figure 5-8. And then, the forest in the forest harvest catchment starts to reproduce new trees to occupy the open spaces in the catchment. The stocking [the number of trees/ha] of the regrowth forest increases. Although the forest stem biomass[kg/ha] accumulates each year (Figure A5-2), the stocking's increment is more significant, making the stem biomass per tree of the regrowth forest decrease (Figure 5-8).

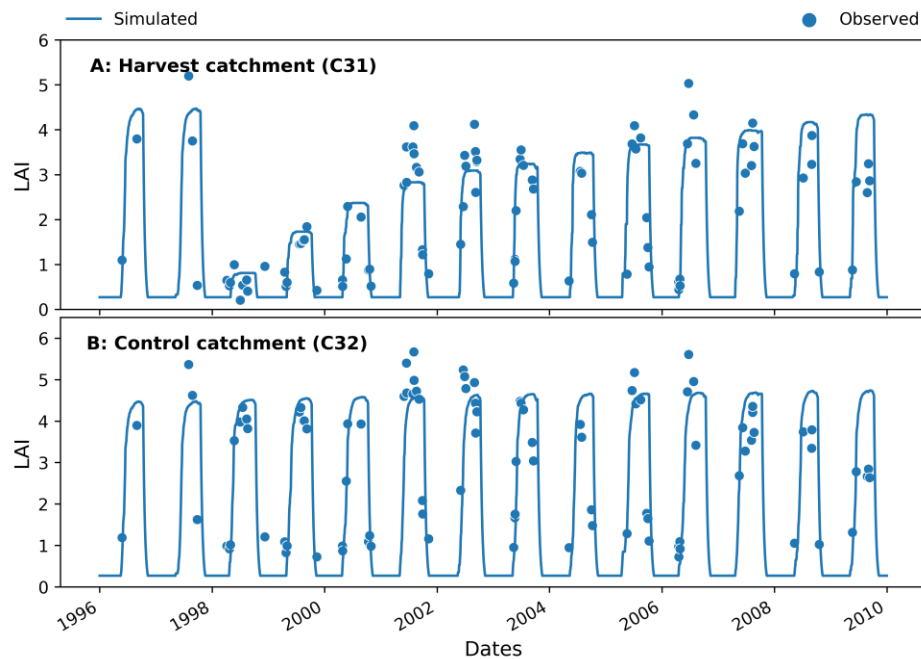


**Figure 5-7.** The Landsat-derived LAI observations and the Raven\_Robin\_3PG simulated LAI at harvest(A) and control(B) catchments.

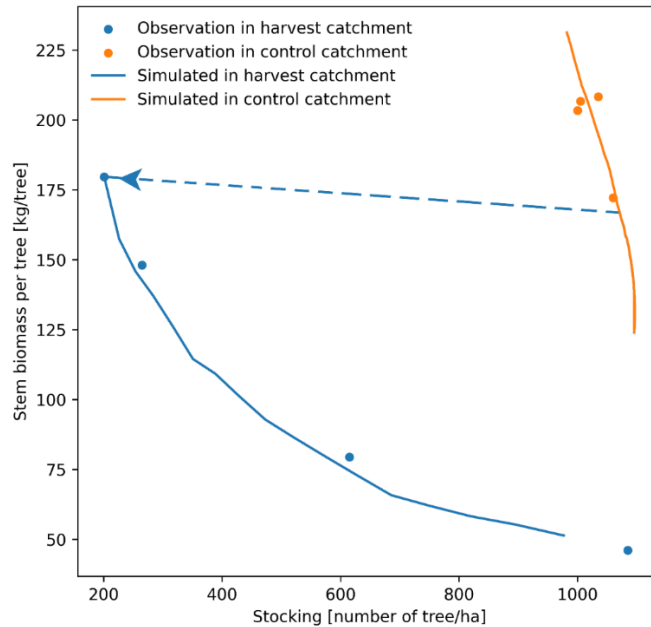


**Figure 5-8.** The simulated and observed forest development in the control and forest harvest catchment. The dashed arrow represents the forest harvest event in the forest harvest catchment. In the pre-harvest period, the simulated forest growth in control and harvest catchment overlap with each other. The forest development in this period is from the lower right to the upper right. The forest harvest management in the harvest catchment reduces the forest density. Thus, the forest development in the forest harvest catchment at the beginning of the post-harvest period moves to the upper left of the plot (the dashed arrow).

In summary, the selected Raven\_Robin\_3PG provides a reasonable forest growth simulation. However, the performance of the Robin\_3PG in simulating the response of the forest growth to the environmental stresses and the long-term forest development still warrants further study.

#### 5.4.2.3 Compared with the observed hydrological signatures

This section evaluates the selected Raven and Raven\_Robin\_3PG models with two hydrological signatures: the annual summer runoff ratio difference and the Budyko framework. The detailed description of methods for calculating these two observed hydrological signatures is in section 5.3.6.2.

The annual summer runoff differences calculated from observation, the selected Raven, and Raven\_Robin\_3PG are shown in Figure 5-9. Before the forest harvest event in 1997, the annual summer runoff differences from observation and both models were close to zero, indicating that both models

could successfully describe the observed annual summer runoff differences between two catchments in this period. The large observed runoff ratio difference in 1986 and 1993 are outliers.

After the forest harvest event in 1997, the observed and the simulated annual summer runoff difference from Raven\_Robin\_3PG is first increased to 0.2 in 1998/1999 and then decreased to zero after around seven years after the forest harvest. The positive increment of the annual summer runoff difference between the harvest and control catchment indicates that more watershed discharge is generated in the summertime due to the forest harvest management in the harvest catchment. With the forest recovery in the following years, the response of the hydrological system to the forest harvest is diminished. While, as expected, the annual summer runoff difference from the Raven model did not demonstrate the impact of forest harvest management on the hydrological systems.

In summary, both models could successfully describe the observed annual summer runoff differences in the pre-harvest period. But only the Raven\_Robin\_3PG reasonably demonstrates the impact of the forest harvest and recovery on the annual summer runoff difference.

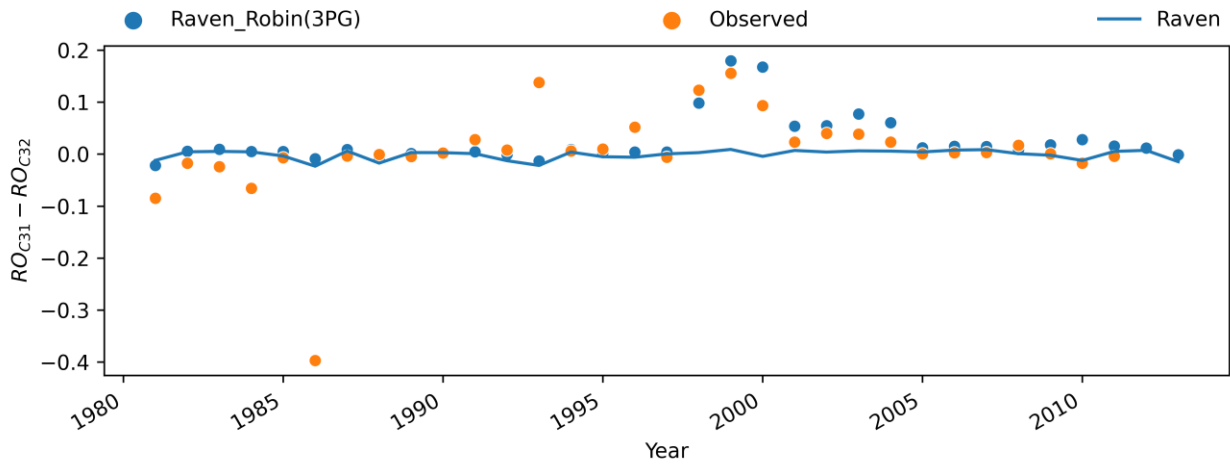


**Figure 5-9.** The annual summer runoff ratio difference calculated from observations and the selected Raven and Raven\_Robin\_3PG models. The difference is between the annual summer (July, August, and September) runoff ratio of the harvest ( $RO_{harvest}$ ) and control ( $RO_{control}$ ) catchment.

The EI and AI of each catchment at the pre-and post-harvest period from observation, Raven, and Raven\_Robin\_3PG are shown in Figure 5-10. A Fu-type Budyko curve was developed using AI and EI in the pre-harvest period. In the post forest harvest period, substantial vertical deviations between EI and the Fu-type curve were apparent in the observations (Figure 5-10A) and the Raven\_Robin\_3PG

(Figure 5-10B) in the harvest catchment. It represents that the forest harvest management reduced the actual evapotranspiration and increased the runoff compared to the same AI in the pre-harvest condition. Moreover, with the recovery of the forest after forest harvest, the EI from the observation (Figure 5-10A) and the Raven\_Robin\_3PG (Figure 5-10B) gradually goes back to the Fu-type curve developed in the pre-harvest period. However, the EI from Raven does not demonstrate such vertical deviations in forest harvest catchment. In the control catchment during the post-harvest period, the EI from observation, Raven, and Raven\_Robin\_3PG is close to the Fu-type curve developed in the pre-harvest period.

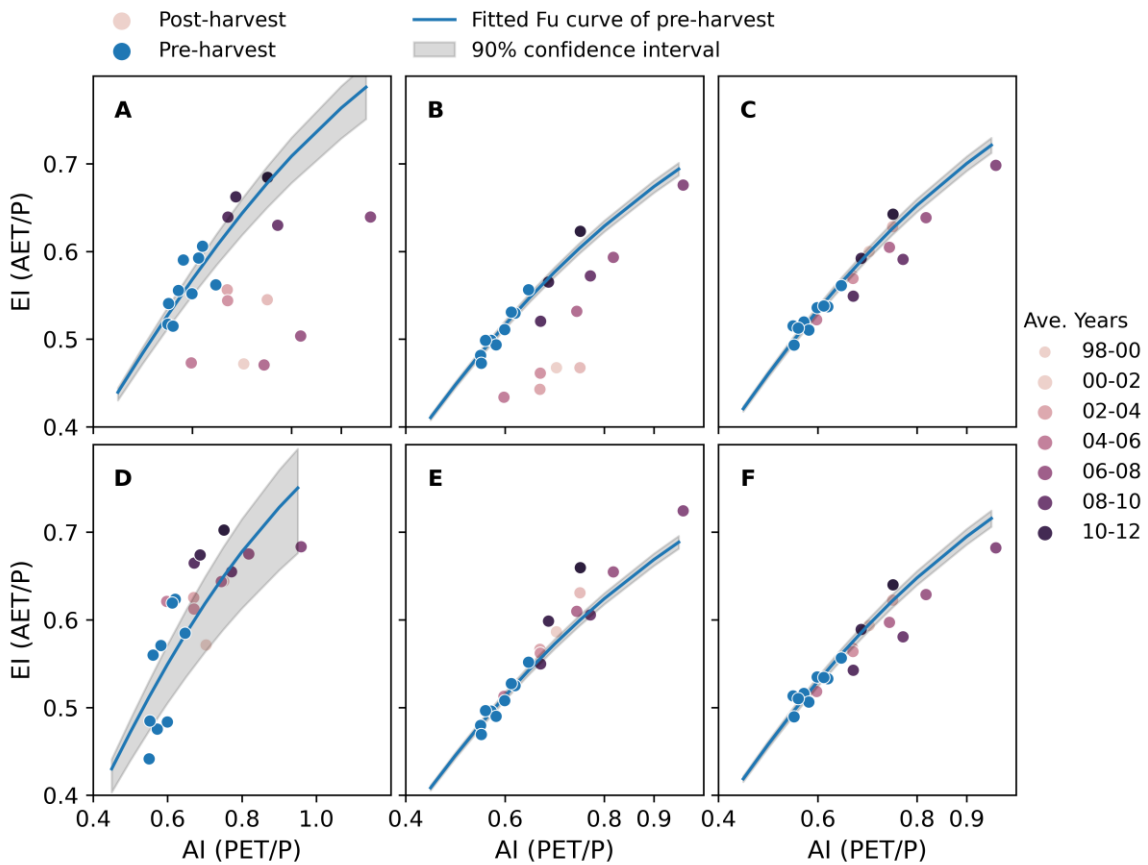


**Figure 5-10.** Time series of 3-year moving averaged evaporative index (EI) versus aridity index (AI) for the forest harvest catchment (A, B, and C) and the control catchment (D, E, F) in the pre- and post-harvest period. The EI and AI is calculated from observations (A and D), the selected Raven\_Robin (B and E), and the selected Raven (C and F). The Fu-type Budyko curve is developed using 3-year moving averaged EI and AI in the pre-harvest period.

In summary, the Raven\_Robin\_3PG can reasonably simulate the response of the EI to the forest harvest and continued forest recovery processes.

#### **5.4.3 The impact of the forest harvest and forest regrowth on the hydrological processes**

After evaluating the selected Raven\_Robin\_3PG model, this section assesses the selected Raven\_Robin\_3PG model to quantify the impact of the forest harvest and forest regrowth on various hydrological processes.

Figure 5-11 shows the Raven\_Robin simulated yearly averaged fluxes during the summer (July, August, and September) at the harvest catchment and the control catchment. The change of the difference between simulated fluxes at harvest and control catchment at pre-and post-harvest period demonstrates the impact of the forest harvest on each flux. In the preharvest period, except for the baseflow from the first soil layer, the simulated fluxes at harvest and control catchment are almost the same. And in the post-harvest period, the forest harvest management in the harvest catchment reduced the canopy interception and increased the infiltration and baseflow from all soil layers (Figure 5-11). The forest management reduced the potential evapotranspiration rate of the harvest catchment, which lead to a decrease in the actual evapotranspiration. The differences between the simulated fluxes in the control and the forest harvest catchment gradually return to the pre-harvest level as the recovery of the forest in the forest harvest catchment.

Based on the assumption of Raven\_Robin\_3PG (section 5.3.5.2), the forest harvest management directly decreased the canopy interception (Figure 5-11A) and potential evapotranspiration (Figure 5-10C). Their decrease changed the other simulated fluxes (Figures 5-11B and D-H). In this watershed, the impact of forest harvest on potential evapotranspiration is more significant. The maximum decrease of potential and actual evapotranspiration are 2.7 and 1.6 mm/day (in July, August, and September), respectively.

The runoff components (Figure 5-11E-H) respond differently to the decreasing canopy interception and potential evapotranspiration. Because of the dry summer climate of the watershed, The response of the quick runoff to the decrease of the canopy interception was not observed. This highlights that the climate factor can vary and diminish the impact of the forest harvest on some hydrological processes.

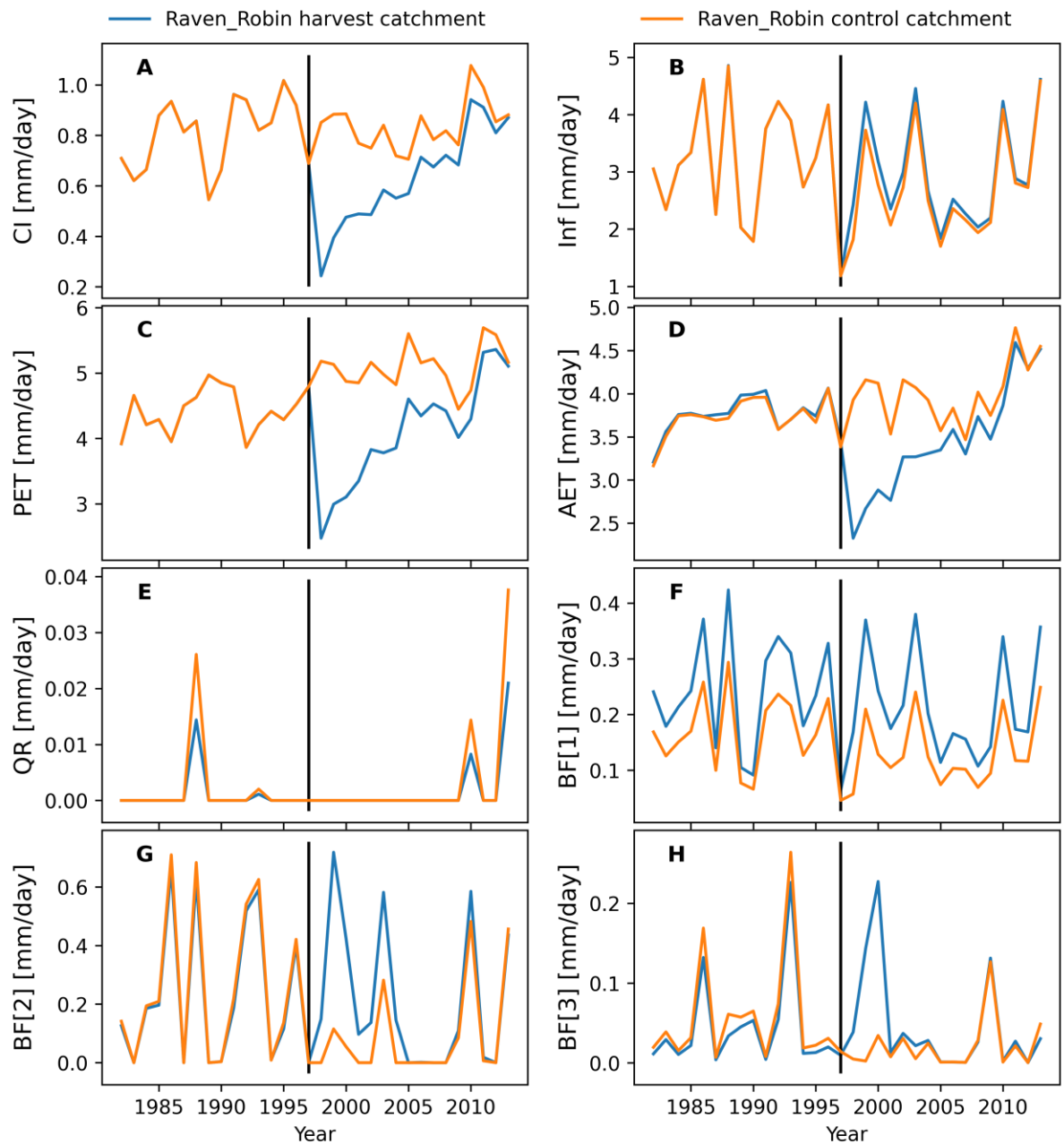


Figure 5-11. The Raven\_Robin simulated yearly averaged fluxes during the summer (July, August, and September) at the harvest catchment and the control catchment. The CI represents the canopy interception. The Inf represents the infiltration. The AET represents the actual evapotranspiration. The PET represents potential evapotranspiration. The QR represents the quick runoff. The BF[i] represents the baseflow from the i (i = 1, 2, 3) soil layer. The simulated daily fluxes in July, August, and September

are used to calculate the yearly average value. The vertical black line represents the year when forest harvest management happened.

Compared to the baseflow at the first (Figure 5-10F) and third soil layer (Figure 5-11H), the baseflow in the second layer (Figure 5-11G) increased more significantly. This is because the root fraction in the second soil layer of the selected Raven\_Robin\_3PG model is larger than the root fraction in the other two layers. The root fraction determines the amount of potential evapotranspiration allocated to each soil layer in the Raven\_Robin\_3PG (Equation (5-7)). Thus, the reduction of the potential and actual evapotranspiration (Figures 5-11C and D) has more impact on the simulated baseflow of the second soil layer. Correctly representing the response of the runoff component to the forest disturbance is essential because it directly impacts the watershed nutrient and sediment transport. This analysis highlights the importance of correctly representing the soil evaporation processes at each soil layer to correctly simulate the response of runoff components to forest disturbance.

In summary, the selected Raven\_Robin\_3PG model can quantify the response of the hydrological processes to forest harvest management. This study also highlights how climate and soil/root evaporation may change the response of the hydrological processes to the forest harvest/disturbance. At the same time, the intention of this study is not to prove that the selected Raven\_Robin\_3PG provides the correct result in simulating the response of hydrological processes in the Turkey Lake watershed. The main point of this section is to demonstrate that Raven\_Robin\_3PG can simulate these responses. It can provide the correct answer when more observed data (i.e., isotope and geochemistry measurements) is available.

#### **5.4.4 Limitations and future work**

This study demonstrates the ability of the Robin\_3PG model to simulate short-term forest growth processes. However, because many changes were made to the original 3PG forest growth model, the ability of Robin\_3PG for long-term forest growth modelling still requires testing at a longer-term forest growth research site.

The impact of the climate variation in the post forest harvest period on the hydrological system is not captured by either the Raven and Raven\_Robin\_3PG model. This might be due to various reasons. For example, it may be caused by improperly representing the potential evapotranspiration in a warmer climate. It may also be due to the non-stationary hydrological behavior from the adaptation of the vegetation to the warmer climate. However, these research questions: how to properly detect the

response of the hydrological system to the climate variations, how to attribute these responses to different hydrological/vegetation processes, and how to correctly model these responses, are a future research topic.

## **5.5 Conclusions**

In this study, a vegetation growth library framework (Robin), which can be easily coupled to any hydrological or land-surface model to add the functionality of crop and vegetation growth, was developed. The monthly 3PG forest growth model was adapted into the Robin library by: 1) changing the timestep of the 3PG model to daily, 2) adding a forest phenology module to the 3PG forest growth model, and 3) adding a forest reproduction module to the 3PG forest growth model. Then, the 3PG model in Robin was coupled with the Raven hydrological model (Raven\_Robin\_3PG). The coupled model was applied to a paired-catchment forest harvesting experiment conducted at the extensively-monitored Turkey Lakes Watershed north of Sault Ste. Marie, Ontario, Canada.

The coupled model is calibrated and validated by comparing it with the streamflow observations, forest allometric measurements, and two hydrological signatures. The result suggests that the Raven\_Robin\_3PG model can reasonably simulate the response of various hydrological processes to the forest harvest management and the forest's growth and regrowth in the control and forest harvest catchments. The analysis of this study also highlights that the climate factor and the evapotranspiration process in each soil layer significantly impacts the response of the runoff components to the forest disturbance.

This study demonstrates the utility of Raven\_Robin\_3PG to simulate/quantify the response of the hydrological processes to the forest disturbances, such as forest harvest management or fire.

## **Chapter 6**

### **Conclusions and future work**

This thesis focuses on improving hydrological model structures to make them more realistic and thus more appropriate tools to simulate past and future hydrological behaviors. Specific hydrological model structural improvements focus on the explicit representation of 1) lake representation in complex lake networks and 2) forest growth/disturbance representation in forest headwater catchments. The following sections outline the conclusions of each chapter.

Chapter 2 presents a proof-of-concept study. The twelve publicly available pan-Canadian lake-river routing networks were developed. And a case study using the Raven hydrological modelling framework to simulate the hydrologic routing process with tens of thousands of lakes in the Hudson Bay watershed was developed.

Chapter 2 conclusions are:

- This is the first routing network available that explicitly and in a hydrologically consistent way represents lakes within drainage networks for the domain of Canada. The routing networks provide the necessary routing network topology and network attributes to enable vector-based hydrological routing anywhere in Canada. This showed that it is feasible to develop a large-scale (Pan-Canadian) vector-based lake-river routing product that incorporates hundreds of thousands of lakes in routing networks.
- It is feasible to simulate hydrologic routing across a massive region (Hudson Bay drainage basin totaling ~3,860,000 km<sup>2</sup>) with the Raven hydrological modelling framework software.
- The case study simulation results demonstrate that there are substantial benefits in terms of improving uncalibrated simulated hydrographs associated with explicitly representing and then simulating numerous, including modest-sized, lakes.

The primary future work to build upon Chapter 2 findings involves using local high-resolution hydrologically conditioned DEM to develop lake-river routing products for Canada.

Chapter 3 continues to improve the lake-river routing network approaches developed in Chapter 2. An open-source GIS toolbox, BasinMaker, was released to delineate and post-process the lake-river routing networks.

Chapter 3 conclusions are:

- An open-source GIS toolbox (BasinMaker) was developed that can automatically and efficiently build vector-based hydrological lake-river routing networks, including flexible discretization choices to explicitly represent an arbitrary number of lakes.
- BasinMaker was used to delineate the North American Lake-River Routing Product v2.1 (available at <http://hydrology.uwaterloo.ca/basinmaker/index.html>) and the Ontario Lake-River Routing Product v1 (available at <https://lake-river-routing-products-uwaterloo.hub.arcgis.com>).
- Two novel post-processing functions in BasinMaker are a) Simplify the lake-river routing network by decreasing the resolution of the stream network and thus increasing the size of subbasins and b) Simplify the lake-river routing network by removing the lakes from it. These post-processing tools enable users to customize the large-scale routing networks already delineated by Basin Maker without the need for complex terrain analysis using the DEM.

The future work to build upon Chapter 3 findings includes:

- Improving BasinMaker to handle the non-contributing areas present in the source DEM correctly. Such noncontributing areas are prevalent, for example, in the prairie pothole region of North America.
- Producing a new version of the Ontario routing product that includes wetlands explicitly. This likely requires an update to BasinMaker software.
- Developing a Canadian semi-distributed hydrological dataset for large-sample studies, including climate forcings, high-resolution lake-river routing networks, and streamflow observations. This would involve a standardized procedure on Google Colab to build semi-distributed hydrological models with different resolutions (i.e., different subbasin/lake representations and different HRU representations) for catchments in the dataset. The semi-distributed hydrological models built with this procedure can be easily reproduced and transferred.

Chapter 4 investigates the impacts of ignoring lakes on the simulated runoff components and model performance at internal watershed gauges by comparing the simulated results from two model structures (with and without lakes) at two Canadian watersheds (Turkey Lake and Petawawa).

Moreover, the value of the lake level measurements in the ungauged and gauged watersheds was evaluated using measurements from fifteen lake level gauges in the Petawawa watershed. Furthermore, the assumptions used to parameterize the outflow structure of lakes was evaluated using the calibrated lake crest width parameter of gauged lakes in the Petawawa watershed.

Chapter 4 conclusions are:

- Compared to the semi-distributed model ignoring lakes, the model representing lakes substantially increases the model performance at internal streamflow/channel water-level gauges with minimal decreases in the performance at the watershed outlet streamflow gauge.
- Because of the model compensation behavior, ignoring lakes in the model has significant impacts on the simulated runoff components. Namely, ignoring lakes in the model will significantly reduce quick runoff, increase the infiltration, and increase the baseflow from the soil storage, relative to these simulated quantities in the model including lakes.
- Not modelling lakes will also decrease the model's flexibility/uncertainty in the simulated runoff components of each flow pathway.
- In a watershed gauged at the outlet, calibrating to the additional lake level measurements in the Petawawa watershed can improve the streamflow simulation at the outlet.
- When considering the Petawawa as ungauged at the outlet, the hydrological model calibrating to fifteen lake level gauges can provide reasonable streamflow simulation at the Petawawa watershed outlet. However, when calibrating to only one large lake level gauge, the hydrological model failed to provide reasonable watershed outlet streamflow simulations. This finding is noteworthy given the upcoming SWOT satellite mission that will monitor lake levels of moderate-sized lakes from space.
- The calibrated lake crest width parameter of fifteen gauged lakes has a significant linear relationship with the lake's drainage area in log-log space, suggesting the assumption used in the literature and in the developed routing products to parametrize the outflow structure of lakes is reasonable.

The future work to build upon Chapter 4 findings includes:

- Evaluate the hydrological model's compensation behavior using different lake simplification approaches to answer questions like what is the best lake simplification strategies. Evaluate how local climate and lake characteristics impact the hydrological model's compensation behavior.
- Investigate the hydrological model's compensation behavior with other model simplification strategies or when we use wrong process equations.
- How do we evaluate two model structures that provide similar streamflow simulation results at the watershed outlet? Evaluate if the model's flexibility of the simulated runoff components can be used as an additional model performance metric for model structure comparisons.
- What is the impact of the prismatic lake assumption on the model calibration result? How to parameterize the lake geometries. Assess alternative assumptions available from the GOLBathry study.

Chapter 5 develops a vegetation growth library framework (Robin), which can be easily coupled to any hydrological or land-surface model to add the functionality of crop and vegetation growth functionality. Moreover, the monthly 3PG forest growth model was adapted into the Robin framework. Then the 3PG model in Robin was coupled with the Raven hydrological modelling framework (Raven\_Robin\_3PG) and applied it to a paired-catchment forest harvesting experiment conducted at the extensively-monitored Turkey Lakes Watershed.

Chapter 5 conclusions are:

- The Raven\_Robin\_3PG model reasonably simulates the hydrological processes' response to the forest harvest management and the forest's growth and regrowth in the control and forest harvest catchments over a period of fifteen years after harvest
- The climate factor and the evapotranspiration process in each soil layer significantly impact the response of the runoff components to the forest disturbance.
- The developed Robin\_3PG forest growth module is useful for forest management and investigating the impact of forest disturbance on hydrological processes.

The future work to build upon Chapter 5 findings includes:

- Adopt the 3PG-mix mixed forest growth model (Forrester & Tang, 2016) into the Robin vegetation growth library to simulate the forest growth of forests of different ages and species in one HRU.
- Carefully evaluate the response of the hydrological system to climate variations and attribute these responses to different hydrological/vegetation processes. Moreover, better model these responses in hydrological models.
- Adapt the Raven\_Robin\_3PG model to more realistically simulate the impact of the forest disturbance on snow accumulation and snowmelt processes.

## References

- Alavi, N., Bélair, S., Fortin, V., Zhang, S., Husain, S. Z., Carrera, M. L., & Abrahamowicz, M. (2016). Warm season evaluation of soil moisture prediction in the Soil, Vegetation, and Snow (SVS) scheme. *Journal of Hydrometeorology*, *17*(8). <https://doi.org/10.1175/JHM-D-15-0189.1>
- Almeida, A. C., & Sands, P. J. (2016). Improving the ability of 3-PG to model the water balance of forest plantations in contrasting environments. *Ecohydrology*, *9*(4), 610–630. <https://doi.org/10.1002/eco.1661>
- Almeida, A. C., Landsberg, J. J., & Sands, P. J. (2004). Parameterisation of 3-PG model for fast-growing *Eucalyptus grandis* plantations. *Forest Ecology and Management*, *193*(1–2), 179–195. <https://doi.org/10.1016/J.FORECO.2004.01.029>
- Almeida, A. C., Smethurst, P. J., Siggins, A., Cavalcante, R. B. L., & Borges, N. (2016). Quantifying the effects of *Eucalyptus* plantations and management on water resources at plot and catchment scales. *Hydrological Processes*, *30*(25), 4687–4703. <https://doi.org/10.1002/hyp.10992>
- Alvarez-Garreton, C., Ryu, D., Western, A. W., Crow, W. T., Su, C. H., & Robertson, D. R. (2016). Dual assimilation of satellite soil moisture to improve streamflow prediction in data-scarce catchments. *Water Resources Research*, *52*(7). <https://doi.org/10.1002/2015WR018429>
- Amorocho, J., & Espildora, B. (1973). Entropy in the assessment of uncertainty in hydrologic systems and models. *Water Resources Research*, *9*(6). <https://doi.org/10.1029/WR009i006p01511>
- Andreadis, K. M., Schumann, G. J.-P., & Pavelsky, T. (2013). A simple global river bankfull width and depth database. *Water Resources Research*, *49*(10), 7164–7168. <https://doi.org/10.1002/wrcr.20440>
- Arnold, J. G., Moriasi, D. N., Gassman, P. W., Abbaspour, K. C., White, M. J., Srinivasan, R., et al. (2012). SWAT: Model use, calibration, and validation. *Transactions of the ASABE*, *55*(4).
- Arora, V. K., & Boer, G. J. (2005). A parameterization of leaf phenology for the terrestrial ecosystem component of climate models. *Global Change Biology*, *11*(1), 39–59. <https://doi.org/10.1111/J.1365-2486.2004.00890.X>
- Asadzadeh, M., & Tolson, B. A. (2009). A new multi-objective algorithm, pareto archived DDS. In *Proceedings of the 11th annual conference companion on Genetic and evolutionary*

*computation conference - GECCO '09* (p. 1963). New York, New York, USA: ACM Press.  
<https://doi.org/10.1145/1570256.1570259>

- Baroni, G., Schalge, B., Rakovec, O., Kumar, R., Schüler, L., Samaniego, L., et al. (2019). A Comprehensive Distributed Hydrological Modeling Intercomparison to Support Process Representation and Data Collection Strategies. *Water Resources Research*, *55*(2), 990–1010.  
<https://doi.org/10.1029/2018WR023941>
- Bart, R. R., Ray, R. L., Conklin, M. H., Safeeq, M., Saksa, P. C., Tague, C. L., & Bales, R. C. (2021). Assessing the effects of forest biomass reductions on forest health and streamflow. *Hydrological Processes*, *35*(3), e14114. <https://doi.org/10.1002/hyp.14114>
- Basso, M., Vieira, D. C. S., Tiago, J., Ramos, B., Mateus, M., & Superior, I. (2019). Assessing the adequacy of SWAT model to simulate postfire effects on the watershed hydrological regime and water quality. <https://doi.org/10.1002/ldr.3476>
- Bennett, A., Nijssen, B., Ou, G., Clark, M., & Nearing, G. (2019). Quantifying Process Connectivity With Transfer Entropy in Hydrologic Models. *Water Resources Research*, *55*(6), 4613–4629.  
<https://doi.org/10.1029/2018WR024555>
- Bennett, K. E., Urrego Blanco, J. R., Jonko, A., Bohn, T. J., Atchley, A. L., Urban, N. M., & Middleton, R. S. (2018). Global Sensitivity of Simulated Water Balance Indicators Under Future Climate Change in the Colorado Basin. *Water Resources Research*, *54*(1).  
<https://doi.org/10.1002/2017WR020471>
- Bernier, N. B., Bélair, S., Bilodeau, B., & Tong, L. (2011). Near-Surface and Land Surface Forecast System of the Vancouver 2010 Winter Olympic and Paralympic Games. *Journal of Hydrometeorology*, *12*(4), 508–530. <https://doi.org/10.1175/2011JHM1250.1>
- Boisramé, G. F. S., Thompson, S. E., Tague, C. (Naomi), & Stephens, S. L. (2019). Restoring a Natural Fire Regime Alters the Water Balance of a Sierra Nevada Catchment. *Water Resources Research*, *55*(7), 5751–5769. <https://doi.org/10.1029/2018WR024098>
- Boryan, C., Yang, Z., Mueller, R., & Craig, M. (2011). Monitoring US agriculture: The US department of agriculture, national agricultural statistics service, cropland data layer program. *Geocarto International*, *26*(5). <https://doi.org/10.1080/10106049.2011.562309>

- Bouaziz, L. J. E., Aalbers, E. E., Weerts, A. H., Hegnauer, M., Buiteveld, H., Lammersen, R., et al. (2022). Ecosystem adaptation to climate change: the sensitivity of hydrological predictions to time-dynamic model parameters. *Hydrology and Earth System Sciences*, 26(5), 1295–1318. <https://doi.org/10.5194/hess-26-1295-2022>
- Bowling, L. C., & Lettenmaier, D. P. (2010). Modeling the Effects of Lakes and Wetlands on the Water Balance of Arctic Environments. *Journal of Hydrometeorology*, 11(2), 276–295. <https://doi.org/10.1175/2009JHM1084.1>
- Brown, T. C., Hobbins, M. T., & Ramirez, J. A. (2008). Spatial Distribution of Water Supply in the Conterminous United States. *JAWRA Journal of the American Water Resources Association*, 44(6), 1474–1487. <https://doi.org/10.1111/J.1752-1688.2008.00252.X>
- Broxton, P. D., Moeser, C. D., & Harpold, A. (2021). Accounting for Fine-Scale Forest Structure is Necessary to Model Snowpack Mass and Energy Budgets in Montane Forests. *Water Resources Research*, 57(12), e2021WR029716. <https://doi.org/10.1029/2021WR029716>
- Bulygina, N., McIntyre, N., & Wheeler, H. (2011). Bayesian conditioning of a rainfall-runoff model for predicting flows in ungauged catchments and under land use changes. *Water Resources Research*, 47(2). <https://doi.org/10.1029/2010WR009240>
- Buttle, J. M., Webster, K. L., Hazlett, P. W., & Jeffries, D. S. (2019). Quickflow response to forest harvesting and recovery in a northern hardwood forest landscape. *Hydrological Processes*, 33(1), 47–65. <https://doi.org/10.1002/HYP.13310>
- Caldwell, P. v., Elliott, K. J., Liu, N., Vose, J. M., Zietlow, D. R., & Knoepp, J. D. (2020). Watershed-scale vegetation, water quantity, and water quality responses to wildfire in the southern Appalachian mountain region, United States. *Hydrological Processes*, 34(26), 5188–5209. <https://doi.org/10.1002/hyp.13922>
- Campos, I., González-Piqueras, J., Carrara, A., Villodre, J., & Calera, A. (2016). Estimation of total available water in the soil layer by integrating actual evapotranspiration data in a remote sensing-driven soil water balance. *Journal of Hydrology*, 534. <https://doi.org/10.1016/j.jhydrol.2016.01.023>
- Cappelaere, B. (1997). Accurate Diffusive Wave Routing. *Journal of Hydraulic Engineering*, 123(3), 174–181. [https://doi.org/10.1061/\(ASCE\)0733-9429\(1997\)123:3\(174\)](https://doi.org/10.1061/(ASCE)0733-9429(1997)123:3(174))

- Chen, J. M., Pavlic, G., Brown, L., Cihlar, J., Leblanc, S. G., White, H. P., et al. (2002). Derivation and validation of Canada-wide coarse-resolution leaf area index maps using high-resolution satellite imagery and ground measurements. *Remote Sensing of Environment*, *80*(1), 165–184. [https://doi.org/10.1016/S0034-4257\(01\)00300-5](https://doi.org/10.1016/S0034-4257(01)00300-5)
- Cheng, F. Y., & Basu, N. B. (2017). Biogeochemical hotspots: Role of small water bodies in landscape nutrient processing. *Water Resources Research*, *53*(6), 5038–5056. <https://doi.org/10.1002/2016WR020102>
- Chlumsky, R., Mai, J., Craig, J. R., & Tolson, B. A. (2021). Simultaneous Calibration of Hydrologic Model Structure and Parameters Using a Blended Model. *Water Resources Research*, *57*(5), e2020WR029229. <https://doi.org/10.1029/2020WR029229>
- Chow, V. te. (1959). Handbook of Applied Hydrology. *International Association of Scientific Hydrology. Bulletin*, *10*(1), 82–83. <https://doi.org/10.1080/02626666509493376>
- Clark, M. P., Slater, A. G., Rupp, D. E., Woods, R. A., Vrugt, J. A., Gupta, H. v., et al. (2008). Framework for Understanding Structural Errors (FUSE): A modular framework to diagnose differences between hydrological models. *Water Resources Research*, *44*(12). <https://doi.org/10.1029/2007WR006735>
- Clark, M. P., Kavetski, D., & Fenicia, F. (2011). Pursuing the method of multiple working hypotheses for hydrological modeling. *Water Resources Research*, *47*(9). <https://doi.org/10.1029/2010WR009827>
- Clark, M. P., Nijssen, B., Lundquist, J. D., Kavetski, D., Rupp, D. E., Woods, R. A., et al. (2015). A unified approach for process-based hydrologic modeling: 1. Modeling concept. *Water Resources Research*, *51*(4), 2498–2514. <https://doi.org/10.1002/2015WR017198>
- Clark, M. P., Schaefli, B., Schymanski, S. J., Samaniego, L., Luce, C. H., Jackson, B. M., et al. (2016). Improving the theoretical underpinnings of process-based hydrologic models. *Water Resources Research*, *52*(3). <https://doi.org/10.1002/2015WR017910>
- Clark, M. P., Bierkens, M. F. P., Samaniego, L., Woods, R. A., Uijlenhoet, R., Bennett, K. E., et al. (2017). The evolution of process-based hydrologic models: Historical challenges and the collective quest for physical realism. *Hydrology and Earth System Sciences*, *21*(7). <https://doi.org/10.5194/hess-21-3427-2017>

- Clark, M. P., Vogel, R. M., Lamontagne, J. R., Mizukami, N., Knoben, W. J. M., Tang, G., et al. (2021). The Abuse of Popular Performance Metrics in Hydrologic Modeling. *Water Resources Research*, 57(9), e2020WR029001. <https://doi.org/10.1029/2020WR029001>
- Collar, N. M., Saxe, S., Rust, A. J., & Hogue, T. S. (2021). A CONUS-scale study of wildfire and evapotranspiration: Spatial and temporal response and controlling factors. *Journal of Hydrology*, 603, 127162. <https://doi.org/10.1016/j.jhydrol.2021.127162>
- Coops, N.C, Waring, R. H., & Landsberg, J. J. (1998). Assessing forest productivity in Australia and New Zealand using a physiologically-based model driven with averaged monthly weather data and satellite-derived estimates of canopy photosynthetic capacity. *Forest Ecology and Management*, 104(1–3), 113–127. [https://doi.org/10.1016/S0378-1127\(97\)00248-X](https://doi.org/10.1016/S0378-1127(97)00248-X)
- Coops, Nicholas C, Waring, R. H., & Hilker, T. (2012). Prediction of soil properties using a process-based forest growth model to match satellite-derived estimates of leaf area index. *Remote Sensing of Environment*, 126, 160–173. <https://doi.org/10.1016/j.rse.2012.08.024>
- Costa, D., Shook, K., Spence, C., Elliott, J., Baulch, H., Wilson, H., & Pomeroy, J. W. (2020). Predicting Variable Contributing Areas, Hydrological Connectivity, and Solute Transport Pathways for a Canadian Prairie Basin. *Water Resources Research*, 56(12). <https://doi.org/10.1029/2020WR027984>
- Coxon, G., Freer, J., Wagener, T., Odoni, N. A., & Clark, M. (2013). Diagnostic evaluation of multiple hypotheses of hydrological behaviour in a limits-of-acceptability framework for 24 UK catchments. <https://doi.org/10.1002/hyp.10096>
- Craig, J. R., Brown, G., Chlumsky, R., Jenkinson, R. W., Jost, G., Lee, K., et al. (2020). Flexible watershed simulation with the Raven hydrological modelling framework. *Environmental Modelling & Software*, 129, 104728. <https://doi.org/10.1016/j.envsoft.2020.104728>
- Crampe, E. A., Segura, C., & Jones, J. A. (2021). Fifty years of runoff response to conversion of old-growth forest to planted forest in the H. J. Andrews Forest, Oregon, <sc>USA</sc>. *Hydrological Processes*, 35(5). <https://doi.org/10.1002/hyp.14168>
- Cuntz, M., Mai, J., Zink, M., Thober, S., Kumar, R., Schäfer, D., et al. (2015). Computationally inexpensive identification of noninformative model parameters by sequential screening. *Water Resources Research*, 51(8), 6417–6441. <https://doi.org/10.1002/2015WR016907>

- David, C. H., Maidment, D. R., Niu, G.-Y., Yang, Z.-L., Habets, F., & Eijkhout, V. (2011). River Network Routing on the NHDPlus Dataset. *Journal of Hydrometeorology*, *12*(5), 913–934. <https://doi.org/10.1175/2011JHM1345.1>
- Dickerson-Lange, S. E., Vano, J. A., Gersonde, R., & Lundquist, J. D. (2021). Ranking Forest Effects on Snow Storage: A Decision Tool for Forest Management. *Water Resources Research*, *57*(10), e2020WR027926. <https://doi.org/10.1029/2020WR027926>
- Downing, J. A. (2010). Emerging global role of small lakes and ponds: little things mean a lot. *Limnetica*, *29*(1), 9–24. <https://doi.org/10.23818/limn.29.02>
- Du, E., Link, T. E., Wei, L., & Marshall, J. D. (2016). Evaluating hydrologic effects of spatial and temporal patterns of forest canopy change using numerical modelling. *Hydrological Processes*, *30*(2), 217–231. <https://doi.org/10.1002/hyp.10591>
- ESRI. (2012). ArcGIS Desktop 10.1. *Redlands CA*.
- Evenson, G. R., Golden, H. E., Lane, C. R., & D'Amico, E. (2015). Geographically isolated wetlands and watershed hydrology: A modified model analysis. *Journal of Hydrology*, *529*(P1), 240–256. <https://doi.org/10.1016/J.JHYDROL.2015.07.039>
- Evenson, G. R., Golden, H. E., Lane, C. R., & D'Amico, E. (2016). An improved representation of geographically isolated wetlands in a watershed-scale hydrologic model. *Hydrological Processes*, *30*(22), 4168–4184. <https://doi.org/10.1002/hyp.10930>
- Feikema, P. M., Morris, J. D., Beverly, C. R., Collopy, J. J., Baker, T. G., & Lane, P. N. J. (2010). Validation of plantation transpiration in south-eastern Australia estimated using the 3PG+ forest growth model. *Forest Ecology and Management*, *260*(5), 663–678. <https://doi.org/10.1016/j.foreco.2010.05.022>
- Fenicia, F., Kavetski, D., Savenije, H. H. G., & Pfister, L. (2016). From spatially variable streamflow to distributed hydrological models: Analysis of key modeling decisions. *Water Resources Research*, *52*(2), 954–989. <https://doi.org/10.1002/2015WR017398>
- Finger, D., Vis, M., Huss, M., & Seibert, J. (2015). The value of multiple data set calibration versus model complexity for improving the performance of hydrological models in mountain catchments. *Water Resources Research*, *51*(4). <https://doi.org/10.1002/2014WR015712>

- Fisette, T., Rollin, P., Aly, Z., Campbell, L., Daneshfar, B., Filyer, P., et al. (2013). AAFC annual crop inventory. <https://doi.org/10.1109/argo-geoinformatics.2013.6621920>
- Fitzgibbon, J. E., & Dunne, T. (1981). Land surface and lake storage during snowmelt runoff in a subarctic drainage system ( Knob Lake, Schefferville Quebec). *Arctic and Alpine Research*, 13(3), 277–285. <https://doi.org/10.2307/1551034>
- Foglia, L., Mehl, S. W., Hill, M. C., & Burlando, P. (2013). Evaluating model structure adequacy: The case of the Maggia Valley groundwater system, southern Switzerland. *Water Resources Research*, 49(1). <https://doi.org/10.1029/2011WR011779>
- Fontes, L., Landsberg, J., Tomé, J., Tomé, M., Pacheco, C. A., Soares, P., & Araujo, C. (2006). Calibration and testing of a generalized process-based model for use in Portuguese eucalyptus plantations. *Canadian Journal of Forest Research*, 36(12), 3209–3221. <https://doi.org/10.1139/x06-186>
- Forrester, D. I., & Tang, X. (2016). Analysing the spatial and temporal dynamics of species interactions in mixed-species forests and the effects of stand density using the 3-PG model. *Ecological Modelling*, 319, 233–254. <https://doi.org/10.1016/j.ecolmodel.2015.07.010>
- Fowler, K., Peel, M., Western, A., & Zhang, L. (2018). Improved Rainfall-Runoff Calibration for Drying Climate: Choice of Objective Function. *Water Resources Research*, 54(5), 3392–3408. <https://doi.org/10.1029/2017WR022466>
- Friedl, M., & Sulla-Menashe, D. (2015). MCD12Q1 MODIS/Terra+ aqua land cover type yearly L3 global 500m SIN grid V006 [data set]. *NASA EOSDIS Land Processes DAAC*, 10.
- Gaborit, É., Fortin, V., Xu, X., Seglenieks, F., Tolson, B., Fry, L. M., et al. (2017). A hydrological prediction system based on the SVS land-surface scheme: Efficient calibration of GEM-Hydro for streamflow simulation over the Lake Ontario basin. *Hydrology and Earth System Sciences*, 21(9). <https://doi.org/10.5194/hess-21-4825-2017>
- Gharari, S., Hrachowitz, M., Fenicia, F., Gao, H., & Savenije, H. H. G. (2014). Using expert knowledge to increase realism in environmental system models can dramatically reduce the need for calibration. *Hydrology and Earth System Sciences*, 18(12). <https://doi.org/10.5194/hess-18-4839-2014>

- Gharari, Shervan, Clark, M. P., Mizukami, N., Knoben, W. J. M., Wong, J. S., & Pietroniro, A. (2020). Flexible vector-based spatial configurations in land models. *Hydrol. Earth Syst. Sci*, 24, 5953–5971. <https://doi.org/10.5194/hess-24-5953-2020>
- Gibbs, M. S., McInerney, D., Humphrey, G., Thyer, M. A., Maier, H. R., Dandy, G. C., & Kavetski, D. (2018). State updating and calibration period selection to improve dynamic monthly streamflow forecasts for an environmental flow management application. *Hydrology and Earth System Sciences*, 22(1), 871–887. <https://doi.org/10.5194/hess-22-871-2018>
- Giles-Hansen, K., & Wei, X. (2021). Improved Regional Scale Dynamic Evapotranspiration Estimation Under Changing Vegetation and Climate. *Water Resources Research*, 57(8), e2021WR029832. <https://doi.org/10.1029/2021WR029832>
- Göhler, M., Mai, J., & Cuntz, M. (2013). Use of eigendecomposition in a parameter sensitivity analysis of the Community Land Model. *Journal of Geophysical Research: Biogeosciences*, 118(2), 904–921. <https://doi.org/10.1002/jgrg.20072>
- Golden, H. E., Sander, H. A., Lane, C. R., Zhao, C., Price, K., D’Amico, E., & Christensen, J. R. (2016a). Relative effects of geographically isolated wetlands on streamflow: a watershed-scale analysis. *Ecohydrology*, 9(1), 21–38. <https://doi.org/10.1002/ECO.1608>
- Golden, H. E., Sander, H. A., Lane, C. R., Zhao, C., Price, K., D’Amico, E., & Christensen, J. R. (2016b). Relative effects of geographically isolated wetlands on streamflow: a watershed-scale analysis. *Ecohydrology*, 9(1), 21–38. <https://doi.org/10.1002/ECO.1608>
- Gong, W., Gupta, H. v, Yang, D., Sricharan, K., Iii, A. O. H., Gupta, H. v, et al. (2013). Estimating epistemic and aleatory uncertainties during hydrologic modeling: An information theoretic approach. *Water Resour. Res*, 49, 2253–2273. <https://doi.org/10.1002/wrcr.20161>
- Goodwell, A. E., & Kumar, P. (2017). Temporal Information Partitioning Networks (TIPNets): A process network approach to infer ecohydrologic shifts. *Water Resources Research*, 53(7). <https://doi.org/10.1002/2016WR020218>
- Grimson, R., Montroull, N., Saurral, R., Vasquez, P., & Camilloni, I. (2013). Hydrological modelling of the Iberá Wetlands in southeastern South America. <https://doi.org/10.1016/j.jhydrol.2013.08.042>

- Guinaldo, T., Munier, S., le Moigne, P., Boone, A., Decharme, B., Choulga, M., & Leroux, D. J. (2021). Parametrization of a lake water dynamics model MLake in the ISBA-CTrip land surface system (SURFEX v8.1). *Geosci. Model Dev*, *14*, 1309–1344. <https://doi.org/10.5194/gmd-14-1309-2021>
- Gunderson, C. A., Edwards, N. T., Walker, A. v., O'Hara, K. H., Campion, C. M., & Hanson, P. J. (2012). Forest phenology and a warmer climate - growing season extension in relation to climatic provenance. *Global Change Biology*, *18*(6). <https://doi.org/10.1111/j.1365-2486.2011.02632.x>
- Günther, D., Marke, T., Essery, R., & Strasser, U. (2019). Uncertainties in Snowpack Simulations—Assessing the Impact of Model Structure, Parameter Choice, and Forcing Data Error on Point-Scale Energy Balance Snow Model Performance. *Water Resources Research*, *55*(4). <https://doi.org/10.1029/2018WR023403>
- Guo, Y., Zhang, L., Zhang, Y., Wang, Z., & Zheng, H. X. (2021). Estimating impacts of wildfire and climate variability on streamflow in Victoria, Australia. *Hydrological Processes*, *35*(12), e14439. <https://doi.org/10.1002/hyp.14439>
- Gupta, H. v., Kling, H., Yilmaz, K. K., & Martinez, G. F. (2009). Decomposition of the mean squared error and NSE performance criteria: Implications for improving hydrological modelling. *Journal of Hydrology*, *377*(1–2). <https://doi.org/10.1016/j.jhydrol.2009.08.003>
- Gupta, H. v., Clark, M. P., Vrugt, J. A., Abramowitz, G., & Ye, M. (2012). Towards a comprehensive assessment of model structural adequacy. *Water Resources Research*, *48*(8). <https://doi.org/10.1029/2011WR011044>
- Hampton, T. B., & Basu, N. B. (2022). A novel Budyko-based approach to quantify post-forest-fire streamflow response and recovery timescales. *Journal of Hydrology*, *608*, 127685. <https://doi.org/10.1016/j.jhydrol.2022.127685>
- Hampton, T. B., Lin, S. G. M., & Basu, N. B. (2022). Forest fire effects on stream water quality at continental scales: a meta-analysis. *Environmental Research Letters*. <https://doi.org/10.1088/1748-9326/AC6A6C>
- Han, M., Mai, J., Tolson, B. A., Craig, J. R., Gaborit, É., Liu, H., & Lee, K. (2020). Subwatershed-based lake and river routing products for hydrologic and land surface models applied over

Canada. <https://doi.org/10.1080/07011784.2020.1772116>, 45(3), 237–251.  
<https://doi.org/10.1080/07011784.2020.1772116>

Harrison, J. A., Maranger, R. J., Alexander, R. B., Giblin, A. E., Jacinthe, P. A., Mayorga, E., et al. (2009). The regional and global significance of nitrogen removal in lakes and reservoirs. *Biogeochemistry*, 93(1–2), 143–157. <https://doi.org/10.1007/s10533-008-9272-x>

Herman, M. R., Nejadhashemi, A. P., Abouali, M., Hernandez-Suarez, J. S., Daneshvar, F., Zhang, Z., et al. (2018). Evaluating the role of evapotranspiration remote sensing data in improving hydrological modeling predictability. *Journal of Hydrology*, 556.  
<https://doi.org/10.1016/j.jhydrol.2017.11.009>

Höge, M., Wöhling, T., & Nowak, W. (2018). A Primer for Model Selection: The Decisive Role of Model Complexity. *Water Resources Research*, 54(3). <https://doi.org/10.1002/2017WR021902>

Hou, Y., Wei, X., Vore, M., Déry, S. J., Pypker, T., & Giles-Hansen, K. (2022). Cumulative forest disturbances decrease runoff in two boreal forested watersheds of the northern interior of British Columbia, Canada. *Journal of Hydrology*, 605, 127362.  
<https://doi.org/10.1016/j.jhydrol.2021.127362>

Hrachowitz, M., Fovet, O., Ruiz, L., Euser, T., Gharari, S., Nijzink, R., et al. (2014). Process consistency in models: The importance of system signatures, expert knowledge, and process complexity. *Water Resources Research*, 50(9). <https://doi.org/10.1002/2014WR015484>

Hrachowitz, Markus, & Clark, M. P. (2017). HESS Opinions: The complementary merits of competing modelling philosophies in hydrology. *Hydrology and Earth System Sciences*, 21(8).  
<https://doi.org/10.5194/hess-21-3953-2017>

Hughes, D. A., Tshimanga, R. M., Tirivarombo, S., & Tanner, J. (2014). Simulating wetland impacts on stream flow in southern Africa using a monthly hydrological model. *Hydrological Processes*, 28(4), 1775–1786. <https://doi.org/10.1002/HYP.9725>

Husain, S. Z., Alavi, N., Bélair, S., Carrera, M., Zhang, S., Fortin, V., et al. (2016). The multibudget Soil, Vegetation, and Snow (SVS) scheme for land surface parameterization: Offline warm season evaluation. *Journal of Hydrometeorology*, 17(8). <https://doi.org/10.1175/JHM-D-15-0228.1>

- Huziy, O., & Sushama, L. (2017). Impact of lake-river connectivity and interflow on the Canadian RCM simulated regional climate and hydrology for Northeast Canada. *Climate Dynamics*, 48, 709–725. <https://doi.org/10.1007/s00382-016-3104-9>
- Hwang, T., Martin, K. L., Vose, J. M., Wear, D., Miles, B., Kim, Y., & Band, L. E. (2018). Nonstationary Hydrologic Behavior in Forested Watersheds Is Mediated by Climate-Induced Changes in Growing Season Length and Subsequent Vegetation Growth. *Water Resources Research*, 54(8), 5359–5375. <https://doi.org/10.1029/2017WR022279>
- Hwang, T., Band, L. E., Vose, J. M., & Tague, C. (n.d.). Ecosystem processes at the watershed scale: Hydrologic vegetation gradient as an indicator for lateral hydrologic connectivity of headwater catchments, 48, 6514. <https://doi.org/10.1029/2011WR011301>
- Ilamooranan, I., van Meter, K. J., & Basu, N. B. (2019). A Race Against Time: Modeling Time Lags in Watershed Response. *Water Resources Research*, 55(5), 3941–3959. <https://doi.org/10.1029/2018WR023815>
- Ines, A. V. M., Das, N. N., Hansen, J. W., & Njoku, E. G. (2013). Assimilation of remotely sensed soil moisture and vegetation with a crop simulation model for maize yield prediction. *Remote Sensing of Environment*, 138. <https://doi.org/10.1016/j.rse.2013.07.018>
- Iroumé, A., Jones, J., & Bathurst, J. C. (2021). Forest operations, tree species composition and decline in rainfall explain runoff changes in the Nacimiento experimental catchments, south central Chile. *Hydrological Processes*, 35(6), e14257. <https://doi.org/10.1002/hyp.14257>
- Jaskierniak, D., Kuczera, G., & Benyon, R. (2016). Predicting long-term streamflow variability in moist eucalypt forests using forest growth models and a sapwood area index. *Water Resources Research*, 52(4), 3052–3067. <https://doi.org/10.1002/2015WR018029>
- Jeffries, D. S., Kelso, J. R. M., & Morrison, I. K. (1988). Physical, Chemical, and Biological Characteristics of the Turkey Lakes Watershed, Central Ontario, Canada. *Canadian Journal of Fisheries and Aquatic Sciences*, 45(S1), s3–s13. <https://doi.org/10.1139/f88-262>
- Jordahl, K., Bossche, J. van den, Fleischmann, M., Wasserman, J., McBride, J., Gerard, J., et al. (2020). geopandas/geopandas: v0.8.1. *Zenodo*. <https://doi.org/10.5281/zenodo.3946761>

- Karan, S., Kidmose, J., Engesgaard, P., Nilsson, B., Frandsen, M., Ommen, D. A. O., et al. (2014). Role of a groundwater–lake interface in controlling seepage of water and nitrate. *Journal of Hydrology*, *517*, 791–802. <https://doi.org/10.1016/J.JHYDROL.2014.06.011>
- Kavetski, D., & Clark, M. P. (2010). Ancient numerical demons of conceptual hydrological modeling: 2. Impact of time stepping schemes on model analysis and prediction. *Water Resources Research*, *46*(10). <https://doi.org/10.1029/2009WR008896>
- Kavetski, D., Binning, P., & Sloan, S. W. (2002). Noniterative time stepping schemes with adaptive truncation error control for the solution of Richards equation. *Water Resources Research*, *38*(10), 29-1-29–10. <https://doi.org/10.1029/2001WR000720>
- Kavetski, D., Kuczera, G., & Franks, S. W. (2006). Bayesian analysis of input uncertainty in hydrological modeling: 1. Theory. *Water Resources Research*, *42*(3). <https://doi.org/10.1029/2005WR004368>
- Kelly, C. N., McGuire, K. J., Miniati, C. F., & Vose, J. M. (2016). Streamflow response to increasing precipitation extremes altered by forest management. *Geophysical Research Letters*, *43*(8). <https://doi.org/10.1002/2016GL068058>
- Khaki, M., Hamilton, F., Forootan, E., Hoteit, I., Awange, J., & Kuhn, M. (2018). Nonparametric Data Assimilation Scheme for Land Hydrological Applications. *Water Resources Research*, *54*(7). <https://doi.org/10.1029/2018WR022854>
- Khaledi, J., Lane, P. N. J., Nitschke, C. R., & Nyman, P. (2022). Wildfire contribution to streamflow variability across Australian temperate zone. *Journal of Hydrology*, *609*, 127728. <https://doi.org/10.1016/j.jhydrol.2022.127728>
- Khan, M. H. (1993). Muskingum flood routing model for multiple tributaries. *Water Resources Research*, *29*(4), 1057–1062. <https://doi.org/10.1029/92WR02850>
- Khazaei, B., Read, L. K., Casali, M., Sampson, K. M., & Yates, D. N. (2022). GLOBathy, the global lakes bathymetry dataset. *Scientific Data* *2022 9:1*, *9*(1), 1–10. <https://doi.org/10.1038/s41597-022-01132-9>
- Kouwen, N. (1988). Watflood: A micro-computer based flood forecasting system based on real-time weather radar. *Canadian Water Resources Journal*, *13*(1). <https://doi.org/10.4296/cwrj1301062>

- Kuczera, G. (1997). Efficient subspace probabilistic parameter optimization for catchment models. *Water Resources Research*, 33(1), 177–185. <https://doi.org/10.1029/96WR02671>
- Kurzweil, J. R., Metlen, K., Abdi, R., Strahan, R., & Hogue, T. S. (2021). Surface water runoff response to forest management: Low-intensity forest restoration does not increase surface water yields. *Forest Ecology and Management*, 496, 119387. <https://doi.org/10.1016/j.foreco.2021.119387>
- Kusumastuti, D. I., Sivapalan, M., Struthers, I., Reynolds, D. A., Murray, K., & Turlach, B. A. (2008). Thresholds in the storm response of a catchment-lake system and the occurrence and magnitude of lake overflows: Implications for flood frequency. *Water Resources Research*, 44(2). <https://doi.org/10.1029/2006WR005628>
- Landsberg, J. J., & Waring, R. H. (1997). A generalised model of forest productivity using simplified concepts of radiation-use efficiency, carbon balance and partitioning. *Forest Ecology and Management*, 95(3), 209–228. [https://doi.org/10.1016/S0378-1127\(97\)00026-1](https://doi.org/10.1016/S0378-1127(97)00026-1)
- Leach, J. A., & Laudon, H. (2019). LETTER Headwater lakes and their influence on downstream discharge. *Limnology and Oceanography Letters*, 4, 105–112. <https://doi.org/10.1002/lol2.10110>
- Leach, J. A., Buttle, J. M., Webster, K. L., Hazlett, P. W., & Jeffries, D. S. (2020). Travel times for snowmelt-dominated headwater catchments: Influences of wetlands and forest harvesting, and linkages to stream water quality. *Hydrological Processes*, 34(10), 2154–2175. <https://doi.org/10.1002/hyp.13746>
- Lehner, B., & Grill, G. (2013). Global river hydrography and network routing: Baseline data and new approaches to study the world's large river systems. *Hydrological Processes*, 27(15), 2171–2186. <https://doi.org/10.1002/hyp.9740>
- Lerat, J., Andréassian, V., Perrin, C., Vaze, J., Perraud, J. M., Ribstein, P., & Loumagne, C. (2012). Do internal flow measurements improve the calibration of rainfall-runoff models? *Water Resources Research*, 48(2), 2511. <https://doi.org/10.1029/2010WR010179>
- Li, H., Wigmosta, M. S., Wu, H., Huang, M., Ke, Y., Coleman, A. M., & Leung, L. R. (2013). A Physically Based Runoff Routing Model for Land Surface and Earth System Models. *Journal of Hydrometeorology*, 14(3), 808–828. <https://doi.org/10.1175/JHM-D-12-015.1>

- Li, Y., Grimaldi, S., Pauwels, V. R. N., & Walker, J. P. (2018). Hydrologic model calibration using remotely sensed soil moisture and discharge measurements: The impact on predictions at gauged and ungauged locations. *Journal of Hydrology*, *557*, 897–909. <https://doi.org/10.1016/j.jhydrol.2018.01.013>
- Lin, P., Yang, Z. L., Cai, X., & David, C. H. (2015). Development and evaluation of a physically-based lake level model for water resource management: A case study for Lake Buchanan, Texas. *Journal of Hydrology: Regional Studies*, *4*. <https://doi.org/10.1016/j.ejrh.2015.08.005>
- Lin, P., Yang, Z. L., Gochis, D. J., Yu, W., Maidment, D. R., Somos-Valenzuela, M. A., & David, C. H. (2018). Implementation of a vector-based river network routing scheme in the community WRF-Hydro modeling framework for flood discharge simulation. *Environmental Modelling and Software*, *107*. <https://doi.org/10.1016/j.envsoft.2018.05.018>
- Lindström, G., Pers, C., Rosberg, J., Strömquist, J., & Arheimer, B. (2010). Development and testing of the HYPE (Hydrological Predictions for the Environment) water quality model for different spatial scales. *Hydrology Research*, *41*(3–4). <https://doi.org/10.2166/nh.2010.007>
- Liu, H., Tolson, B. A., Craig, J. R., & Shafii, M. (2016). A priori discretization error metrics for distributed hydrologic modeling applications. *Journal of Hydrology*, *543*, 873–891. <https://doi.org/10.1016/j.jhydrol.2016.11.008>
- Liu, Y., Weerts, A. H., Clark, M., Hendricks Franssen, H. J., Kumar, S., Moradkhani, H., et al. (2012). Advancing data assimilation in operational hydrologic forecasting: Progresses, challenges, and emerging opportunities. *Hydrology and Earth System Sciences*, *16*(10). <https://doi.org/10.5194/hess-16-3863-2012>
- Lo, M.-H., Famiglietti, J. S., Yeh, P. J.-F., & Syed, T. H. (2010). Improving parameter estimation and water table depth simulation in a land surface model using GRACE water storage and estimated base flow data. *Water Resources Research*, *46*(5). <https://doi.org/10.1029/2009WR007855>
- Lohmann, D., Nolte-Holube, R., & Raschke, E. (1996). A large-scale horizontal routing model to be coupled to land surface parametrization schemes. *Tellus, Series A: Dynamic Meteorology and Oceanography*, *48*(5). <https://doi.org/10.3402/tellusa.v48i5.12200>

- Lu, D., Ye, M., Meyer, P. D., Curtis, G. P., Shi, X., Niu, X.-F., & Yabusaki, S. B. (2013). Effects of error covariance structure on estimation of model averaging weights and predictive performance. *Water Resources Research*, *49*(9), 6029–6047. <https://doi.org/10.1002/wrcr.20441>
- Lvovich, M. I. (1979). World water resources, present and future. *GeoJournal*, *3*(5). <https://doi.org/10.1007/BF00455981>
- MacKay, D. J. C. (1992). Bayesian Interpolation. *Neural Computation*, *4*(3). <https://doi.org/10.1162/neco.1992.4.3.415>
- Maidment, D. R. (2002). *Arc Hydro: GIS for water resources. Agriculture*.
- Martinez, G. F., & Gupta, H. v. (2011). Hydrologic consistency as a basis for assessing complexity of monthly water balance models for the continental United States. *Water Resources Research*, *47*(12). <https://doi.org/10.1029/2011WR011229>
- McMillan, H., Tetzlaff, D., Clark, M., & Soulsby, C. (2012). Do time-variable tracers aid the evaluation of hydrological model structure? A multimodel approach. *Water Resources Research*, *48*(5). <https://doi.org/10.1029/2011WR011688>
- Meerveld, H. J. (Ilja), Zhang, J., Tripoli, R., & Bruijnzeel, L. A. (2019). Effects of Reforestation of a Degraded *Imperata* Grassland on Dominant Flow Pathways and Streamflow Responses in Leyte, the Philippines. *Water Resources Research*, *55*(5), 4128–4148. <https://doi.org/10.1029/2018WR023896>
- Mendiguren, G., Koch, J., & Stisen, S. (2017). Spatial pattern evaluation of a calibrated national hydrological model - A remote-sensing-based diagnostic approach. *Hydrology and Earth System Sciences*, *21*(12). <https://doi.org/10.5194/hess-21-5987-2017>
- Messenger, M. L., Lehner, B., Grill, G., Nedeva, I., & Schmitt, O. (2016). Estimating the volume and age of water stored in global lakes using a geo-statistical approach. *Nature Communications*, *7*. <https://doi.org/10.1038/ncomms13603>
- Miehle, P., Battaglia, M., Sands, P. J., Forrester, D. I., Feikema, P. M., Livesley, S. J., et al. (2009). A comparison of four process-based models and a statistical regression model to predict growth of *Eucalyptus globulus* plantations. *Ecological Modelling*, *220*(5), 734–746. <https://doi.org/10.1016/J.ECOLMODEL.2008.12.010>

- Mielko, C., & Woo, M. K. (2006). Snowmelt runoff processes in a headwater lake and its catchment, subarctic Canadian Shield. In *Hydrological Processes* (Vol. 20).  
<https://doi.org/10.1002/hyp.6117>
- Miller, J. R., Russell, G. L., & Caliri, G. (1994). Continental-scale river flow in climate models. *Journal of Climate*, 7(6). [https://doi.org/10.1175/1520-0442\(1994\)007<0914:CSRFIG>2.0.CO;2](https://doi.org/10.1175/1520-0442(1994)007<0914:CSRFIG>2.0.CO;2)
- Mitterer, J. A. (2022). TATOO – Python Topographic Analysis Tool Library for semi-automated setup of high-resolution integrated hydrologic models. *Environmental Modelling & Software*, 153, 105406. <https://doi.org/10.1016/J.ENVSOFT.2022.105406>
- Mizukami, N., Clark, M. P., Sampson, K., Nijssen, B., Mao, Y., McMillan, H., et al. (2016). MizuRoute version 1: A river network routing tool for a continental domain water resources applications. *Geoscientific Model Development*, 9(6). <https://doi.org/10.5194/gmd-9-2223-2016>
- Moeser, C. D., Broxton, P. D., Harpold, A., & Robertson, A. (2020). Estimating the Effects of Forest Structure Changes From Wildfire on Snow Water Resources Under Varying Meteorological Conditions. *Water Resources Research*, 56(11), e2020WR027071.  
<https://doi.org/10.1029/2020WR027071>
- Moges, E., Demissie, Y., & Li, H. Y. (2016). Hierarchical mixture of experts and diagnostic modeling approach to reduce hydrologic model structural uncertainty. *Water Resources Research*, 52(4).  
<https://doi.org/10.1002/2015WR018266>
- Molina-Navarro, E., Nielsen, A., & Trolle, D. (2018). A QGIS plugin to tailor SWAT watershed delineations to lake and reservoir waterbodies. *Environmental Modelling & Software*, 108, 67–71. <https://doi.org/10.1016/j.envsoft.2018.07.003>
- Moradkhani, H., Hsu, K. L., Gupta, H., & Sorooshian, S. (2005). Uncertainty assessment of hydrologic model states and parameters: Sequential data assimilation using the particle filter. *Water Resources Research*, 41(5). <https://doi.org/10.1029/2004WR003604>
- Morrison, I. K. (1990). Organic matter and mineral distribution in an old-growth *Acer saccharum* forest near the northern limit of its range. *Canadian Journal of Forest Research*, 20(9), 1332–1342. <https://doi.org/10.1139/x90-177>
- Muma, M., Assani, A. A., Landry, R., Quessy, J. F., & Mesfioui, M. (2011). Effects of the change from forest to agriculture land use on the spatial variability of summer extreme daily flow

- characteristics in southern Quebec (Canada). *Journal of Hydrology*, 407(1–4).  
<https://doi.org/10.1016/j.jhydrol.2011.07.020>
- Murray, S. J., Foster, P. N., & Prentice, I. C. (2012). Future global water resources with respect to climate change and water withdrawals as estimated by a dynamic global vegetation model. *Journal of Hydrology*, 448–449. <https://doi.org/10.1016/j.jhydrol.2012.02.044>
- Narasimhan, B., & Srinivasan, R. (2005). Development and evaluation of Soil Moisture Deficit Index (SMDI) and Evapotranspiration Deficit Index (ETDI) for agricultural drought monitoring. *Agricultural and Forest Meteorology*, 133(1–4), 69–88.  
<https://doi.org/10.1016/j.agrformet.2005.07.012>
- Naseem, B., Ajami, H., Cordery, I., & Sharma, A. (2015). A multi-objective assessment of alternate conceptual ecohydrological models. *Journal of Hydrology*, 529.  
<https://doi.org/10.1016/j.jhydrol.2015.08.060>
- Nearing, G., & Gupta, H. (2018). Ensembles vs. information theory: supporting science under uncertainty. *Frontiers of Earth Science*, 12(4), 653–660. <https://doi.org/10.1007/s11707-018-0709-9>
- Nearing, G., Yatheendradas, S., Crow, W., Zhan, X., Liu, J., & Chen, F. (2018). The Efficiency of Data Assimilation. *Water Resources Research*, 54(9). <https://doi.org/10.1029/2017WR020991>
- Nearing, G. S., & Gupta, H. v. (2015). The quantity and quality of information in hydrologic models. *Water Resources Research*, 51(1). <https://doi.org/10.1002/2014WR015895>
- Neitsch, S. L., Arnold, J. G., Kiniry, J. R., & Williams, J. R. (2011). *Soil & Water Assessment Tool Theoretical Documentation Version 2009*. Texas Water Resources Institute.  
<https://doi.org/10.1016/j.scitotenv.2015.11.063>
- Neteler, M., Bowman, M. H., Landa, M., & Metz, M. (2012). GRASS GIS: A multi-purpose open source GIS. *Environmental Modelling and Software*, 31.  
<https://doi.org/10.1016/j.envsoft.2011.11.014>
- Nguyen, V. T., Dietrich, J., Uniyal, B., & Tran, D. A. (2018). Verification and correction of the hydrologic routing in the soil and Water Assessment Tool. *Water (Switzerland)*, 10(10).  
<https://doi.org/10.3390/w10101419>

- Niemeyer, R. J., Bladon, K. D., & Woodsmith, R. D. (2020). Long-term hydrologic recovery after wildfire and post-fire forest management in the interior Pacific Northwest. *Hydrological Processes*, 34(5), 1182–1197. <https://doi.org/10.1002/hyp.13665>
- Nijzink, R. C., Almeida, S., Pechlivanidis, I. G., Capell, R., Gustafssons, D., Arheimer, B., et al. (2018). Constraining Conceptual Hydrological Models With Multiple Information Sources. *Water Resources Research*, 54(10), 8332–8362. <https://doi.org/10.1029/2017WR021895>
- Nunes, J. P., Bernard-Jannin, L., Rodríguez-Blanco, M. L., Boulet, A., Santos, J. M., & Keizer, J. J. (2020). Impacts of wildfire and post-fire land management on hydrological and sediment processes in a humid Mediterranean headwater catchment. *Hydrological Processes*, 34(26), 5210–5228. <https://doi.org/10.1002/hyp.13926>
- Ocio, D., le Vine, N., Westerberg, I., Pappenberger, F., & Buytaert, W. (2017). The role of rating curve uncertainty in real-time flood forecasting. *Water Resources Research*, 53(5), 4197–4213. <https://doi.org/10.1002/2016WR020225>
- Oda, T., Egusa, T., Ohte, N., Hotta, N., Tanaka, N., Green, M. B., & Suzuki, M. (2021). Effects of changes in canopy interception on stream runoff response and recovery following clear-cutting of a Japanese coniferous forest in Fukuroyamasawa Experimental Watershed in Japan. *Hydrological Processes*, 35(5), e14177. <https://doi.org/10.1002/hyp.14177>
- Olivera, F., Famiglietti, J., & Asante, K. (2000). Global-scale flow routing using a source-to-sink algorithm. *Water Resources Research*, 36(8). <https://doi.org/10.1029/2000WR900113>
- Parr, D., Wang, G., & Bjerklie, D. (2015). Integrating remote sensing data on evapotranspiration and leaf area index with hydrological modeling: Impacts on model performance and future predictions. *Journal of Hydrometeorology*, 16(5). <https://doi.org/10.1175/JHM-D-15-0009.1>
- Pathiraja, S., Marshall, L., Sharma, A., & Moradkhani, H. (2016). Detecting non-stationary hydrologic model parameters in a paired catchment system using data assimilation. *Advances in Water Resources*, 94. <https://doi.org/10.1016/j.advwatres.2016.04.021>
- Paul, K. I., Booth, T. H., Jovanovic, T., Sands, P. J., & Morris, J. D. (2007). Calibration of the forest growth model 3-PG to eucalypt plantations growing in low rainfall regions of Australia. *Forest Ecology and Management*, 243(2–3), 237–247. <https://doi.org/10.1016/J.FORECO.2007.03.029>

- Pauwels, V. R. N., Hoeben, R., Verhoest, N. E. C., & de Troch, F. P. (2001). The importance of the spatial patterns of remotely sensed soil moisture in the improvement of discharge predictions for small-scale basins through data assimilation. *Journal of Hydrology*, *251*(1–2).  
[https://doi.org/10.1016/S0022-1694\(01\)00440-1](https://doi.org/10.1016/S0022-1694(01)00440-1)
- Pechlivanidis, I. G., Jackson, B., McMillan, H., & Gupta, H. (2014). Use of an entropy-based metric in multiobjective calibration to improve model performance. *Water Resources Research*, *50*(10), 8066–8083. <https://doi.org/10.1002/2013WR014537>
- Pérez-Cruzado, C., Muñoz-Sáez, F., Basurco, F., Riesco, G., & Rodríguez-Soalleiro, R. (2011). Combining empirical models and the process-based model 3-PG to predict *Eucalyptus nitens* plantations growth in Spain. *Forest Ecology and Management*, *262*(6), 1067–1077.  
<https://doi.org/10.1016/J.FORECO.2011.05.045>
- PICKARD, W. F. (1983). Three Interpretations of the Self-thinning Rule. *Annals of Botany*, *51*(6), 749–757. <https://doi.org/10.1093/oxfordjournals.aob.a086526>
- Pietroniro, A., Fortin, V., Kouwen, N., Neal, C., Turcotte, R., Davison, B., et al. (2007). Development of the MESH modelling system for hydrological ensemble forecasting of the Laurentian Great Lakes at the regional scale. *Hydrology and Earth System Sciences*, *11*(4), 1279–1294.  
<https://doi.org/10.5194/HESS-11-1279-2007>
- Poeter, E., & Anderson, D. (2005). Multimodel ranking and inference in ground water modeling. *Ground Water*, *43*(4). <https://doi.org/10.1111/j.1745-6584.2005.0061.x>
- Rajagopalan, K., Chinnayakanahalli, K. J., Stockle, C. O., Nelson, R. L., Kruger, C. E., Brady, M. P., et al. (2018). Impacts of Near-Term Climate Change on Irrigation Demands and Crop Yields in the Columbia River Basin. *Water Resources Research*, *54*(3).  
<https://doi.org/10.1002/2017WR020954>
- Rajib, A., Evenson, G. R., Golden, H. E., & Lane, C. R. (2018). Hydrologic model predictability improves with spatially explicit calibration using remotely sensed evapotranspiration and biophysical parameters. *Journal of Hydrology*, *567*.  
<https://doi.org/10.1016/j.jhydrol.2018.10.024>

- Rajib, A., Merwade, V., & Yu, Z. (2018). Rationale and Efficacy of Assimilating Remotely Sensed Potential Evapotranspiration for Reduced Uncertainty of Hydrologic Models. *Water Resources Research*, *54*(7). <https://doi.org/10.1029/2017WR021147>
- Rajib, A., Golden, H. E., Lane, C. R., & Wu, Q. (2020). Surface Depression and Wetland Water Storage Improves Major River Basin Hydrologic Predictions. *Water Resources Research*, *56*(7), e2019WR026561. <https://doi.org/10.1029/2019WR026561>
- Razavi, S., & Tolson, B. A. (2013). An efficient framework for hydrologic model calibration on long data periods. *Water Resources Research*, *49*(12), 8418–8431. <https://doi.org/10.1002/2012WR013442>
- Roche, J. W., Goulden, M. L., & Bales, R. C. (2018). Estimating evapotranspiration change due to forest treatment and fire at the basin scale in the Sierra Nevada, California. *Ecohydrology*, *11*(7), e1978. <https://doi.org/10.1002/eco.1978>
- Rodríguez, R., Real, P., Espinosa, M., & Perry, D. A. (2009). A process-based model to evaluate site quality for Eucalyptus nitens in the Bio-Bio Region of Chile. *Forestry: An International Journal of Forest Research*, *82*(2), 149–162. <https://doi.org/10.1093/FORESTRY/CPN045>
- Roy, A., Royer, A., & Turcotte, R. (2010). Improvement of springtime streamflow simulations in a boreal environment by incorporating snow-covered area derived from remote sensing data. *Journal of Hydrology*, *390*(1–2). <https://doi.org/10.1016/j.jhydrol.2010.06.027>
- Ruddell, B. L., Drewry, D. T., & Nearing, G. S. (2019). Information Theory for Model Diagnostics: Structural Error is Indicated by Trade-Off Between Functional and Predictive Performance. *Water Resources Research*, *55*(8). <https://doi.org/10.1029/2018WR023692>
- Sands, P. J., & Landsberg, J. J. (2002). Parameterisation of 3-PG for plantation grown Eucalyptus globulus. *Forest Ecology and Management*, *163*(1–3), 273–292. [https://doi.org/10.1016/S0378-1127\(01\)00586-2](https://doi.org/10.1016/S0378-1127(01)00586-2)
- Schöniger, A., Wöhling, T., Samaniego, L., & Nowak, W. (2014). Model selection on solid ground: Rigorous comparison of nine ways to evaluate Bayesian model evidence. *Water Resources Research*, *50*(12). <https://doi.org/10.1002/2014WR016062>

- Shaad, K. (2018). Evolution of river-routing schemes in macro-scale models and their potential for watershed management. *Hydrological Sciences Journal*, 63(7).  
<https://doi.org/10.1080/02626667.2018.1473871>
- Shafii, M., & Tolson, B. A. (2015). Optimizing hydrological consistency by incorporating hydrological signatures into model calibration objectives. *Water Resources Research*, 51(5).  
<https://doi.org/10.1002/2014WR016520>
- Shafii, M., Basu, N., Craig, J. R., Schiff, S. L., & van Cappellen, P. (2017). A diagnostic approach to constraining flow partitioning in hydrologic models using a multiobjective optimization framework. *Water Resources Research*, 53(4). <https://doi.org/10.1002/2016WR019736>
- Shafii, M., Craig, J. R., Macrae, M. L., English, M. C., Schiff, S. L., van Cappellen, P., & Basu, N. B. (2019). Can Improved Flow Partitioning in Hydrologic Models Increase Biogeochemical Predictability? *Water Resources Research*, 55(4), 2939–2960.  
<https://doi.org/10.1029/2018WR024487>
- Shahzad, K. M., & Plate, E. J. (2014). Flood forecasting for River Mekong with data-based models. *Water Resources Research*, 50(9), 7115–7133. <https://doi.org/10.1002/2013WR015072>
- Shamir, E., Imam, B., Morin, E., Gupta, H. v., & Sorooshian, S. (2005). The role of hydrograph indices in parameter estimation of rainfall-runoff models. *Hydrological Processes*, 19(11).  
<https://doi.org/10.1002/hyp.5676>
- Shannon, C. E. (1997). The Mathematical Theory of Communication. *M.D. Computing*, 14(4).  
<https://doi.org/10.2307/410457>
- Shaw, G. D., White, E. S., & Gammons, C. H. (2013). Characterizing groundwater–lake interactions and its impact on lake water quality. *Journal of Hydrology*, 492, 69–78.  
<https://doi.org/10.1016/J.JHYDROL.2013.04.018>
- Shen, H., Tolson, B. A., & Mai, J. (2022). Time to Update the Split-Sample Approach in Hydrological Model Calibration. *Water Resources Research*, 58(3).  
<https://doi.org/10.1029/2021WR031523>
- Shimizu, T., Tamai, K., Hosoda, I., Noguchi, S., Kominami, Y., Abe, T., et al. (2021). Long-term precipitation and stream discharge records at seven forested experimental watersheds along a latitudinal transect in Japan: Jozankei, Kamabuchi, Takaragawa, Tsukuba, Tatsunokuchi-yama,

Kahoku and Sarukawa. *Hydrological Processes*, 35(10), e14376.

<https://doi.org/10.1002/hyp.14376>

Smettem, K. R. J., Waring, R. H., Callow, J. N., Wilson, M., & Mu, Q. (2013). Satellite-derived estimates of forest leaf area index in southwest Western Australia are not tightly coupled to interannual variations in rainfall: implications for groundwater decline in a drying climate.

*Global Change Biology*, 19(8), 2401–2412. <https://doi.org/10.1111/gcb.12223>

Smith Tripp, S., Griffith, A., Pasquarella, V. J., & Matthes, J. H. (2021). Impacts of a regional multiyear insect defoliation event on growing-season runoff ratios and instantaneous streamflow characteristics. *Ecohydrology*, 14(7), e2332. <https://doi.org/10.1002/eco.2332>

Son, K., & Sivapalan, M. (2007). Improving model structure and reducing parameter uncertainty in conceptual water balance models through the use of auxiliary data. *Water Resources Research*, 43(1). <https://doi.org/10.1029/2006WR005032>

Spence, C. (2007). On the relation between dynamic storage and runoff: A discussion on thresholds, efficiency, and function. *Water Resources Research*, 43(12).

<https://doi.org/10.1029/2006WR005645>

Spence, C., Guan, X. J., Phillips, R., Hedstrom, N., Granger, R., & Reid, B. (2010). Storage dynamics and streamflow in a catchment with a variable contributing area. *Hydrological Processes*, 24(16). <https://doi.org/10.1002/hyp.7492>

Spence, C., Ali, G., Oswald, C. J., & Wellen, C. (2019). An Application of the T-TEL Assessment Method to Evaluate Connectivity in a Lake-Dominated Watershed after Drought. *JAWRA Journal of the American Water Resources Association*, 55(2), 318–333.

<https://doi.org/10.1111/1752-1688.12702>

Spence, Christopher. (2000). The Effect of Storage on Runoff from a Headwater Subarctic Shield Basin. *ARCTIC*, 53(3), 237–247.

Spence, Christopher. (2006). Hydrological processes and streamflow in a lake dominated watercourse. *Hydrological Processes*, 20(17), 3665–3681. <https://doi.org/10.1002/HYP.6381>

Spence, Christopher, Hedstrom, N., Tank, S. E., Quinton, W. L., Olefeldt, D., Goodman, S., & Dion, N. (2020). Hydrological resilience to forest fire in the subarctic Canadian shield. *Hydrological Processes*, 34(25), 4940–4958. <https://doi.org/10.1002/hyp.13915>

- Stisen, S., McCabe, M. F., Refsgaard, J. C., Lerer, S., & Butts, M. B. (2011). Model parameter analysis using remotely sensed pattern information in a multi-constraint framework. *Journal of Hydrology*, *409*(1–2). <https://doi.org/10.1016/j.jhydrol.2011.08.030>
- Tague, C. L., & Band, L. E. (2004). RHESSys: Regional Hydro-Ecologic Simulation System—An Object-Oriented Approach to Spatially Distributed Modeling of Carbon, Water, and Nutrient Cycling. *Earth Interactions*, *8*(19), 1–42. [https://doi.org/10.1175/1087-3562\(2004\)8<1:RRHSSO>2.0.CO;2](https://doi.org/10.1175/1087-3562(2004)8<1:RRHSSO>2.0.CO;2)
- Tang, Q., Gao, H., Yeh, P., Oki, T., Su, F., & Lettenmaier, D. P. (2010). Dynamics of terrestrial water storage change from satellite and surface observations and modeling. *Journal of Hydrometeorology*, *11*(1). <https://doi.org/10.1175/2009JHM1152.1>
- Tarboton, D. G. (2015). Terrain Analysis Using Digital Elevation Models (TauDEM). *Terrain Analysis Using Digital Elevation Models (TauDEM)*, (July 2003).
- Thyer, M., Renard, B., Kavetski, D., Kuczera, G., Franks, S. W., & Srikanthan, S. (2009). Critical evaluation of parameter consistency and predictive uncertainty in hydrological modeling: A case study using Bayesian total error analysis. *Water Resources Research*, *45*(12). <https://doi.org/10.1029/2008WR006825>
- Tolson, B. A., & Shoemaker, C. A. (2007). Dynamically dimensioned search algorithm for computationally efficient watershed model calibration. *Water Resources Research*, *43*(1). <https://doi.org/10.1029/2005WR004723>
- Vore, M. E., Déry, S. J., Hou, Y., & Wei, X. (2020). Climatic influences on forest fire and mountain pine beetle outbreaks and resulting runoff effects in large watersheds in British Columbia, Canada. *Hydrological Processes*, *34*(24), 4560–4575. <https://doi.org/10.1002/hyp.13908>
- Vrugt, J. A., ter Braak, C. J. F., Clark, M. P., Hyman, J. M., & Robinson, B. A. (2008). Treatment of input uncertainty in hydrologic modeling: Doing hydrology backward with Markov chain Monte Carlo simulation. *Water Resources Research*, *44*(12). <https://doi.org/10.1029/2007wr006720>
- Wagenbrenner, J. W., Ebel, B. A., Bladon, K. D., & Kinoshita, A. M. (2021). Post-wildfire hydrologic recovery in Mediterranean climates: A systematic review and case study to identify current knowledge and opportunities. *Journal of Hydrology*, *602*, 126772. <https://doi.org/10.1016/j.jhydrol.2021.126772>

- Wang, W. J., He, H. S., Spetich, M. A., Shifley, S. R., Thompson III, F. R., Larsen, D. R., et al. (2013). A large-scale forest landscape model incorporating multi-scale processes and utilizing forest inventory data. *Ecosphere*, 4(9), art106. <https://doi.org/10.1890/ES13-00040.1>
- Waring, R. H., Coops, N. C., & Landsberg, J. J. (2010). Improving predictions of forest growth using the 3-PGS model with observations made by remote sensing. *Forest Ecology and Management*, 259(9), 1722–1729. <https://doi.org/10.1016/j.foreco.2009.05.036>
- Webster, K. L., Leach, J. A., Hazlett, P. W., Fleming, R. L., Emilson, E. J. S., Houle, D., et al. (2021). Turkey Lakes Watershed, Ontario, Canada: 40 years of interdisciplinary whole-ecosystem research. *Hydrological Processes*, 35(4), e14109. <https://doi.org/10.1002/HYP.14109>
- Westerberg, I., Guerrero, J. L., Seibert, J., Beven, K. J., & Halldin, S. (2011). Stage-discharge uncertainty derived with a non-stationary rating curve in the Choluteca River, Honduras. *Hydrological Processes*, 25(4). <https://doi.org/10.1002/hyp.7848>
- Westra, S., Thyer, M., Leonard, M., Kavetski, D., & Lambert, M. (2014). A strategy for diagnosing and interpreting hydrological model nonstationarity. *Water Resources Research*, 50(6). <https://doi.org/10.1002/2013WR014719>
- Winchell, M., Srinivasan, R., di Luzio, M., & Arnold, J. (2007). ArcSWAT interface for SWAT 2005. *User's Guide*.
- Wöhling, T., Schöniger, A., Gayler, S., & Nowak, W. (2015). Bayesian model averaging to explore the worth of data for soil-plant model selection and prediction. *Water Resources Research*, 51(4), 2825–2846. <https://doi.org/10.1002/2014WR016292>
- Wollstadt, P., Martínez-Zarzuela, M., Vicente, R., Díaz-Pernas, F. J., & Wibral, M. (2014). Efficient transfer entropy analysis of non-stationary neural time series. *PLoS ONE*, 9(7). <https://doi.org/10.1371/journal.pone.0102833>
- Woo, M. K., & Mielko, C. (2007). An integrated framework of lake-stream connectivity for a semi-arid, subarctic environment. *Hydrological Processes*, 21(19), 2668–2674. <https://doi.org/10.1002/HYP.6789>
- Woo, M. K., & Mielko, C. (2008). Flow connectivity of a lake-stream system in a semi-arid precambrian shield environment. In *Cold Region Atmospheric and Hydrologic Studies. The Mackenzie GEWEX Experience* (Vol. 2). [https://doi.org/10.1007/978-3-540-75136-6\\_12](https://doi.org/10.1007/978-3-540-75136-6_12)

- Woodward, F. I., Lomas, M. R., & Kelly, C. K. (2004). Global climate and the distribution of plant biomes. In *Philosophical Transactions of the Royal Society B: Biological Sciences* (Vol. 359). <https://doi.org/10.1098/rstb.2004.1525>
- Xia, Y., Mitchell, K., Ek, M., Cosgrove, B., Sheffield, J., Luo, L., et al. (2012). Continental-scale water and energy flux analysis and validation for North American Land Data Assimilation System project phase 2 (NLDAS-2): 2. Validation of model-simulated streamflow. *Journal of Geophysical Research: Atmospheres*, *117*(D3), n/a-n/a. <https://doi.org/10.1029/2011JD016051>
- Xie, Y., Crosbie, R., Yang, J., Wu, J., & Wang, W. (2018). Usefulness of Soil Moisture and Actual Evapotranspiration Data for Constraining Potential Groundwater Recharge in Semiarid Regions. *Water Resources Research*, *54*(7). <https://doi.org/10.1029/2018WR023257>
- Xu, X., Li, J., & Tolson, B. A. (2014). Progress in integrating remote sensing data and hydrologic modeling. *Progress in Physical Geography*, *38*(4). <https://doi.org/10.1177/0309133314536583>
- Yamazaki, D., Kanae, S., Kim, H., & Oki, T. (2011). A physically based description of floodplain inundation dynamics in a global river routing model. *Water Resources Research*, *47*(4). <https://doi.org/10.1029/2010WR009726>
- Yamazaki, D., de Almeida, G. A. M., & Bates, P. D. (2013). Improving computational efficiency in global river models by implementing the local inertial flow equation and a vector-based river network map. *Water Resources Research*, *49*(11). <https://doi.org/10.1002/wrcr.20552>
- Ye, M., Meyer, P. D., & Neuman, S. P. (2008). On model selection criteria in multimodel analysis. *Water Resources Research*, *44*(3). <https://doi.org/10.1029/2008WR006803>
- Yilmaz, K. K., Gupta, H. v., & Wagener, T. (2008). A process-based diagnostic approach to model evaluation: Application to the NWS distributed hydrologic model. *Water Resources Research*, *44*(9). <https://doi.org/10.1029/2007WR006716>
- Zajac, Z., Revilla-Romero, B., Salamon, P., Burek, P., Hirpa, F., & Beck, H. (2017). The impact of lake and reservoir parameterization on global streamflow simulation. *Journal of Hydrology*, *548*, 552–568. <https://doi.org/10.1016/J.JHYDROL.2017.03.022>
- Zeide, B. (2010). Comparison of self-thinning models: an exercise in reasoning. *Trees* *24*:6, *24*(6), 1117–1126. <https://doi.org/10.1007/S00468-010-0484-Z>

- Zhang, S., Yang, Y., McVicar, T. R., & Yang, D. (2018). An Analytical Solution for the Impact of Vegetation Changes on Hydrological Partitioning Within the Budyko Framework. *Water Resources Research*, 54(1). <https://doi.org/10.1002/2017WR022028>
- Zhang, Y., Chiew, F. H. S., Li, M., & Post, D. (2018). Predicting Runoff Signatures Using Regression and Hydrological Modeling Approaches. *Water Resources Research*, 54(10). <https://doi.org/10.1029/2018WR023325>
- Zhao, F., Zhang, L., Xu, Z., & Scott, D. F. (2010). Evaluation of methods for estimating the effects of vegetation change and climate variability on streamflow. *Water Resources Research*, 46(3), 3505. <https://doi.org/10.1029/2009WR007702>
- Zhou, F., Xu, Y., Chen, Y., Xu, C. Y., Gao, Y., & Du, J. (2013). Hydrological response to urbanization at different spatio-temporal scales simulated by coupling of CLUE-S and the SWAT model in the Yangtze River Delta region. *Journal of Hydrology*, 485. <https://doi.org/10.1016/j.jhydrol.2012.12.040>
- Zink, M., Mai, J., Cuntz, M., & Samaniego, L. (2018). Conditioning a Hydrologic Model Using Patterns of Remotely Sensed Land Surface Temperature. *Water Resources Research*, 54(4), 2976–2998. <https://doi.org/10.1002/2017WR021346>
- Zou, L., Zhan, C., Xia, J., Wang, T., & Gippel, C. J. (2017). Implementation of evapotranspiration data assimilation with catchment scale distributed hydrological model via an ensemble Kalman Filter. *Journal of Hydrology*, 549. <https://doi.org/10.1016/j.jhydrol.2017.04.036>

# Appendices

## Appendix A

### A1 The extent of the Hudson Bay watershed

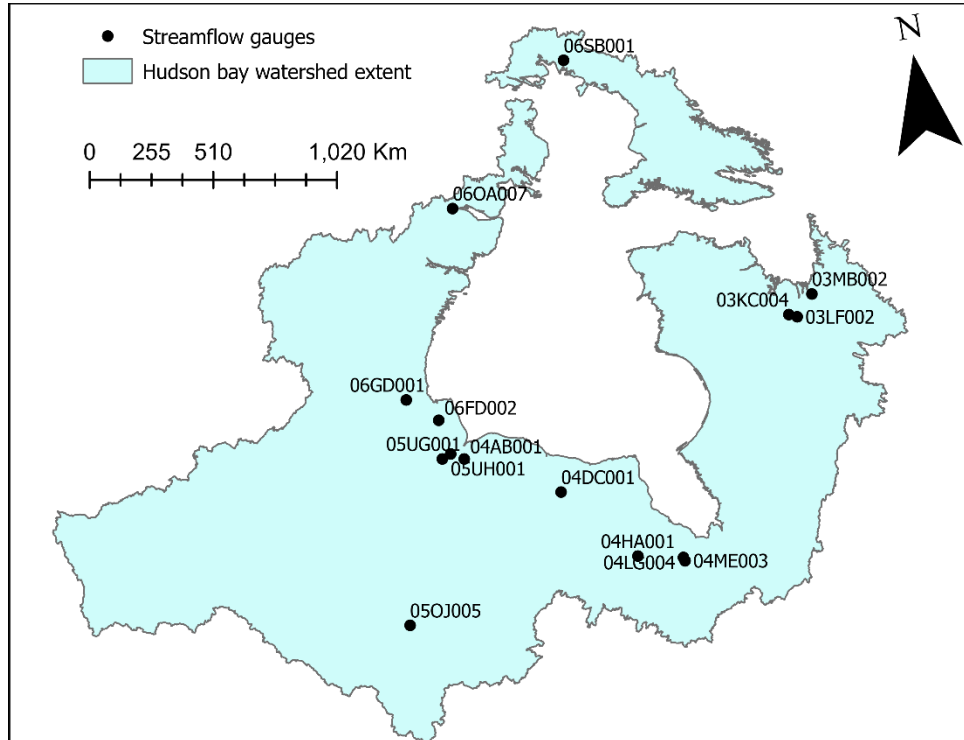


Figure A1-1 The extent of the Hudson Bay watershed and streamflow gauges used in Chapter 2.

### A2 Attributes in the lake-river routing products

**Table A2-1.** The included attributes in the lake river routing products and networks produced by BasinMaker v2.0 and v3.0. The attributes DA\_Chn\_L, DA\_Slope, DA\_Chn\_Slp, outletLng, and outletLat only exist in (Ontario Lake and River Routing network) generated with basinmaker v3.0. Moreover, the FRAL is generated outside of BasinMaker v3.0 and it only exists in Ontario Lake and River Routing network.

Name	Unit	Type	Description and Specific Values
SubId	[-]	Integer	Subbasin (catchment) ID
DowSubId	[-]	Integer	ID of subbasin (catchment) downstream of current subbasin
RivSlope	m/m	Float	Slope of river channel in the subbasin. It is limited to a range of 0.000001 to 1. It is -1.2345 for non-connected lake subbasin and headwater subbasins since these have no river channels.

RivLength	m	Float	Length of river channel in the subbasin. It is -1.2345 for non-connected lake subbasin and headwater subbasins since these have no river channels.
BasSlope	degree	Float	Averaged slope over the subbasin. It is limited to a range of 0 to 60°
BasAspect	degree	Float	Averaged aspect over the subbasin, it is counterclockwise from East: 90 degrees is North, 180 is West, 270 is South, 360 is East
BasArea	[m <sup>2</sup> ]	Float	Area of subbasin
BkfWidth	m	Float	Bankfull width of river channel in the subbasin (width of river when full). If this catchment is a lake catchment, and the lake is not a reservoir, this should be used as an initial estimate of lake's effective crest width. It is limited to a range of 0.1 to 3000
BkfDepth	m	Float	Bankfull depth river channel in the subbasin (depth of river when full). It is limited to a range of 0.1 to 10
Lake_Cat	[-]	Integer	Lake category 0: subbasin without lake 1: subbasin with lake that is directly connected to a downstream river channel. 2: subbasin with lake that is not directly connected to a downstream river channel.
HyLakeId	[-]	Integer	The lake ID in HydroLAKES database
LakeVol	[km <sup>3</sup> ]	Float	Volume of lake in HydroLAKES database; 0.0 for subbasins without lake
LakeArea	[m <sup>2</sup> ]	Float	Area of lake in HydroLAKES database; 0.0 for subbasins without lake
Laketype	[-]	Integer	Type of lake (assigned by HydroLAKES) 0: Subbasin without lake 1: Subbasin with natural lake 2: Subbasin with lake that is reservoir 3: Subbasin with lake that is natural with regulation
Has_POI	[-]	Integer	Subbasin has point of interest (POI) at outlet 0: subbasin has no POI 1: subbasin has POI, which comes from the following sources: streamflow and/or water level gauge station and or water quality station and/or subbasin outlets extracted from the Quaternary Ontario Watershed Boundaries
MeanElev	m	Float	Subbasin average elevation
FloodP_n	[s/m <sup>1/3</sup> ]	Float	Averaged flood plain Manning's coefficient (based on landcover along river channel). It is limited to a range of <i>Ch_n</i> to 1.5. It is -1.2345 for non-connected lake subbasin and head water subbasins since these have no river channels and thus no delineated flood plain.
Q_Mean	[m <sup>3</sup> /s]	Float	Subbasin outlet bankfull discharge (estimated). It is limited to a range of 0.00001 to 150000.
Ch_n	[s/m <sup>1/3</sup> ]	Float	River channel Manning's coefficient. It is limited to a range of 0.025 to 0.15. It is -1.2345 for non-connected lake subbasin and head water subbasins since these have no river channels.
DrainArea	[m <sup>2</sup> ]	Float	Drainage area of subbasin outlet
Strahler	[-]	Integer	The Strahler order of river channel
Seg_ID	[-]	Integer	The unique river reach ID the subbasin belongs to (each river reach can include multiple river channels). Only useful as an internal variable for BasinMaker

Seg_order	[-]	Integer	The sequence of the river channel denoting the direction of water flow in the corresponding river reach. Only useful as an internal variable for BasinMaker
Max_DEM	m	Float	The maximum elevation along the river channel
Min_DEM	m	Float	The minimum elevation along the river channel
DA_Obs	[km <sup>2</sup> ]	Float	Subbasin drainage area reported by institution providing point of interest. 0.0 for subbasins without point of interest or if no value is provided
DA_error	[-]	Float	Relative ratio between drainage area based on routing network (DrainArea) and basin drainage area reported by institution providing point of interest (DA_Obs). A value of 1.0 indicates DrainArea equals DA_Obs. Null for subbasins with DA_Obs=0.
Obs_NM	[-]	String	The point of interest ID as reported by agency providing the location. Null for subbasins with Has_POI=0. .
SRC_obs	[-]	String	Source of the point of interest (POI). HYDAT: POI from HYDAT database, PWQMN: POI from PWQMN water quality monitoring site, QUAT: POI from subbasin outlets extracted from the Quaternary Ontario Watershed Boundaries. Null for subbasins with Has_POI=0.
DA_Chnl_L	m	Float	For the entire upstream drainage area, the longest flow path to the subbasin outlet. It is -1.2345 for non-connected lake subbasin and headwater subbasins since these have no river channels. Note that this attribute and the other DA attributes below can be used in various empirical time of concentration formulas.
DA_Slope	degree	Float	For the entire upstream drainage area, the averaged slope over the drainage area. It is limited to a range of 0 to 60°. Computed as the area-weighted average of all subbasins in the drainage area.
DA_Chnl_Slp	m/m	Float	For the entire upstream drainage area, the slope of river channel along the longest flow path in the drainage area. Computed as the area-weighted average of all subbasins in the drainage area. It is limited to a range of 0.000001 to 1. It is -1.2345 for non-connected lake subbasin and headwater subbasins since these have no river channels.
FRAL	[-]	Float	It is the index of Flood Attenuation by Reservoirs and Lakes ranging from 0 to 1. Note attribute name should have been FARL (not FRAL). The lake attenuation effect increases as FARL decreases from 1 to 0. FARL is an index described in the Institute of Hydrology (1999) Flood Estimation Handbook.
outletLng	[deg_W]	Float	Subbasin outlet longitude
outletLat	[deg_N]	Float	Subbasin outlet latitude
centroid_x	[deg_W]	Float	Subbasin centroid longitude
centroid_y	[deg_N]	Float	Subbasin centroid latitude

### A3 The hydrological processes used in the Raven model

Three soil layers were included in this Raven model application. The hydrological processes applied in the model, and their parameters can be found in Table A3-1. The equation of each process can be found in Craig et al. (2020).

**Table A3-1.** The hydrological processes and parameters used in this application

Location	Process	Method (Name in Raven)	Parameters	Note	Unit
	Potential evapotranspiration	PET_PRIESTLEY_TAYLOR	PET_CORRECTION	Potential evapotranspiration correction factor	-
	Canopy interception	PRECIP_ICEPT_LAI	RAIN_ICEPT_FACT	The fraction of precipitation intercept by canopy	-
			MAX_CAPACITY	The maximum canopy storage	mm
Above the soil profile	Snowmelt	POTMELT_HBV	REFREEZE_FACTOR	The maximum refreeze factor used in degree day models	mm/day/ °C
			MELT_FACTOR	The maximum snow melt factor used in degree day models	mm/day/ °C
			MIN_MELT_FACTOR	The minimum snow melt factor used in degree day models	mm/day/ °C
			HBV_MELT_ASP_CORR	The snow melt aspect correction factor	-
	Infiltration	INF_GREEN_AMPT	HYDRAUL_COND	The saturated hydrological conductivity	mm/day
			WETTING_FRONT_PSI	The Green-Ampt wetting front pressure	-mm
Soil Layer 1	Soil Evaporation	SOILEVAP_SEQUEN	-	-	-
			MAX_BASEFLOW_RATE	The maximum baseflow rate	mm/day
	Baseflow	BASE_THRESH_POWER	FIELD_CAPACITY	The field capacity	-
			BASEFLOW_N	The baseflow exponent	

**Table A3-1.** continued from previous page

Location	Process	Method (Name in Raven)	Parameters	Note	Unit
	Soil Evaporation	SOILEVAP_SEQUEN	-	-	-
Soil Layer 2	Baseflow	BASE_THRESH_POWER	MAX_BASEFLOW_RATE	The maximum baseflow rate	mm/day
			FIELD_CAPACITY	The field capacity	-
			Depth	The soil layer depth	m
			BASEFLOW_N	The baseflow exponent	
	Percolation	PERC_GAWSER	MAX_PERC_RATE	The maximum percolation rate	mm/day
Soil Layer 3	Baseflow	BASE_THRESH_POWER	MAX_BASEFLOW_RATE	The maximum baseflow rate	mm/day
			FIELD_CAPACITY	The field capacity	-
			Depth	The soil layer depth	m
			BASEFLOW_N	The baseflow exponent	
	Capillary Rise	CRISE_HBV	MAX_CAP_RISE_RATE	The maximum capillary rate	mm/day

#### A4 The simulated hydrographs and lake levels in Chapter 4

This appendix includes the observed and simulated hydrographs at streamflow and water level gauges from the best-calibrated model of scenarios: 1-1, 1-1L, 1-2, 1-2L and 1-3. See Tables 4-1 and 4-2 for the descriptions of the scenarios.

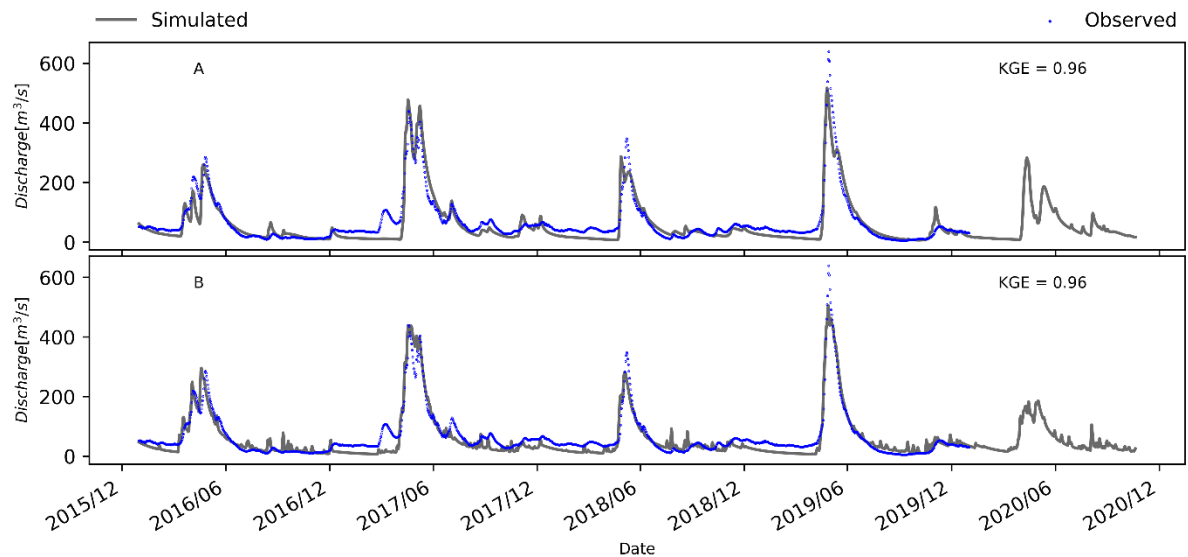


**Figure A4-1.** (A and B) The daily simulated and observed streamflow from the model with lakes (A, scenario 1-1L) and the ignoring lakes (B, scenario 1-1) in the Petawawa watershed. See Table 4-1 for scenario descriptions. For each model scenario, the simulated time series in this figure comes from the best-calibrated model in 40 independent calibration trials.

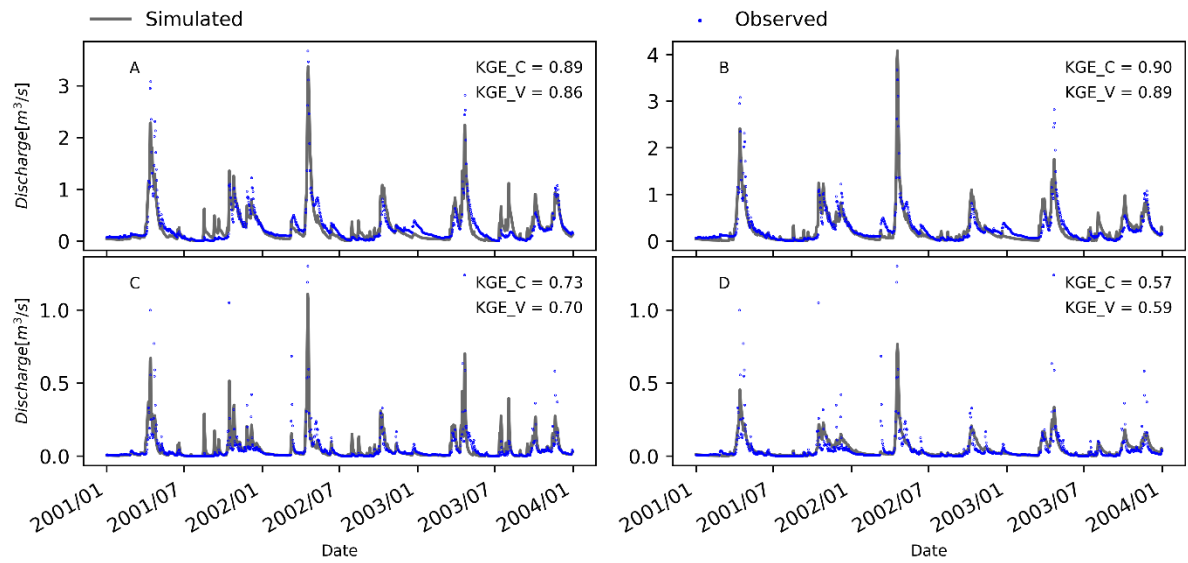


**Figure A4-2.** The daily simulated and observed streamflow from the model with lakes (A and C, scenario 1-2L) and the ignoring lakes (B and D, scenario 1-2) at gauges S5 and S1 in the Turkey Lake watershed. See Table 4-1 for scenario descriptions. For each model scenario, the simulated time series in this figure comes from the best-calibrated model in 40 independent calibration trials.

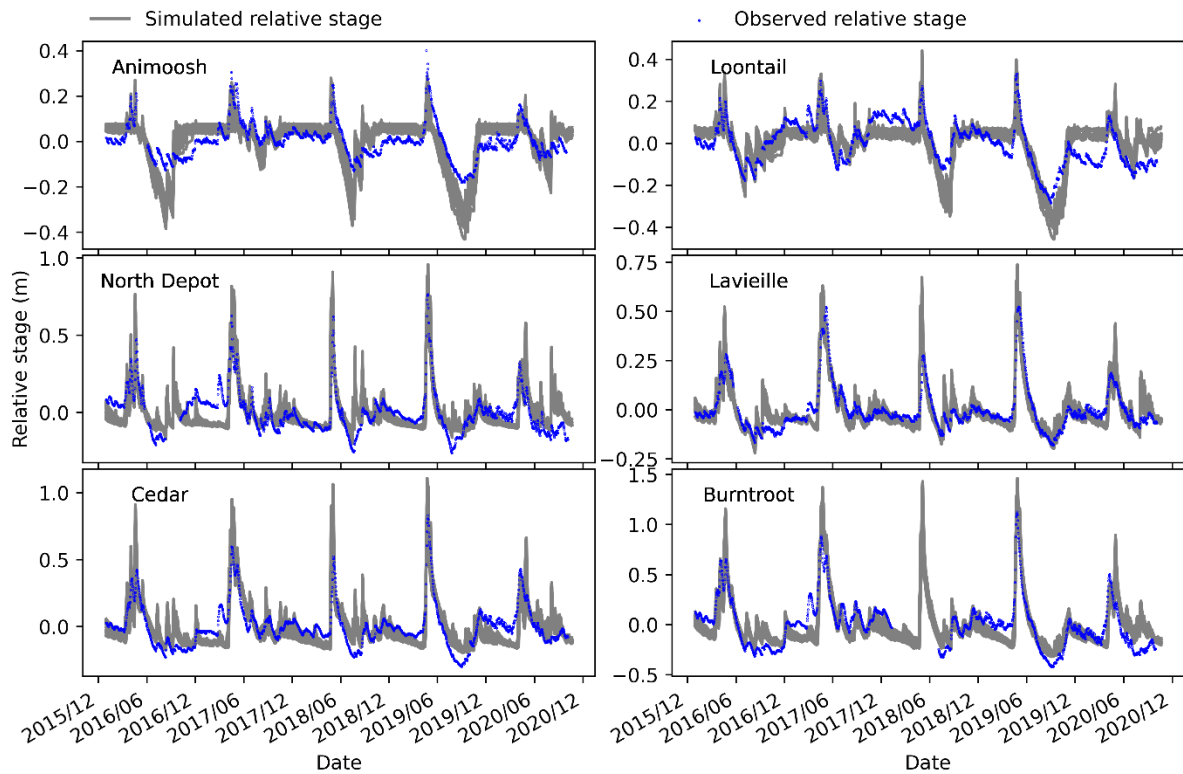


**Figure A4-3.** The daily simulated and observed lake levels from the hydrological model that was calibrated to lake observations and the streamflow with 15 additional lake crest width parameters (2-1c, Table 4-2). See Table 4-2 for scenario descriptions. For each model scenario, the simulated time series in this figure comes from the best-calibrated model in 40 independent calibration trials.

## **A5 Description of the 3PG forest growth model in Robin**

This section will first introduce the conceptual procedure to coupled Robin with hydrological models in section A5.1. The input files of the Robin will be described in section A5.2, and the mathematical equation of the 3PG forest growth model in Robin will be described in section A5.3. More detailed documentation of the Robin vegetation growth library is under development.

### **A5.1 Connected Robin with the hydrological model**

The procedure to connect Robin to the hydrological model is straightforward with Robin's interface functions. A conceptual procedure will be presented in this section, and a more detailed step-by-step documentation (Figure A5-1) will be available later. First, user need to call Robin's 'SetupCropgrowthmodel()' to let Robin read its input files, allocate memory for state variables, and open output files. This function should be called outside of the daily/HRU loops of the Hydrological model (Figure A5-1), where the hydrological processes of each HRU at each time step are calculated.

Within the daily/HRU loops, user can call the function 'Getcropmodelstatevalue()' of Robin to obtain the Robin simulated vegetation state variables at the current time step and update these values in the hydrological model. For example, suppose the hydrological model calculates potential evapotranspiration with the Penman-Monteith method. User can call 'Getcropmodelstatevalue()' to obtain the Robin simulated LAI and provide this LAI to the Penman-Monteith method in the hydrological model. Currently, Robin can return the simulated LAI, height, crop coefficient, nutrient demand, and root fraction.

Users can call the Robin function 'OptimalCropGrowth' and 'ActualCropGrowth' within the daily/HRU loops to let Robin simulate the vegetation growth of this HRU at this timestep. The inputs of 'OptimalCropGrowth' are the daily mean temperature, net radiation, the daily length, and the vapor pressure deficit of this HRU at the current time step. The 'OptimalCropGrowth' will calculate the gross primary production, the potential phenology development, and the potential nutrient uptake demand (only when the nutrient simulation is activated). The inputs of 'ActualCropGrowth' are the hydrological model simulated actual/potential evapotranspiration and the actual nutrient uptake. The 'ActualCropGrowth' will calculate the environmental stresses and vegetation's actual growth and update the root distributions of each soil layer. If the vegetation nutrient update is not activated, 'OptimalCropGrowth' and 'ActualCropGrowth' can be called sequentially. User can use a negative value as an actual nutrient update and provide it to 'ActualCropGrowth'. The Robin will ignore the

nutrient stress when vegetation nutrient update is not activated. However, when vegetation nutrient update is activated, the function ‘OptimalCropGrowth’ should be called before the hydrological model simulates the soil nutrient processes. In this way, the hydrological model could use the Robin simulated vegetation potential nutrient uptake to calculate the actual nutrient uptake in soil. The function ‘ActualCropGrowth’ should be called after the hydrological model simulates the soil nutrient processes. The actual nutrient uptake stimulated by the hydrological model can be provided to ‘ActualCropGrowth’ and Robin will use it to calculate the nutrient stresses.

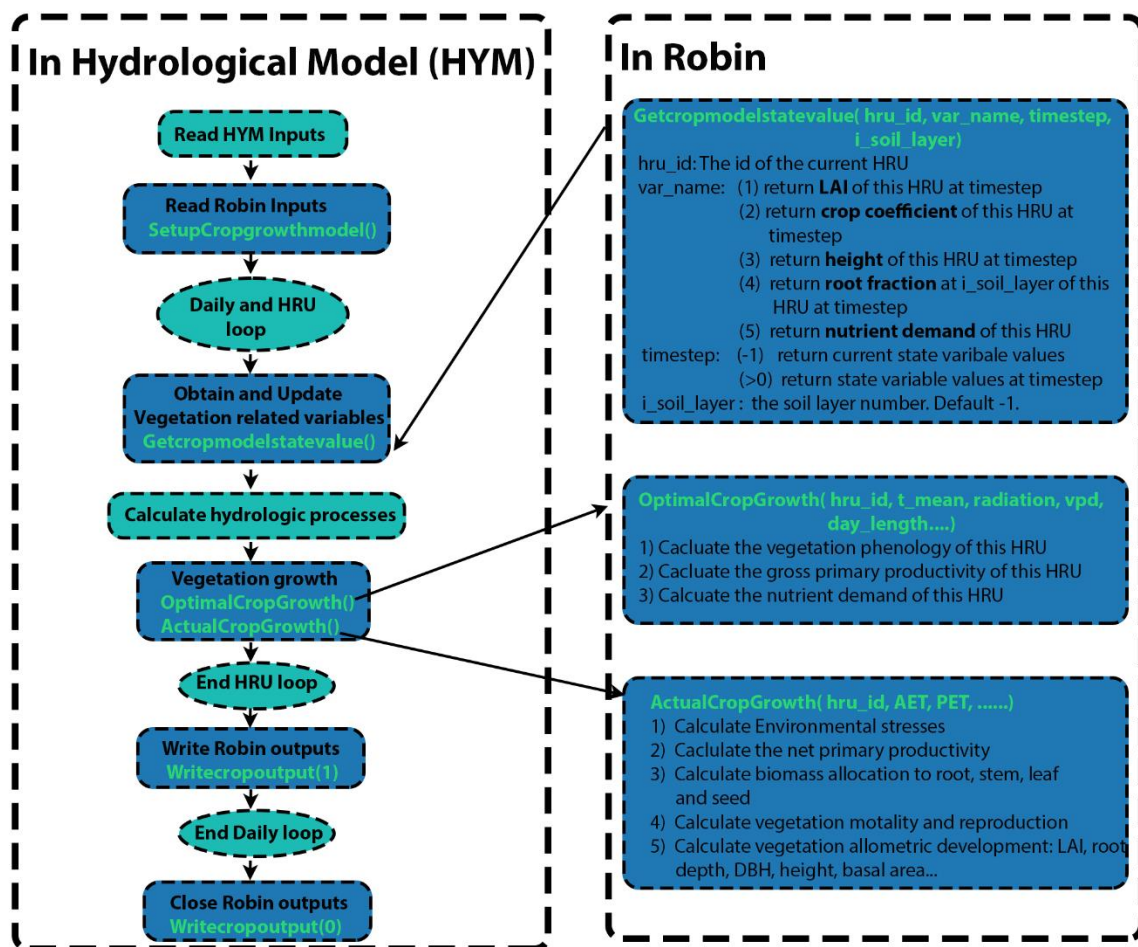


**Figure A5-1.** The conceptual procedure to connect Robin with the hydrological model is with Robin’s interface functions.

The Robin function ‘Writecropoutput()’ should be called at two locations with different inputs. First, it should be called outside the HRU loop and within the daily loop with one as its input. Robin will

write this day's simulated vegetation growth state variables in the output file. Second, the Robin function 'Writecropoutput()' should be called outside the daily/HRU loop with zero as its input. Robin will close the output files.

## A5.2 The input files of the Robin vegetation growth library.

### A5.2.1 The Primary Model Input File (.info)

The \*.info file specifies information about the model simulation, including the simulation period, the number of vegetation types, sub-basins, vegetation type arrays, HRUs, and growing seasons. It also defines the display and files output options. An example of an example .info file is the following.

```

1981      # starting year
1         # starting Julian day
12050    # number of days in simulation
38       # number of subbasins
169      # number of HRUs
2        # number of the vegetation types
88       # number of the seeding event
88       # number of the harvest event
2        # number of vegetation type arrays
88       # number of growing season
999      # max HRU id
999      # max Subbasin id
1        # 1 or 0: toggles off/activate nutrient simulation
1981 01 01 # starting YEAR MON DAY
1        # 1 or 0: suppresses/turn off the screen output
###
./cropout/ # the output directory
1         # the number of the customized output commands
TIMESERIES # the type of the customized output (row 1)
-1        # the output state variable, -1 for all variables (row 2)
27 63 144 # the HRU IDs, -1 means no HRU level output (row 3)
-1        # the subbasin IDs, -1 means no subbasin level output (row 4)
-1        # the write state variables at specific time step. -1 means all time steps (row 5)

```

**Figure A5-2.** An example of the Robin .info input file

Each customized output command defined in .info files includes five rows. The first row of the customized output command defines the type of the customized output. Three options included are 'TIMESERIES', 'WATERSHED' and 'STATEVARS'.

The 'TIMESERIES' type output will generate one file for each specific HRU (third row of customized output command) or Subbasin (fourth row of customized output command). Each file includes the subbasin or HRU average specific state variables (second row of customized output command) value at specific time steps (fifth row of the customized output command).

The specific state variables can be 'LAI' or -1. The -1 in the second row of the customized output command means all state variable values in each output file.

The specific time steps in the fifth row of the customized output command can be a list of model time steps or -1. The -1 means the specific state variables at all time steps will be included in each file.

The 'WATERSHED' type output will generate one file for each specific state variable (second row of customized output command) at each specific time step (fifth row of the customized output command). This file will include the Robin simulated state variable values of all HRUs at one time step. When 'WATERSHED' is used in the first row of the customized output command, the specific state variable (the second row of the customized output command) has to be 'LAI'. The specific HRU (third row of customized output command) and Subbasin (fourth row of customized output command) should be -1.

The 'STATEVARS' type output will generate one file for each state variable. Each file will contain the simulated state variable value of each HRU at each specific time step (fifth row of the customized output command). When 'STATEVARS' is used in the first row of the customized output command, the specific state variable (the second row of the customized output command) must be 'LAI'. The specific HRU (third row of customized output command) and Subbasin (fourth row of customized output command) should be -1.

### A5.2.2 The HRU and vegetation type array mapping file (.hrucrop)

The \*.hrucrop file specifies the mapping between HRUs and the vegetation type arrays. An example of an example \*.hrucrop file is the following.

```

subid hruid  vegetation_type_array  ave_temperature
2      11    R1                    18
2      33    R1                    16
...
...
2      342   R1                    15
vegetation_type_array  vegetation_type_gs1  vegetation_type_gs2  ...  vegetation_type_gs100
R2                    undisturbed_forest  undisturbed_forest  ...  regrowth_forest
R1                    undisturbed_forest  undisturbed_forest  ...  undisturbed_forest

```

**Figure A5-3.** An example of the Robin .hrucrop input file

The \*.hrucrop file contains two sections. The first section will define the vegetation type array of each HRU in the hydrological model. The subbasin and the HRU ID in this section should be the same as the ID in the hydrological model.

The second section defines the vegetation types of each vegetation type array in each growing season. It represents how landuse may change in the model simulation periods. For example, the forest may suffer from forest disturbances such as forest fires and forest harvest management. After the forest disturbance, the different vegetation types (regrowth forest) will start growing in the following growing seasons.

### A5.2.3 The vegetation model file (.model)

The \*.model file specifies the vegetation growth models for each vegetation type defined in .hrucrop. An example of an example \*.model file is the following.

```

21
VEG_NAME                undisturbed_forest      regrowth_forest
LAI_MODEL                3PG_LAI                 3PG_LAI
PHENOLOGY_MODEL         3PG_PNLG                3PG_PNLG
HT_MODEL                Ht_3PG                  Ht_3PG
WATER_STRESS_MODEL      AETPET                  AETPET
TEMP_STRESS_MODEL       Temp_3PG                 Temp_3PG
VPD_STRESS_MODEL        VPD_3PG                 VPD_3PG
TOTAL_STRESS_MASS_ACC_MODEL MA_3PG                  MA_3PG
OPTIMAL_GPP_MODEL       Beer_LAW                 Beer_LAW
RESPIRATION_MODEL       R_Const_C                R_Const_C
MASS_DIS_ROOT_MODEL     BioA_Rt_3PG              BioA_Rt_3PG
MASS_DIS_LEAF_MODEL     BioA_LF_3PG              BioA_LF_3PG
MASS_DIS_SEED_MODEL     BioA_SD_3PG              BioA_SD_3PG
DBH_MODEL               DBH_3PG                  DBH_3PG
BASAL_AREA_MODEL        BasA_3PG                 BasA_3PG
STAND_VOLUME_MODEL      StVol_3PG                StVol_3PG
MASS_LOSS_ROOT_MODEL    WL_Rt_3PG                WL_Rt_3PG
MASS_LOSS_LEAF_MODEL    WL_LF_3PG                WL_LF_3PG
MASS_LOSS_VEG_NUM_MODEL WL_NV_3PG                WL_NV_3PG
ROOT_DISTRIBUTION_MODEL ROOT_SWAT                 ROOT_SWAT
REPRODUCTION_MODEL      ReProd_3PG               ReProd_3PG

```

**Figure A5-4.** An example of the Robin \*.model input file

The vegetation growth in Robin is divided into different vegetation growth processes, and users can choose different models for each vegetation growth process. In Figure A5-4, both vegetation types are modeled with 3PG in Robin. However, the root distribution is modeled with the method in the SWAT model. More description about the available model options and mathematic equation of each model option is under preparation. The number in the first row represents the number of vegetation growth processes that will be defined for each vegetation type.

### A5.2.4 The vegetation model file (.par)

The \*.par file specifies the parameters of each vegetation growth model for each vegetation type. An example of an example \*.par file is the following.

```
#####  vegetation  parameter
59
Veg_Name          undisturbed_forest  regrowth_forest
extcoef           5.750153E-01  5.750153E-01
rue               3.423747    3.362715E+00
alpha_r           0.4          0.4
base_temp         5.008859E+00    7.940524E+00
opt_temp          15           15
max_temp          40           40
declr_rue         0.5          9.106525E-03
.....
```

**Figure A5-5.** An example of the Robin \*.par input file

The number in the second row of the example (Figure A5-5) defines the total number of parameters for both vegetation types. More detailed information about the parameters and models is under preparation. Note that when vegetation types choose a different vegetation model in \*.model file, the parameter in the parameter list used by one type of vegetation may not be used by another type of vegetation. The user can provide -1.2345 if this vegetation type does not use the parameter.

### A5.2.5 The vegetation model file (.inc)

The \*.inc file specifies the initial conditions for each vegetation type. An example of an example \*.par file is the following.

```
#####  vegetation  Initial condition
13
CropName          undisturbed_forest  regrowth_forest
w_total           305725.7438    4
w_leaf            5399.823839    1056
w_stems           1.358499E+05    36114.64968
w_seed            0          1
w_root            33000    500
ht                15          5
rootdep           5          5
dbh               17.5    20
basa_area         22          6.3
volume            176          1
yr_c              182    182
vg_number         1.095562E+03  201
stage             1          1
```

**Figure A5-6.** An example of the Robin \*.inc input file

The number in the second row defines the total number of the initial conditions defined for both vegetation types. Robin will use the value provided in the \*.inc file to initialize the state variables of vegetation type only when 1) it is the beginning of the model simulation or 2) the vegetation type in the previous growing season is different from the vegetation type in the current growing season.

#### A5.2.6 The vegetation observation file (.obs)

The \*.obs file specifies the high-level summary of each observation of one state. An example of an example \*.obs file is the following.

```
#add observation file definition in here
number_of_observation_files 7
# obsfile 1
./cropmodel/obs/LAI.txt           #(row 1)
obs_state_variables LAI           #(row 2)
level_of_observation Subbasin     #(row 3)
number_of_obs_time_step 166       #(row 4)
number_of_obs_levels 2            #(row 5)
# obsfile 2
./cropmodel/obs/Stocking.txt
obs_state_variables Stocking
level_of_observation Subbasin
number_of_obs_time_step 10
number_of_obs_levels 2
```

**Figure A5-7.** An example of the Robin \*.obs input file

In \*.obs, each observation file is defined by five rows. The first row of the observation file section defines the relative path to the observation file. The second row of the observation file section defines the type of state variable value contained in this observation file. The third row of the observation file defines the type of observed value. For example, if Subbasin is provided at here, the observed value in the observation file is the subbasin averaged value. Robin will calculate the subbasin averaged value to compare it with the observed value in this file. The fourth row of the observation file section defines the total number of timesteps in the observation file (number of rows). And the fifth row of the observation file defines the total number of observed subbasins/HRUs in the observation file (number of columns). An example of the LAI observation file is shown in the following. With the definition in the first section of the \*.obs (Figure A5-7), the value in the file represents the observed LAI for subbasins 116 and 178 at these model time steps. The -1.2345 represents NaN and will not be used by Robin. Robin will use the value in the observation files to calculate the model performance metric for

each observed state variable and each subbasin/HRU defined in the \*.obs and observation file. A more detailed description of the model performance metric calculated by Robin is under preparation.

-1	116	178
1281	-1.2345	-1.2345
1320	-1.2345	-1.2345
1640	-1.2345	-1.2345
1681	-1.2345	-1.2345
1688	-1.2345	-1.2345
2001	4.22879491	4.274688526
2017	3.895642958	3.890727671
2033	4.111508901	4.112517717
2056	4.328375176	4.432081169
2129	0.910387561	1.040205597

**Figure A5-8.** An example of the Robin LAI observation input file

### A5.3 The mathematical equation of the 3PG forest growth model in Robin

#### A5.3.1 The mass balance equation for Robin\_3PG storage components

The Robin\_3PG forest growth model, or simply Robin\_3PG, includes three biomass components: leaf, stem, and root. The unit of biomass storage components in Robin\_3PG is kg/ha representing the averaged forest biomass of leaf, stem, and root of one hydrological response unit (HRU). The input of each storage component is the net primary production. Each storage component can lose biomass due to forest mortality. The leaf and root biomass storage components will also lose biomass due to leaf drop-off and root turnover. Equation (A5-1) through Equation (A5-4) below defines the Robin\_3PG biomass change in each time step.

$$m_{leaf,i} = m_{leaf,i-1} + \phi_{leaf,i}NPP_i - \lambda_{leaf,i}m_{leaf,i-1} - \lambda_{leaf}^N \Delta N_i^m \frac{m_{leaf,i-1}}{N_{i-1}} \quad (A5-1)$$

$$m_{root,i} = m_{root,i-1} + \phi_{root,i}NPP_i - \lambda_{root,i}m_{root,i-1} - \lambda_{root}^N \Delta N_i^m \frac{m_{root,i-1}}{N_{i-1}} \quad (A5-2)$$

$$m_{stem,i} = m_{stem,i-1} + \phi_{stem,i}NPP_i - \lambda_{stem}^N \Delta N_i^m \frac{m_{stem,i-1}}{N_{i-1}} \quad (A5-3)$$

$$N_i = N_{i-1} - \Delta N_i^m + \Delta N_i^r \quad (A5-4)$$

In the above four equations,  $m_{root}$ ,  $m_{stem}$ , and  $m_{leaf}$  are the mass storage components for leaf, root and stem in [kg/ha], respectively.  $I$  and  $i-1$  represent the current time step and the previous timestep.  $\phi$

is the biomass allocation coefficient for each storage component.  $\lambda_{leaf,i}$  and  $\lambda_{root,i}$  is percentage of biomass loss in leaf and root storage component due to leaf dropoff and root turnover.  $\lambda^N$  is the percentage of biomass loss of each storage component due to the vegetation mortality.  $N$  is the number of vegetation per ha.  $\Delta N^m$  is the vegetation mortality rate [tree/day],  $\Delta N^r$  is the vegetation reproduction rate.  $NPP$  is the net primary production rate in [kg/ha/day]

### A5.3.2 The net primary production (NPP)

The amount of the daily intercepted photosynthetically active radiation ( $R_{IPAR}$ ) is calculated by the Beer's law (N.C Coops et al., 1998; Landsberg & Waring, 1997):

$$R_{IPAR,i} = R_{n,i} \times \left(1 - \exp(-k_l \times (LAI_i + virtual\_LAI))\right) \quad (A5-5)$$

where,  $R_n$  is the incoming net short wave solar radiation in [MJ m<sup>-2</sup>].  $LAI$  is the current leaf area index, and  $k_l$  is the light extinction coefficient. The unit of  $R_{IPAR,i}$  is the [MJ m<sup>-2</sup>]. The  $virtual\_LAI$  is the initial LAI of the forest at the beginning of the growing season. The  $virtual\_LAI$  is zero after the simulated  $LAI_i$  larger than the  $virtual\_LAI$ . The concept of  $virtual\_LAI$  represents the vegetation's ability to utilize the biomass in the nonstructural carbohydrate storage to initiate leaf onset (Arora & Boer, 2005). Because the Robin\_3PG does not include the nonstructural carbohydrate storage, the  $virtual\_LAI$  is an input parameter.

The gross primary production ( $GPP$ ), the amount of the dry biomass vegetation produced from the  $R_{IPAR}$ , is calculated using the radiation use efficiency approach, as shown in Equation (A5-6). The radiation use efficiency ( $RUE$ ) is the potential amount of the dry biomass produced per unit of  $R_{IPAR}$ . The amount of the  $R_{IPAR}$  that can be utilized by vegetation is reduced by the environmental stresses such as water, temperature, and vapor pressure deficit (N.C Coops et al., 1998; Landsberg & Waring, 1997), which will be introduced in section A5.3.3.

$$GPP_i = 10 \times \eta_{ma,i} \times RUE \times R_{IPAR,i} \quad (A5-6)$$

In the above equation  $\eta_{ma}$  is the stress component for mass accumulation. The unit of  $GPP$  is in [kg/ha]. The unit of  $RUE$  is in [g MJ<sup>-1</sup>]. The 10 in the equation is unit conversion factor [g/m<sup>2</sup>] to [kg/ha].

The ratio between the respiration and the  $GPP$  is a constant, then the net primary production ( $NPP$ ) is calculated by (N.C Coops et al., 1998; Landsberg & Waring, 1997):

$$NPP_i = GPP_i - \alpha_R \times GPP_i \quad (A5-7)$$

where  $\alpha_R$  is the vegetation respiration coefficient. The unit of the  $NPP$  is in  $[\text{kg ha}^{-1}]$ .

### A5.3.3 The environmental stresses

The environmental stresses included in the original 3PG forest growth model includes water, temperature, vapor pressure deficit, forest age, and nutrient (N.C Coops et al., 1998; Landsberg & Waring, 1997). In the Robin\_3PG, the impact of the nutrient stresses on forest growth were ignored. This section will describe how the environmental stresses are calculated in the Robin\_3PG. How these environmental stresses impact forest growth is described in another section.

The Landsberg & Waring (1997) use the soil water content in the soil storage to calculate water stress ( $\eta_w$ ) suffered by the forest. Instead, the Robin\_3PG uses the ratio between actual evapotranspiration ( $AET$ ) and potential evapotranspiration ( $PET$ ) to calculate the water stress. This change is needed because the Robin\_3PG is designed to be coupled with the hydrological models without a forest growth module. The soil water storage components in the hydrological model, such as the GR4J, are not equivalent to root-zone soil storage used in Landsberg & Waring (1997). For the purpose of more conveniently coupled with the hydrological models, the water stress in the Robin\_3PG is calculated as:

$$\eta_{w_i} = 1 - (AET_i/PET_i) \quad (A5-8)$$

The Landsberg & Waring (1997) use the daily averaged temperature ( $T_a$  in  $[\text{°C}]$ ) to calculate the temperature stress ( $\eta_t$ ). When the  $T_a$  is smaller than the base temperature ( $T_{base}$  in  $[\text{°C}]$ ) or  $T_a$  is larger than maximum temperature ( $T_{max}$  in  $[\text{°C}]$ ), the  $\eta_t = 0$ . In other cases, the  $\eta_t$  is calculated by:

$$\eta_{t,i} = \left( \frac{T_{a,i} - T_{base}}{T_{opt} - T_{base}} \right) \times \left( \frac{T_{max} - T_{a,i}}{T_{max} - T_{opt}} \right)^{(T_{max} - T_{opt}) / (T_{opt} - T_{base})} \quad (A5-9)$$

where  $T_{opt}$  is the optimal temperature for the forest to grow in  $[\text{°C}]$ .

The stress comes from the vapor pressure deficit ( $\eta_{vpd}$ ) is calculated by Landsberg & Waring (1997):

$$\eta_{vpd,i} = e^{-DeclR_{rue}VPD_i} \quad (A5-10)$$

where the  $VPD_i$  vapor pressure deficit in  $[\text{kPa}]$  and  $DeclR_{rue}$  is the rate of decline in radiation use coefficient per unit increase of the vapor pressure deficit in  $[(\text{g MJ}^{-1}) \text{kPa}^{-1}]$ .

Following the Landsberg & Waring (1997), the stress comes from the forest age ( $\eta_{age}$ ) is calculated by:

$$\eta_{age,i} = \frac{1}{1 + [(yr_{c,i}/yr_{max})/\alpha_{sts\_age1}]^{\alpha_{sts\_age2}}} \quad (\text{A5-11})$$

where  $yr_{c,i}$  is the current forest age, and  $yr_{max}$  is the maximum forest age,  $\alpha_{sts\_age1}$  and  $\alpha_{sts\_age2}$  are two coefficient parameters.

The total stress that impacts the gross primary production of the forest ( $\eta_{ma}$ ) is calculated by Landsberg & Waring (1997):

$$\eta_{ma,i} = \eta_{age,i} \times \eta_{t,i} \times \min(\eta_{w,i}, \eta_{vpd,i}) \quad (\text{A5-12})$$

And the total stress that impacts the biomass allocation of the forest is calculated by Landsberg & Waring (1997):

$$\eta_{md,i} = \eta_{age,i} \times \min(\eta_{w,i}, \eta_{vpd,i}) \quad (\text{A5-13})$$

#### **A5.3.4 The forest phenology development**

The original 3PG forest growth model does not include forest phenology development components. However, as discussed in section 5.3.2, the four forest phenology stages in the Canadian Terrestrial Ecosystem Model (CTEM, Arora & Boer, 2005) were adjusted and adapt into the Robin\_3PG to improve the LAI simulation within one growing season. The four forest phenology stages are the maximum growth stage, the normal growth stage, the leaf fall stage, and the dormancy stage (Arora & Boer, 2005). This section will describe the definition of each phenology stage and how the forest will move from one stage to the next stage.

The dormancy stage is when the environmental condition is unfavorable for the growth of the delicious forest. The forest will move from the dormancy stage to the maximum growth stage when the number of consecutive days with a daily averaged temperature larger than the forest base temperature ( $T_{base}$  in [°C]) is equal to  $cum\_day\_t\_lg\_tbase$ , which is an input parameter in the number of days.

The deciduous forest would end the maximum growth stage and move to the normal growth stage when leaf biomass reaches a certain percentage ( $r\_mleaf\_max$ ) of the maximum leaf biomass ( $m_{leaf}^{max}$ ) given that stem and root biomass can support (Arora & Boer, 2005). The  $r\_mleaf\_max$  is the input parameter and the  $m_{leaf}^{max}$  is determined at the beginning of each growing season by:

$$m_{leaf}^{max} = N^{ini} \times \alpha_{leaf}^a \times (dbh^{ini})^{\alpha_{leaf}^n} \quad (A5-14)$$

where  $\alpha_{leaf}^a$  and  $\alpha_{leaf}^n$  are two coefficients parameters.  $N^{ini}$  is the forest density/stocking at the beginning of the growing season ([number of tree ha<sup>-1</sup>]). The  $dbh^{ini}$  is the forest averaged DBH at the beginning of the growing season.

The deciduous forest would transit to the leaf fall stage based on the day length below certain hours and the average air temperature smaller than the cold temperature ( $T_{cold}$  in [°C]) for several ( $cum\_day\_t\_lt\_tcold$ ) consecutive days. Both  $T_{cold}$  and  $cum\_day\_t\_lt\_tcold$  are input parameters.

The deciduous forest will move from the leaf fall stage to the dormant stage when several consecutive days ( $cum\_day\_t\_lg\_tbase$ ) with a daily averaged temperature smaller than the forest base temperature ( $T_{base}$  in [°C]).

### A5.3.5 The biomass allocation

The biomass allocation strategy of the forest is the same in the entire growing season because the forest phenology component is not needed for the original 3PG forest growth model in the monthly timestep. However, as discussed in section 5.3.2, the four forest phenology stages in the Canadian Terrestrial Ecosystem Model (CTEM, Arora & Boer, 2005) were adapted into the Robin\_3PG to improve the LAI simulation within one growing season. The four forest phenology stages are: the maximum growth stage, the normal growth stage, the leaf fall stage, and the dormancy stage (Arora & Boer, 2005). In each forest phenology stage, the biomass allocation strategy is different, which will be introduced in this section. The definition of each phenology is described in section A5.3.4.

In the maximum growth stage, all the  $NPP$  will be allocated to the leaf. The  $\phi_{r,i} = 0$ ,  $\phi_{stem,i} = 0$  and  $\phi_{leaf,i} = 1$ .

When the forest arrives at the normal growth stage, the  $NPP$  will be allocated to the leaf, stem, and root. Following the Landsberg & Waring (1997) the  $NPP$  allocated to the root is impacted by the environmental stresses  $\eta_{md}$ :

$$\phi_{r,i} = \frac{\phi_{Root_{min}} \phi_{Root_{max}}}{\phi_{Root_{min}} + (\phi_{Root_{max}} - \phi_{Root_{min}}) \eta_{md,i}} \quad (A5-15)$$

where  $\phi_{Root_{min}}$  and  $\phi_{Root_{max}}$  are the minimum and maximum root biomass allocation fraction.

Then, the amount of the *NPP* allocated to the leaf storage components is calculated by:

$$\phi_{leaf,i} = (1 - \phi_{r,i}) \times \frac{m_{leaf}^{max} - m_{leaf,i-1}}{m_{leaf,i-1} - r\_mleaf\_max \times m_{leaf}^{max}} \quad (A5-16)$$

where  $m_{leaf}^{max}$  is the maximum leaf biomass for the current growing season, the  $r\_mleaf\_max$  is the fraction of the leaf biomass at the end of the maximum growth stage, which is an input parameter.

The fraction of the *NPP* allocated to the leaf is

$$\phi_{stem,i} = 1 - \phi_{r,i} - \phi_{leaf,i} \quad (A5-17)$$

When the forest reaches the leaf fall stage, the *NPP* won't allocate to the leaf ( $\phi_{leaf,i} = 0$ ), and the *NPP* allocated to the root and stem is the same as Equation (A5-15) and Equation (A5-17).

### A5.3.6 Leaf fall and root turnover losses

The root turnover rate is a constant ( $\lambda_{root,i} = \lambda_{root}$ , in % day<sup>-1</sup>). The leaf fall rate at the fast growth stage is zero.

The leaf fall rate in the normal and leaf fall stage is calculated by :

$$\lambda_{leaf,i} = \lambda_{leaf,i}^n + \lambda_{leaf,i}^w + \lambda_{leaf,i}^t \quad (A5-18)$$

where  $\lambda_{leaf,i}^n$  is the normal leaf fall rate,  $\lambda_{leaf,i}^w$  is the leaf fall rate due to water stress,  $\lambda_{leaf,i}^t$  is the leaf fall rate due to temperature stress.

The leaf fall rate due to water stress is calculated by:

$$\lambda_{leaf,i}^w = \lambda_{leaf,i}^{w,max} \times (1 - \eta_{w,i})^{\lambda_{leaf}^{wn}} \quad (A5-19)$$

where  $\lambda_{leaf,i}^{w,max}$  is the maximum leaf fall due to water stress in [% day<sup>-1</sup>].  $\eta_{w,i}$  is the water stress, and  $\lambda_{leaf}^{wn}$  is a coefficient.

The leaf fall rate due to temperature stress is calculated by:

$$\lambda_{leaf,i}^t = \lambda_{leaf,i}^{t,max} \times (1 - \eta_{t,i})^{\lambda_{leaf}^{tn}} \quad (A5-20)$$

where  $\lambda_{leaf,i}^{t,max}$  is the maximum leaf fall due to temperature stress in [% day<sup>-1</sup>].  $\eta_{t,i}$  is the water stress, and  $\lambda_{leaf}^{tn}$  is an coefficient.

The normal leaf fall rate is zero in the forest's normal growth stage. In the leaf fall stage, the leaf fall rate is calculated by:

$$\lambda_{leaf,i}^n = \frac{\lambda_{leaf}^{n,max} \lambda_{leaf}^{n,min}}{\lambda_{leaf}^{n,min} + (\lambda_{leaf}^{n,max} - \lambda_{leaf}^{n,min}) \exp\left(-yr_{c,i}/yr_{\lambda_{leaf}} \left(1 + \ln\left(1 + \lambda_{leaf}^{n,max} / \lambda_{leaf}^{n,min}\right)\right)\right)} \quad (A5-21)$$

where  $\lambda_{leaf}^{n,min}$  and  $\lambda_{leaf}^{n,max}$  is the minimum and maximum leaf fall rate at different forest ages.  $yr_{\lambda_{leaf}}$  is the forest age when  $\lambda_{leaf,i}^n$  is in the middle of the  $\lambda_{leaf}^{n,min}$  and  $\lambda_{leaf}^{n,max}$

### A5.3.7 Forest mortality

The forest mortality rate ( $\Delta N_i^m$  in [number of tree ha<sup>-1</sup>]), the decrease of the number of trees per hectare, may be caused by two causes: the forest age and the density. It is calculated by:

$$\Delta N_i^m = \Delta N_i^{m,age} + \Delta N_i^{m,selfthin} \quad (A5-22)$$

where  $\Delta N_i^{m,age}$  is the vegetation mortality rate [number of tree ha<sup>-1</sup>] due to age, and  $\Delta N_i^{m,selfthin}$  is the mortality rate [number of tree ha<sup>-1</sup>] due to the self-thinning process.

The forest age-induced mortality is calculated by the following two equations (A5-23 and A5-24):

$$\Delta N_i^{m,age} = \lambda_i^{m,age} \times N_{i-1} \quad (A5-23)$$

$$\lambda_i^{m,age} = \lambda_{min}^{m,age} + (\lambda_{max}^{m,age} - \lambda_{min}^{m,age}) \times \exp\left(-\ln 2 \times \left(yr_{c,i}/yr_{\lambda_{age}}\right)^{\alpha_{\lambda_{age}}}\right) \quad (A5-24)$$

where  $\lambda_{min}^{m,age}$  and  $\lambda_{max}^{m,age}$  is the minimum and maximum vegetation mortality due to age in the unit [% day<sup>-1</sup>],  $yr_{\lambda_{age}}$  is the vegetation age when the age-related mortality rate in the middle of the  $\lambda_{min}^{m,age}$  and  $\lambda_{max}^{m,age}$ .  $\alpha_{\lambda_{age}}$  is the coefficient parameter.

The density-induced forest mortality is calculated using the self-thinning line. The self-thinning line is an observed relationship between averaged stem biomass/DBH and forest density in the mature forest (Landsberg & Waring, 1997; Pickard, 1983; Zeide, 2010). It shows that the forest density of a mature forest would decrease with the increase of the forest averaged stem biomass/DBH. The forest models like 3PG (N.C Coops et al., 1998; Landsberg & Waring, 1997) and the LANDIS PRO (Wang et al., 2013) use the forest density on this line as a threshold value. The forest density-induced mortality will occur when the modeled forest density is larger than the forest density on the self-thinning line. In Robin\_3PG, the self-thinning line is defined as:

$$N_{i,selfthin} = 1000 \left( \frac{m_{stem,i-1}}{N_{i-1}} \right)^{\alpha_{N,stem} m_{stem,1000}} \quad (A5-25)$$

where the  $m_{stem,1000}$  is the stem biomass per tree when the  $N$  is 1000/ha,  $\alpha_{N,stem}$  is an coefficient parameter. Both  $m_{stem,1000}$  and  $\alpha_{N,stem}$  are input parameters.

And then, when the current forest density ( $N_{i-1}$ ) larger than the  $N_{i,selfthin}$  at the current stem biomass  $m_{stem,i-1}$ , the density-induced forest mortality is calculated by:

$$\Delta N_i^{selfthin} = \frac{\max(N_{i-1} - N_{i,selfthin}, 0)}{\alpha_N^m} \quad (A5-26)$$

where  $\alpha_N^m$  is the delay of the self-thinning process in days.

### A5.3.8 Forest reproduction

The vegetation reproduction rate is impacted by the current vegetation density when vegetation density is smaller than the canopy's full closer density ( $N_{i,closer}$ ), the vegetation reproduction rate will be a constant `reproduct_rate`. The vegetation reproduction rate will decrease to zero when the vegetation density reaches its maximum value.

The vegetation number when the forest got canopy closer ( $N_{i,closer}$ )

$$N_{i,closer} = pec\_full\_occupied \times N_{i,selfthin} \quad (A5-27)$$

Where `pec_full_occupied` is an input coefficient in (0,1).

The maximum forest density is calculated by:

$$N_{i,max} = pec\_full\_occupied \times N_{i,selfthin} \quad (A5-28)$$

When the forest density smaller than the canopy's full closer density ( $N_{i,closer}$ ). The rate of the forest reproduction is calculated by:

$$\Delta N_i^r = N_{i-1} \times reproduct\_rate \quad (A5-29)$$

When the forest density larger than the canopy's full closer density ( $N_{i,closer}$ ). The rate of the forest reproduction is calculated by:

$$\Delta N_i^r = N_{i-1} \times reproduct\_rate \times \frac{N_{i,max} - N_{i-1}}{N_{i,max} - N_{i,closer}} \quad (A5-30)$$

### A5.3.9 Forest geometries

The averaged specific leaf area [ $SLA$ ,  $m^2 kg^{-1}$ ] is calculated by:

$$SLA_i = SLA_{min} + (SLA_{max} - SLA_{min}) \times \exp\left(-\ln 2 \times (yr_{c,i}/yr_{SLA})^2\right) \quad (A5-31)$$

where  $SLA_{min}$  and  $SLA_{max}$  is the minimum and maximum forest specific leaf area in [ $SLA$ ,  $m^2 kg^{-1}$ ],  $yr_{SLA}$  is the vegetation age when the  $SLA$  at the middle of the  $SLA_{min}$  and  $SLA_{max}$ .

The forest leaf area index is calculated by:

$$LAI_i = m_{leaf,i-1} \times SLA_i \times 0.0001 \quad (A5-32)$$

The averaged DHB of the forest is calculated by

$$dbh_i = \left(\frac{m_{stem,i-1}}{N_{i-1}} \times \frac{1}{\alpha_{dbh_a}}\right)^{\frac{1}{\alpha_{dbh_n}}} \quad (A5-33)$$

where  $\alpha_{dbh_a}$  and  $\alpha_{dbh_n}$  are two coefficient parameters.

The basal area of the forest is calculated by:

$$basal\_area_i = N_{i-1} \times 3.14 \times \left(\frac{dbh_{i-1}}{200}\right)^2 \quad (A5-34)$$

## A6 The performance of Raven\_Robin\_3PG in forest growth modeling

This appendix includes the observed and simulated forest allometric measurements (i.e., density, stem biomass and basal area) of regrowth forest and undisturbed forest from the best calibrated Raven\_Robin\_3PG model from Chapter 5.

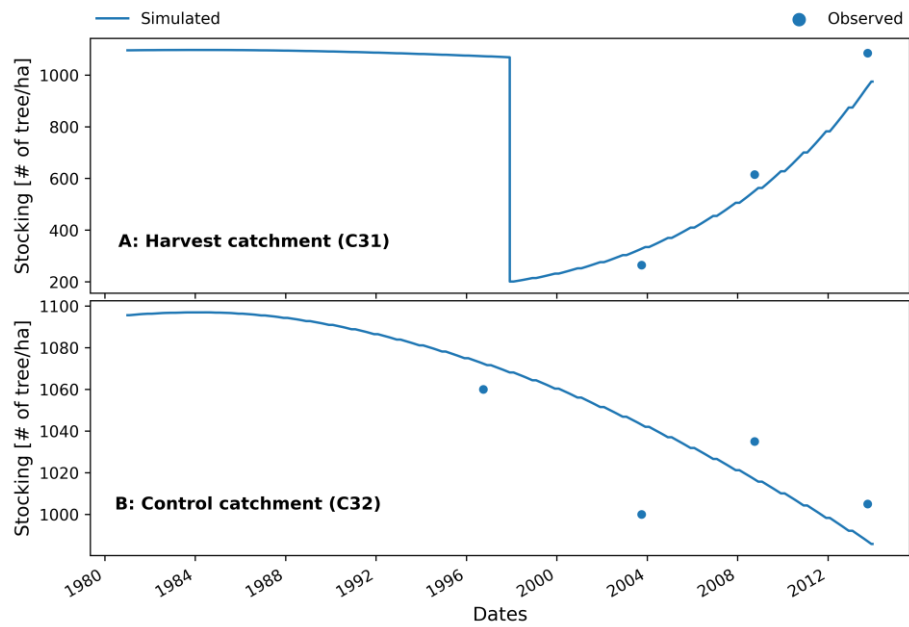


**Figure A6-1.** The observed and simulated stocking [number of the tree/ha] of harvest and control catchment from the best-calibrated Raven\_Robin\_3PG model.

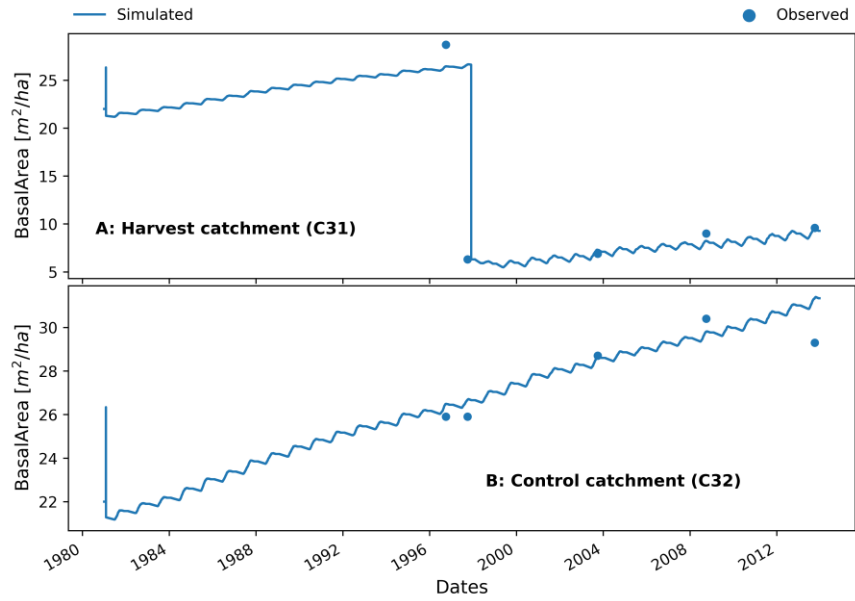


**Figure A6-2.** The observed and simulated basal area [ $m^2/ha$ ] of harvest and control catchment from the best-calibrated Raven\_Robin\_3PG model.

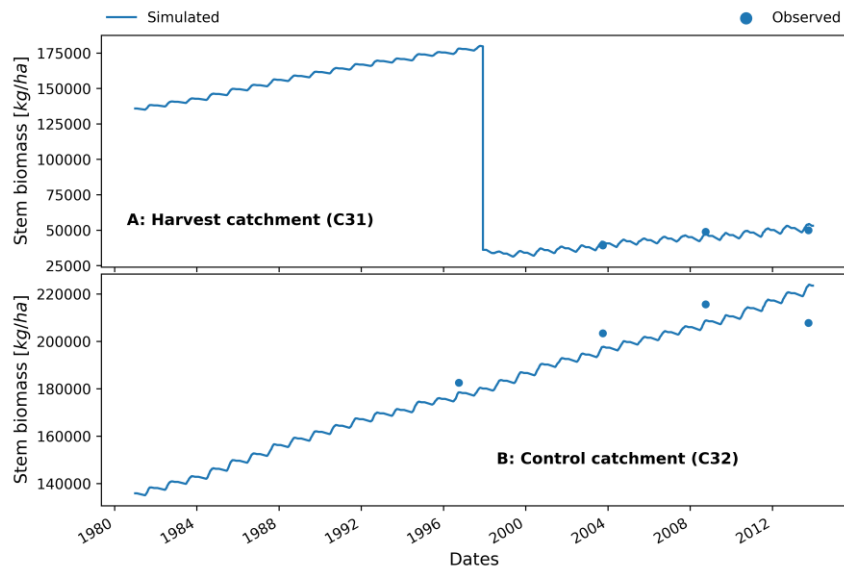


**Figure A6-3.** The observed and simulated stem biomass [ $kg/ha$ ] of harvest and control catchment from the best-calibrated Raven\_Robin\_3PG model.